Università degli Studi di Padova
Centro Ricerche Fusione (CRF)

Ghent University

Joint research doctorate in

FUSION SCIENCE AND ENGINEERING - XXXV Cohort

3D Nonlinear MHD modelling studies:
Plasma Flow and Realistic Magnetic Boundary Impact
on Magnetic self-organisation in Fusion Plasmas

Thesis realised thanks to the funding offered by CARIPARO

Student: Luca Spinicci
Identification Number: 1227392

Padova, 31 March 2023.

Abstract

The reversed-field pinch (RFP) is a toroidal device for the magnetic confinement of a fusion plasma, similar to the tokamak but with a relatively stronger induced plasma current. RFP plasmas are subject to various relaxation processes, the most macroscopic of which, the kink and the tearing modes, are suitably described in a fluid-dynamics framework called magnetohydrodynamics (MHD).

In the past two decades a new enhanced-confinement scenario has been experimentally demonstrated for the RFP. This is known as "Quasi Single Helicity" (QSH) state and consists in the intermittent dominance of a single Fourier mode over the rest of the magnetic spectrum, generating a significant part of the magnetic field through a self-organised electrostatic dynamo effect. QSH states can be stimulated by resonant edge magnetic perturbations or they can emerge as a spontaneous self-organisation when the plasma current exceeds a device-specific threshold (1 MA for RFX-mod).

Advanced numerical modelling has traditionally played a key role in the study of this process, and indeed the spontaneous helical states in the RFP were found to form in nonlinear MHD simulations even before their experimental observation. However, some features of the experimentally observed spontaneous and systematic emergence of QSH states with a certain preferential toroidal periodicity still lack of a fully self-consistent quantitative predictability. Past studies performed with the 3D nonlinear MHD simulations code SpeCyl suggest that a key role is played by the interplay between the plasma and its magnetic boundary.

For this reason the past decade marked a consistent endeavour towards the implementation of more realistic boundary conditions (BCs) in SpeCyl. First qualitative experimental-like QSH states could be reproduced by implement-

iii

ing a fixed magnetic perturbation at plasma boundary, on the top of the traditional formulation, featuring an ideal wall in direct contact with the plasma. At the beginning of my PhD, an effort to model the boundary as a thin resistive shell had already started and was awaiting to be completed and carefully validated.

The main goal of my PhD research was the formulation, implementation in SpeCyl, and verification of a realistic set of BCs, representing a resistive shell in contact with the plasma, and surrounded by a vacuum region and an ideal wall placed at finite tuneable distance, along with a realistic description of the edge flow. This is a very general set-up, of interest for various magnetic configurations, that allows to reproduce a full range of experimental conditions, from the previous ideal-wall limit to a free plasma-vacuum interface.

My work was articulated in several steps: 1) in-depth study of the linear theory of current-driven MHD instabilities, along with the implementation of a linear-stability numeric tool to provide a reliable benchmark for SpeCyl; 2) careful analysis of the SpeCyl code and of its existing BCs (the ideal-wall and the resistive-shell formulations) and characterisation against the linear MHD theory. This made possible to reveal critical inconsistencies in the thin-shell BCs, motivating a major reframe in the modelling of the velocity boundary; 3) formulation and implementation of the new BCs (thin-shell, surrounding vacuum and outer ideal wall, realistic 3D edge flow). This required the implementation of an original deconvolution technique, to deal with the 3D velocity BCs in the spectral code SpeCyl; 4) nonlinear verification of the new BCs module against the independent 3D nonlinear MHD code Pixie3D, and verification benchmark against the linear MHD theory of external kink instabilities.

The excellent results obtained in both verification studies clearly demonstrate the correctness of the implementation of the new SpeCyl's BCs and motivate future validation studies against real experimental data from the RFX-mod device and its next upgrade RFX-mod2.

Abstract in Dutch

De reversed-field pinch (RFP) is een toroïdale configuratie voor de magnetische opsluiting van een fusieplasma, vergelijkbaar met de tokamak maar met een relatief sterkere geïnduceerde plasmastroom. RFP-plasma's zijn onderhevig aan verschillende relaxatieprocessen, waarvan de meest macroscopische, de kink- en tearing-modes, adequaat worden beschreven in een vloeistofdynamisch kader dat magnetohydrodynamica (MHD) wordt genoemd. In de afgelopen twee decennia is voor de RFP experimenteel een nieuw scenario van verbeterde opsluiting aangetoond. Dit staat bekend als de "Quasi Single Helicity"- toestand (QSH) en bestaat uit de intermitterende dominantie van een enkele Fourier-mode over de rest van het magnetische spectrum, waarbij een aanzienlijk deel van het magnetisch veld wordt opgewekt door een zelfgeorganiseerd elektrostatisch dynamo-effect. QSH-toestanden kunnen worden gestimuleerd door resonante magnetische randstoringen, of ze kunnen ontstaan als spontane zelforganisatie wanneer de plasmastroom een apparaatspecifieke drempel overschrijdt (1 MA voor RFX-mod).

Geavanceerde numerieke modellering heeft traditioneel een sleutelrol gespeeld in de studie van dit proces, en de spontane helische toestanden in de RFP bleken zich inderdaad te vormen in niet-lineaire MHD-simulaties, zelfs vóór hun experimentele waarneming. Sommige kenmerken van het experimenteel waargenomen spontane en systematische ontstaan van QSH-toestanden met een bepaalde preferentiële toroïdale periodiciteit zijn echter nog steeds niet volledig zelfconsistent kwantitatief te voorspellen. Eerdere studies met de 3D niet-lineaire MHD simulatiecode SpeCyl suggereren dat de wisselwerking tussen het plasma en zijn magnetische rand een sleutelrol speelt.

Daarom is het afgelopen decennium consequent gewerkt aan de implementatie van meer realistische randvoorwaarden in SpeCyl. Eerst konden kwali-

tatieve experimentele QSH-toestanden worden gereproduceerd door een vaste magnetische perturbatie aan de plasmagrens te implementeren, bovenop de traditionele formulering met een ideale wand in direct contact met het plasma. Aan het begin van mijn doctoraatsonderzoek was al begonnen met het modelleren van de rand als een dunne resistieve mantel, die nog moest worden voltooid en zorgvuldig gevalideerd.

Het hoofddoel van mijn doctoraatsonderzoek was de formulering, implementatie in SpeCyl, en verificatie van een realistische reeks randvoorwaarden, die een resistieve mantel in contact met het plasma voorstellen, omgeven door een vacuümgebied en een ideale wand op een eindig instelbare afstand, samen met een realistische beschrijving van de randstroming. Dit is een zeer algemene opstelling, van belang voor verschillende magnetische configuraties, die het mogelijk maakt een volledig scala van experimentele omstandigheden te reproduceren, van de eerdere ideale-wand tot een vrij plasma-vacuüm grensvlak.

Mijn werk bestond uit verschillende stappen: 1) grondige studie van de lineaire theorie van stroom-gedreven MHD instabiliteiten, samen met de implementatie van een numerieke tool voor lineaire stabiliteit, om een betrouwbare benchmark te bieden voor SpeCyl; 2) zorgvuldige analyse van de SpeCyl code en van de bestaande randvoorwaarden (de formulering met ideale-wand en resistieve schil) en karakterisering in het licht van lineaire MHD-theorie. Dit maakte het mogelijk kritieke inconsistenties in de randvoorwaarden van de dunne schil aan het licht te brengen, hetgeen een belangrijke herziening rechtvaardigde van de modellering van de snelheidsgrens; 3) formulering en implementatie van de nieuwe randvoorwaarden (dunne schil, omringend vacuüm en buitenste ideale wand, realistische 3D-randstroming). Dit vereiste de implementatie van een originele deconvolutietechniek, om de randvoorwaarden voor de snelheid in 3D te kunnen behandelen in de spectrale code SpeCyl; 4) niet-lineaire verificatie van de nieuwe module voor randvoorwaarden ten opzichte van de onafhankelijke 3D-niet-lineaire MHD-code Pixie3D, en verificatiebenchmark tegen de lineaire MHD-theorie van externe kinkinstabiliteiten.

De uitstekende resultaten verkregen in beide verificatiestudies tonen duidelijk de correctheid aan van de implementatie van de nieuwe randvoorwaarden in SpeCyl en motiveren toekomstige validatiestudies tegen echte experimentele gegevens van RFX-mod en zijn volgende upgrade RFX-mod2.

Summary

The increasing World energy demand compellingly requires new and clean energy sources to sustain the human population growth and provide decent life standards to everyone. Nuclear fusion comes as a promising solution to face this indispensable challenge.

One of the most advanced lines of research for nuclear fusion relies on the magnetic confinement of a hot hydrogen plasma in toroidal devices: such as the tokamak, the stellarator, and the reversed-field pinch (RFP). The confined plasma equilibrium is yet subject to relaxation processes of diverse nature and scale: some of the most macroscopic are suitably described with a fluid-dynamics approach, called magneto-hydrodynamics (MHD).

My thesis was conducted in Padova, where the world largest reversed-field pinch experiment (RFX-mod) is located. Among the above-mentioned relaxation processes, a central relevance for this class of devices has the nonlinear saturation of a current-driven instability, which produces the intermittent dominance of a single MHD mode over the rest of the magnetic spectrum. This is called a quasi-single helicity state (QSH) and yields a significant enhancement of confinement properties.

Advanced numerical modelling has traditionally played a key role in the study of this process, and indeed RFP spontaneous helical states were found to form in nonlinear 3D MHD modelling even before their experimental discovery. However, some features of the experimentally observed spontaneous and systematic emergence of QSH states with a certain preferential toroidal periodicity still lack of a fully self-consistent quantitative predictability. Past studies performed with the 3D nonlinear MHD simulations code SpeCyl suggest that a key role is played by the interplay between the plasma and its

magnetic boundary.

For this reason, the past decade marked a consistent endeavour towards the implementation of more realistic boundary conditions (BCs) in SpeCyl. A first important step in this direction was made with the implementation at the plasma boundary of fixed applied magnetic perturbations, replacing the original assumption of a perfectly conducting wall, in direct contact with the plasma. This led to the first simulations qualitatively reproducing experimental-like QSH states, although the toroidal periodicity of such states was enforced by the applied magnetic perturbations, mimicking the experimental observations. In the quest for a self-consistent model for the emergence of QSH states, the second step was to focus on the implementation of resistive shell boundary conditions replacing the conventional ideal wall approximation. At the beginning of my PhD, an effort to model the boundary as a thin resistive shell had already started and was awaiting to be completed and carefully validated.

The main goal of this PhD thesis is the formulation, implementation in SpeCyl, and verification of a realistic set of BCs, representing a resistive shell in contact with the plasma, and surrounded by a vacuum region and an ideal wall placed at finite tunable distance. This is a very general set-up, of interest for various magnetic configurations, that allows to reproduce a full range of experimental conditions, from the previous ideal-wall limit to a free plasma-vacuum interface (by raising the thin shell resistivity to a large value and displacing the external ideal wall far from the plasma).

To achieve such a goal, my PhD had to face several stages: I list here after the major milestones

- Detailed analytical study of current-driven instabilities, such as the ideal external kink and the tearing mode.

- Development and extended testing of a linear-stability numeric tool, dubbed LENS (*i.e.*, Linear Euler-Newcomb Solver, from the names of the main differential problems it solves), providing reliable benchmark for SpeCyl.

- Comprehensive reorganisation of diverse documentary material about the work-flow of the SpeCyl code (early publications, unpublished or cumulated hand-written notes, the source-code...).

- Nonlinear benchmark of the main pre-existing sets of boundary conditions against the linearised theory of ideal kink modes and tearing

modes.

- Progressive formulation and implementation of an upgraded set of boundary conditions (thin shell, vacuum, external ideal wall, realistic modelling of edge flow). Table 1 illustrates for every Chapter of this Thesis the nickname and the main features of the set of BCs used therein. The pre-existing sets of BCs are marked in green, the ones that I developed are in red. A general scheme of the evolution of SpeCyl's boundary conditions can be found in Fig. 1.

- Nonlinear verification against the independent advanced 3D MHD nonlinear code Pixie3D (massively parallel, fully implicit, finite-elements, arbitrary curvilinear geometry). The two codes had already been successfully verified with ideal wall boundary conditions, in [Bonfiglio10].

Table 1: Scheme of the BCs used in different chapters of this thesis. **Green** marks the pre-existing sets of BCs, in **red** are the ones that I implemented.

	plasma + ideal wall	plasma + resistive wall + vacuum + ideal wall
axisymmetric edge flow	"SpeCyl.1" Chap. 5	"SpeCyl.2.V00" Chap. 6
full-spectrum edge flow	"SpeCyl.1.Vmn" Chap. 7	"SpeCyl.2" Chaps. 8-10

The work presented in my thesis concerns both the tokamak and the RFP geometry, although the preliminary analytical studies are mostly restrained to the large aspect ratio tokamak ("straight tokamak") that presents minor analytical complexity.
The above stages are presented in the following Chapters.

Preliminary analytical studies (in the straight tokamak, with circular cross section) (Chaps. 3-4). With the purpose of testing the new set of BCs against some well established results of the linear theory of MHD instabilities, I started my PhD with an in-depth study of analytical models, concerning in particular two peculiar MHD instabilities of fusion plasmas: the ideal external kink mode and the resistive tearing mode.
For the ideal kink instability, the linearisation of the MHD equations can be reduced to a variational principle, the "Energy principle", that can be treated as an eigenvalue-eigenvector differential problem. The stability analysis against the tearing modes of an initially small perturbation of the toroidal
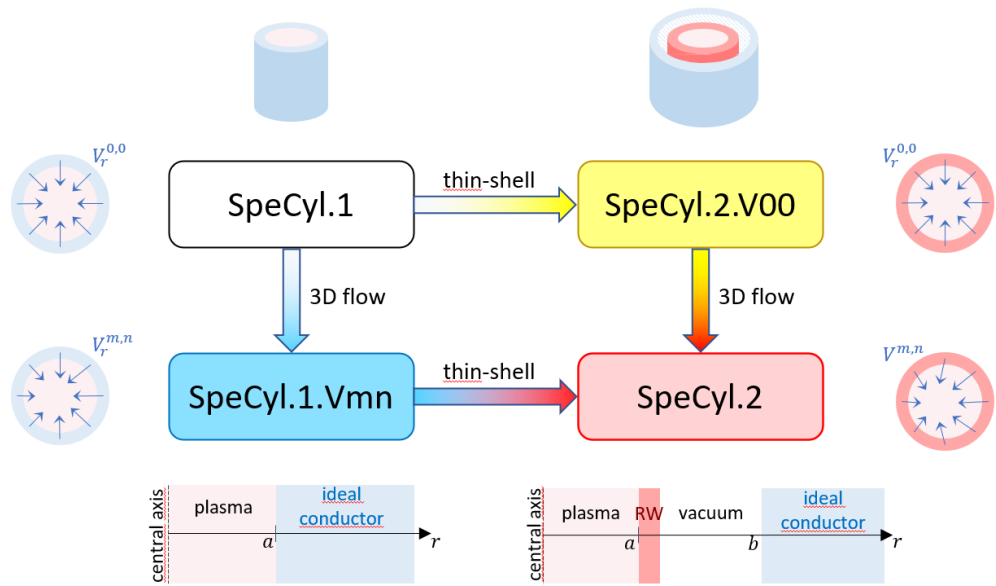
x

Figure 1: General scheme of the evolution of SpeCyl's BCs. SpeCyl.1 features an ideal wall in contact with the plasma and axisymmetric radial flow. SpeCyl.1.Vmn introduces a thin resistive wall (RW) at plasma edge, surrounded by vacuum and by an outer conductor, but keeps the flow boundary unchanged. SpeCyl.1.Vmn is obtained from SpeCyl.1 by adding a 3D velocity boundary formulation. SpeCyl.2 combines the thin shell magnetic boundary to the 3D edge flow into a more realistic and comprehensive set of boundary conditions.

magnetic flux, instead, relies on a geometric property of the flux perturbation itself, and it is still amenable of an eigenvalue-eigenvector differential approach.

I implemented and numerically tested a numeric tool dubbed LENS, solving the involved ordinary-differential equations, to produce reliable figures of merit for the benchmark verification of SpeCyl.

Nonlinear benchmark of the existing BCs modules (SpeCyl.1 and SpeCyl.2.V00) (Chaps. 5-6). Thanks to the pseudo-analytical figures of merit provided by LENS, the first benchmark studies revealed some major inconsistencies in the growth rates and radial profiles. Indeed, the assumption of a null radial plasma velocity at the boundary (except from the axisymmetric pinch velocity component) has been speculated (and finally proved to be) as a possible source of such unsatisfactory benchmaking, especially against free-boundary instabilities as the external kinks, hence motivating a major reformulation.

Formulation of a new set of BCs (Chaps. 7-8). The above observation led to the main challenge of my PhD thesis: the generalisation of the new BCs to the case of non-axisymmetric, radial or three-dimensional velocity boundary. This is a highly non-trivial task, in particular because SpeCyl is a spectral code (*i.e.*, its model equations are written in Fourier space with respect to the two periodic - axial and azimuthal - coordinates). This implies that every product in the physical space is mapped into a nonlinear convolution of modes by the Fourier transform. This problem was totally avoided by the previous radial-axisymmetric implementation for the edge flow velocity. A deconvolution approximated technique was developed and new, more comprehensive magneto-fluid boundary conditions were obtained. A preliminary implementation of non-axisymmetric flow components was tested in the ideal wall BCs ("SpeCyl.1.Vmn", in Tab. 1), to cut complexity down and test the deconvolution method in a simpler environment. Very promising results were found in a nonlinear verification against the independent 3D MHD simulations code Pixie3D, in the same limit of ideal wall boundary conditions.

As a result of this development, the same deconvolution technique was also applied to produce the final full set of thin resistive shell magneto-fluid boundary conditions: "SpeCyl.2".

Verification and nonlinear benchmark (Chaps. 9-10) To perform a careful verification of the new implementation of resistive shell boundary conditions in both SpeCyl and Pixie3D codes, I started to collaborate with Dr. Chacón, thanks to a one month stay at Los Alamos NL (partially funded by LANL). The scope of this collaboration was a nonlinear cross-verification benchmark, aimed at ensuring mathematical and numerical correctness of both codes.

This challenging endeavour eventually produced the final version of our new boundary conditions, which constitutes the greatest achievement presented in this dissertation. Excellent linear and nonlinear agreement has been found against Pixie3D simulations on several case studies, both in tokamak and RFP geometries.

Complementary to mathematical correctness is physical faithfulness, which was consequently ensured by a finally successful benchmark against linear theory predictions.

The code is now ready to investigate the physics of fusion plasmas with a more realistic set of boundary conditions.

Outline for this thesis This dissertation is organised in six parts: Part I consists in a general introduction to nuclear fusion and magnetic confinement. MHD equations are presented, along with an introduction to the QSHs in the RFP. Part II deals with the analytical theory of the linear MHD instabilities driven by plasma current. Along with the analytical derivations and the details on the implementation of my linear-instabilities numeric solver, great attention is paid to the physical understanding of such phenomena. Part III offers a detailed overview of the state of art of SpeCyl's implementation at the beginning of my PhD programme: this is the valuable and structured synthesis of early documentary works, sparse unpublished material and thorough reading of the source code. Chapter 5 presents the work flow of the code's main loop and the ideal wall boundary conditions. Chapter 6 illustrates the thin resistive shell theory and its preliminary implementation as a plasma interface. At the end of each of these chapters, I present the outcomes of a linear benchmark study against MHD instabilities, performed with either set of BCs. Part IV presents the formulation, and implementation of our new set of boundary conditions, starting from the deconvolution technique in Chap. 7 and concluding with a detailed description of the final set-up in Chap. 8. Part V presents the verification and linear-benchmark studies. Finally, Part VI presents my conclusions and final remarks.

Contents

Part I

Introduction

General introduction to fusion energy and confinement concepts

1.1 Global energy demand

No form of life can exist without energy. Human life is no exception. During the Neolithic age, our ancestors would get 15 to 40 calories per muscular calory spent in harvesting or hunting and a few hectares were needed to sustain a single human being [Smil94]. Today, the supply of much larger energy flows (fertilisers, agricultural machinery, electricity, fossil fuels...) has decoupled the yield from the human labour energy investment: only 0.2 hectares in average suffice nowadays to feed a human life [Alimonti17]. A similar portrait can be drawn for every human activity [IEA98]: from travelling to working we strongly depend on external energy sources, be them of fossil origin, geothermal, solar-, wind-, or hydro-power, biomass, or nuclear. Such a convenient condition, along with the progress of scientific research, has certainly contributed to the World population growth by five billions in the last sixty years, as reported in Fig. 1.1. We can also see that the current estimates indicate all but an inverted trend for the rest of this century. Not only a larger worldwide population requires a greater deal of energy to feed and survive, but there is a precise link between the quality of life and the access to a minimum amount of primary energy supply per person. Any explicit quantifier of human life "quality" is of course subject to some arbitrariness: we refer here to the one adopted by the United Nations. In [Rezaee21] we read: "The Human Development Index (HDI) is an indicator of social standards that consists of three areas: life expectancy, access to education and literacy, and living conditions and income. The index depends on a number of factors based on development, including the ability to perform tasks, such
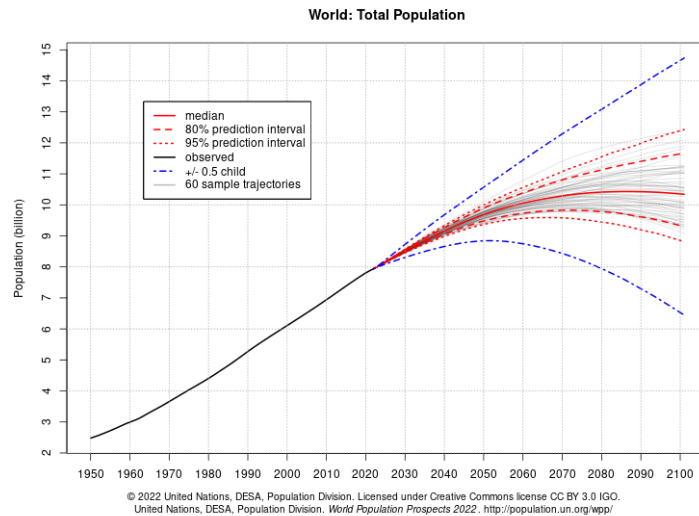
Figure 1.1: World population growth from 1950 and prospective growth by the end of the century

as access to proper nutrition, health, occupation, education, and community participation."

Figure 1.2 shows quite incontestably that the life standards that we consider as a prerequisite for decent fulfilment of the human rights is very tightly bound to a minimum energy consumption per capita. This utterly poses the stress on a mandatory reconsideration of the available resources on our planet, to put also in the context of the Climate Change and the compelling opposite requirement of nullifying within the century the anthropogenic greenhouse-gas emissions [Lee23].

As much as the renewable energy sources offer a promising alternative to the fossil fuels, to present date they also suffer from unpredictability and require a very flexible energy distribution grid. On the other hand, the nuclear fission technologies often pay the price of poor social acceptance and pose the problem of the nuclear wastes.

Nuclear fusion stands as a possible future alternative emission-free energy source, characterised by the same predictability as the nuclear fission, but with reduced production of radioactive waste and - extrapolating from present impressions - a much larger social acceptance.

Several energetic scenarios have been realised (see, *e.g.*, [Han09] for a study on the European scale, [Bustreo19] for the specific Italian market, and [Griffiths22] for a review), suggesting also a comparable economic palatability of fusion
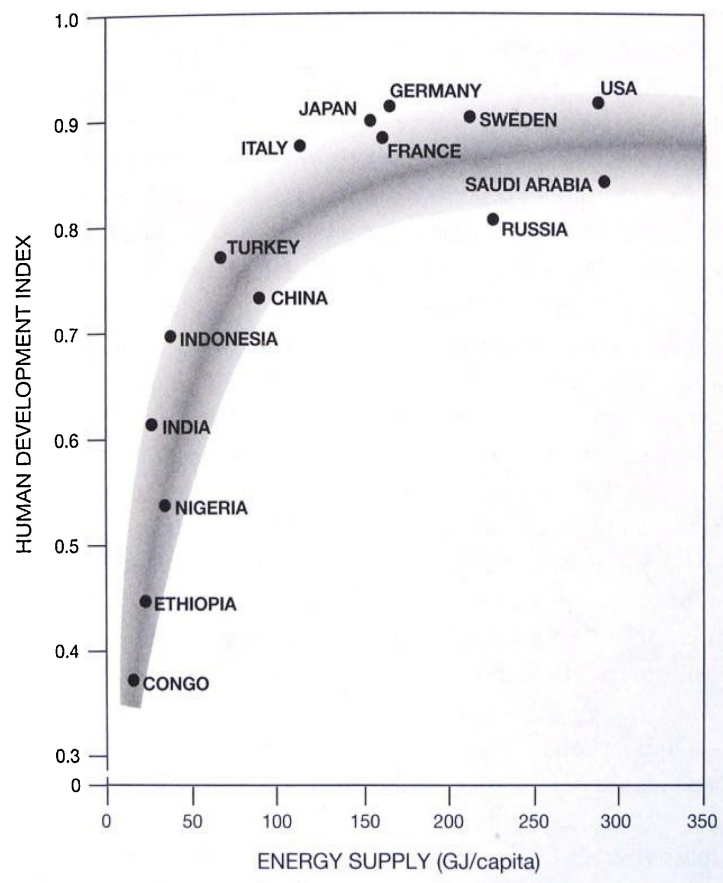
Figure 1.2: Human Development Index compared with the energy supply per person. Image taken from [Hagens20].
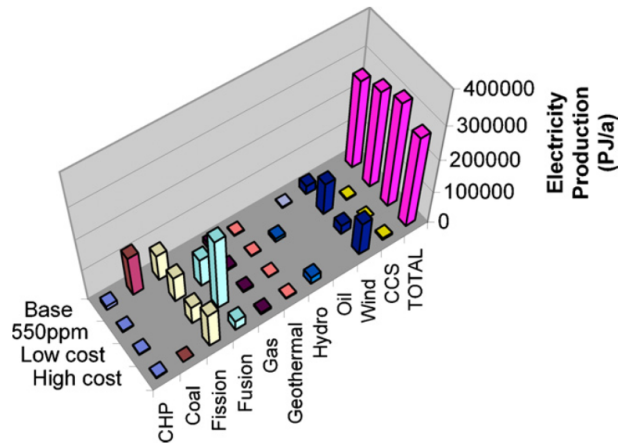
Figure 1.3: Four alternative scenarios for the European energy mix by the end of this century. All but the "base" one constraint the carbon dioxide concentration in the atmosphere below 550 ppm. The "base" scenario is almost the present one and does not consider fusion, the others present three different estimates for the costs of a future fusion power plant. Image taken from [Han09].

technologies with respect to the renewable energies, in the second half of this century when the technology could be mature for a first generation of reactors.

Concerning the European contest, [Han09] presents four alternative predictions for a future energy mix by the end of this century, here presented in Fig. 1.3: the first one is very close to the present one and foresees no contribution from fusion technologies, in the other three, the assumption is made that the CO_2 concentration in the atmosphere is constrained to stay below 550 ppm and rely on three different estimates for the economic cost of a fusion power plant. It is seen that in the intermediate and in the "low cost" scenarios the role assigned to fusion results at least as important as wind power generation. Apart from electric energy generation, [Griffiths22] remarks that very interesting employments for this technology could be found in heat-generation related applications: mostly water desalination, but also district heating, fossil fuel reformation, production of cements and wider industrial applications.

1.2   Nuclear fusion

Atomic nuclei are made of two components: positively charged protons and particle without electric charge called neutrons. The number of protons determines the way in which atoms combine together and thus the macroscopic properties of matter, while the neutrons act as a glue, that keeps mutually repelling ions from disintegrating the nucleus. All along, protons and neutrons are sometimes synthetically referred to as "nucleons".

Some nuclear configurations are however more energetically convenient than other, in the sense that the transition to a more convenient configuration is exothermic. This is what is represented by the Aston curve, in Fig. 1.4: the aforementioned "convenience" is measure in terms of a higher position along this curve, representing the binding energy per nucleon, as a function of number of mass (*i.e.*, number of nucleons composing various nuclei).

It is apparent that Aston curve breaks the periodic table of the elements in two regions: all the elements whose nuclei are heavier than approximately $A = 56$ (which is iron) will exothermically transition towards lighter configurations, whereas all elements with $A \lesssim 56$ will exothermically evolve to heavier configurations. The first kind of reaction, from heavier to lighter, is what we call nuclear fission. The second reaction is called nuclear fusion.

We can also observe that the average energy released per single nucleon in a fusion reaction, jumping up from, *e.g.*, a D (Deuterium) configuration to a ^{4}He (α particle), than what is released per single nucleon in a nuclear fission reaction. This accounts for a much higher energy density, which is another important prospected advantage of a future energetic employment of such a process. Luckily for us, there are strong barriers that prevent nuclear fusion of light nuclei to happen spontaneously on Earth (which would be quite hostile to life otherwise). In particular, the aforementioned Coulomb repulsion between neutrons make it extremely unlikely in normal conditions that two light nuclei bounce on each other with the right energy to start a reaction. In particular the likelihood of a nuclear reaction is measured by the cross section.

Figure 1.5 presents the cross sections for nuclear fusion reactions between various couples of light nuclei against their initial kinetic temperature. It is evident that the first non-negligible cross section met coming from lower temperatures is the one characterising the reaction between Deuterium and Tritium. This peaks around $T \approx 60\,\mathrm{keV}$, corresponding to a thermodynamic temperature over $10^9\,\mathrm{K}$, which is hardly feasible in a reactor. Anyway, acceptable values are already obtained around $10\,\mathrm{keV}$, which approximately corresponding to $1.5 \cdot 10^6\,\mathrm{K}$, which is challenging but compatible with modern technological means, especially because we only need the high-energy tail
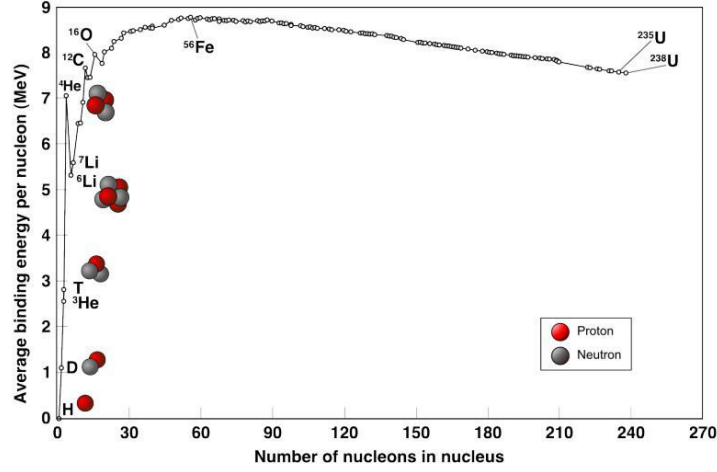
Figure 1.4:   Aston curve, representing the binding energy per nucleon as a function of the mass number. For $A < 56$ the nuclear fusion is exothermic. Image taken from [Fil15].

of the distribution function to reach ignition temperature.

The Deuterium-Tritium reaction is represented schematically in Figure 1.6: the two nuclei re-arrange their components in forming a heavier α particle and a spare neutron. The interaction does not conserve the mass of the reactants, part of which is turned into kinetic energy, which is distributed into the two reaction products, according to their mass ratio. The total (binding) energy release is $17.6\,\mathrm{MeV}$, of which $\sim 4/5$ are taken by the neutron and the rest goes to the α.

In nature, Deuterium is abundantly present and can be extracted from water through electrolysis. Tritium is instead a mildly radioactive substance, whose short half-time ($\sim 12\,\mathrm{y}$) makes it difficult to stock. In future reactors it will be mainly produced from lithium, leveraging the escaping neutrons produced by the fusion reactions, according to either of the following processes:

$$
\begin{aligned}
^{6}\mathrm{Li} + n &\rightarrow\; ^{4}\mathrm{He} + T + 4.8\,\mathrm{MeV}\,, \\
^{7}\mathrm{Li} + n + 2.5\,\mathrm{MeV} &\rightarrow\; ^{4}\mathrm{He} + T\,.
\end{aligned}
$$
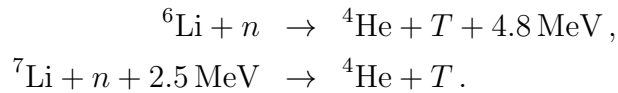
1.3   Magnetic and inertial confinement

As we said in the previous section, despite the $D - T$ reaction has comparatively higher cross section for comparatively lower kinetic temperatures,
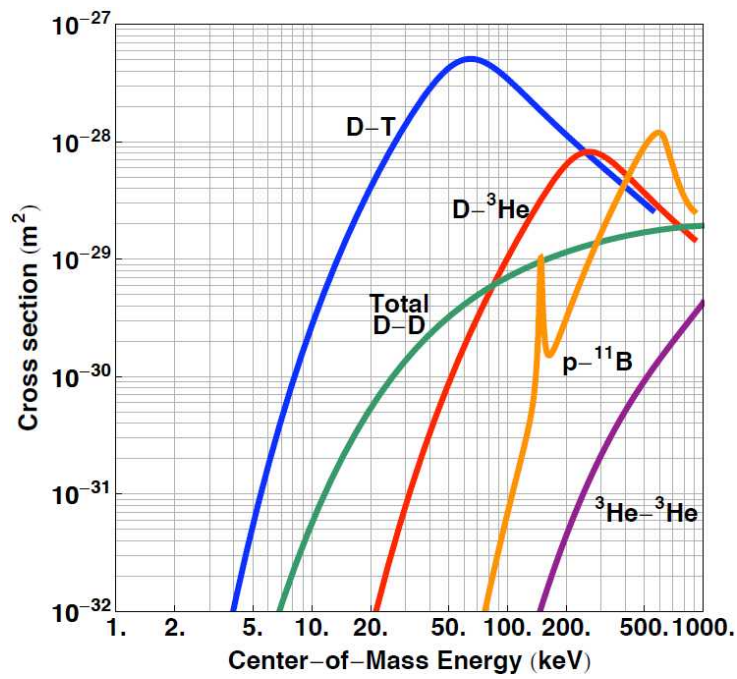
Figure 1.5: Cross section of nuclear fusion reaction between various couples of light nuclei. The $D - T$ cross section is the highest for relatively lower energies.
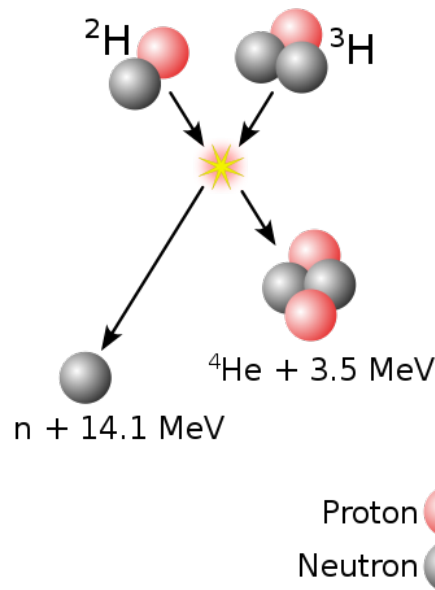
Figure 1.6: Visual representation of a $D-T$ fusion reaction: the net energy yield is 17.6 MeV, divided between the reaction products according to their mass-ratio.

nuclear fusion still requires extremely challenging conditions to be produced on Earth.

The research focuses on two alternative approaches to produce these energies: the inertial confinement and the magnetic confinement. In the first, a very small amount of solid pellet is charged with an immense isotropic pressure, that materially pushes the nuclei against each other. The latter consists in heating a large amount of gaseous fuel and rely on random collisions to produce a statistically relevant number of reactions.

In this section, we give a brief presentation of such two approaches, also focusing on the presentation of the three main classes of devices aimed at the magnetic confinement: namely, the tokamak, the stellarator, and the reversed-field pinch.

1.3.1   Inertial confinement

The inertial confinement constitutes an attempt to convert to energy production the same general mechanism of the H-bomb.

The working scheme can be found for instance here: [Betti16]. A very intense beam of lasers is made converge onto a tiny sphere of metal (called "ablator",
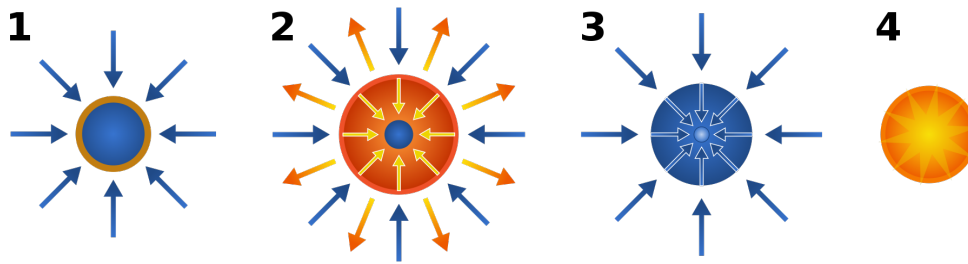
Figure 1.7: Working scheme of the inertial confinement: 1) an isotropic beam of lasers hits the ablator, containing $D-T$ fuel, 2) this causes the explosion of the exterior part of the ablator, producing an inward shock-wave, 3) the fuel sphere contracts by approximately a factor 5, igniting the core, 4) the hot α particles produced in the central hotspot produce an outwards heating of the rest of the fuel.

about 1 mm in diameter) containing gaseous $D-T$ fuel. The strong radiation - preliminarily converted in intense X-rays by hitting on a hohlraum - heats up the exterior part of the ablator, which turns into a plasma and blows off, producing an inwards shockwave that compresses the remaining part of the ablator and the gas inside it, shrinking the sphere by a factor 5 and thus igniting the core. The α particles produced in the "hotspot" progressively warm up the rest of the fuel, producing an outwards chain reaction.

The passages just described are schematically represented in Figure 1.7. The largest facility of this kind is the National Ignition Facility (Livermore, USA), and the second largest is Laser Mégajoule (Bordeaux, France), which is however mostly devoted to military research.

2022 has been an important year for inertial confinement [NIF22], since for the first time the condition of ignition was achieved, extracting more energy from the target than the energy impinging on it. In December 2022, during a shot, 2.05 MJ laser energy was used to compress the capsule, with a return of 3.15 MJ. Despite this still does not count in the energy cost of charging the lasers (which is still much larger than the final energetic outcome), this experiment is considered as a crucial milestone and a proof of concept.

1.3.2 Magnetic confinement

The magnetic confinement concept pursues the alternative strategy of employing large volumes of warm fuel, in whose hot core fusion reactions may happen. At the required temperatures of the reaction ignition, the fuel is in the state of a plasma (*i.e.*, an ionised gas), which responds very effectively to magnetic fields.
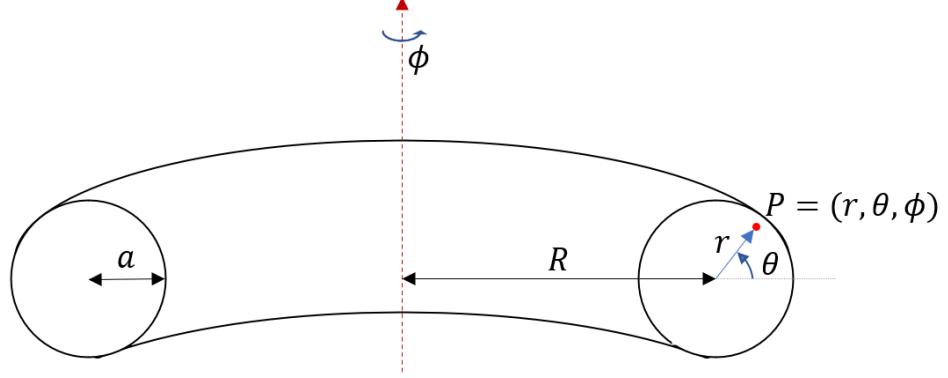
Figure 1.8: Toroidal coordinates (r, θ, ϕ) in a circular-cross section torus of minor radium a and major radius R.

This concept is most profitably employed in a class of toroidal devices, where a magnetic "cage" confines the plasma so that it does not directly interact with the vessel walls, which would both cool it down and get damaged.

The main three toroidal devices devices are the tokamak, the stellarator, and the reversed-field pinch (RFP). In the next three sections we will give a brief presentation to each of them.

Despite being quite different among themselves, the three of these devices are toroidally shaped pinches. From now and for the rest of this Part I we will only focus on toroidal geometry. The toroidal coordinates are schematically represented in Fig. 1.8: in a torus of major radius R, and minor radius a, a point P is identified by the distance r from the toroidal axis, the poloidal angle θ around the toroidal axis, and the toroidal angle φ around the vertical axis. There are some important figures of merit to be considered when dealing with toroidal devices. The first one serves to describe the confining magnetic field and it is called the "safety factor". The reasons for this name will be mostly clear throughout Part. II, where we will see how entangled this quantity is with the stability of the confined plasma. Its definition for a circular cross-section configuration is the following:

$$q \equiv \frac{B_\phi r}{B_\theta R} \qquad \text{safety factor,} \qquad (1.1)$$

where B_ϕ and B_θ are the toroidal and poloidal projections of the magnetic field, and R and r are defined as in Fig. 1.8. When q is a rational number, it represents the ratio between the number of poloidal windings to toroidal windings of a magnetic field line before it closes back on itself.

A second important figure of reference is the magnetic field shear, that gives the progressive screwing of the magnetic field lines at different radii:

$$s \equiv -\frac{r}{q}\frac{\mathrm{d}q}{\mathrm{d}r} \qquad \text{magnetic shear.} \qquad (1.2)$$

Looking now at the inertial response of the plasma to the confining field, a very important figure of merit is the normalised pressure β, *i.e.*, thermodynamic plasma pressure normalised to the confining magnetic pressure:

$$\beta \equiv \frac{2\mu_0 \langle p \rangle}{\langle |\mathbf{B}|^2 \rangle} \qquad \text{normalised pressure,} \qquad (1.3)$$

where $\langle \rangle$ indicates volume averaging.
Finally, for the reversed field pinch specifically, great importance have the pinch parameter Θ and the reversal parameter F:

$$\Theta \equiv \frac{B_{\theta,a}}{\langle B_\phi \rangle} \qquad \text{pinch parameter,} \qquad (1.4)$$

$$F \equiv \frac{B_{\phi,a}}{\langle B_\phi \rangle} \qquad \text{reversal parameter,} \qquad (1.5)$$

where this time $\langle \rangle$ indicates poloidal cross-section averaging, and the subscript a means evaluation at the minor radius $r = a$.

1.3.3 Tokamak

Tokamaks are the most advanced and promising class of devices for the magnetic confinement of a plasma. It was originally invented in 1950 by Andrej Sacharov and Igor Tamm in Russia: its name is an acronym meaning "toroidal chamber with magnetic field windings".
The main idea behind it is to produce the poloidal part of the confining magnetic field by inductively driving a current inside the plasma. The more intense toroidal field is instead produced by a set of poloidally arranged coils, that embrace the plasma, as in Fig. 1.9. Some other sets of coils are also present, to provide stabilisation of the plasma position. The configuration stability has been demonstrated when the safety factor at the toroidal axis is higher than 1. This allows to prevent dangerous relaxation processes that will be described more in detail in Chap. 4.
Since the plasma current is inductively driven (leveraging the inner poloidal magnetic field coil as the primary circuit, as in Fig. 1.9), the tokamak presents the strong limitation of requiring pulsed discharges. This limit can only be
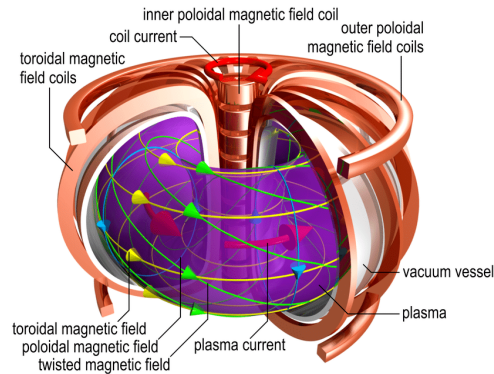
Figure 1.9: Simplified model of a tokamak (taken from [Proll14]).

overcome by driving additional currents inside the plasma. Hence, great interest has the study of pressure-gradients induced "bootstrap currents", that spontaneously arise under specific conditions [Wilson, Peeters00]. Other ways to drive additional currents from outside the plasma are through the additional heating systems, as in [Hu22, Zhang14] for large-scale currents, and [Ono22] for local current drives.

The largest operating tokamak in the World is JET (Abingdon, UK), while the largest project for the years to come is ITER (Cadarache, France), which aims to achieve a full proof of concept, with long-lasting pulses (above 300 sec) and a fusion energy gain (*i.e.*, the ratio of the energy outcome to the total energy input) larger than 10.

The year 2022 has been a very interesting one for the tokamak, since in the Deuterium-Tritium campaign in the JET tokamak a new important record in energy production was achieved, yielding 59 MJ of output energy over 5 sec of flat-top discharge duration, with an ITER-like wall configuration [JET22]. This is considered as a crucial milestone, on the way to ITER.

1.3.4 Stellarator

The stellarator is a toroidal device for the magnetic confinement of a plasma, where, unlike the tokamak, no net macroscopic current is present in the plasma. Instead, the request for a poloidal field component is dealt with either through two independent sets of coils or through a single and complex system of three-dimensional coils, that are optimised to produce an already helical magnetic field. A conceptual representation of this class of devices is reported in Fig. 1.10. The strength of this concept is that since it does not rely on inductive plasma currents, its pulses do not present time limits, in line of principle. Furthermore, the great deal of current-driven instabilities
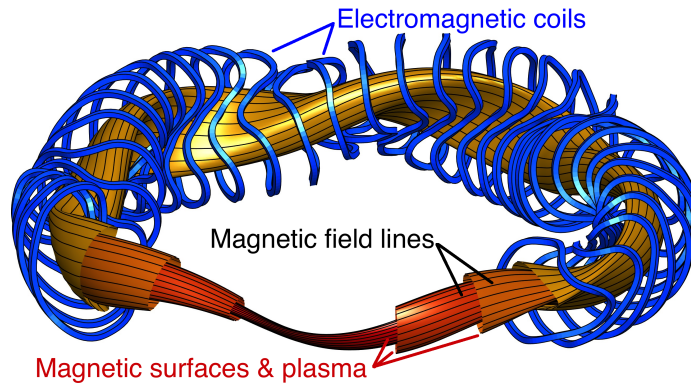
Figure 1.10: Simplified model of a stellarator.
(image taken from the web page of UMD stellarator goup:
`https://terpconnect.umd.edu/`~mattland/projects/1_stellarators/).

(some of which are described in this thesis), which are concerning for the tokamak equilibrium, is instead absent in this configuration.

Its main limitation lays in the high complexity of its geometry, which exhibits typically a discrete periodicity in the toroidal angle and is largely responsible for longer times both in design and in modelling phase.

The concept was initially introduced in 1950 by Lyman Spitzer, in what would have become the Princeton Plasma Physics Laboratory. The largest stellarator in the world is Wendelstein 7-X (Greifswald, Germany), while other projects of this kind are HSX (Madison, USA), and LHD (Toki, Japan).

1.3.5 Reversed-Field Pinch

The reversed-field pinch [Escande13, Marrelli21] is a toroidally symmetric device, similar to the tokamak, where however the poloidal and toroidal components of the magnetic field have comparable amplitudes, and the plasma current is one order of magnitude larger for comparable values of resistivity. As a result of comparable magnetic field components, the safety factor on the toroidal axis is typically smaller than 1 (in the range of $q_0 = a/(2R)$), and decreases radially towards the edge. This feature makes the RFP particularly prone to intense instabilities activity and is ultimately responsible for the "dynamo effect". The latter is the self-consistent sustainment of a toroidal magnetic field produced by one or more non-axisymmetric components of the flow of charged particles. Such a field is opposite at the edge with respect to the much less intense one produced by the toroidal-field coils, so that B_ϕ has a reversal at the edge of the plasma, motivating the name of the configuration. The radial profile of the magnetic field components and
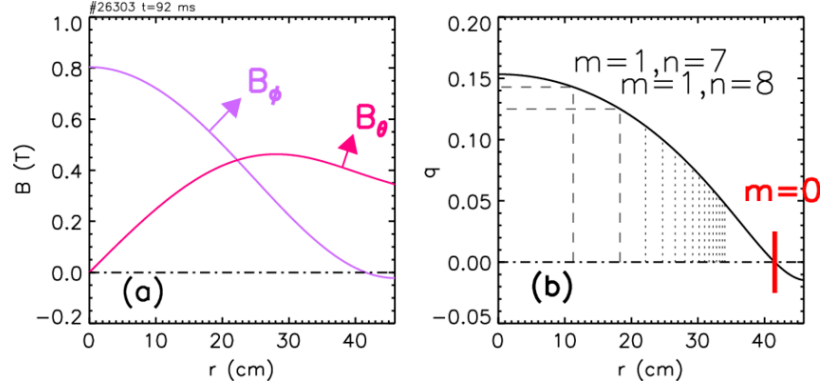
Figure 1.11: (a) Magnetic fields and (b) safety factor radial profiles in the RFP. For this case, the reference values of $R = 2$ m, $a = 0.459$ m, and $q_0 = a/(2R) \approx 1/7$ are taken from the RFX-mod device. Images taken from [Escande13].

the safety factor of a typical RFP discharge are reported in Fig. 1.11 A great advantage of this configuration is that it does not require additional heating: in fact, since the plasma current is one order of magnitude larger than in the tokamak, for the same plasma resistivity, the resulting ohmic heating is two orders of magnitude larger. In addition, unlike the tokamak, the RFP is disruption-free, since the strong self-organisation of the plasma already constitutes a relaxed state. In this sense, the three magnetic confinement devices described in this section can be seen in a spectrum of increasing plasma self-organisation, with one extreme taken by the stellarator, where few degrees of freedom are left to the plasma, and the other take by the RFP, with the tokamak in the middle [Escande13].

The main disadvantages of this configuration are connected with the much shorter pulse duration with respect to both the tokamak and the stellarator (RFX-mod plasma shots last approximately 0.5 sec), and to the requirement of either a thick ideal wall near the plasma or a very sophisticated feedback control system [Marchiori09] to deal with the intense magneto-fluid instabilities of the confined plasma.

The largest RFP experiment in the world is RFX-mod (Padua, Italy), while the second largest is MST (Madison, USA) [Sarff15].

2

The reversed-field pinch configuration: main experimental observations and modelling results

In the previous Chapter we have defined the main concepts for the confinement of a fusion plasma. In this chapter we deal more directly with the reversed-field pinch (RFP) configuration, which is the main focus of the research at Consorzio RFX.

The Chapter is divided in two parts: in the first one, we start in Sec. 2.1 by describing the physics of this configuration more in deep than what already done, and in Sec. 2.2 by describing the main RFP device, RFX-mod, and its ongoing upgrade to a new configuration dubbed RFX-mod2 [Marrelli19].

The second part is dedicated to theory and modelling. In Sec. 2.3 we introduce the general equations of MHD and some other useful theoretical tools such as the adimensional numbers of Lundquist, Reynolds (also called "viscous Lundquist"), Prandtl and Hartmann. Sec. 2.4 is devoted to the role of advanced modelling in the physics of the RFP, with particular regard for the SpeCyl code.

Finally, Sec. 2.5 presents a final summary and the outline of this thesis.

2.1 The physics of the RFP

For several years, the operational scenario of the reversed-field pinch has been considered inherently chaotic and turbulent, bound to remain in a Multiple Helicity (MH) state, with a wide spectrum of magnetic modes of comparable amplitude, each in the form of $\mathbf{B}^{m,n} \propto e^{im\theta+in\phi}$. The magnetic topology of MH states presents no conserved flux surfaces, apart from a chain of $m = 0$ "islands" at the reversal of the toroidal field, hence allowing intense

particles and heat transport towards the edge of the plasma. Another interesting experimental observation are the so-called "slinky modes", consisting in toroidally localised bulging of the plasma shape, usually related to the locking of some modes onto the wall [Fitzpatrick99].

Later on, some modelling works [Cappello92, Cappello96, Finn92] anticipated the possibility of a completely new operational scenario, based on the dominance of one saturated mode over the rest of the spectrum. We will comment on this later in this Chapter, but eventually the experiments confirmed this speculation and proposed to the scientific community in a milestone publication on Nature Physics [Lorenzini09], made possible by the exploration of new high-current regimes above 1 MA in RFX-mod and by the sophisticated feedback control system adopted on this same device.

These states are called Quasi-Single Helicity (QSH) states and correspond to a system bifurcation from the MH initial equilibrium [Cappello08]. As Fig. 2.1 reports, the current flat-top - Fig. 2.1.(a) - is populated by their intermittent emergence and subsequent crash, back to a MH state, as shown in Fig. 2.1.(b). During the QSH states the transport is strongly reduced and there is the formation of conserved flux surfaces.

Indeed, the global electron energy confinement time τ_E, defined as the characteristic time on which the electrons plasma energy damps, gets enhanced by approximately a factor 2 as the plasma transitions from the MH state into a QSH state, up to $\tau_E \sim 1.3$ ms in RFX-mod [Marrelli21].

A further improvement is achieved when the dominant mode exceeds some threshold-amplitude (around $3 - 4\%$ of the equilibrium magnetic field amplitude at plasma edge): a topological change brings to the expulsion of the initial toroidal axis, in favour of the centre of the island corresponding to the helical mode. Such a situation is called Single-Helical Axis (SHAx) state and is shown in Fig. 2.1.(c). Here, in black are marked the helical flux surfaces for the dominant mode, that separate regions of increasing temperature, as we move inwards, indicating the formation of strong barriers against transport. Accordingly, the electron energy confinement time is further increased, up to $\tau_E \sim 1.8$ ms in RFX-mod, while the maximum achieved particle confinement time in RFX-mod is $\tau_P = 12$ ms, in a SHAx QSH state at 1.5 MA [Marrelli21].

However, Fig. 2.1.(c) may result a bit deceiving, since a full Poincaré plot of the magnetic field reveals that most of the plasma volume is still ergodic. Figure 2.2.(a) reports the full Poincaré plot for a standard QSH shot, where the conserved flux surfaces are marked in red: we can indeed observe that they occupy a small fraction of the poloidal cross section, in the direct proximity of the helical axis. However, Fig. 2.2.(b) illustrates for the same shot the outcome of the tomographic reconstruction of SXR emission measurement
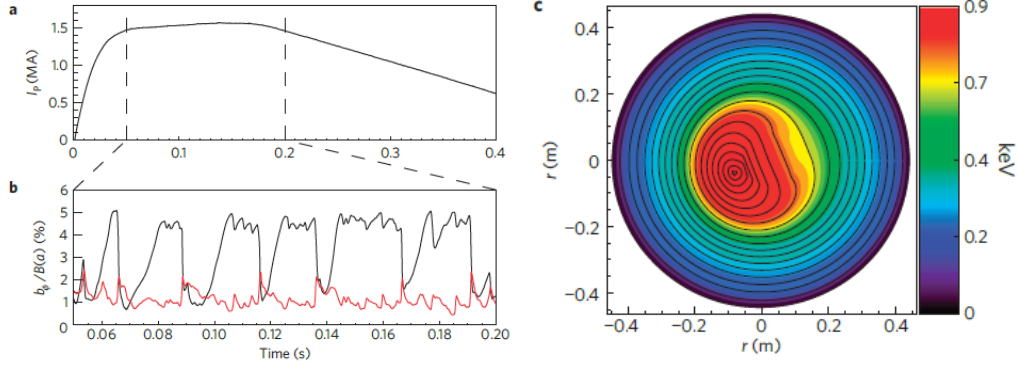
Figure 2.1: QSH states in RFX-mod. During the current flat-top (a), and above the threshold of 1 MA, a bifurcation happens from the initial MH equilibrium, into a QSH state (b). This is however intermittent: the amplitude of the dominant mode (black) intermittently crashes down to meet the amplitude of the secondary modes (red). (c) represents a SHAx state, where the magnetic flux surfaces of the dominant mode (black) seem to divide regions of different temperatures, increasing towards the island core. Images taken from [Lorenzini09].

of the plasma temperature, highlighting the presence of internal transport barriers that are not directly visible from the Poincaré plot aside. These internal transport barriers have been interpreted by the theoretical modelling as Cantori (*i.e.*, traces left by the dissolution of KAM tori) [Veranda20].

The same concept already expressed is confirmed also by Fig. 2.3, showing the electron temperature measurement for a typical QSH with a single helical axis, produced in a high plasma current regime. The temperature profile along a diametrical cut - Fig. 2.3.(a), in red and blue - is visibly asymmetric. This is also highlighted by the shaded regions that mark the sharper gradients. Such an asymmetry is removed when plotting against the effective radius ρ, as in Fig. 2.3.(b), proving that the iso-flux surfaces of the helical flux function of the dominant mode are also isothermal surfaces (as already suggested in Fig. 2.1.(c)). The electron temperature profile for a typical MH state is also reported in Fig. 2.3.(a), demonstrating the important implications that QSH states have on the plasma confinement.

The QSH has represented a change of paradigm in the RFP baseline scenario. A first convenient way to induce them was studied at MST, and consisted in varying the toroidal field at plasma edge, so to induce a plasma-current profile transient modification that concentrates the magnetic flux in its core [Sarff94]. This technique, dubbed "Pulsed Poloidal Current Drive" (PPCD), is effective in reducing temporarily the amplitude of the $m = 0$

(a) Poincaré plot.   (b) SXR tomographic reconstruction.
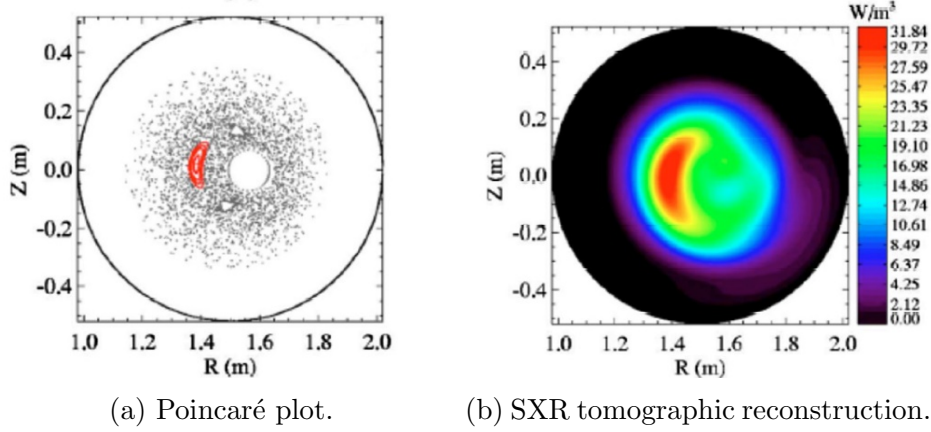
Figure 2.2: Experimental observations for a typical QSH shot in RFX-mod: (a) Poincaré plot of the magnetic field, highlighting a small region of conserved magnetic flux surfaces (red), and (b) tomographic reconstruction of SXR emissivity highlighting the presence of internal transport barriers even in the magnetic-chaos region. Images taken from [Marrelli21].
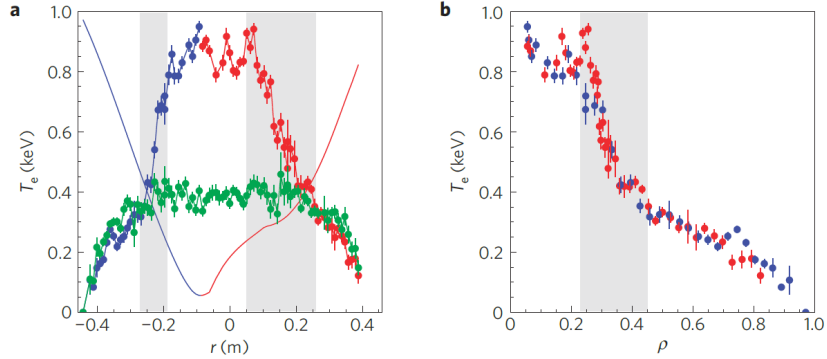
Figure 2.3: Temperature measurement in a typical SHAx QSH state for currents above 1.5 MA: (a) radial profile of the temperature (**blue** and **red** for the two sides of the island). The regions of large temperature gradients are shaded and the two smooth curves show the temperature radial gradient, revealing a substantial asymmetry along the diametrical cut. An electron temperature profile is shown for reference (**green**); (b) the same temperature profile plotted against the effective radial coordinate ρ, showing that iso-flux surfaces for the flux function of the dominant mode are isothermal: in the effective radius the profile is now symmetric. Images taken from [Lorenzini09].

secondary modes.

An improved method [Terranova07] was subsequently developed in RFX-mod, consisting in the repetition of the same principle in time, through an "Oscillating Poloidal Current Drive" (OPCD) at a given frequency. This way the pulsed nature of the PPCD could be overcome.

The OPCD works because the oscillating current drive matches for one half of its period the same direction of the current produced by the spontaneous turbulent dynamo, thus reducing the need of it. This condition is called "co-dynamo", and is alternated with a "counter-dynamo" phase (the other half of the OPCD cycle) during which the plasma often falls back into an MH state [Bolzonella01].

Another experimental way to trigger a QSH state in RFX-mod is to provide a non-axisymmetric magnetic perturbation (MP) [Piovesan11, Piovesan13] through the 192 feedback-control coils. It is empirically observed that the plasma reacts to the MP by reproducing a QSH where the dominant mode has the same periodicity of the seed perturbation at its edge.

In any case, the most profitable way to access the QSH regime is through its spontaneous and consistent emergence, experimentally obtained at high plasma currents. Importantly, the dominating mode in RFX-mod has a fixed periodicity $m = 1$, $n = -7$, corresponding to the first internally resonating mode, meaning that the safety factor on axis is just larger than $1/7$. As we will see in Part II, this condition is extremely relevant in the classification of instabilities.

2.1.1 Analogy between RFP QSH states and tokamak "snakes"

Long-lived helical structures (so-called "snakes") in the tokamak plasma core have been widely documented in a number of devices (see, *e.g.*, [Weller87, Gill92, Delgado13, Chapman10, Petty16]). They are usually linked to the accumulation of impurities within the magnetic-flux surface with periodicity $1/1$ and present locally positive density and temperature fluctuations. They are generally described as saturated resistive kink modes, and their dynamics is intermittent however very robust: remarkably, they are observed to survive from tens to hundreds of sawtooth cycles [Delgado13].

Tokamak snakes are strongly associated with the hybrid scenario [Petty16] for the tokamak, which has also been proposed among ITER's advanced modes of operation [Gormezano04, Chapman14]. A large non-inductive current is

Table 2.1: Main features of the RFX-mod device: major radius R, minor radius a, maximum nominal plasma current, maximum nominal magnetic field

$R\,[\mathrm{m}]$	$a\,[\mathrm{m}]$	$I_p^{\max}\,[\mathrm{MA}]$	$B^{\max}\,[\mathrm{T}]$
2	0.459	2	2

driven in the plasma via additional heating systems, producing a relatively flat safety factor profile in the plasma core, just above unity, sustained by a mechanism known as flux-pumping, through the formation of a 1/1 core helical structure. Such an equilibrium allows remarkable values of the normalised pressure β.

There is a strong analogy between the tokamak snakes and the SHAx QSH states in the RFP, since they both consist in the long-lived and intermittent dominance of an internal $m = 1$ mode over the rest of the magnetic spectrum, in high-current operation of toroidally symmetric devices. There is indeed some very interesting space for connections in the modelling of these two processes: a promising example is reported in Sec. 2.4.2, where the attempt of explaining the flux-pumping mechanism in the tokamak hybrid scenario in terms of the MHD dynamo is reported.

As a matter of fact, from an experimental point of view, the same technique of equilibrium reconstructions implemented for the SHAx QSH states in RFX-mod [Terranova13] and MST [Koliner16] has also been leveraged for the tokamak snakes in DIII-D [Cianciosa17], using the VMEC code [Hirshman83, Hirshman85] combined with the data-fitting tool V3FIT [Cianciosa17, Terranova13].

2.2   RFX-mod and its upgrade to RFX-mod2

RFX-mod is the largest reversed-field pinch device in the world, and it is located in Padua (Italy), operated by the Consorzio RFX.

Its main features are reported in Table 2.1, whereas a picture of the device is reported in Fig. 2.4.(a). Figure 2.4.(b) reports instead the sophisticate feedback control system for the plasma instabilities. This is a set of 192 individually-fed saddle-shaped coils, entirely surrounding the plasma in 4 toroidal arrays by 48 coils each. Initially installed to simulate an ideally conducting shell, for the stabilization of $m = 1$ modes, the system can also be used to produce magnetic seed perturbations at the edge of the plasma, to induce QSH states of various periodicities.

An overview of the experimental activity of this device can be found here:

(a)   (b)
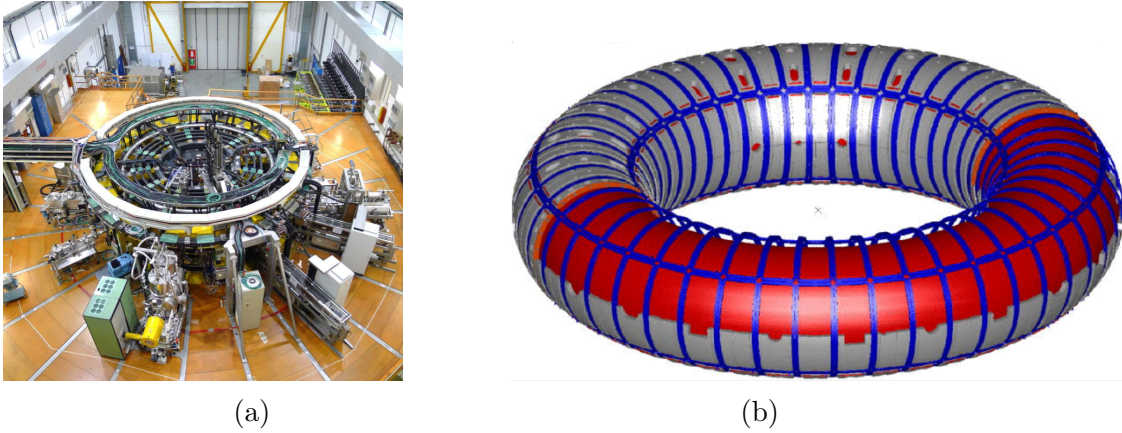
Figure 2.4:   RFX-mod: (a) picture of the device, (b) 192 active coils
for the feedback control of the plasma.   Taken from (a) [Fellin95] and (b)
[Piovesan13].

[Zuin17].

RFX-mod is currently in shut-sown since 2016, due to a major upgrade to
a new configuration, dubbed RFX-mod2 [Marrelli19, Peruzzo18, Bettini17].
The main aim of this upgrade is to complete the study of the physics of RFP
devices in the current regime up to $2\,\mathrm{MA}$, with a particular stress on the QSH
states. This upgrade is made possible also by the rich funding provided by the
Italian Government through the NEFERTARI[1] project (part of the PNRR
funding campaign for high-priority national infrastructures), and RFX-mod2
should be operable by 2024.
Figure 2.5 synthesises the major modifications to the structure of the device:
the vacuum vessel is removed, transforming the stainless steel mechanical
support structure into a vacuum-tight shell. This has the effect of bringing
the plasma edge ($r = a$) closer to the stabilising copper shell, at radius b:
this way, the conductive shell proximity to the plasma edge changes from
$b/a = 1.11$ into $b/a = 1.04$. This is expected to have a strong damping effect
on the secondary modes, thus enhancing the QSH state, since the $m = 1$
modes are predicted to be linearly stable for $b/a \leq 1.03$ [Marrelli19]. This of
course poses several engineering challenges, mostly related to the fact that
extending the vacuum to regions that used to be in air, there is an increased
risk of arching and effective insulation must be performed.
Great interest has also the problem of the so-called magnetic field errors

---

[1] "New Equipment For the Experimental Research and Technological Advancement for
the Rfx Infrastructure".
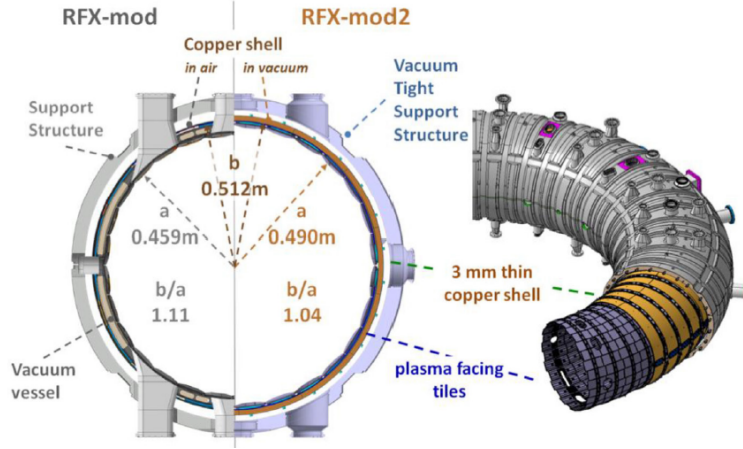
Figure 2.5: Modifications to the structure of RFX-mod, in the upgrade towards RFX-mod2. The plasma results closer to the stabilising copper shell. Image taken from [Marrelli19].

[Bettini17], that are small imperfections in the conducting wall response, resulting from the necessity of having holes in the copper shell, to let, *e.g.*, the confining magnetic field reach the plasma from the coils.
In addition, several new diagnostic tools will be added in the new device, along with a neutral beam injector [Peruzzo18]. The presence of an additional heating system may result confusing, as we said that the RFP can reliably warm up just by means of Ohmic heating. The rationale is that, as already RFX-mod, RFX-mod2 is designed to operate also as a tokamak.

2.3   Magneto-Hydro Dynamics

Before switching our focus onto the modelling and its fundamental role in the advance of research for the RFP, let us introduce some useful definitions.

Magneto hydrodynamics, or MHD for short, is the particular regime in which the ions and electrons composing the quasi-neutral plasma have higher energies than the thermal energy [Fitzpartick22]. In most applications, the plasma can be treated as a single fluid, governed by the usual hydrodynamic equations, along with Maxwell's equations.
The first two fluid equations are dubbed continuity and momentum balance equations, respectively, and read:

$$\frac{\mathrm{d}f}{\mathrm{d}t} = -f\nabla \cdot \boldsymbol{v}\,, \tag{2.1}$$

$$\rho\frac{\mathrm{d}\boldsymbol{v}}{\mathrm{d}t} = \mathbf{J} \times \mathbf{B} - \nabla p + \rho\nu\nabla^2\boldsymbol{v}\,, \qquad (2.2)$$

being f the number-density of the plasma, $\boldsymbol{v}$ the flow velocity, $\mathbf{J}$ and $\mathbf{B}$ the current density and the externally applied magnetic field, respectively, $\rho = m_{\mathrm{proton}}f$ the mass density, p the internal pressure, ν the dynamic viscosity and $\mathrm{d}/\mathrm{d}t$ the Lagrangian or convective derivative, defined as:

$$\frac{\mathrm{d}}{\mathrm{d}t} \equiv \left[\frac{\partial}{\partial t} + \boldsymbol{v}\cdot\nabla\right]\,.$$

Equations 2.1 and 2.2 enforce mass conservation and momentum balance, respectively.

Maxwell's equations are used to close the previous set:

$$\begin{aligned} \nabla\cdot\mathbf{E} &= 0 && \text{Gauss' law,}\\[4pt] \nabla\times\mathbf{E} &= -\frac{\partial\mathbf{B}}{\partial t} && \text{Faraday's law,}\\[4pt] \nabla\cdot\mathbf{B} &= 0 && \text{solenoidal property,}\\[4pt] \nabla\times\mathbf{B} &= \mu_0\mathbf{J} && \text{Ampère's law,} \end{aligned}$$

where the Gauss' law is generally specialised for the quasi-neutral plasma and in Faraday's law the displacement field term is generally set to zero, due to the high conductivity of the medium.

Finally, the plasma response to the imposed electromagnetic fields is expressed in the fluid Ohm's law:

$$\mathbf{E} + \boldsymbol{v}\times\mathbf{B} = \eta\mathbf{J}\,, \qquad (2.3)$$

being η the plasma resistivity.

There is a distinction which is going to be important in the following between *resistive* (dissipative) MHD, where ν and η are finite, and *ideal* MHD, where $\nu = \eta = 0$ and plasma energy is conserved. Also, as we will discuss, ideal MHD magnetic flux is said to be *frozen* inside the plasma flow, yielding proportionality between small perturbations to these two quantities.

2.3.1 Characteristic time-scales

The momentum balance equation Eq. 2.2 as well as the Faraday's law contain an explicit time derivative, that can be used to set an argument by general terms, in order to highlight the characteristic time-scales of the system.

Let us start from the Faraday's law:

$$\nabla\times\mathbf{E} = -\frac{\partial\mathbf{B}}{\partial t}$$

and write the electric field in terms of the Ohm's law, assuming static conditions ($\boldsymbol{v} = 0$): $\mathbf{E} = \eta\mathbf{J}$. Using Ampère's law, the current can be written in terms of the curl of the magnetic field, so that, assuming also for simplicity that η is uniform:

$$\frac{\partial \mathbf{B}}{\partial t} = -\frac{\eta}{\mu_0}\nabla \times \nabla \times \mathbf{B} = \frac{\eta}{\mu_0}\nabla^2\mathbf{B}\,.$$

Switching now to general arguments, the Laplacian operator can be written as $\nabla^2 \sim 1/\ell^2$, where ℓ is a characteristic length of the system, and $\partial_t \sim 1/\tau_R$, where τ_R is the typical time-scale of resistive processes in the plasma. It results then that

$$\tau_R \equiv \frac{\mu_0\ell^2}{\eta}\,, \tag{2.4}$$

where ℓ is a characteristic diffusion length.

A similar argument applies for the momentum balance equation and viscosity. In fact, if we isolate in Eq. 2.2 the left member and the term proportional to ν we can find

$$\frac{\mathrm{d}\boldsymbol{v}}{\mathrm{d}t} = \nu\nabla^2\boldsymbol{v}\,,$$

and thus, by similar considerations,

$$\tau_\nu \equiv \frac{\ell^2}{\nu}\,, \tag{2.5}$$

where τ_ν is the viscous diffusion time-scale in the plasma and ℓ is a typical length-scale of the system.

Finally, it is important to consider the typical time-scal of convective processes in the plasma, that relies on the characteristic velocity within the MHD regime: this is the Alfvèn velocity, defined as [Fitzpartick22]

$$\upsilon_A \equiv \sqrt{\frac{|\mathbf{B}|^2}{\mu_0\rho}}\,, \tag{2.6}$$

where ρ_0 is the plasma density evaluated at the axis position. This leads to the definition of the typical dynamic time-scale of MHD processes, defined as

$$\tau_A \equiv \frac{\ell}{\upsilon_A} \qquad \text{Alfvèn time,} \tag{2.7}$$

where, again, ℓ is the characteristic length of the given system.

2.3.2 Dimensionless numbers

The characteristic time-scales of resistivity and diffusion define two important dimensionless numbers, such as the Lundquist number and the Viscous Lundquist number (also called Reynolds number):

$$L \equiv \frac{\tau_R}{\tau_A} \qquad \text{Lundquist number}, \qquad (2.8)$$

$$M \equiv \frac{\tau_\nu}{\tau_A} \qquad \text{Viscous Lundquist number}. \qquad (2.9)$$

As obvious, the two dimensionless numbers just defined measure the relative weight of resistive and viscous phenomena as compared to the typical scales of the MHD dynamics.

It is useful to define two additional dimensionless numbers, namely the magnetic Prandtl number and the Hartmann nuber:

$$P \equiv \frac{L}{M} = \frac{\nu}{\eta} \qquad \text{Magnetic Prandtl number}, \qquad (2.10)$$

$$H \equiv \frac{1}{\sqrt{\eta\nu}} \qquad \text{Hartmann number}, \qquad (2.11)$$

where we normalised $\mu_0 = 1$, in order to agree with the notation used in literature.

The relevance of Eqs. 2.10-2.11 is that if we write again the momentum balance equation and the Faraday-Ohm equation in normalised units ($\rho = 1$, $\hat{\eta} = \eta/\eta(0)$, $\hat{\nu} = \nu/\nu(0)$, $\hat{t} = \sqrt{\frac{\eta(0)}{\nu(0)}}t$, and $\hat{\boldsymbol{v}} = \sqrt{\frac{\nu(0)}{\eta(0)}}\boldsymbol{v}$) we get [Cappello04]:

$$\frac{\partial \mathbf{B}}{\partial \hat{t}} = \nabla \times (\hat{\boldsymbol{v}} \times \mathbf{B}) - \nabla \times \left(\frac{\hat{\eta}\mathbf{J}}{H}\right),$$

$$\frac{1}{P}\frac{\mathrm{d}\hat{\boldsymbol{v}}}{\mathrm{d}\hat{t}} = \mathbf{J} \times \mathbf{B} + \nabla^2\left(\frac{\hat{\nu}\hat{\boldsymbol{v}}}{H}\right),$$

so that, if the inertial term at first member of the second equation becomes negligible (or if $P \gg 1$), the whole dynamics is ruled by the sole Hartmann number.

2.4   The important role of modelling in RFP research

2.4.1   The role of numerical tools

Nonlinear MHD modelling has played and increasing role in the understanding of key relaxation processes in magnetic-confinement fusion devices such as the RFP.

Indeed, starting in the 1980s, with the advent of the first supercomputers, numerical simulations could produce some very useful understanding. Despite the simplicity of the MHD models being enforced, qualitatively good agreement could be achieved between early simulations and experimental data, both in standard ohmic discharges and in presence of externally driven edge magnetic perturbations through pulsed or oscillating parallel current drive (PPCD/OPCD) [Bolzonella01, Puiatti03, Ebrahimi03]. In all these cases, numerical tools reliably reproduced dynamics and composition of dynamo-current sustained magnetic spectra, from the linear onset of modes growth to their nonlinear saturation, and their interaction with external drives.

In the past two decades, numerical modelling of the RFP has intensively relied on numerical codes such as NIMROD [Kruger04], DEBS [Paccagnella07], SpeCyl [Cappello96, Veranda17], and Pixie3D [Chacón04, Chacón06, Chacón08].

2.4.2   Some of the results obtained with SpeCyl in the past decades

The content of this section does not aim at producing a complete review of the results obtained with the SpeCyl code in the past two decades, but only to define the frame in which this thesis is set. In doing so, we will select only those lines of research that are in direct continuity with the work presented in the next Chapters.

First fundamental studies on the QSH states.   The SpeCyl code has played an important role in the discovery of QSH states, since its simulations already anticipated this feature [Cappello92, Cappello96], several years before their successful observation in RFX-mod discharges.

We already discussed in Sec. 2.3 the importance of the Prandtl and Hartmann numbers (Eqs. 2.10-2.11) in regulating the MHD dynamics. As we said, in the common case in which plasma inertia can be neglected (or $P \gg 1$), the Hatmann number is the sole variable that weights the visco-resistive contribution in the MHD equations. This result was presented for the first
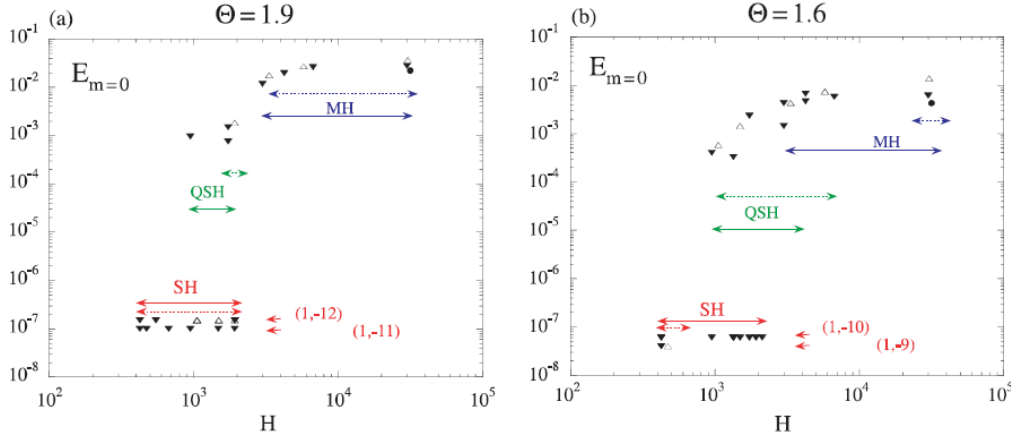
Figure 2.6: Results of visco-resistive nonlinear simulations with SpeCyl: the transition from a MH state, to a QSH state, to a further laminar SH, is regulated by $H = (\nu\eta)^{-0.5}$. $E_{m=0}$ is the averaged energy of secondary modes $m = 0$, whose amplitude is high in turbulent MH states, and lower for increasingly laminar states. Images taken from [Cappello04].

time in [Cappello00, Cappello04]. In the same works, a numerical study performed with SpeCyl is presented, proving for different values of the pinch parameter (Eq. 1.4) that the transition from the turbulent MH state, to a QSH state, to an even further laminar "Single Helicity" (SH) state, is indeed ruled by different regimes of Hartmann number, as reported in Fig. 2.6. This result, apart from confirming a very interesting dynamical property, suggests the existence of a second bifurcation point, to a further laminar Single Helicity (SH) state, whose confinement and stability properties would be even further increased. However, to present days, this still remains a theoretical speculation never achieved in experiments.

QSH studies with an OPCD. Some effort was dedicated in the early 2000's to the modelling of OPCD experimental conditions, not only in SpeCyl [Cappello03, Puiatti03, Bonfiglio07, Veranda13], but also in other codes as in DEBS [Ebrahimi03]. Concerning SpeCyl's simulations, several experimental aspects could be faithfully reproduced: first of all, the transition to QSH states in the presence of a time-dependent toroidal magnetic field boundary, used to model the OPCD in SpeCyl.

Figure 2.7 represents the secondary modes suppression in SpeCyl's simulations as the OPCD is turned on. Figure 2.7.(a) represents the radial profile of some plasma quantities before the OPCD is turned on: in particular, $v_r B_z$ is the laminar dynamo (due to the dominant QSH mode) while $\langle \delta V \times \delta B \rangle$
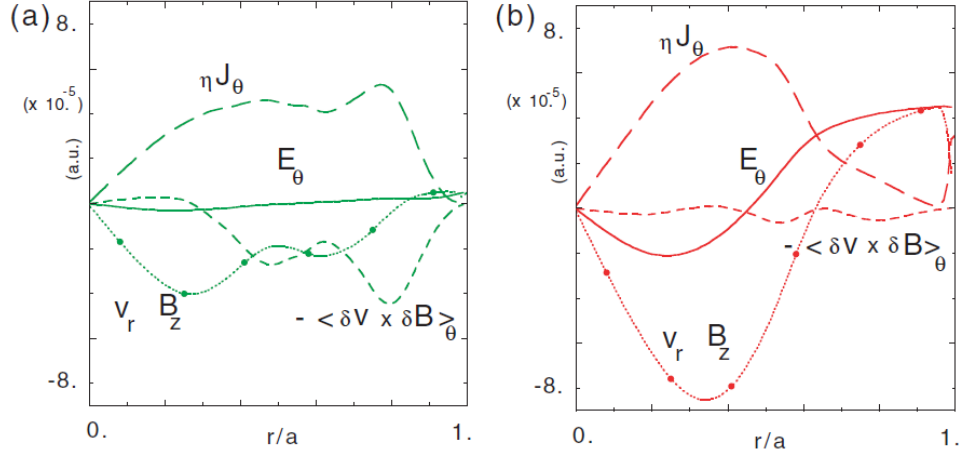
Figure 2.7:   Modelling of an OPCD in SpeCyl's simulations: (a) without the OPCD, the turbulent dynamo $\langle \delta V \times \delta B \rangle$ and the laminar dynamo $v_r B_z$ present comparable contributions. (b) When the OPCD is turned on, the laminar dynamo grows in importance, at the expences of the turbulent dynamo. Images taken from [Puiatti03].

is the turbulent dynamo, produced by the secondary modes. It is seen from Figure 2.7.(b) that the introduction of an OPCD almost nullifies this latter contribution, while reshaping all the quantities, and, in particular, the laminar flow contribution whose amplitude visibly raises. Also the experimentally observed variable reactivity of the plasma to different OPCD frequencies was successfully reproduced [Bonfiglio07].

Some aspects of the modelling yet remain in conflict with the experimental observations, possibly related to the simplified assumptions, especially in the formulation of the plasma boundary. The major are a different reactivity of various modes to the OPCD stimulation (as mode $(1, -8)$ seems to respond better than mode $(1, -7)$ in SpeCyl, in contrast with the experimental observations), and the tendency of forming the QSH during the counter-dynamo phase, unlike the real plasma behaviour.

QSH studies with a seed MP at plasma edge.   Some very successful studies [Bonfiglio13, Veranda17] were performed in the modelling of seed MP at plasma edge. These were produced in SpeCyl by artificially assigning a finite edge radial component to a single mode of the magnetic spectrum, while keeping all the other edge-$B_r^{m,n}$ null, in compliance with the ideal-wall implementation of SpeCyl's boundary conditions.

For the first time in [Bonfiglio13] a consistent repetition of a QSH state with
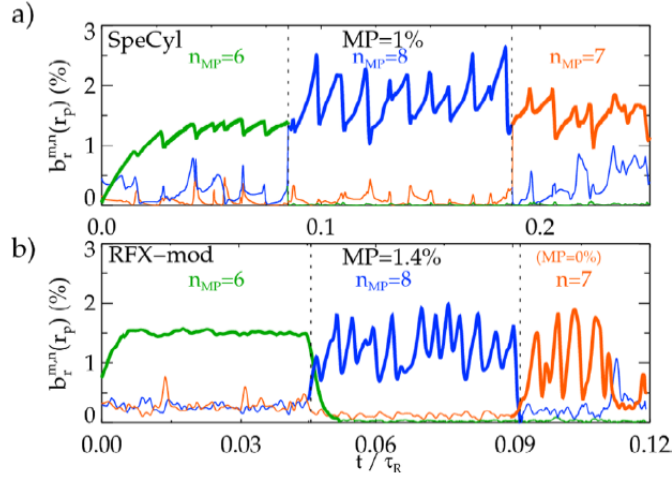
Figure 2.8: Experimental-like repetition of QSH states with the same dominant mode, as a result of the application of a seed MP at the plasma edge. (a) Above, the normalised radial magnetic field component of various modes at $r = 0.9 \cdot a$, a being the ideal shell radius. (b) Below, shot #30932 in RFX-mod. Both panels are divided in three parts, where different modes are excited as a consequence of different seed MPs. Images taken from [Veranda17].

the same dominant mode was observed in a 3D nonlinear MHD simulation of a RFP. These results were further developed in [Veranda17], where excellent qualitative agreement with the experimental findings were reported (see Fig. 2.8).

Electrostatic dynamo and flux pumping in the hybrid tokamak scenario. Some very interesting works [Bonfiglio05, Cappello06] are dedicated to the dynamo effect in the reversed field pinch, with some later application also to the tokamak physics [Piovesan17].

In [Bonfiglio05, Cappello06] a fundamental study is presented about the electrostatic nature of the dynamo effect in the RFP. Figures 2.9.(a-b) show the nonlinear simulation of a SH state in RFP configuration, consisting in an almost purely helical plasma self-organised state - in grey in Fig. 2.9.(a) - as a result of the saturation of a kink or tearing instability. The helical flux projection on the poloidal cross-section is visible (in black) on the top of Fig. 2.9.(a).

We have then a helical modulation in the current density, that requires a corresponding helical modulation in the electric field. The electric field is thus the sum of two contributions: the purely axial inductive loop field $\mathbf{E}_{\text{loop}}$

and a helically modulated electrostatic potential:

$$\mathbf{E} = \mathbf{E}_{\text{loop}} - \nabla\varphi\,.$$

The potential φ is represented in Fig. 2.9.(a) with the two colors, orange and blue, that mark its maxima and minima, respectively. The helical plasma thus behaves as a helical capacitor, enclosed between two helical "plates" at opposite electrostatic potential. Ultimately, Fig. 2.9.(a) represents also the electrostatic field $-\nabla\varphi$ as (almost axial) red lines, between the plates of the helical capacitor.

Figure 2.9.(b) is a representation of the same concept, as a Poincaré plot on the toroidal cross-section.

The helically modulated electric field produces a helical drift flow, which is almost exactly the one responsible for the dynamo. To prove this, Fig. 2.9.(c) reports the helical deformation of the (initially axisymmetric) plasma flow: in the upper part (in blue) the whole velocity field projection onto the poloidal plane is represented, while in the bottom part (in red) there is just its component perpendicular to the magnetic field, which is the one responsible for the dynamo.

The $E \times B$ drift velocity (see [Fitzpartick22]) produced by the helically modulated electric field can be computed directly (from the resistive Ohms law):

$$\boldsymbol{v}_\perp = \frac{(\mathbf{E}_{\text{loop}} - \nabla\varphi - \eta\mathbf{J}) \times \mathbf{B}}{|\mathbf{B}|^2} = \boldsymbol{v}_{E \times B} + \boldsymbol{v}_{\boldsymbol{\nabla}\varphi \times B} + \boldsymbol{v}_{\eta J \times B}\,,$$

where the last term is usually negligible as we usually work in a force-free assumption. The other two terms are represented in Fig. 2.9.(d): the fist one (upper half, in blue) is a uniformly axisymmetric "pinch" velocity $\boldsymbol{v}_{E \times B}$ that is not influenced by the helical modulation, unlike the second one (lower half, in red) $\boldsymbol{v}_{\boldsymbol{\nabla}\varphi \times B}$ that is in fact visibly similar to the bottom part of Fig. 2.9.(c). This proves that the electrostatic drift $\boldsymbol{v}_{\nabla\varphi \times B}$ is in fact the main actor in the dynamo process. The aforementioned observation can be easily extended to QSH and MH states with analogous results: in the latter case, the potential and the resulting flow will not be laminar.

The conclusion that the RFP dynamo is a mostly electrostatic process is extremely interesting from a theoretical point of view. In recent years, the same concept has found an application in the attempt of explaining the flux-pumping mechanism for the tokamak in analogy with the RFP dynamics [Piovesan17].

Flux pumping is an important mechanism in the hybrid scenario of tokamak operation explored for instance in DIII-D [Petty16], where a quite promising energy confinement is achieved with a low safety factor on axis ($q_{\text{min}} \geq 1$)
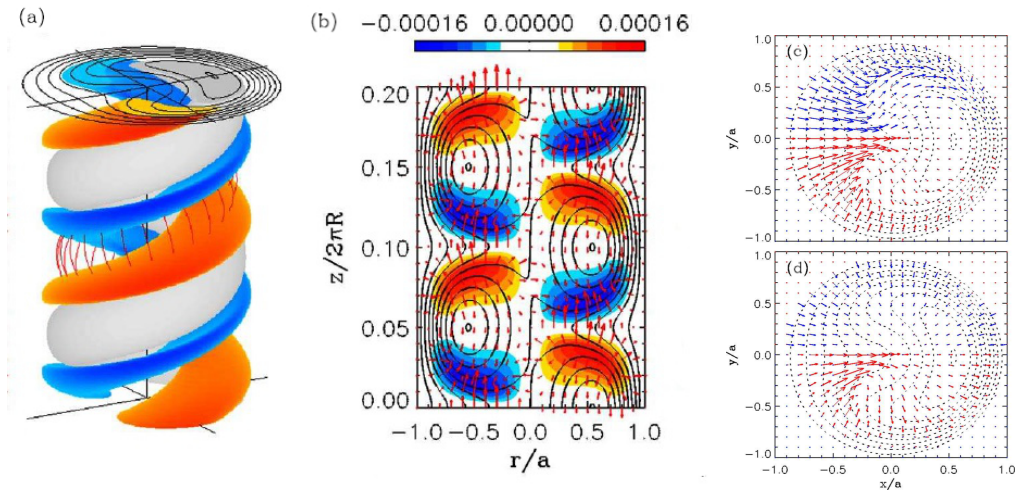
Figure 2.9: Predominantly electrostatic nature of the dynamo effect in the RFP: (a) presents a SH state, with a helical modulation of the current density (grey), sustained by a helical electric potential φ (orange and blue mark its maximum and minimum iso-surfaces). A helical electric field $-\nabla\varphi$ is represented in red, between the "plates" of the "winding capacitor". (b) Representation of the same concept as a Poincaré plot in the toroidal plane. (c) Helical flow velocity (blue) and its component responsible for the dynamo (orthogonal to the magnetic field, in red). (d) Axisymmetric component of the $E \times B$ drift velocity (blue), and $-\nabla\varphi \times E$ drift velocity (red), evidently very similar to the dynamo flow in (c). Images taken from [Cappello06].

and a strong non-inductive current is driven in the core by means of external actuators (*e.g.*, NBI or ECCD). This configuration is sometimes subject to a sawtooth instability, which is triggered whenever q_{min} crosses 1. However, the nonlinear saturation of an internal mode, resonating in the core, can redistribute the current density in the centre of the plasma, producing a locally flat q-profile just above 1: this is dubbed poloidal flux pumping and is highly beneficial for the scenario stability, allowing to reach higher β and avoiding the sawtoothing. The flux pumping mechanism still lacks of a validated model, which would be needed to extrapolate towards larger scale devices. Of great theoretical interest is also whether or not the flux pumping mechanism can be reproduced in an ELM-free steady state operation, as it is mostly observed in conjunction with edge localised modes (ELMs) [Zohm96]. In [Piovesan17] a model is proposed, in analogy to the dynamo process typically observed in the RFP. Given the electrostatic nature of the process, this explanation would suggest that the flux pumping can in fact work in stationary conditions, with no need for transient phenomena.

Figure 2.10 reports the key results in [Piovesan17] for one of the considered case studies, corresponding to the saturation of a tearing mode $(1, 1)$. We start from $q_{min} < 1$, so that the examined tearing mode is immediately triggered: as already discussed in [Bonfiglio05], a helically modulated electrostatic potential φ is expected to build up and saturate with the mode. Its saturated final shape should be alike what we described before as a helical capacitor, as in Fig. 2.10.(a). The modulated electric field produces an $E \times B$ drift whose non-axisymmetric part is the dynamo flow, represented in Fig. 2.10.(b). Figure 2.10.(c) shows that an intense electric field in the parallel direction to the magnetic field is expected to develop, whose strongly negative value on axis should fight against the current peaking in the plasma core. The time evolution from the initial state (black) to the final one is in good qualitative agreement with the experimental observations, both concerning the current density profile in Fig. 2.10.(d) and the safety factor profile in Fig. 2.10.(e). Finally, Fig. 2.10.(f) reports the terms in the resistive Ohm's law, for completeness of information.

Preliminary studies with more realistic boundary conditions.   There remains yet one key aspect that SpeCyl's simulations have never been able to reproduce, which is the recurring spontaneous formation of a QSH state with dominant mode $(1, -7)$, routinely observed in high current shots in RFX-mod, without any applied external triggering.

It is possible that this discrepancy can be motivated with the oversimplified assumption of ideal wall boundary conditions at plasma edge. Indeed, a
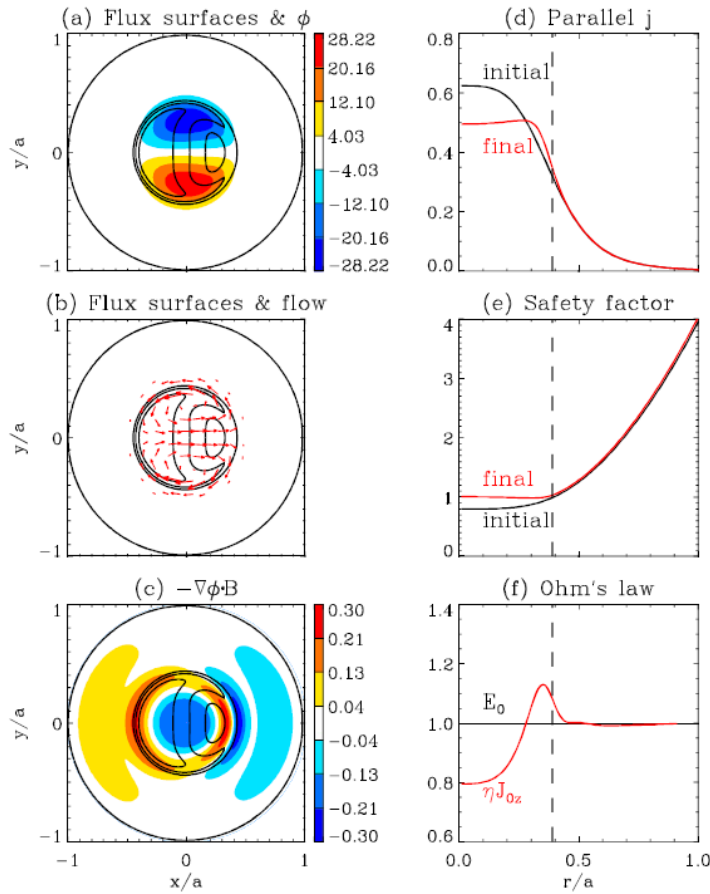
Figure 2.10: Proposed description of the flux pumping mechanism in terms of the electrostatic dynamo. (a) Helical electrostatic potential and Poincaré plot of the flux; (b) perpendicular $\boldsymbol{v}_{\nabla\varphi\times B}$ flow producing the dynamo; (c) parallel component of the helical electric field, negative in the core, with a limiting effect on the current-peaking on axis; (d) evolution of the parallel current profile; (e) evolution of the safety factor; (f) terms in the Ohm's law at the final helical equilibrium. Images taken from [Piovesan17].

first major reformulation of the magnetic boundary was operated by Daniele Bonfiglio in 2017 [Bonfiglio19], introducing a thin resistive shell at plasma boundary, surrounded by a vacuum region and by an outer ideal wall. The two main formulations of SpeCyl's boundary conditions (the ideal wall, and the resistive wall) are presented in the detail throughout Part III.

With this new resistive-shell formulation of the plasma boundary, some preliminary but promising results have been found. Several simulations in RFP geometry have been performed, all presenting an ubiquitous experimental-like sawtoothing mechanism: the safety factor at the edge of the plasma follows quasi-periodic cycles of saturating growth, followed by a rapid crash, corresponding to a major reconnection event. In particular, a mild but consistent emergence of mode $(1, -7)$ is observed when the resistive diffusion time of the magnetic field through the thin resistive shell is comparable with the time-scale of these reconnection events, as shown if Fig. 2.11.(a). This preliminary result, if confirmed, suggests that behind the spontaneous emergence of the observed mode in RFX there might be a self-consistent interplay between the internal plasma MHD and the resistive shell at boundary. The idea is that each cycle of the sawtooting sees in the wall the "footprint" left behind by the previous cycle, which has not yet disappeared because the resistive time of the wall is comparable with the sawtooth period.

The same implementation was also employed in producing a predictive scan on the energy of secondary modes in dependence of the ideal wall proximity to the edge of the plasma, so as to anticipate the new device configuration RFX-mod2. This is reported in Fig. 2.11.(b), and largely confirms the prediction that a more closely-fitting copper shell should indeed stabilise the MH background and favour the emergence of QSH states in the new device.

2.5 Conclusive summary and outline of the present work

In this chapter we have presented more in detail the reversed-field pinch configuration and the dedicated modelling.

In Sec. 2.2 we have given an overview of the main physical aspects, with particular emphasis on the recent radical change in its baseline scenario, from the inherently chaotic MH states, to a self-organised QSH state where conserved flux surfaces are present, along with transport barriers. QSH states result from the nonlinear saturation of a single MHD mode over the rest of the magnetic spectrum.

Section 2.2 presented RFX-mod, the largest RFP device in the world, and
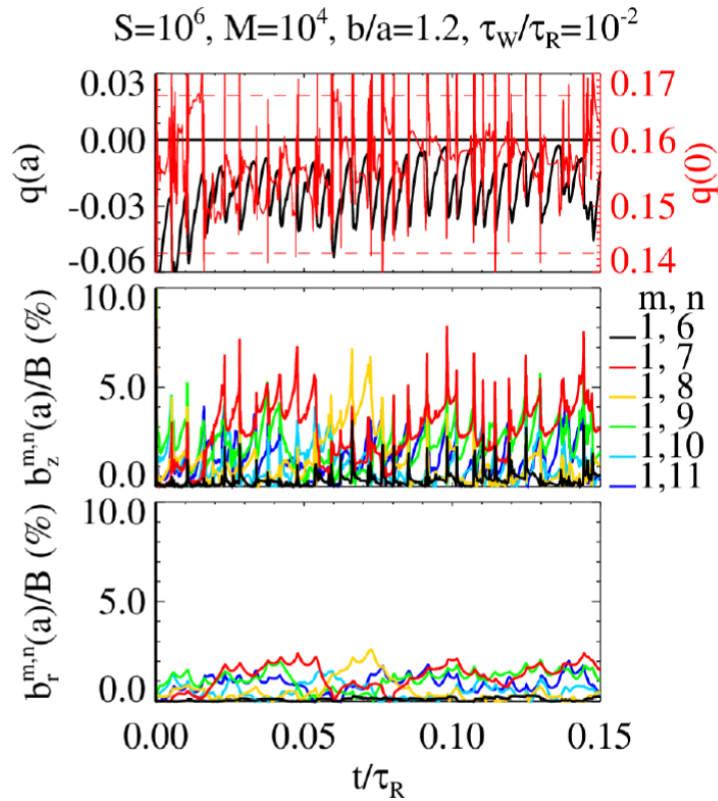
(a) When the resistive diffusion time of the wall (τ_W) matches the average period of the sawtoothing in the q profile, there is a mild but consistent spontaneous emergence of mode $(1, -7)$.
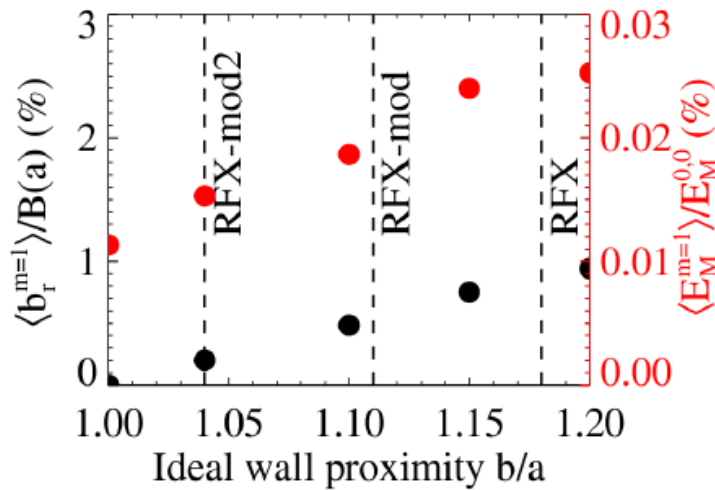
(b) Scan on secondary modes energy for various ideal wall proximimities.

Figure 2.11: First simulations with the thin shell formulation of SpeCyl's boundary conditions. Images taken from [Bonfiglio19].

its upgrade RFX-mod2, which will be operative next year. RFX-mod is endowed with a versatile set of 192 individually fed saddle-coils for the feedback control of MHD modes: they can be either used so as to simulate the presence of an ideally conducting wall at the plasma edge, or to introduce new degrees of freedom in the shaping of the edge radial magnetic field. Such a system, along with the toroidal magnetic field coils can be used to trigger the otherwise spontaneous QSH states through PPCDs, OPCDs, or MPs.

The upgrade to the new device will bring the stabilising wall closer to the plasma, reducing the amplitude of secondary modes and thus fostering the QSH performance and stability.

Section 2.3 has quickly presented the MHD equations and the relevant dimensionless parameters, which will be used through all this Thesis. In particular, we have motivated the crucial relevance of the Hartmann number in defining the visco-resistive dynamics of MHD plasmas.

The central role of modelling in the RFP research line has been explored in Sec. 2.4, with particular emphasis on some important results found with the code SpeCyl in the past twenty years. 3D nonlinear self-consistent MHD simulations predicted the viability of high-current QSH states before their consistent experimental observation, and could qualitatively reproduce most of their physical aspects. However, the spontaneous emergence of a QSH state dominated by mode $(1, -7)$ in the RFX-mod device has never been faithfully reproduced in a self-consistent way.

A first major reformulation of the magnetic boundary conditions has been proposed by Daniele Bonfiglio, finding preliminary but extremely promising results, that could lead to a deeper understanding of the underlying physical mechanisms behind this phenomenon.

It would be of outstanding theoretical interest to faithfully reproduce the spontaneous and consistent emergence of a QSH state in a 3D, nonlinear and self-consistent tool as SpeCyl.

Despite some qualitative testing of this new set of boundary conditions has already been performed (see [Bonfiglio19]), a more quantitative benchmark verification is mandatory to assess its mathematical correctness and its faithfulness to physics.

A very challenging test, to this extent, can be provided by a nonlinear verification benchmark against the linear theory of free-boundary instabilities, *e.g.*, the external kink modes. Another, less challenging, case-study could be provided by fixed-boundary instabilities as the tearing modes.

2.5.1 Outline of my Thesis

The next chapters are organised in four main parts, each composed by two chapters, and the final conclusions:

- Part II contains a detailed description of the linear MHD theory of current-driven instabilities. We also describe the implementation and testing of a linear-stability numeric tool, instrumental for establishing quantitative benchmark verifications of SpeCyl's implementations.

- Part III presents the SpeCyl code and its two existing sets of boundary conditions: the ideal wall formulation and the resistive wall formulation. We present in particular a verification benchmark of the latter against the numerical predictions of our linear-stability tool, that leads us to conclude that a major reformulation of the fluid part of SpeCyl's boundary conditions need to be found.

- Part IV illustrates the formulation and implementation of the new and comprehensive magneto-fluid set of boundary conditions for SpeCyl, which self-consistently combines the already present resistive shell formulation with a 3D velocity boundary.

- Part V contains the rigorous verification benchmark that we performed against the independent 3D nonlinear MHD self-consistent code Pixie3D, where similar resistive-shell boundary conditions have been recently implemented, in parallel with SpeCyl. In addition, a final verification benchmark study is reported also against the numeric predictions of our linear-stability code, this time achieving excellent results.

- Part VI presents the final conclusions and remarks.

Part II

Linear stability of current-driven MHD modes

3

Linear stability theory and numerical tools

Part II illustrates some elements of the linear theory of small perturbations in the larger frame of MHD. The precise knowledge of some aspects of typical plasma relaxation processes, namely the ideal kink modes and the tearing modes, is instrumental to the verification of our new set of boundary conditions. However, a precise effort has been put in enlarging the scope to curiosities and particular cases, fruit of personal theoretical exercises, that we hope will render this Chapter more interesting and instructive.

Almost none of the results presented in this part is original, since very large literature is already present on this topic. Such literature has been condensed in the next two Chapters, paired with the incremental report of the implementation of a linear-instability numeric tool, dubbed LENS (Linear Euler-Newcomb Solver), implemented using the IDL coding language.

The aim of this (rather technical) Chapter is to provide the reader with the basic tool-kit to face the rest of Part II. In particular, after a general introduction to current-driven instabilities, we present two alternative ways to rewrite in more convenient variables the momentum balance equation of MHD: namely, the Newcomb's and Euler's equations. We derive such equations almost from first principles and in general toroidal geometry, still assuming circular poloidal cross section, then we specialize them to the large aspect-ratio limit of a periodic-cylinder geometry, later used as a linear benchmark for SpeCyl. In doing so we also wish to highlight important physical aspects contained in the equations, especially relying on the insight provided by the LENS code.

3.1   Static one-dimensional equilibrium

The perturbative theory treats instabilities as small perturbations to a given initial equilibrium. The first natural step is thus to define this equilibrium.

It is general to assume that at the onset of an experimental plasma discharge can be approximated to a static equilibrium, governed by the following set of equations:

$$\boldsymbol{v}_0 = 0 \qquad \text{static condition,}$$
$$\nabla \cdot \mathbf{B}_0 = 0 \qquad \text{solenoidal property,}$$
$$\nabla \times \mathbf{B}_0 = \mu_0 \mathbf{J}_0 \qquad \text{Faraday's law,}$$
$$\mathbf{J}_0 \times \mathbf{B}_0 = \nabla p_0 \qquad \text{static momentum equation,}$$

where the subscript "0" marks equilibrium quantities.

One important consequence of the static momentum balance equation is that we may write the equilibrium current density as the sum of two parts

$$\mathbf{J}_0 = \frac{\sigma}{\mu_0} \mathbf{B}_0 + \mathbf{J}_{0,\perp} \,, \tag{3.1}$$

where

$$\sigma \equiv \mu_0 \frac{\mathbf{J}_0 \cdot \mathbf{B}_0}{|\mathbf{B}_0|^2} \,, \tag{3.2}$$

and μ_0 is added for future convenience. The first term in Eq. 3.1 is usually called *force-free* since it gives no contribution to momentum balance equation, while the second term is dubbed *diamagnetic* current, and is obtained by taking the vector product of $\mathbf{B}_0$ with the static momentum equation:

$$(\mathbf{J}_0 \times \mathbf{B}_0) \times \mathbf{B}_0 = -|\mathbf{B}_0|^2 \mathbf{J}_{0,\perp} = \nabla p_0 \times \mathbf{B}_0 \,,$$

thus

$$\mathbf{J}_{0,\perp} = -\frac{\nabla p_0 \times \mathbf{B}_0}{|\mathbf{B}_0|^2} \,. \tag{3.3}$$

Throughout this work, we will always assume that our equilibrium is axisymmetric. This brings to some further simplification since for all quantities

$$\nabla \equiv \frac{\mathrm{d}}{\mathrm{d}r} \,.$$

Thus, from the solenoidal property we get that $B_{0,r} = 0$. This combined with Faraday's law yields for the current density:

$$J_{0,r} = 0 \,, \qquad J_{0,\theta} = -\frac{\mathrm{d}}{\mathrm{d}r} B_{0,z} \,, \qquad J_{0,z} = \frac{1}{r} \frac{\mathrm{d}}{\mathrm{d}r} B_{0,\theta} \,.$$

Our one-dimensional static momentum equation reads:

$$J_{0,\theta} B_{0,z} - J_{0,z} B_{0,\theta} = \frac{\mathrm{d}p_0}{\mathrm{d}r} \,,$$

and the diamagnetic current density (Eq. 3.3) becomes:

$$\mathbf{J}_{0,\perp} = \frac{B_{0,z}\hat{\boldsymbol{\theta}} - B_{0,\theta}\hat{\mathbf{z}}}{|\mathbf{B}_0|^2} \frac{\mathrm{d}p_0}{\mathrm{d}r} \,. \tag{3.4}$$

3.2 Physical overview of current-driven instabilities

To a general overview, current driven instabilities in a magnetised plasma present some important similarities: due to some small initial perturbation in the current profile or intensity, the magnetic geometry is deformed and may, in some cases, undergo some topological change.

As geometry plays such an important role in these phenomena, one should start by considering the overall symmetries of the system. Since we will adopt a cylindrical symmetry, hence it is generally convenient to Fourier analyse the perturbation, in such a way that every quantity $\mathbf{Q}$ can be expressed as

$$\mathbf{Q}(r,\theta,\varphi,t) = \sum_{m,n} \mathbf{Q}^{m,n}(r,t) \cdot e^{im\theta - in\varphi} \,, \quad \varphi = \frac{z}{R} \tag{3.5}$$

being r the radial coordinate, pointing out from the toroidal axis, θ the poloidal angle, φ the toroidal angle, z the cylinder axis, R the major radius of the device and t the time.

Furthermore, we will always imply that small perturbations may be assumed to depend trivially upon time, so that

$$\mathbf{Q}^{m,n}(r,t) = \mathbf{Q}^{m,n}(r) \cdot e^{-i\omega t} \,, \quad \forall m,n \tag{3.6}$$

being in general $\omega \in \mathbb{C}$, so that $\mathrm{Re}(\omega)$ is a mode frequency, while $\mathrm{Im}(\omega) \equiv \gamma$ is the mode growth/damping rate.

Fourier decomposition has the advantage that one can work on single perturbation modes, having well-defined periodicity. As the equilibrium presents a set of nested flux surfaces, characterised by a smoothly varying toroidal pitch of magnetic field-lines, it may well happen that a mode has the same periodicity as the equilibrium field at some given radius: this condition is dubbed a resonance and is a fundamental trait in defining the type of the instability.

Indeed, MHD instabilities are classified into *internal* or *external* modes, depending on whether the resonant surface lays inside or outside the plasma. Internal modes are usually *fixed-boundary* instabilities, as their development does not affect significantly the plasma edge. In opposition, external modes are mostly *free-boundary* instabilities, since they may only become unstable if the boundary is free to deform.

Another important distinction is between *resistive* and *ideal* modes. Ideal modes can be either internal or external and are dubbed *kinks* as they only deform the magnetic geometry without affecting topology, whereas the resistive ones are only internal and are dubbed *tearing modes* as they tear and rejoin field lines.

Dealing with the ideal modes, the magnetic field is frozen into the plasma and timescales are faster, in the order of the Alfvènic timescale, already defined as

$$\tau_A \equiv \frac{\sqrt{\mu_0 \rho_0}}{B_{0,z}} L$$

where μ_0 is the vacuum permeability, ρ_0 is the mass-density on the toroidal axis, $B_{0,z}$ is the toroidal field on axis and L is a typical length of the system, which is usually identified either with the poloidal radius a or the toroidal radius R of the device. In the following we will deal with phenomena evolving on both length-scales, so we define by now

$$\tau_A \equiv \frac{\sqrt{\mu_0 \rho_0}}{B_{0,z}} a \tag{3.7}$$

while the toroidal Alfvènic time will be referred as $\tau_A R/a$. Assuming standard values from RFX-mod with a Deuterium-Tritium plasma: $B_{0,z} \approx 1\,\mathrm{T}$, $\rho_0 \approx 2.5 \times m_{\mathrm{proton}} \times 10^{19}\,\mathrm{m}^{-3}$, $a = 0.46\,\mathrm{m}$ yields $\tau_A = O(\mu s)$.

Finite resistivity allows field detachment from the flow and thus magnetic topological changes, but acting on slower *resistive magnetic-diffusion* timescales (Eq. 2.4):

$$\tau_R \equiv \frac{\mu_0}{\eta} L^2$$

being η the plasma resistivity and L a characteristic spacial scale, which is usually identified with the minor radius a of the plasma. As stated before, it is always assumed that $\tau_R \gg \tau_A$.

3.2.1 Physical drive

This Section reports a quite useful toy model, presented by Wesson in [Wesson78] to explain the how not uniform currents may affect plasma equilibrium stability. Albeit pertaining more directly to the next Chapter, where

current-driven instabilities are introduced and studied, we think this can offer a very good lead into the rest of part II. We think so because it introduces and explains from a deeply physics-centred viewpoint the linearised momentum balance equation, which is going to bear a leading part in this Chapter. Also, it motivates the central relevance of the radial component of small perturbations to a given equilibrium, which will be implied through this whole Chapter.

Let us take into account the curl of the momentum equation, which gives us the torque balance equation (let us assume for now an inviscid plasma):

$$\nabla \times \left(\rho \frac{\mathrm{D}}{\mathrm{D}t} \boldsymbol{v} \right) = \nabla \times (\mathbf{J} \times \mathbf{B}) \equiv \mathbf{T}. \tag{3.8}$$

Note that the pressure gradient does not apply any torque, being in first approximation an axi-symmetrical force[1].

At equilibrium, both terms in Eq. 3.8 are null. However, let us assume that the initially axi-symmetric equilibrium is slightly deformed, *e.g.* into an ellipse, as in Figure 3.1. As symmetry gets broken, the magnetic field acquires a radial component, b_r.

Let us make the assumption of a linear perturbation so that we can write perturbed quantities as the sum of the equilibrium plus a first order term: $\mathbf{B} = \mathbf{B_0} + \mathbf{b}$ and $\mathbf{J} = \mathbf{J_0} + \mathbf{j}$. Making use of vector identities and linearising we can write Eq. 3.8 as:

$$\mathbf{T} = \mathbf{b} \cdot \nabla \mathbf{J}_0 - \mathbf{j} \cdot \nabla \mathbf{B}_0 + \mathbf{B}_0 \cdot \nabla \mathbf{j} - \mathbf{J}_0 \cdot \nabla \mathbf{b} \,. \tag{3.9}$$

We will discuss more extensively this equation in the next Section. For the moment, let us just focus on the first term, neglecting all components of the perturbation but the radial one. For it to contribute to the torque, we require that $\mathbf{J}_0$ depend on the radius.

Figure 3.1 focuses on the torque produced by the $b_r \nabla_r J_z$ term: in an initially axi-symmetric plasma, as in panel (a), we consider a cylindrical slab of plasma, enclosed between two magnetic flux tubes (in green and red the inner and outer, respectively). Suppose that some oscillation of any kind produces an initial ripple on this slab, like the dashed contour in panel (a), thus breaking cylindrical symmetry.

Panels (b) and (c) show the detail of a perturbed slab: the point is that the two magnetic surfaces (green and red) are composed by magnetic field lines, that acquire a radial component throughout the bending (see panel (c) for

---

[1]Moreover, the curl of the gradient of a scalar field is always null. To prove it, think of ∇p as a conservative field, whose potential is of course $-p$: being conservative, the work done on a closed path must always be null, whence the thesis, via the Stokes theorem
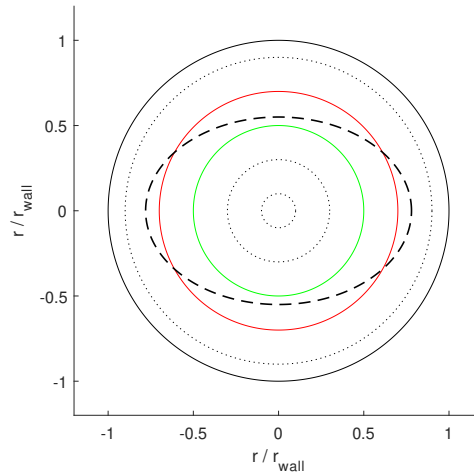
(a) Poloidal cross section
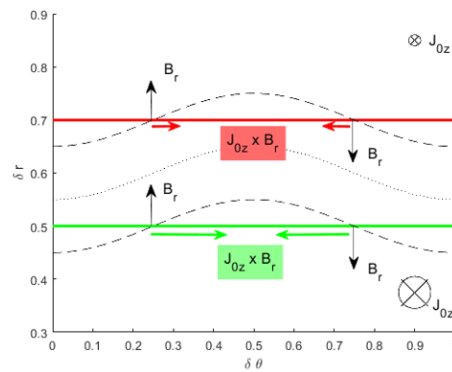
(b) Detail of slab deformation
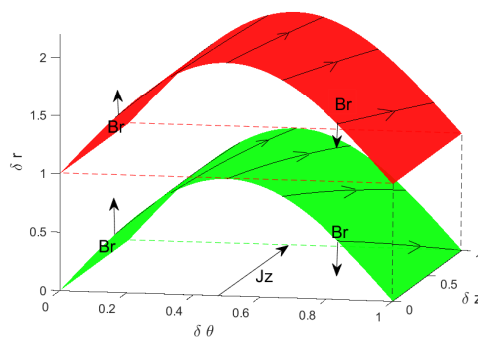
(c) Detail of slab deformation

Figure 3.1: Physical drive at the onset of a kink: the initially circular magnetic surfaces are perturbed into an ellipse. The slab between the green and the red surfaces is analysed in detail: field bending produces a radial component that combines with toroidal current in a $\mathbf{J} \times \mathbf{B}$ force, which is unbalanced if there is a finite $\nabla J_{0,z}$, providing net destabilising torque onto the slab.

better understanding of this). This initial b_r combines with the equilibrium current density, in such a way that $J_z b_r$ couples of forces develop on both faces of the slab, oriented so as to compress each face azimuthally. Panel (b) shows just two of them for each magnetic surface, but indeed every point of the (dashed) deformed magnetic surface is subject to such forces, mirroring each other on the two sides of each ripple.

The contribution of the field lines on the internal (green) face exerts a destabilising torque onto the central slit of the deformed slab (dotted in panel (b)), whereas the external (red) face opposes the instability. Take into account the forces on the right-hand side of both surfaces: albeit pointing in the same direction, their torques onto the central slit of our slab must be in contrast, since the moment arms are opposite in sign. The same of course holds for the left-hand side of the ripple.

In principle, opposite effects could end up cancelling each other. However, if there exists some finite radial gradient of $J_{0,z}$ the two effects do not balance, yielding instability if $J_{0,z}$ decreases towards the edge of the plasma.

As we will see in next Sections, the presence of magnetic shear can influence and help stabilise the process. This can be understood by looking at panel (c), that shows how varying the equilibrium pitch across each slab, different values of b_r can be found, so that the reduction in the $J_{0,z}$ intensity can be either amplified or compensated in the $\mathbf{J} \times \mathbf{b}$ term.

3.3   Newcomb's equation

We introduce in this Section a powerful tool to determine up to some precision the shape of the linearly perturbed magnetic field and current density, under the hypothesis of marginal stability. The content of this Section is the yield of a theoretical exercise, but an analogous derivation can be found also in [Fitzpatrick99, Calabrese13].

Newcomb's equation is usually derived for a case in which the role of pressure is neglected. In this case, force balance at equilibrium would require:

$$\mathbf{J}_0 \times \mathbf{B}_0 = 0$$

and thus we can define a function $\sigma(r)$ such that $\mu_0 \mathbf{J}_0 = \sigma \mathbf{B}_0$, or

$$\sigma \equiv \mu_0 \frac{\mathbf{J}_0 \cdot \mathbf{B}_0}{|\mathbf{B}_0|^2}$$

as in Eq. 3.2. This is the same as retaining only the force-free term out of Eq. 3.1.

What we want to derive here is a slightly more general equation and from that we will extract the pressureless case as a particular limit. We have already seen that pressure cannot contribute to the current-driven torque and thus one may think that it should automatically slip away from our equations. Nonetheless, the complete picture is quite different and may be worth a look. Perhaps the most instructive piece of information that we will derive from specifically tracking all terms depending on finite pressure is that they can be neglected in the relevant limit case of a large aspect ratio: since SpeCyl operates in a pressure-less assumption, this lesson will be crucial in setting our future benchmarks.

Let us start by taking into account the linearised torque equation, as we found it in Eq. 3.9:

$$\mathbf{T} = \mathbf{b} \cdot \nabla \mathbf{J}_0 - \mathbf{j} \cdot \nabla \mathbf{B}_0 + \mathbf{B}_0 \cdot \nabla \mathbf{j} - \mathbf{J}_0 \cdot \nabla \mathbf{b}.$$

Marginal stability requires $\mathbf{T} = 0$. Let us approximate our toroidal geometry to a cylinder and analyse individually every Fourier mode of our perturbation. Combining the above constraint with Faraday's equation and magnetic field incompressibility we get:

$$T_r = \left(\frac{imB_{0,\theta}}{r} - \frac{inB_{0,z}}{R} \right) j_r - \left(\frac{imJ_{0,\theta}}{r} - \frac{inJ_{0,z}}{R} \right) b_r \equiv 0$$

$$T_\theta = \left(\frac{imB_{0,\theta}}{r} - \frac{inB_{0,z}}{R} \right) j_\theta - \left(\frac{imJ_{0,\theta}}{r} - \frac{inJ_{0,z}}{R} \right) b_\theta + \left(b_r \frac{\mathrm{d}J_{0,\theta}}{\mathrm{d}r} - j_r \frac{\mathrm{d}B_{0,\theta}}{\mathrm{d}r} \right)$$
$$+ \frac{B_{0,\theta} j_r - J_{0,\theta} b_r}{r} \equiv 0$$

$$T_z = \left(\frac{imB_{0,\theta}}{r} - \frac{inB_{0,z}}{R} \right) j_z - \left(\frac{imJ_{0,\theta}}{r} - \frac{inJ_{0,z}}{R} \right) b_z + \left(b_r \frac{\mathrm{d}J_{0,z}}{\mathrm{d}r} - j_r \frac{\mathrm{d}B_{0,z}}{\mathrm{d}r} \right) \equiv 0$$

$$(\nabla \times \mathbf{b})_r = \frac{imb_z}{r} + \frac{inb_\theta}{R} \equiv \mu_0 j_r$$

$$(\nabla \times \mathbf{b})_\theta = -\frac{inb_r}{R} + \frac{\mathrm{d}b_\theta}{\mathrm{d}r} \equiv \mu_0 j_\theta$$

$$(\nabla \times \mathbf{b})_z = \frac{1}{r} \frac{\mathrm{d}}{\mathrm{d}r} (rb_\theta) - \frac{imb_r}{r} \equiv \mu_0 j_z$$

$$\nabla \cdot \mathbf{b} = \frac{1}{r} \frac{\mathrm{d}}{\mathrm{d}r} (rb_r) + \frac{imb_\theta}{r} - \frac{inb_z}{R} \equiv 0$$

where $\mathbf{b} = (b_r, b_\theta, b_z)$ and $\mathbf{j} = (j_r, j_\theta, j_z)$ are the Fourier components of the perturbation, having m-fold periodicity in θ and n-fold in $\varphi = z/R$, as in

Eq. 3.5.
From the first equation we can derive that $\mu_0 j_r = \Sigma b_r$, having defined Σ as:

$$\Sigma \equiv \mu_0 \frac{m J_{0,\theta} - n J_{0,z} \varepsilon}{m B_{0,\theta} - n B_{0,z} \varepsilon} \,; \qquad \varepsilon = \frac{r}{R} \,. \tag{3.10}$$

Making use of Eqs. 3.1 and 3.4 we may write

$$\Sigma = \sigma + \frac{\mu_0}{|\mathbf{B}_0|^2} \frac{m B_{0,z} + n B_{0,\theta} \varepsilon}{m B_{0,\theta} - n B_{0,z} \varepsilon} \frac{\mathrm{d} p_0}{\mathrm{d} r} \,.$$

This way we made apparent the force-free and the diamagnetic contributions in this scalar function.

It is convenient to introduce the magnetic flux perturbation, $\psi(r) = -i r b_r$, as a parameter in terms of which we can find all the other quantities. In fact, after quite a long manipulation we can find that:

$$b_r = \frac{i \psi}{r} \tag{3.11}$$

$$b_\theta = \frac{n \varepsilon \Sigma \psi}{H} - \frac{m}{H} \frac{\mathrm{d} \psi}{\mathrm{d} r} \tag{3.12}$$

$$b_z = \frac{m \Sigma \psi}{H} + \frac{n \varepsilon}{H} \frac{\mathrm{d} \psi}{\mathrm{d} r} \tag{3.13}$$

being $H = m^2 + n^2 \varepsilon^2$. Current density components are then:

$$\mu_0 j_r = \frac{i \Sigma \psi}{r} \tag{3.14}$$

$$\mu_0 j_\theta = \frac{n \varepsilon \Sigma^2 \psi}{H} - \frac{m \Sigma}{H} \frac{\mathrm{d} \psi}{\mathrm{d} r} + \frac{\psi}{F} \left[\left(\Sigma \frac{\mathrm{d} B_{0,\theta}}{\mathrm{d} r} - \mu_0 \frac{\mathrm{d} J_{0,\theta}}{\mathrm{d} r} \right) - \frac{\Sigma B_{0,\theta} - \mu_0 J_{0,\theta}}{r} \right] \tag{3.15}$$

$$\mu_0 j_z = \frac{m \Sigma^2 \psi}{H} + \frac{n \varepsilon \Sigma}{H} \frac{\mathrm{d} \psi}{\mathrm{d} r} + \frac{\psi}{F} \left(\Sigma \frac{\mathrm{d} B_{0,z}}{\mathrm{d} r} - \mu_0 \frac{\mathrm{d} J_{0,z}}{\mathrm{d} r} \right) \tag{3.16}$$

having also defined F as:

$$F \equiv m B_{0,\theta} - n \varepsilon B_{0,z} \,. \tag{3.17}$$

Finally, either of the remaining two constraints yields a second order ODE for ψ:

$$\frac{\mathrm{d}}{\mathrm{d} r} \left(\frac{r}{H} \frac{\mathrm{d} \psi}{\mathrm{d} r} \right) = \left[\frac{1}{r} + \frac{2 m n \varepsilon \Sigma}{H^2} - \frac{r \Sigma^2}{H} + \frac{n \varepsilon r}{m H} \frac{\mathrm{d} \Sigma}{\mathrm{d} r} + \frac{r}{m F} \left(\mu_0 \frac{\mathrm{d} J_{0,z}}{\mathrm{d} r} - \Sigma \frac{\mathrm{d} B_{0,z}}{\mathrm{d} r} \right) \right] \psi \,. \tag{3.18}$$

Equation 3.18 is the generalisation of Newcomb's equation to the case in which no assumption is made on pressure. To recover the standard Newcomb's equation, we must only retain the force-free contribution to current density: each component of $\mathbf{J}$ is proportional via $\sigma(r)/\mu_0$ to the corresponding component of $\mathbf{B}$, and there is a full identity between Σ and σ. Hence, the last two terms in the square bracket of Eq. 3.18 condense in one and we get the actual Newcomb's equation:

$$\frac{\mathrm{d}}{\mathrm{d}r}\left(\frac{r}{H}\frac{\mathrm{d}\psi}{\mathrm{d}r}\right) = \left[\frac{1}{r} + \frac{2mn\varepsilon\sigma}{H^2} - \frac{r\sigma^2}{H} + \frac{r(n\varepsilon B_{0,\theta} + mB_{0,z})}{FH}\frac{\mathrm{d}\sigma}{\mathrm{d}r}\right]\psi. \quad (3.19)$$

Regarding equations 3.11-3.16, the components of $\mathbf{b}$ and j_r keep almost unchanged, if not for the specification that $\Sigma = \sigma$, whereas in j_θ and j_z become

$$j_\theta = \sigma b_\theta - B_{0,\theta}\frac{\mathrm{d}\sigma}{\mathrm{d}r}\frac{\psi}{F}$$

$$j_z = \sigma b_z - B_{0,z}\frac{\mathrm{d}\sigma}{\mathrm{d}r}\frac{\psi}{F}. \quad (3.20)$$

Hence, we see that the equilibrium pressure gradient mostly affects the current profile, being them both related to the plasma flow and mass distribution, while it produces a minor effect on the (externally applied) magnetic field.

3.3.1 The vacuum equation

Another interesting aspect to point at is that we can use Newcomb's equation to find vacuum profiles for the magnetic field. This aspect will become handy when we will discuss the improvements to the magnetic boundary in SpeCyl.

Vacuum field is easily recovered by setting $\Sigma = 0$ in Eq. 3.18 (or $\sigma = 0$ in Eq. 3.19) and assuming there is no current flowing: $\mathbf{J_0} = 0$. This way, our ODE reads

$$\frac{\mathrm{d}}{\mathrm{d}r}\left(\frac{r}{H}\frac{\mathrm{d}\psi}{\mathrm{d}r}\right) = \frac{\psi}{r} \quad (3.21)$$

and the field components result as

$$b_r = \frac{i\psi}{r}, \quad (3.22)$$

$$b_\theta = -\frac{m}{H}\frac{\mathrm{d}\psi}{\mathrm{d}r}, \quad (3.23)$$

$$b_z = \frac{n\varepsilon}{H}\frac{\mathrm{d}\psi}{\mathrm{d}r}, \quad (3.24)$$

while of course $j_r = j_\theta = j_z = 0$.

It should be noted that in this context there is no difference between vacuum and a highly resistive plasma. This comes from the fact that our analysis completely missed the left hand side of momentum balance equation and thus only focuses on the electromagnetic part of dynamics.

In the next Section, we will see a different approach, that allows us to make a more complete picture. It will be seen also through simulations that there is indeed some difference between a *pseudo-vacuum*, consisting in a cold and resistive plasma, and the actual vacuum.

It is also important to say that in the case of vacuum, there is a simple solution for Newcomb's equation. If we integrate Eq. 3.21 with respect to $x = |n|\,\varepsilon$ we get:

$$\frac{x}{m^2 + x^2}\frac{\mathrm{d}\psi}{\mathrm{d}x} = \int \frac{\psi}{x}\,\mathrm{d}x\,,$$

so that, for the new variable $\Psi = \int \psi/x\,\mathrm{d}x$, such that

$$\psi(x) = \frac{\mathrm{d}}{\mathrm{d}x}\left(x\Psi(x)\right) - \Psi(x)$$

we have

$$x^2\frac{\mathrm{d}^2\Psi}{\mathrm{d}x^2} + x\frac{\mathrm{d}\Psi}{\mathrm{d}x} = \left(m^2 + x^2\right)\Psi(x)\,, \tag{3.25}$$

which is known as *modified Bessel's equation* and has solution:

$$\Psi(x) = \mathcal{A}I_m(x) + \mathcal{B}K_m(x) \tag{3.26}$$

$$\implies \quad \psi(|n|\varepsilon) = \mathcal{A}\,|n|\,\varepsilon\,I'_m(|n|\varepsilon) + \mathcal{B}\,|n|\,\varepsilon\,K'_m(|n|\varepsilon)\,, \tag{3.27}$$

$\mathcal{A}, \mathcal{B} \in \mathbb{R}$ being two constants and I_m and K_m the modified Bessel functions of order m. The primes represent the first-order derivative in the function argument.

Finally, making use of Eq. 3.21 once more, we find

$$\frac{\mathrm{d}\psi}{\mathrm{d}r} = \frac{H}{r}\int\frac{\psi}{x}\,\mathrm{d}x = \frac{m^2 + n^2\varepsilon^2}{r}\cdot\Psi(|n|\,x)\,. \tag{3.28}$$

For the specific case of vacuum, Eqs. 3.22-3.24 are sometimes derived in terms of a potential function ϕ [Jackson99]. In fact, in vacuum $\mathbf{J} = \nabla \times \mathbf{B} = 0$, hence there must exist a scalar potential such that $\nabla\phi = (\mathbf{B}_0 + \mathbf{b})$. The solenoidal property of the magnetic field becomes, in cylindrical coordinates and for each Fourier mode individually, a modified Bessel's equation:

$$\nabla \cdot \mathbf{B}_0 = \nabla^2\phi^{0,0} = \frac{1}{r}\frac{\mathrm{d}}{\mathrm{d}r}\left(r\frac{\mathrm{d}\phi^{0,0}}{\mathrm{d}r}\right) = 0\,, \tag{3.29}$$

$$\nabla \cdot \mathbf{b}^{m,n} = \nabla^2\phi^{m,n} = \frac{1}{r^2}\left[r\frac{\mathrm{d}}{\mathrm{d}r}\left(r\frac{\mathrm{d}\phi^{m,n}}{\mathrm{d}r}\right) - \left(m^2 + n^2\varepsilon^2\right)\phi^{m,n}\right] = 0\,. \tag{3.30}$$

From here the derivation is almost identical to the above. Flux and potential relate to each other through

$$\psi^{m,n} = -ir\frac{\mathrm{d}\phi^{m,n}}{\mathrm{d}r} \qquad \text{for } (m,n) \neq (0,0)\,.$$

Finally, it should be added that the axi-symmetric component of the scalar potential must contain some multiple-valued terms in order to reproduce the equilibrium magnetic field produced in vacuum by a cylindrical current-carrying plasma surrounded by a solenoid:

$$\phi^{0,0}(r,\theta,z) = \Phi^{0,0}(r) + B_\theta^{0,0}(a) \cdot a\theta + B_z^{0,0}(a) \cdot z\,, \qquad (3.31)$$

where $\Phi^{0,0}$ is determined through Eq. 3.29. This way,

$$\{B_z^{0,0}\}^{\mathrm{vac}} = B_z^{0,0}(a)\,, \qquad\qquad \{B_\theta^{0,0}\}^{\mathrm{vac}} = \frac{a}{r}B_\theta^{0,0}(a)\,.$$

3.3.2   The straight tokamak limit

A second and very instructive limit case is when we assume the major radius $R \to \infty$, *i.e.* we work in large aspect ratio approximation. This comes with a typical ordering which is known as *straight tokamak ordering* and basically corresponds to setting $\varepsilon \to 0$ while keeping the MHD safety factor $q = B_{0,z}\varepsilon/B_{0,\theta} = \mathcal{O}(1)$. This, of course, involves:

$$B_{0,\theta} \sim \varepsilon \cdot B_{0,z}\,.$$

Also, since in tokamaks $B_{0,z} \propto 1/R$, we get $\mathrm{d}B_{0,z}/\mathrm{d}r \sim \varepsilon B_{0,z}$.
In this ordering, by letting ε vanish and approximating $H = m^2 + n^2\varepsilon^2 \approx m^2$, our "generalised" Newcomb's equation 3.18 now reads:

$$\frac{\mathrm{d}}{\mathrm{d}r}\left(r\frac{\mathrm{d}\psi}{\mathrm{d}r}\right) = \left[\frac{m^2}{r} - r\Sigma_{\varepsilon\to0}^2 + \frac{mr}{F}\left(\mu_0\frac{\mathrm{d}J_{0,z}}{\mathrm{d}r} - \Sigma\frac{\mathrm{d}B_{0,z}}{\mathrm{d}r}\right)_{\varepsilon\to0}\right]\psi\,. \qquad (3.32)$$

By making use of Faraday's law on the equilibrium fields we get:

$$\mu_0 J_{0,\theta} = -\frac{\mathrm{d}B_{0,z}}{\mathrm{d}r}\,; \qquad\qquad \mu_0 J_{0,z} = \frac{1}{r}\frac{\mathrm{d}}{\mathrm{d}r}(rB_{0,\theta})\,,$$

whence

$$\Sigma = \mu_0\frac{mJ_{0,\theta} - n\varepsilon J_{0,z}}{F} = -\frac{1}{F}\left[m\frac{\mathrm{d}B_{0,z}}{\mathrm{d}r} + n\varepsilon\frac{\mathrm{d}B_{0,\theta}}{\mathrm{d}r} + n\frac{B_{0,\theta}}{R}\right]\,.$$

In the previous equation, the last addend should then be dropped[2], while the first one is of the same order of $B_{0,z}$, since $F \sim \varepsilon B_{0,z}$. The middle term should also be dropped, since

$$\frac{\mathrm{d}B_{0,\theta}}{\mathrm{d}r} \approx \frac{1}{m}\left(\frac{\mathrm{d}F}{\mathrm{d}r} - n\varepsilon B_{0,z}\right)$$

must be the same order as $\varepsilon B_{0,z}$. This way, $r\Sigma^2$ cancels out with the last term of Eq. 3.32, yielding our final Newcomb's equation for the tokamak limit:

$$\frac{\mathrm{d}}{\mathrm{d}r}\left(r\frac{\mathrm{d}\psi}{\mathrm{d}r}\right) = \left[\frac{m^2}{r} + \frac{mr}{F}\mu_0\frac{\mathrm{d}J_{0,z}}{\mathrm{d}r}\right]\psi\,. \tag{3.33}$$

This equation brings us to two very important considerations:

a. Our final equation does not contain any term relating to pressure and in fact coincides with the large aspect ratio limit of pressureless Newcomb's equation (3.19). Such a result will be confirmed numerically by the end of this Chapter.

b. This is the same result obtained by Wesson in [Wesson78] by considering only the $\mathbf{b}\cdot\nabla\mathbf{J}_0$ contribution to the overall torque, showing that in the straight tokamak the kink/tearing instability is solely determined by the current gradient.

3.3.3 Plasma displacement

In ideal MHD the magnetic flux is said to be frozen into the plasma, so we expect to find a trivial relation that correlates the flux function ψ to the flow $\boldsymbol{v}$ or its time integral $\boldsymbol{\xi}$, dubbed *Lagrangian displacement* and representing the small spacial offset of the fluid element related to the instability:

$$\frac{\mathrm{d}\boldsymbol{\xi}}{\mathrm{d}t} \approx \frac{\partial\boldsymbol{\xi}}{\partial t} = \boldsymbol{v}\,.$$

The flux freezing condition is enclosed in the ideal Ohm's equation:

$$\mathbf{E} + \boldsymbol{v}\times\mathbf{B} = 0\,.$$

By taking its curl and getting rid of the electric field $\mathbf{E}$ throughout the Faraday's law, we get to an equation that does only depend on the magnetic field and the flow. Let us assume a static equilibrium ($\boldsymbol{v}_0 = 0$) and cylindrical

---

[2] $B_{0,\theta}/R \sim \mathcal{O}(\varepsilon^2)$, since $B_{0,\theta} \sim \varepsilon B_{0,z}$ and of course $1/R \sim \varepsilon$.

geometry and introduce a linear perturbation to the magnetic field $\mathbf{B} = \mathbf{B}_0 + \mathbf{b}$:

$$\frac{\partial}{\partial t}\left(\mathbf{B}_0 + \mathbf{b}\right) = \nabla \times \left(\frac{\partial \boldsymbol{\xi}}{\partial t} \times \left(\mathbf{B}_0 + \mathbf{b}\right)\right) \quad \implies \quad \mathbf{b} = \nabla \times \left(\boldsymbol{\xi} \times \mathbf{B}_0\right) . \quad (3.34)$$

In the last step, a linearisation has been made, since $\partial_t \boldsymbol{\xi} \times \mathbf{b}$ is second order in the perturbation.

Let us now take the radial projection of the above equation and work onto a single Fourier mode: the same vector identities already employed in the torque equation yields

$$b_r = \mathbf{B}_0 \cdot \nabla \xi_r = \left(\frac{imB_{0,\theta}}{r} - \frac{inB_{0,z}}{R}\right)\xi_r .$$

The LHS of the above equation is formally identical to $T_r = 0$, provided that one substitutes j_r with ξ_r.

Recall now that $\psi = -irb_r$, whence the required relation:

$$\psi = F\,\xi_r \qquad\qquad (3.35)$$

where $F = \left(mB_{0,\theta} - n\varepsilon B_{0,z}\right)$ as in Eq. 3.17.

3.4   Numerical solution of Newcomb's equation

Let us now briefly discuss about LENS, the numerical solver we developed to produce the linear magnetic flux perturbation to a given arbitrary equilibrium, defined by the choice of a current density profile $\mathbf{J}_0(r)$.

This consists of an explicit fourth-order Runge-Kutta method (see [Süli14] and [Fitzpatrick13]). The integration is performed with IDL built-in `RK4` function.

Our ultimate goal is to produce reliable numerical solutions to be benchmarked with results from the SpeCyl code. Since SpeCyl neglects pressure gradients in its model equations, we seek to solve the pressure-less Newcomb Eq. 3.19, reported below for ease:

$$\frac{\mathrm{d}}{\mathrm{d}r}\left(\frac{r}{H}\frac{\mathrm{d}\psi}{\mathrm{d}r}\right) = \left[\frac{1}{r} + \frac{2mn\varepsilon\sigma}{H^2} - \frac{r\sigma^2}{H} + \frac{r(n\varepsilon B_{0,\theta} + mB_{0,z})}{FH}\frac{\mathrm{d}\sigma}{\mathrm{d}r}\right]\psi .$$

This second-order ODE is then broken by LENS into the following first order ODEs to be solved iteratively:

$$\frac{\mathrm{d}}{\mathrm{d}r}\mathtt{Y}_0(r) = \frac{\mathtt{Y}_1(r)}{f(r)}$$

$$\frac{\mathrm{d}}{\mathrm{d}r}\mathtt{Y}_1(r) = g(r)\mathtt{Y}_0(r)$$

where $\mathtt{Y}_0(r) = \psi(r)$, $\mathtt{Y}_1(r) = f(r)\psi'(r)$, $f = \frac{r}{H}$, and $g(r)$ is the long term in square brackets in the initial second-order equation. The prime represents a first-order derivative in the function main argument.

Since the $g(r)$ is singular on axis, the solver substitutes a linear approximant to the solution for the first few radial integration steps Δr. This can be built in the following manner: since very close to axis $r = N_{\text{steps}} \times \Delta r \ll a$, with N_{steps} small, for any geometry of interest $R \geq a$ implies $\Delta r/R \ll 1$, we may use the large aspect ratio limit of Newcomb's equation (Eq. 3.33). Furthermore in a small interval around axis, we can assume $J'_{0,z} \approx 0$, so that we have:

$$\frac{\mathrm{d}}{\mathrm{d}r}\left(r\frac{\mathrm{d}\psi}{\mathrm{d}r}\right) \approx \frac{m^2}{r}\psi,$$

whose solution is indeed $\psi = \mathcal{A}\,r^m + \mathcal{B}\,r^{-m}$, with free coefficients $\mathcal{A}$ and $\mathcal{B}$. Hence, regularity conditions on axis impose (up to a scaling factor):

$$\psi \approx r^m, \qquad \frac{\mathrm{d}\psi}{\mathrm{d}r} \approx m\,r^{m-1}$$

for any $0 \leq r \leq N_{\text{steps}} \times \Delta r$. Convergence studies on limit cases and manufactured solutions [DiGiannatale19, Salari02] have identified the optimal domain for this linear approximation in $0 \leq r/a \leq 3 \cdot 10^{-3}$: wider linear domain may limit solver precision regardless of the integration step, while thinner could slow or prevent algorithm convergence when using relatively large Δr.

The LENS solver has been tested to prove its correctness and robustness against analytical solutions. We report here two tests, the first of which is the limit case of the vacuum solution. Albeit its physical relevance, any limit case does not retain the full complexity of the original equation and thus is not suitable for a full verification of the solver. A more complete picture can be acquired through the convergence study on a manufactured solution: these are the exact solutions of the original set of equations, after having added an *ad hoc* forcing term, corresponding to a known analytical solution. This will be better introduced and motivated in Sec. 3.4.2.

3.4.1   Limit case study: the vacuum equation

The convergence study on limit cases is relevant since it allows to maintain physical relevance of the sought solution. Moreover, the vacuum solution will play an important role in the next Chapter, in the study of both kink and tearing modes.

The numerical set-up is achieved by feeding LENS with a uniform current density profile $\mathbb{J}_0 = 0$, which coincides to setting $\sigma = \sigma' = 0$ in our pressure-less Newcomb equation, without changing any other variable.

Let us consider the case of a infinitely thin current-ring at a given radius $r = 1$, enclosed in a perfectly conducting coaxial shell, that a 2D representation crosses the plane of the page in $r = 0$ and $r = 2$. The analytical vacuum solution for ψ in the two resulting regions, $L = \{0 \leq r \leq 1\}$ and $R = \{1 \leq r \leq 2\}$, comes from enforcing regularity conditions on the ideal conductor and flux continuity in $r = 1$, along with Eq. 3.27 and 3.28:

$$\psi_L(0) = \psi_R(2) = 0,$$

$$\psi_L(1) = \psi_R(1) = 1 .$$

In particular, for the left-hand side vacuum region we get

$$\psi_L(r) = \frac{r\, I'_m(|n|\varepsilon)}{I'_m(|n|\varepsilon_1)} \qquad \Longrightarrow \qquad \frac{\mathrm{d}\psi_L}{\mathrm{d}r}(r) = \frac{H}{r} \frac{I_m(|n|\varepsilon)}{\frac{|n|}{R} I'_m(|n|\varepsilon_1)} ,$$

where of course $\mathcal{B}_L = 0$. For the other branch of the solution, a quick manipulation yields:

$$\psi_R(r) = \frac{K'_m(|n|\varepsilon_2)I'_m(|n|\varepsilon) - I'_m(|n|\varepsilon_2)K'_m(|n|\varepsilon)}{K'_m(|n|\varepsilon_2)I'_m(|n|\varepsilon_1) - I'_m(|n|\varepsilon_2)K'_m(|n|\varepsilon_1)} r$$

$$\Longrightarrow \qquad \frac{\mathrm{d}\psi_R}{\mathrm{d}r}(r) = \frac{H}{|n|\varepsilon} \frac{K'_m(|n|\varepsilon_2)I_m(|n|\varepsilon) - I'_m(|n|\varepsilon_2)K_m(|n|\varepsilon)}{K'_m(|n|\varepsilon_2)I'_m(|n|\varepsilon_1) - I'_m(|n|\varepsilon_2)K'_m(|n|\varepsilon_1)}$$

For the numerical integration, we fed LENS with an infinitely thin current ring, as described by $J_{0,z} = j_0\delta(r-1)$ and solved within the two domains, starting from the external edges (where the conductor is) and matching the solutions so that they are equal at $r = 1$. For the right-had side branch solution, since there is no singlularity of the governing equation in $r = 2$, no linear approximant was deployed and instead we just enforced initial conditions:

$$(\psi_R)_{\text{ext. conductor}} = 0 \qquad \left(\frac{\mathrm{d}\psi_R}{\mathrm{d}r}\right)_{\text{ext. conductor}} = -1 . \qquad (3.36)$$
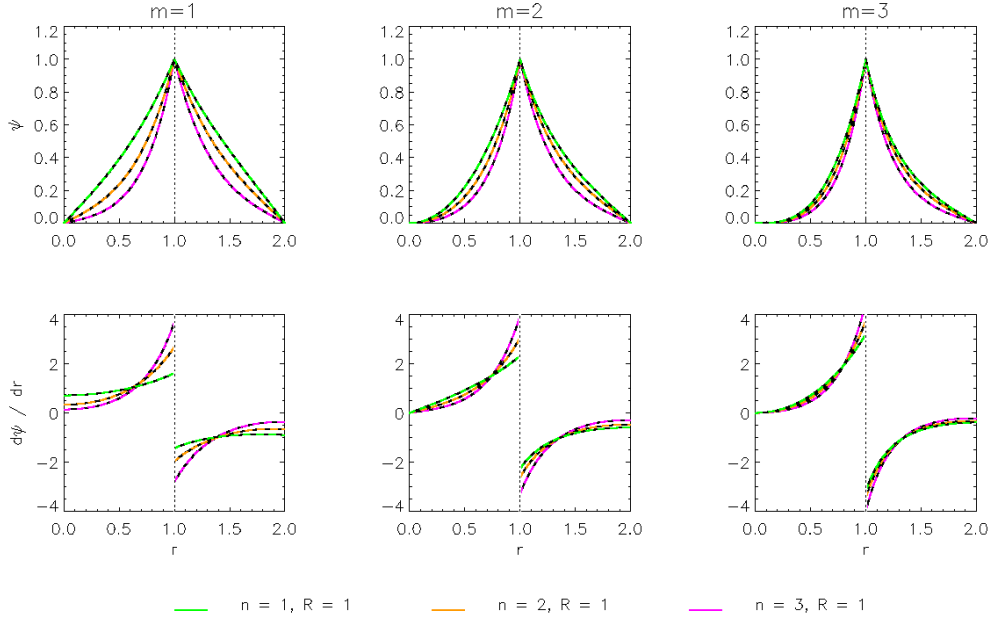
Figure 3.2: Magnetic flux around an infinitely thin current-channel ring, $j_z = j_0\delta(r-1)$, enclosed in a coaxial conductor. LENS's results for integration step $\Delta r = 10^{-4}$ (black) are compared to analytical predictions, for various values of m and n.

Figure 3.2 presents LENS's outcomes compared to the analytical vacuum solutions, for all the combinations of $m = 1, 2, 3$ and $n = 1, 2, 3$ and for $R = 1$. LENS's precision is set to an integration step $\Delta r = 10^{-4}$ and the analytical predictions are quite indistinguishable from the numeric solution. Indeed, Fig. 3.3 reports the relative error as an exponentially decreasing function of Δr. Note that, albeit monotonically decreasing, the rate is only little more than linear in Δr, instead of being proportional to $(\Delta r)^4$ as the fourth-order Runge-Kutta method should guarantee. This is motivated by the wide number of parameters and subroutines that need to be computed or called at each step, including *e.g.* a second-order precision derivative-method to compute σ' from a generic user input current-density, and the linear interpolation performed by IDL in the discretisation of the radial profiles.

3.4.2   Convergence study using manufactured solutions

Despite retaining more physical meaning, limit cases are inherently poor tests of the overall performances of a numeric tool, because they unavoidably project the system in some particular subset of parameters space. One would
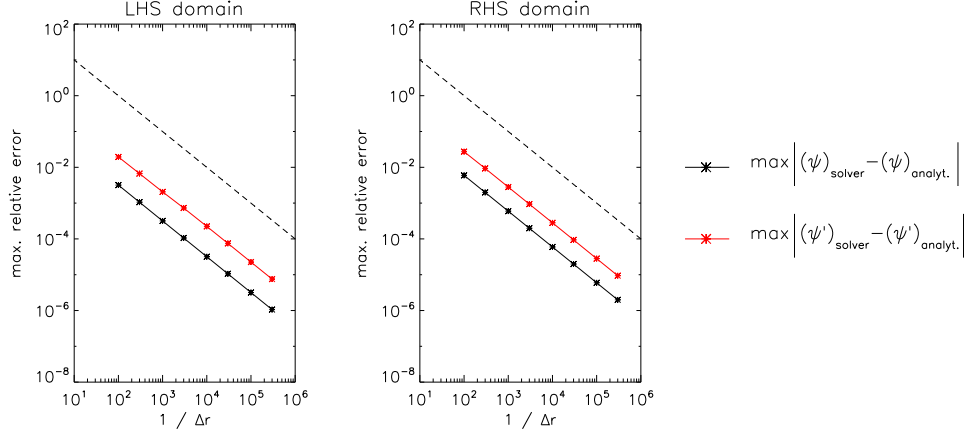
Figure 3.3:   Scan on the errors for a specific solution ($m = 2$, $n = 1$, $R = 1$) of the thin current-ring problem, against increasing solver precision. The error is evaluated as the maximum absolute discrepancy over each domain between LENS's solution and analytical prediction, normalised in such a way that $\psi_L(1) = \psi_R(1) = 1$. A dashed line marks the slope $(\Delta r)^{-1}$.
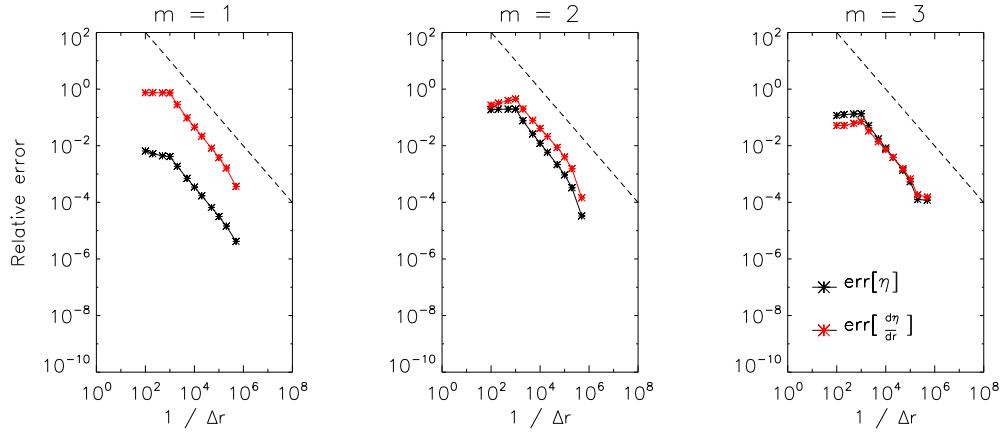
Figure 3.4:   Convergence study of the LENS solver using a manufactored solution in the form of $\eta(r) = e^{mr} - 1$. Numerical set-up: $1 \leq m \leq 3$, $n = 1$, $R = 4$, $\nu = 1$, and resonance position $r_s = a$. A dashed line marks the slope $(\Delta r)^{-1}$.
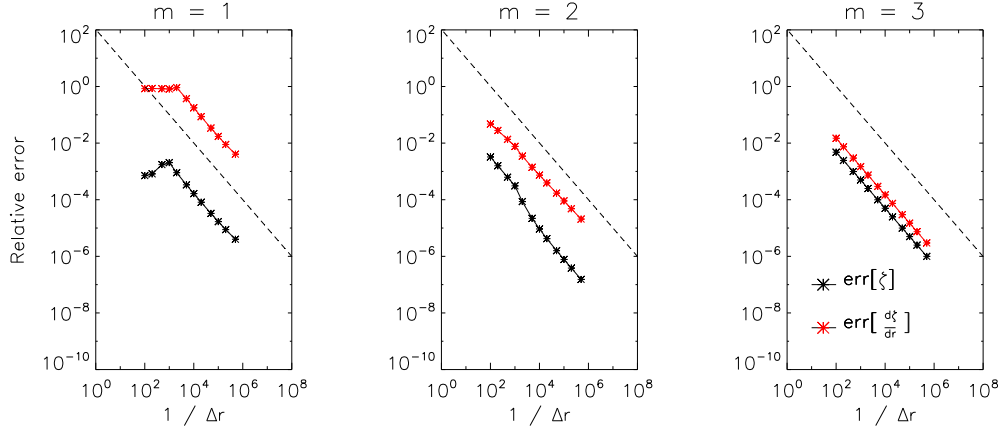
Figure 3.5: Convergence study of the LENS solver using a manufactored solution in the form of $\zeta(r) = n \cdot \sqrt{1 + r^m}$. Numerical set-up: $1 \leq m \leq 3$, $n = 1$, $R = 4$, $\nu = 1$, and resonance position $r_s = a$. A dashed line marks the slope $(\Delta r)^{-1}$.

much rather test the solutions produced by one numeric tool in the most general case against some suitable figure of merit.

Of course, the problem is that very seldom there is such a thing like a fully general known (analytical) expectation for the outcome. Nonetheless, it is always possible to study the solver's convergence against the exact analytical solution of the original governing equation plus a wisely chosen forcing term. This is dubbed a manufactured solution [Salari02] and can be constructed in the way that follows:

- we start from a linear ODE we want to solve: $\mathcal{A}[\psi] = 0$, being $\mathcal{A}$ a differential operator and ψ the unknown eigenfunction

- we make a *guess* ζ for the eigenfunction, which almost surely is not a solution for our problem, so that we will find $\mathcal{A}[\zeta] = \mathcal{S} \neq 0$ (if $\mathcal{S} = 0$ we would have found by chance an exact solution of our ODE)

- nonetheless, we now have an inhomogeneous ODE whose analytical solution is known by construction and that presents the same grade as numerical complexity of the initial one.

Manufactured functions are then simple dummy solutions for an alternative problem that still retains at least the same complexity as the original one. For this reason, it is not important that they have any physical consistency and can be chosen freely.

For the sake of this study, we focused on two very different manufactured solutions: the first one is null on axis and presents very rapid growth, that tends to magnify quickly any deviance of LENS from the right solution:

$$\eta(r) := e^{mr} - 1 \, .$$

The second was chosen in antithesis as finite on axis and with slower (polynomial) growth:

$$\zeta(r) := n \cdot \sqrt{1 + r^m} \, .$$

The linear approximant for such functions (in a small domain around the axis) are then:

$$\eta(r) \sim mr, \qquad \zeta(r) \sim n \left(1 + \frac{x^m}{2} \right) .$$

The full differential problem passed to LENS is now:

$$\frac{\mathrm{d}}{\mathrm{d}r} \mathrm{Y}_0(r) = \frac{\mathrm{Y}_1(r)}{f(r)}$$

$$\frac{\mathrm{d}}{\mathrm{d}r} \mathrm{Y}_1(r) = g(r)\mathrm{Y}_0(r) + \mathcal{S}[\mu(r)] \, ,$$

where

$$\mathcal{S}[\mu(r)] := \frac{\mathrm{d}f}{\mathrm{d}r}\mu(r) + f(r)\frac{\mathrm{d}\mu}{\mathrm{d}r} - g(r) \, ,$$

f and g being defined as above, and μ standing alternatively for the explicit expression of η or ζ.

The equilibrium chosen for this test implements a current-density profile like that in [Wesson78] and uniform axial magnetic field:

$$B_{0,z} = 1 \, , \qquad J_{0,z} = j_0 \left[1 - \left(\frac{r}{a} \right)^2 \right]^{\nu} \qquad \Longrightarrow \qquad \sigma = j_0 \left[1 - \left(\frac{r}{a} \right)^2 \right]^{\nu}$$

with $\nu \in \mathbb{R}$ as free current-peaking parameter.

As Fig. 3.4 and 3.5 show for a specific set of parameters, convergence study on both manufactured functions achieved overall very similar results: here the error is defined as the relative discrepancy at $r = 1$. However, almost identical convergence plots were obtained on a wide range of parameters, spacing

$$0 \le m \le 3 \, , \qquad -5 \le n \le 5 \, , \qquad 0.5 \le R \le 5000 \, ,$$

$$a \le r_s \le 2a \, , \qquad 0 \le \nu \le 5 \, ,$$

where r_s is the resonance position and the other variables have their usual meaning.

Once more, as expected, the convergence rate is little more than linear in Δr and LENS is consistently more precise in evaluating η and ζ than η' and ζ'. The effect of the linear approximant is well visible on both η and ζ: as long as $\Delta r > 3 \cdot 10^{-3}$ there are too few mesh points for one of them to fall in the linear approximation domain. For these cases (left part of each plot) we see comparatively slower convergence of η (and ζ) and almost stalled convergence of η' (and ζ').

Finally (and unsurprisingly) the convergence error on the spiky η function is generally higher than the one on the flatter ζ and the linear approximant seems to have a more beneficial effect for the first one.

3.5 The Energy formulation

The aim of this Section is to give a brief introduction to the Energy Principle. This is an alternative way to treat linear fluid instabilities in the frame of ideal MHD: the main difference is that we rather describe the perturbation in terms of the fluid displacement $\boldsymbol{\xi}$ instead of ψ and rely on flux freezing condition contained in Eq. 3.35 to recover the magnetic counterpart.

Albeit this may sound a little reductive, the energy formulation somehow completes the information enclosed in the Newcomb's approach, also envisaging the contribution of the plasma inertia. In addition, the theory involved is very elegant and instructive.

Unfortunately, a rigorous introduction would take too long: a thorough presentation can be found in [Freidberg14], whereas a shorter but still precise version is to be found in [White06]. In the next few pages we just want to present some of the key results.

3.5.1 Force density operator

We start from the usual static equilibrium:

$$\mathbf{J}_0 \times \mathbf{B}_0 = \nabla p_0$$

$$\boldsymbol{v}_0 = 0 \,.$$

Let us now introduce a small perturbation in the form of a mass displacement field $\boldsymbol{\xi}(r, \theta, z, t)$, which is the Lagrangian displacement already defined at the end of the previous Sec. 3.3. Our aim is now to determine the *force-density* $\mathcal{F}(\boldsymbol{\xi})$ representing the plasma response. This will allow us to study the

equilibrium stability in terms of virtual work principle, which is applicable for ideal MHD, enforcing energy conservation.

Linearised force density reads as

$$\mathcal{F}(\boldsymbol{\xi}) = \mathbf{j}(\boldsymbol{\xi}) \times \mathbf{B}_0 + \mathbf{J}_0 \times \mathbf{b}(\boldsymbol{\xi}) - \nabla p_1(\boldsymbol{\xi}) \,,$$

where $\mathbf{j}$, $\mathbf{b}$ and p_1 are linear perturbations of current-density, magnetic field and pressure, respectively, representing the plasma response.

We have already discussed the $\mathbf{b}(\boldsymbol{\xi})$ relation in Eq. 3.34 and $\mathbf{j}(\boldsymbol{\xi})$ is just $\nabla \times \mathbf{b}(\boldsymbol{\xi})/\mu_0$. First order pressure term can be found combining continuity and entropy-conservation equations and linearising:

$$p_1(\boldsymbol{\xi}) = -\boldsymbol{\xi} \cdot \nabla p_0 - \gamma_{ad}\, p_0 \nabla \cdot \boldsymbol{\xi} \,. \tag{3.37}$$

being γ_{ad} the adiabatic constant of the plasma, given by the ratio of its specific heats.

Our perturbation will be Fourier-developed in an analogous way to what we did for ψ in the previous Section, so that, assuming also a dependence on time like that in Eq. 3.6:

$$\boldsymbol{\xi}(r, t, \theta, z) = \sum_{m,n} \boldsymbol{\xi}^{mn}(r) \cdot e^{im\theta - inz/R - i\omega t} \,.$$

In the following, we will always refer to the single mode $\boldsymbol{\xi}^{mn} = [\xi_r^{mn}, \xi_\theta^{mn}, \xi_z^{mn}]$, so we will drop the apex without loss of clarity. Let us now write the second principle of dynamics for our small perturbation:

$$\rho_0 \frac{\partial^2 \boldsymbol{\xi}}{\partial t^2} \equiv -\rho_0\, \omega^2 \boldsymbol{\xi} = \mathcal{F}(\boldsymbol{\xi})$$

and the potential energy perturbation produced on the plasma against the force density $\mathcal{F}$:

$$\delta W(\boldsymbol{\xi}, \boldsymbol{\xi}^*) = -\frac{1}{2} \int_V \mathcal{F}(\boldsymbol{\xi}) \cdot \boldsymbol{\xi}^* \, \mathrm{d}\tau \equiv \frac{1}{2} \int_V \rho_0\, \omega^2\, |\boldsymbol{\xi}|^2 \, \mathrm{d}\tau \tag{3.38}$$

where the asterisk indicates complex conjugation, V is the volume of the system we consider, and the inessential factor $1/2$ has been added to render the RHS formally identical to a kinetic term.

3.5.2 $\delta W(\xi, \xi^*)$ and its self-adjointness

Equation 3.38 is an actual energy balance equation. For this to be, it is essential that the force field $\mathcal{F}$ is conservative, meaning that the work done

does not depend on the choice of the path, so that $\mathcal{F}(\boldsymbol{\xi}_1) \cdot \boldsymbol{\xi}_2^* \equiv \mathcal{F}(\boldsymbol{\xi}_2) \cdot \boldsymbol{\xi}_1^*$, for any two displacements $\boldsymbol{\xi}_1$, $\boldsymbol{\xi}_2$. This property of the force operator (and consequently of the energy variation δW) is called self-adjointness.

We give in this Section the most general form of the δW operator. Following [Freidberg14] we can write the energy variation in the region occupied by the plasma as:

$$\delta W_p(\boldsymbol{\xi}, \boldsymbol{\xi}^*) = \int_{V_p} \mathrm{d}\tau \left\{ \frac{|\mathbf{b}_\perp|^2}{2\mu_0} \right. \tag{3.39}$$

$$+ \quad \frac{B_0^2}{2\mu_0} |\nabla \cdot \boldsymbol{\xi}_\perp + 2\boldsymbol{\xi}_\perp \cdot \mathbf{k}|^2 \tag{3.40}$$

$$+ \quad \frac{\gamma_{ad}\, p_0}{2} |\nabla \cdot \boldsymbol{\xi}|^2 \tag{3.41}$$

$$- \quad (\boldsymbol{\xi}_\perp \cdot \nabla p_0)(\boldsymbol{\xi}_\perp^* \cdot \mathbf{k}) \tag{3.42}$$

$$- \quad \left. \frac{|\mathbf{J}_{0,\parallel}|}{2} \left(\boldsymbol{\xi}_\perp \times \frac{\mathbf{B_0}}{|B_0|} \right) \cdot \mathbf{b}_\perp \right\} \tag{3.43}$$

were the different terms in the integral are respectively related to:

- the shear Alfvèn wave, which is perpendicular to the equilibrium;

- the compressional Alfvèn wave, which is enhanced by fluid compressibility;

- the pressure *sound* wave, proportional to the adiabatic constant γ_{ad} and to the squared compression $|\nabla \cdot \boldsymbol{\xi}|^2$;

- pressure-driven instabilities, that vanish with pressure gradients and contain the field-curvature unit vector $\mathbf{k} = (\mathbf{B}_0/|B_0|) \cdot \nabla(\mathbf{B}_0/|B_0|)$;

- current-driven instabilities, where the $\boldsymbol{v} \times \mathbf{B}_0$ term is still recognisable.

It should be noted that the three terms concerning wave dissipation of accumulated energy have positive sign, meaning that they raise the plasma energy and are thus stabilising, while the other two have negative sign and thus tend to lower the plasma energy, leading to instability.

Along with this plasma contribution, in case we have a vacuum region between the plasma and the conducting shell, there are also a surface and a vacuum term to take into account to evaluate the whole potential energy change:

$$\delta W = \delta W_p + \delta W_s + \delta W_v \,. \tag{3.44}$$

The vacuum term can be easily obtained from δW_p by eliminating all the terms that involve fluid properties, such as the displacement $\boldsymbol{\xi}$ and pressure, and currents (and recovering the $b_\parallel$ component, which was implicit in Eqs. 3.40-3.43):

$$\delta W_{\mathrm{v}} = \int_{V_{\mathrm{vac}}} \frac{|b|^2}{2\mu_0} \mathrm{d}\tau \, .$$

Finally, the surface term includes the jump condition of the hydromagnetic energy density across the fluid interface:

$$\delta W_{\mathrm{s}} = \int_{\partial V_{\mathrm{pl}}} (\mathbf{n} \cdot \boldsymbol{\xi}) \, \boldsymbol{\xi} \cdot \left[\nabla \left(\frac{\mathbf{B_0} \cdot \mathbf{b}}{2\mu_0} + p_1 \right) \right]_{\mathrm{pl}}^{\mathrm{vac}} \mathrm{d}\sigma \, ,$$

where $\mathbf{n}$ is the unit vector perpendicular to the interface and the term in square brackets is intended as a difference between the evaluation of its argument in vacuum and in the plasma, very close to the interface. The physical meaning of this term is to balance the energy fluxes across the fluid interface and is formulated by enforcing pressure balance and the request that the perturbed plasma surface is a constant-flux surface for the perturbed field.

Two important corollaries of self-adjointness

There are two immediate properties of self-adjoint operators that play a crucial role for the study of ideal MHD instabilities. We report them without proof, which the reader can find in Appendix A.1.

Property 1. Discrete modes are a basis
Whenever only a discrete set of $(\omega, \boldsymbol{\xi})$ couples is a solution to the eigenvalue problem in Eq. 3.38, this is a basis for all possible initial displacements.

In other words, we can study the stability against whatever initial perturbation by looking at normal modes stability. In fact, only the projection of a given perturbation on this base has a chance to grow.
It should be also said that there are also regions in the space of allowable displacements in which the spectrum of solutions is a continuum. Nonetheless, it seems like it is the case that all continua lie in the stability region [Freidberg14].

Property 2. Ideal modes either rotate or grow
All discrete eigenvalues ω^2 must be real.
This implies that ideal modes can either grow with purely imaginary rate $\omega \equiv -i\gamma$ or rotate with purely real frequency.

3.5.3 The variational form of MHD equations

The last step we need towards the Energy Principle is to re-formulate the MHD equations in a variational form.

First of all, referring to Eq. 3.38, we can isolate our eigenvalue so that we find

$$\omega^2(\boldsymbol{\xi}) = \frac{\delta W(\boldsymbol{\xi}, \boldsymbol{\xi}^*)}{(1/2) \int_V \rho_0 |\boldsymbol{\xi}|^2 \, \mathrm{d}\tau} \, . \tag{3.45}$$

In this case, we are basically considering the eigenvalue ω^2 as a functional of its eigenfunction $\boldsymbol{\xi}$. To this point, it is convenient to define $K(\boldsymbol{\xi}, \boldsymbol{\xi}^*)$, so that

$$\omega^2(\boldsymbol{\xi}) = \frac{\delta W(\boldsymbol{\xi}, \boldsymbol{\xi}^*)}{K(\boldsymbol{\xi}, \boldsymbol{\xi}^*)} \, ; \qquad K(\boldsymbol{\xi}, \boldsymbol{\xi}^*) = \int_V \frac{\rho_0}{2} \, \boldsymbol{\xi} \cdot \boldsymbol{\xi}^* \, \mathrm{d}\tau \, .$$

It turns out that the solutions of our eigenvalue problem (which is completely equivalent to MHD equations) corresponds to the stationary condition for the functional $\omega^2(\boldsymbol{\xi})$. The full proof is available in Appendix A.2.

In other words, the whole batch of information contained in the MHD equations is also contained in the request that:

$$\omega^2(\boldsymbol{\xi} + \delta\boldsymbol{\xi}) - \omega^2(\boldsymbol{\xi}) = 0 \, , \qquad \text{for an arbitrary } \delta\boldsymbol{\xi} \to 0 \, . \tag{3.46}$$

3.5.4 The Energy Principle

The variational principle just discussed allows us to identify system stability with the sign of the eigenvalue ω: Eq. 3.45 shows us that it depends on the sign of the potential energy variation.

In other words we are left with two possible cases:

- $\omega^2 \propto \delta W \geq 0$: the mode oscillates with purely real frequency;

- $\omega^2 \propto \delta W < 0$: the mode amplitude changes at a purely real growth-rate $\gamma = -\operatorname{Im}(\omega)$.

This is just a consequence of energy conservation: any initial perturbation producing a favourable jump in potential energy is bound to increase its kinetic energy.

In fact, the most general formulation of the Energy Principle states that a system is stable if and only if there is no such a perturbation ξ that produces a negative $\delta W(\boldsymbol{\xi}, \boldsymbol{\xi}^*) < 0$ and its proof is almost straightforward in the relevant case in which discrete normal modes are a basis for all possible displacements. More pragmatically, we can draw from these consideration an approximated version of the exact (to linear order) variational problem described in the

previous Section.

The approximation consists in assuming that the stationary condition of $\omega^2(\boldsymbol{\xi})$ can be transposed into stationary potential variation $\delta W(\boldsymbol{\xi}, \boldsymbol{\xi}^*)$. This is the same as assuming that K does not take part in the variation $\delta[\omega^2(\boldsymbol{\xi})]$. Of course this is completely accurate only in the case of marginal stability, hence this procedure yields exact stability boundaries. Nonetheless, energy conservation implies that a minimum in potential energy variation gives us the displacement that makes the whole system transition to the most possibly favourable energetic state, which can rightfully be assumed to be a very close approximation to the actual solution of the exact problem.

On the other hand, by doing so we can solve for our eigenfunction with an equation that does not contain ω, which is a huge simplification.

Energy minimisation

So, we are left with a new variational principle in order to find $\boldsymbol{\xi}$:

$$\delta\left[\delta W(\boldsymbol{\xi}, \boldsymbol{\xi}^*)\right] = \left[\delta W(\boldsymbol{\xi} + \delta\boldsymbol{\xi}, \boldsymbol{\xi}^* + \delta\boldsymbol{\xi}^*) - \delta W(\boldsymbol{\xi}, \boldsymbol{\xi}^*)\right] \equiv 0 . \qquad (3.47)$$

Referring to the general form of the potential energy, given in Sec. 3.5.2, the main contribution of Equation 3.44 that needs minimisation is the plasma potential δW_p. Leaving out for the moment the vacuum and interface contributions, minimisation of Eqs. 3.39-3.43 leads to the requirement for an incompressible perturbation[3], in order to rid off positive terms [White06]. The potential energy becomes a functional of the sole radial component of $\boldsymbol{\xi}$ and assumes the shape below:

$$\delta W_p(\xi_r) = 4\pi^2 R \int_0^a \left[f(r) \left(\frac{\mathrm{d}\xi_r}{\mathrm{d}r}\right)^2 + g(r)\,(\xi_r)^2 \right] \mathrm{d}r + \mathrm{ET}_a \qquad (3.48)$$

$$f(r) = \frac{n^2 r^3 B_{0,z}^2}{R^2 \left(m^2 + n^2\varepsilon^2\right)} \left(1 - \frac{m}{nq}\right)$$

$$g(r) = \frac{r\,(n + m/q)^2\,B_{0,z}^2}{R^2\left(m^2 + n^2\varepsilon^2\right)} + \frac{1}{R}B_{0,z}^2\varepsilon\left(n - \frac{m}{q}\right)^2$$

$$- \frac{2B_{0,z}}{R^2 q}\frac{\mathrm{d}}{\mathrm{d}r}\left(\frac{r^2}{q}\right) - \frac{\mathrm{d}}{\mathrm{d}r}\left[\frac{\varepsilon^2}{m^2 + n^2\varepsilon^2}\left(n^2 - \frac{m^2}{q^2}\right)\right]B_{0,z}^2$$

$$\mathrm{ET}_a = 4\pi^2 R \left[\frac{\left(n^2\varepsilon^2 B_{0,z}^2 - m^2 B_{0,\theta}^2\right)(\xi_r)^2}{m^2 + n^2\varepsilon^2}\right]_{r=a}$$

---

[3]This is true in most cases: see pp. 363-366, chap. 8 [Freidberg14]

$B_{0,z}$ being the equilibrium toroidal field, $\varepsilon = r/R$, a the plasma radius and $q = B_{0,z}r/(B_{0,\theta}R)$ the safety factor. The plasma edge term ET_a (resulting as a boundary term from an integration by parts [Freidberg14]) will be discussed in a second moment, along with the surface term δW_{s}.

In the reference books, it is common to change names to variables and to drop the subscript from ξ_r: this is done for ease of notation, but introduces some ambiguity, since K is still a functional of the whole vector $\boldsymbol{\xi}$. Hence, we will keep variables' names unchanged, at the cost of some formal discrepancy with respect to all the rest of dedicated literature.

The minimisation of this functional is straightforward once one notices that the term in square brackets in Eq. 3.48 is formally a Lagrangian, so that, assuming $\delta\xi_r(0) = \delta\xi_r(a) = 0$:

$$\delta\left[\delta W\right] = \delta\left\{\int_0^a \mathcal{L}\left(\xi_r, \xi_r'; r\right)\,\mathrm{d}r\right\}$$
$$= \int_0^a \left\{\frac{\partial\mathcal{L}}{\partial\xi_r} - \frac{\mathrm{d}}{\mathrm{d}r}\frac{\partial\mathcal{L}}{\partial\xi_r'}\right\} \cdot \delta\xi_r\,\mathrm{d}r \equiv 0\,,$$

with

$$\frac{\partial\mathcal{L}}{\partial\xi_r} = 2g(r)\xi_r\,; \qquad\qquad \frac{\mathrm{d}}{\mathrm{d}r}\frac{\partial\mathcal{L}}{\partial\xi_r'} = 2\frac{\mathrm{d}}{\mathrm{d}r}\left[f(r)\frac{\mathrm{d}\xi_r}{\mathrm{d}r}\right]\,.$$

Thus, we are left with the following Euler's equation for the plasma radial displacement ξ_r:

$$\frac{\mathrm{d}}{\mathrm{d}r}\left[f(r)\frac{\mathrm{d}\xi_r}{\mathrm{d}r}\right] - g(r)\xi_r = 0\,. \tag{3.49}$$

We can now compute the minimal potential energy variation, using the fact that $g(r)\,\xi_r^2 = \left[\,f(r)\,\xi_r'\,\right]'\xi_r$, so that

$$\delta W_p^{\min} = \int_0^a \frac{\mathrm{d}}{\mathrm{d}r}\left[f(r)\cdot\frac{\mathrm{d}\xi_r}{\mathrm{d}r}\cdot\xi_r\right]\,\mathrm{d}r = f(a)\cdot\frac{\mathrm{d}\xi_r}{\mathrm{d}r}(a)\cdot\xi_r(a)\,, \tag{3.50}$$

where the eigenfunction is obtained via the Euler's equation.

The surface term is generally null, if no surface currents are present, so we are left with the plasma edge term ET_a, which needs no minimisation and is just to be considered the way it is, to compute the eigenvalue.

Finally, the vacuum contribution can be found in a formally identical (Lagrangian) way as the one followed for the plasma contribution. This is thoroughly done in Appendix A.3, yielding:

$$\delta W_{\mathrm{v}}^{\min} = \frac{2\pi^2 R}{\mu_0}m^2 B_{0,z}^2\xi_a^2 n\varepsilon_a\lambda \tag{3.51}$$

$$\lambda = -\frac{K_m'(n\varepsilon_b)I_m(n\varepsilon_a) - I_m'(n\varepsilon_b)K_m(n\varepsilon_a)}{K_m'(n\varepsilon_b)I_m'(n\varepsilon_a) - I_m'(n\varepsilon_b)K_m'(n\varepsilon_a)}\,. \tag{3.52}$$

3.5.5   Large aspect ratio tokamak approximation

We have already discussed the large aspect-ratio limit for the Newcomb's equation. The main two assumptions are that $R \rightarrow \infty$ while still $q = B_{0,z}\,\varepsilon/B_{0,\theta} \sim 1$. This brings the typical tokamak ordering:

$$B_{0,\theta} \sim \varepsilon B_{0,z}\,; \qquad \frac{\mathrm{d}B_{0,z}}{\mathrm{d}r} \sim \frac{B_{0,z}}{R} \sim \varepsilon B_{0,z}\,.$$

The incompressibility condition now reads:

$$\nabla \cdot \boldsymbol{\xi} = \frac{1}{r}\frac{\mathrm{d}}{\mathrm{d}r}\left(r\,\xi_r\right) + \frac{im}{r}\xi_\theta - \frac{in\varepsilon}{r}\xi_z = 0\,, \qquad (3.53)$$

yielding

$$\xi_r \sim \xi_\theta = \frac{i}{m}\frac{\mathrm{d}}{\mathrm{d}r}\left(r\,\xi_r\right)\,; \qquad \xi_z = 0\,.$$

All equations are drastically simplified: starting with the plasma contribution, the Euler's equation now reads

$$\frac{\mathrm{d}}{\mathrm{d}r}\left[r^3\left(\frac{1}{q} - \frac{n}{m}\right)^2 \frac{\mathrm{d}\xi_r}{\mathrm{d}r}\right] = (m^2 - 1)\left(\frac{1}{q} - \frac{n}{m}\right)^2 r\xi_r\,, \qquad (3.54)$$

yielding

$$\delta W_p = \frac{2\pi^2 B_{0,z}^2}{\mu_0 R}\int_0^a \left(\frac{1}{q} - \frac{n}{m}\right)^2\left[r^3\left(\frac{\mathrm{d}\xi_r}{\mathrm{d}r}\right)^2 + (m^2-1)\xi_r^2\right]\mathrm{d}r \qquad (3.55)$$

$$= \frac{2\pi^2 B_{0,z}^2}{\mu_0 R}\left(\frac{1}{q_a} - \frac{n}{m}\right)^2 a^3 \xi_a \xi_a'\,, \qquad (3.56)$$

the second being the minimised form.
The edge ET_a and vacuum term δW_{v} greatly simplify, so that, by taking the leading order in Bessel's polynomial development: $I_m(x) \approx x^m$ and $K_m(x) \approx x^{-m}$,

$$\delta W = \frac{2\pi^2 B_{0,z}^2}{\mu_0 R}\left\{\int_0^a \left(\frac{1}{q} - \frac{n}{m}\right)^2\left[r^3\left(\frac{\mathrm{d}\xi_r}{\mathrm{d}r}\right)^2 + (m^2-1)\xi_r^2\right]\mathrm{d}r\right.$$

$$\left. + \left(\frac{n}{m} - \frac{1}{q_a}\right)\left[\left(\frac{n}{m} + \frac{1}{q_a}\right) + m\lambda\left(\frac{n}{m} - \frac{1}{q_a}\right)\right]a^2\xi_a^2\right\}$$

where

$$\lambda = \frac{1 + (a/b)^{2m}}{1 - (a/b)^{2m}}\,.$$

3.6   Numerical solution of Euler's equation

As previously done for Newcomb's equation, we implemented a solver also for the Euler's equation in the LENS code. However, this time we simply focused on the large aspect-ratio limit equation, to avoid more cumbersome manipulations.

Analogously to the other case, we made use of the IDL built-in fourth-order explicit Runge-Kutta `RK4` function. The initial ODE is thus broken into the following simpler ODEs to be solved iteratively:

$$\frac{\mathrm{d}}{\mathrm{d}r}\mathtt{Y}_0(r) = \frac{\mathtt{Y}_1(r)}{f(r)}$$

$$\frac{\mathrm{d}}{\mathrm{d}r}\mathtt{Y}_1(r) = g(r)\mathtt{Y}_0(r)$$

where $\mathtt{Y}_0(r) = \xi_r(r)$, $\mathtt{Y}_1(r) = f(r)\xi_r'(r)$, $f = r^3\left(\frac{1}{q} - \frac{n}{m}\right)^2$, and $g(r) = (m^2 - 1)\left(\frac{1}{q} - \frac{n}{m}\right)^2 r$.

The first of these equations presents a third-order singularity on axis. Hence the problem is much less amenable to numerical solution than Newcomb's equation and must be treated with some care. This is especially true since we must integrate from axis outwards, to isolate among the two solutions of the second-order ODE the particular one that is regular on axis.

Also in this case, convergence can be enhanced by adopting a linear approximant in a narrow interval around the axis. Convergence studies confirmed the same optimal interval-width as for the Newcomb's equation: $I_{\mathrm{lin}} := \{0 \leq r/a \leq 3 \cdot 10^{-3}\}$.

Concerning the approximant itself, since most equilibria of interest have $J_{0,z}'(r = 0) = 0$, we can regard $q(r) \approx q_0$ as a constant. Equation 3.54 greatly simplifies:

$$\frac{\mathrm{d}}{\mathrm{d}r}\left[r^3\frac{\mathrm{d}\xi_r}{\mathrm{d}r}\right] = (m^2 - 1)r\xi_r\,,$$

and its analytical solution is

$$\xi_r(r) = \mathcal{A}\,r^{m-1} + \mathcal{B}\,r^{-m-1}.$$

Enforcing regularity on axis we can thus write (up to a constant factor):

$$\xi_r(r \to 0) \sim r^{m-1}\,, \qquad \xi_r'(r \to 0) \sim (m-1)\,r^{m-2}\,.$$

Also in this case LENS underwent thorough verification, to assess its numerical accuracy. We present in the following some convergence studies,

conducted with the aid of manufactured solutions, as in Sec. 3.4.2. Convergence to the analytical solution of a flat current profile was also positively conducted, but is not presented here, since the sought ODE solution coincides with its linear approximant: this makes the test much less of interest, since there are far trivial ways of forcing outstandingly good convergence by extending the linear domain little beyond $3 \cdot 10^{-3}$.

3.6.1   Convergence study using manufactored solutions

For this verification we adopted the same equilibrium already used in Sec. 3.4.2:

$$J_{0,z}(r) = \left[1 - \left(\frac{r}{a} \right)^2 \right]^\nu , \qquad B_{0,z} = 1 .$$

Since Euler's equation presents a third-order singularity on axis, LENS has been extensively tested against three different manufatured solutions, that are reported for convenience with their linear approximant aside ($x = r/a$ and ν is the usual current-peaking parameter):

$$\text{peaked:} \qquad \lambda(x) = (1 + x^m)^{10\nu} - 1, \qquad \lambda(x \to 0) \sim 10 \, \nu \, r^m,$$

$$\text{flat:} \qquad \zeta(r) = \sqrt{1 + x^m}, \qquad \zeta(x \to 0) \sim 1 + \frac{x^m}{2},$$

The solver works now iteratively on two ODEs in the form of

$$\frac{\mathrm{d}}{\mathrm{d}r} \mathsf{Y}_0(r) = \frac{\mathsf{Y}_1(r)}{f(r)}$$

$$\frac{\mathrm{d}}{\mathrm{d}r} \mathsf{Y}_1(r) = g(r)\mathsf{Y}_0(r) + \mathcal{S}[\mu(r)] ,$$

where

$$\mathcal{S}[\mu(r)] := \frac{\mathrm{d}f}{\mathrm{d}r}\mu(r) + f(r)\frac{\mathrm{d}\mu}{\mathrm{d}r} - g(r) ,$$

f and g being defined as above, and μ standing alternatively for λ or ζ. Figure 3.6 and 3.7 present the convergence study against the "peaked" λ and the "flat" ζ manufactured solutions, for $\nu = 1$ and $m = 1, 2, 3$. The safety factor must be chosen differently for the three cases, so that the solver domain contains no resonances (where the governing Euler's equation gets singular): we have thus used $q_a = \frac{m}{n} - \alpha$, where $\alpha > 0$ is a free parameter. For the case of Fig. 3.6, $\alpha = 0.6$. The relative error on the y-axis is defined as
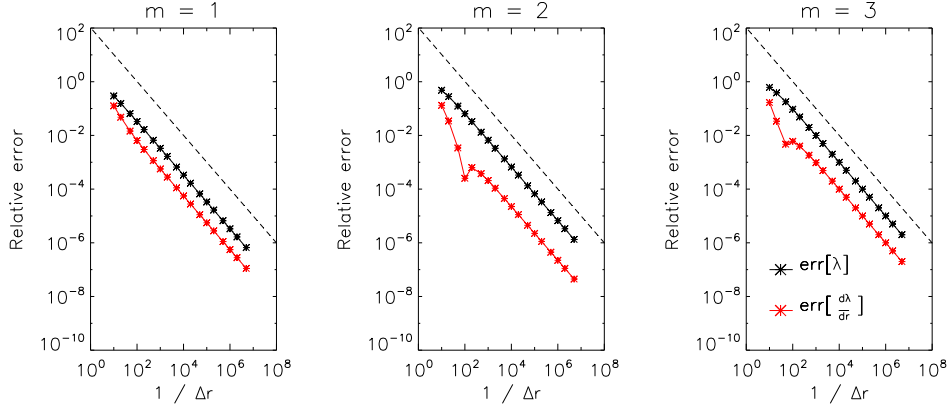
Figure 3.6: Convergence study against the "peaked" manufactured solution $\lambda(x) = (1 + x^m)^{10\nu} - 1$, for $m = 1, 2, 3$, $\nu = 1$, $q_a = \frac{m}{n} - 0.6$. A dashed line marks the slope $(\Delta r)^{-1}$.

the absolute discrepancy between the solver solution and the manufactured solution at $x = 1$, divided by their average:

$$\mathrm{err}[\mu] := \left| \frac{(\mu)^{\mathrm{LENS}} - (\mu)^{\mathrm{manuf.}}}{0.5 \left[(\mu)^{\mathrm{LENS}} + (\mu)^{\mathrm{manuf.}} \right]} \right|_{x=1} ,$$

and the same holds for $\mathrm{err}\left[\frac{\mathrm{d}\mu}{\mathrm{d}r} \right]$, where $\mu = \lambda$, ζ. The same first-order exponential convergence rate of the Newcomb's solver is retrieved in both cases, despite formally using a fourth-order method. This suggests that the problem is more intrinsic in the structure of the governing equation, and it does not depend on the presence of first-order precise subroutines, such as to compute derivative. In fact, even doing analytically all the numerical passages that could apparently lower the convergence rate, no improvement is found. On the other hand, very minor changes in the arrangement of terms within solver's parameters may visibly alter the numerical accuracy. For instance, it was found quite beneficial to rewrite the model parameter f in such a way that

$$f = \left(\frac{n}{m} - \frac{1}{q} \right)^2 r^3 \quad \rightarrow \quad \left(\frac{nq}{m} - 1 \right)^2 \frac{r^3}{q^2} ,$$

suggesting that the ODE is particularly prone to numerical instabilities. However, the first-order convergence rate visible in Fig. 3.6 and 3.7, being the final result of some parameters optimization, appears to be very robust for both profiles, on a wide range of modes and equilibria, spanning

$$1 \le m \le 4 , \qquad 0 \le \nu \le 10 , \qquad 0.001 \le \frac{m}{n} - q_a \le 0.999 .$$
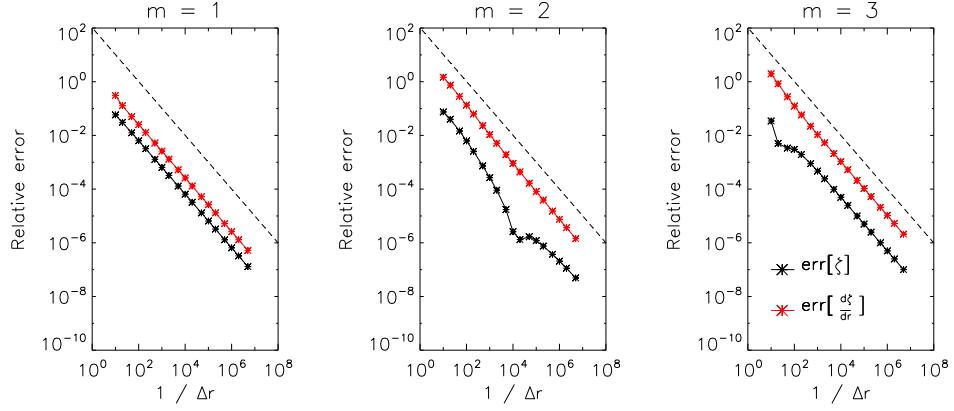
Figure 3.7:   Convergence study against the "flat" manufactured solution $\zeta(x) = \sqrt{1 + x^m}$, for $m = 1, 2, 3$, $\nu = 1$, $q_a = \frac{m}{n} - 0.6$. A dashed line marks the slope $(\Delta r)^{-1}$.

3.7   Relation between Newcomb's and Euler's equations

Before discussing instabilities, there is still an interesting point to highlight. Up to now we have derived two differential equations describing linear instabilities from two complementary points of view: Euler's equation aims at the flow, whereas Newcomb's equation focuses on the magnetic flux.
We may be tempted to see whether these two equations are actually the same, up to a change of variables.
The proof is very simple and comes from a personal analytical exercise: this is why I am not able to give any reference book or article on this.
We start from leveraging the flux-freezing relation Eq. 3.34 into the straight tokamak limit of Newcomb's equation (Eq. 3.33):

$$\frac{\mathrm{d}}{\mathrm{d}r}\left(r \frac{\mathrm{d}}{\mathrm{d}r}(F\xi_r) \right) = \left[\frac{m^2}{r} + \frac{mr}{F}\mu_0 \frac{\mathrm{d}J_{0,z}}{\mathrm{d}r} \right] F\xi_r \,.$$

The LHS can be written as $[(r F^2 \xi_r')' + (F' r)' F \xi_r]/F$, while, via tokamak ordering

$$\mu_0 \frac{\mathrm{d}J_{0,z}}{\mathrm{d}r} = \frac{\mathrm{d}}{\mathrm{d}r}\left[\frac{1}{r}\frac{\mathrm{d}}{\mathrm{d}r}\left(rB_{0,\theta} \right) \right] \approx \frac{1}{m}\frac{\mathrm{d}^2 F}{\mathrm{d}r^2} + \frac{1}{mr}\frac{\mathrm{d}F}{\mathrm{d}r} - \frac{F}{mr^2}$$

and thus, after short algebra and making explicit the dependence of F in terms of q we finally recover the Euler's equation.

This is interesting, as it shows on the one hand that Newcomb's solution - at least in the straight tokamak case - is the most energetically favourable whenever a potential can be defined. On the other hand, since we proved that for $\varepsilon \to 0$ both generalized and pressure-less Newcomb's equation converge to a same limit, which is also equivalent to Euler's equation, we can learn that the plasma instabilities in the large aspect ratio limit will only be driven by current density.

What is also interesting is that we may use this identity as a final test on the convergence of the two independent solvers composing the LENS code, by solving for the same current profiles, the same values of m and n, and for very large aspect-ratio in the Newcomb's solver. Figure 3.8 shows the outcome of such endeavour, for a current profile like the one used in [Wesson78] (with current-peaking parameter $\nu = 1$)

$$ J_{0,z}(r) = j_0 \left[1 - \left(\frac{r}{a} \right)^2 \right]^\nu $$

and assuming uniform and constant $B_{0,z} = 1$. We can see from upper panels the shape of the profiles of Newcomb's eigenfunction divided by F converging the Euler's eigenfunctions as ε approaches 0.

The second line of panels reports the mutual-convergence study of the two solvers for various aspect ratios. The solver error is in the form of

$$ \text{err} := \max \left| (\xi_r)^{\text{Euler}} - (\psi/F)^{\text{Newcomb}} \right|, $$

having normalized the two eigenfunction in such a way that they are both unitary at plasma edge.

We can see that mutual-convergence error generally comes in the shape of an exponential convergence, up to a final saturation that comes lower and lower for decreasing ε and for increasing m. This brings us to some very interesting conclusions.

First off, since initial convergence slope goes with the same rate we saw in the convergence studies of both Newcomb's and Euler's equation, we are reassured that they are both converging to the same solution and at the same rate.

Then, having ruled out numerical issues, the convergence-saturation level can be read as a metric of convergence of Newcomb's equation to the straight-tokamak limit, as an explicit function of ε. This may serve us as a frame of reference for future simulations with SpeCyl, when we will attempt linear benchmark in the large aspect ratio limit.

From the evident dependence of this convergence saturation on m (in addition to ε, of course), we can see that higher-m modes can already be treated in a
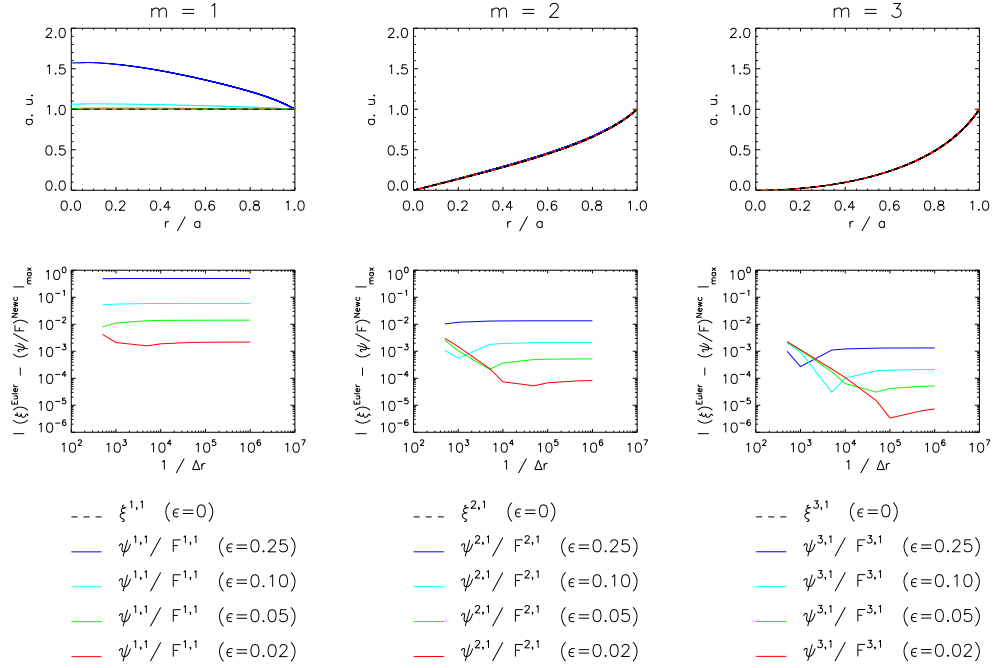
Figure 3.8: Mutual convergence of pressure-less Newcomb's equation solver and large aspect ratio Euler's equation solver. The first row presents eigenfunctions convergence for $m = 1, 2, 3$ and various aspect ratios. The second row reports the convergence studies for each of the above panels.

large aspect ratio approximation for comparatively larger values of ε. This is possibly linked to their eigenfunction being more localized at the edge of the plasma, so that the major radius is even larger when compared to their length-scale, with respect to the typical length of global $m = 1$ modes.

<div style="text-align: right">*4*</div>

Linear stability of current-driven MHD modes

This Chapter contains an introduction on two current driven MHD instabilities, namely the ideal kink mode and the tearing mode. In the previous Chapter we presented two ways to rewrite the linearised momentum balance equation and discussed of the convergence of numerical solvers. Finally, we introduced the Energy principle. In this Chapter, we will put all these tools to use.

In Sec. 4.1 we present the ideal kink instability in the straight tokamak limit, for various equilibrium-current profiles. We briefly present the internal kink mode $m = 1$, and immediately switch our focus onto the external kink mode, which is more interesting for the sake of the verification benchmark of SpeCyl's boundary.

In Sec. 4.2.1 we discuss about the resistive internal instability called tearing mode, again in the large aspect-ratio limit. Two dispersion relations are derived for the tearing mode, corresponding to the two relevant physical cases in which resistive effects dominate over viscous ones, and the opposite regime of predominant viscosity.

At the end of this Chapter, some partial conclusions relative to Part II are reported.

4.1 Ideal kinks

Kinks are ideal instabilities that bend and wind the plasma into a helix. They act to relax the magnetic field stress, thus releasing energy. Reference material for this part will be, once more the books by Freidberg and White [Freidberg14, White06], along with works by Wesson [Wesson04, Wesson78] and Shafranov [Shafranov70].

For simplicity, we will limit our scope to the straight tokamak approximation. Recall that

$$\delta W = \frac{2\pi^2 B_{0,z}^2}{\mu_0 R} \left\{ \int_0^a \left(\frac{1}{q} - \frac{n}{m} \right)^2 \left[r^3 \left(\frac{\mathrm{d}\xi_r}{\mathrm{d}r} \right)^2 + (m^2 - 1)\xi_r^2 \right] \mathrm{d}r \right.$$
$$\left. + \left(\frac{n}{m} - \frac{1}{q_a} \right) \left[\left(\frac{n}{m} + \frac{1}{q_a} \right) + m\lambda \left(\frac{n}{m} - \frac{1}{q_a} \right) \right] a^2 \xi_a^2 \right\}$$

being $\lambda = [1 + (a/b)^{2m}]/[1 - (a/b)^{2m}]$. We can now make some relevant observations:

1. For instability, we require $\delta W < 0$. However, the only term that can possibly be negative is the product $\left(\frac{n}{m} - \frac{1}{q_a} \right)\left(\frac{n}{m} + \frac{1}{q_a} \right)$, and only if $|q_a| < \frac{n}{m}$. In other terms, a mode can be unstable only if it resonates with the equilibrium field at a given radius outside the plasma.

2. The boundary term in the second line of the equation above is proportional to the radial displacement at edge ξ_a. Hence, we can distinguish between *internal* and *external* kinks, which have null and finite ξ_a value, respectively. Note that, according to point 1, the absence of the boundary term in the internal modes case implies that $\delta W > 0$, $\forall \xi$ to this order in ε.

3. The integral part of δW is the same for either internal and external kinks and can be greatly simplified in the case of $m = 1$ modes.

4.1.1   Internal kinks ($m = 1$)

Internal kinks stability cannot be dealt with at this order in the aspect ratio development, as the boundary term is absent and thus $\delta W \geq 0$ intrinsically.
Energy minimisation thus requires finding the eigenfunction that makes the potential $\delta W = 0$ and this is only possible if $m = 1$ and $\xi_r' = 0$. Since the radial displacement at the plasma edge is fixed ($\xi_a = 0$), the only allowed non-trivial radial eigenfunction is a step function, which keeps constant everywhere if not on a tiny resonant layer where it rapidly shrinks to zero. As a matter of fact, internal modes present internal resonant surfaces, unlike external ones. Figure 4.1 reports the 2D shape of a possible step-like radial eigenfunction on the poloidal plane $z = 0$. The poloidal component is obtained through 3.53 and gives rise to a convective cell, that pushes the plasma core outwards, while keeping the edge constrained. Progressing along
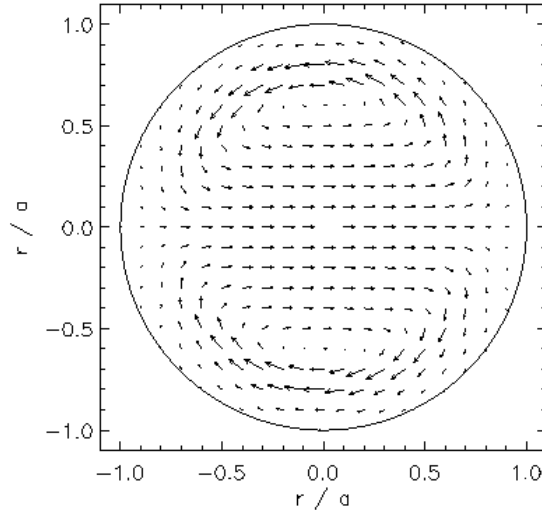
Figure 4.1: Shape of the eigenfunction on the $z = 0$ plane. A convective cell results from incompressibility, pushing outwards the plasma core, inside the resonant surface. Progressing along z, the figure rotates, with phase-shift given by nz/R.

the cylinder axis, we see a rotation of the pattern in the figure, with a phase-shift given by nz/R.

As stated, we need further expansion in the ε development of δW, leaving us with a fairly complicated expression that involves both current and pressure drives (see [Wesson04] for a simplified overview).

Nonetheless, since our ultimate goal is to validate SpeCyl's boundary conditions, such internal modes are outside of the scope of this Thesis and they will not be discussed any further.

4.1.2   External kinks

Let us now move back to the energy variation equation: as previously observed, the case of $m = 1$ is particularly easy to solve. In fact, the integral contribution is once more intrinsically non-negative and is thus minimized by a constant eigenfunction $\xi_r = const$. We are then left with just the boundary term. In other terms, in the case of $m = 1$ mode, the stability analysis does not depend on current profiles but only on its total value (via q_a).

Stability boundaries are easily found for the case without wall ($\lambda = 1$):

$$\delta W = \frac{2\pi^2 B_{0,z}^2}{\mu_0 R} \left(\frac{a\xi_a}{q_a}\right)^2 2nq_a(nq_a - 1)$$

so that the mode is unstable only if $0 \leq nq_a \leq 1$.

Being the radial eigenvalue $\xi_r = \xi_a$, the poloidal component is found via the incompressibility condition as $\xi_\theta = i\xi_a$, so that the effect is a rigid shift of the plasma column to a side, producing a helix around the cylinder axis, having phase $\phi(z) = nz/R$. The shape of plasma displacement and magnetic field perturbation are reported in Fig. 4.2.(a-b). It is worth noticing that the phase of the magnetic perturbation is shifted by $\pi/2$ with respect to the displacement: this is motivated by the presence of the imaginary unit in the flux-freezing law, $-irb_r = F\xi_r$, and should be understood in terms of Wesson's toy model, as given in Fig. 3.1. In fact, given the direction of the current $J_{0,z} > 0$ pointing out from the plane of the page, we can easily obtain the local directions of $\mathbf{J}_0 \times \mathbf{b}$ forces from the magnetic perturbation plots. We can see that where $\mathbf{J}_0 \times \mathbf{b}$ forces point towards each other, the displacement points outwards ($\xi_r > 0$), defining the peaks of the unstable ripple on the perturbed magnetic surfaces. Instead, where they point away from each others, we find the ripple troughs ($\xi_r < 0$).

The kinetic term is easily obtained for a flat density profile as:

$$K = 2\pi^2 R \int_0^a \rho_0 (\xi_a)^2 |1 + i|^2 r \, \mathrm{d}r = 4\pi^2 R \rho_0 (a\xi_a)^2$$

so that the growth rate for $\lambda = 1$ is:

$$\gamma^2 \left(\frac{\tau_A}{\varepsilon_a}\right)^2 = \frac{2}{q_a^2} nq_a(1 - nq_a) \tag{4.1}$$

with $\tau_A = \sqrt{\mu_0 \rho_0} a / B_{0,z}$, as in Eq. 3.7, and τ_A/ε_a is the toroidal Alfvén time. From eq. 4.1 we see that ideal growth rates are of the same order as the inverse Alfvén time, as is also evident from fig. 4.3. This figure, though, will be better commented once we have introduced the other $m > 1$ modes.

For the case of $m \geq 2$, the variational energy problem (*i.e.* the Euler's equation) is completely fixed, up to the choice of a current density profile. The simplest choice one can make is to assume the plasma to be a current-channel, bearing constant homogeneous density $\mathbf{J} = J_{0,z}\mathbf{z}$. This profile was initially studied and proposed by Shafranov in [Shafranov70] and turns out to be the maximally unstable current profile for external kinks, leaving no range of current values to modes stability. Yet, it is very present in literature, as for instance on [Liu08, Finn95].

Flat-current model: to complete our model, let us assume a homogeneous plasma and a uniform axial magnetic field $B_{0,z}\,\hat{\mathbf{z}}$, so that the profiles of the main equilibrium quantities are:

$$J_z(r) = J_{0,z}\,\Theta(a - r) \tag{4.2}$$

$$\rho_0(r) = \rho_0\,\Theta(a - r) \tag{4.3}$$

$$q(r) = \begin{cases} q_a & \text{if } r \le a \\ q_a \left(\frac{r}{a}\right)^2 & \text{if } r > a \end{cases} \tag{4.4}$$

being $\Theta(r - a)$ the Heavyside step-distribution, a the plasma radius and $q_a = 2B_{0,z}R/(\mu_0 J_{0,z})$.
Euler's equation greatly simplifies to

$$\frac{\mathrm{d}}{\mathrm{d}r}\left[r^3\frac{\mathrm{d}\xi_r}{\mathrm{d}r}\right] = (m^2 - 1)\,r\,\xi_r$$

having physical solution:

$$\xi_r = \xi_a \left(\frac{r}{a}\right)^{m-1} \tag{4.5}$$

whence, via incompressibility,

$$\xi_\theta = i\xi_a \left(\frac{r}{a}\right)^{m-1}.$$

Figure 4.2.(c-e) show the corresponding plasma displacement and magnetic field perturbations for modes $m = 2$ and $m = 3$. What we see is that mode $m = 2$ deforms the plasma cross section into an ellipse, as we anticipated in figure 3.1.(a), whereas $m = 3$ shapes it into a triangle. Once more, the poloidal cross-section at $z = 0$ is rotated into a screw as we proceed along the axis, with phase shift given by $\phi = nz/R$. Both displacement and magnetic field plots show that the higher is m, the more edge-localised the eigenfunction gets.
While the plasma displacement on the first column is obtained by solving numerically the Euler's equation for the given equilibrium, the magnetic field perturbation in the second column comes from the large aspect ratio limit of Newcomb's solver[1]. Two separate branches of solution have been produced and matched at plasma boundary, just as we did for the case study of the thin current-ring in Sec. 3.4.1: the magnetic flux inside the plasma is obtained by integrating from axis to the plasma edge (grey circle in the plot), while the

---

[1]Using the same solver for both $\boldsymbol{\xi}$ and ψ and relying on the linearised frozen-flux relation would lead to the results, as already seen in Fig. 3.8.

external solution is achieved by integrating backwards from a far-displaced ideal wall, past resonance radius (green circle in the plot) up to the edge of the plasma. The two branch-solutions are then matched at plasma edge, to guarantee the solenoidal property of the magnetic field.

The stability analysis yields

$$\delta W^{\min} = \frac{2\pi^2 B_{0,z}^2}{\mu_0 R} \left(\frac{a\xi_a}{q_a}\right)^2 \frac{2}{m} \left(m - nq_a\right) \left[\frac{m - nq_a}{1 - (a/b)^{2m}} - 1\right]$$

having used Eq. 3.55 and the identities: $a\xi_a'/\xi_a = m - 1$ and $(\lambda + 1)/2 = 1/\left[1 - (a/b)^{2m}\right]$. The kinetic term reads

$$K = 4\pi^2 \rho_0 R \frac{(a\xi_a)^2}{m}$$

so that

$$\gamma^2 \left(\tau_A/\varepsilon_a\right)^2 = \frac{2}{q_a^2} \left(m - nq_a\right) \left[1 - \frac{m - nq_a}{1 - (a/b)^{2m}}\right], \qquad (4.6)$$

where $\varepsilon_a = a/R$ and τ_A/ε_a is the toroidal Alfvén time. Such a time-scale naturally emerges from equations since it matches with the typical space-length (R) of the toroidal current.

In the case without ideal wall, $1 - (a/b)^{2m} \to 1$ and it is evident that for each possible nq_a there exists a value of $m - 1 \le nq_a \le m$ that makes the growth-rate real and thus the corresponding mode unstable. We see that the instability regions of various modes cover the whole parameter space without overlapping: this property is however lost when the poloidal cross-section of the plasma is not circular and the instability domains of different modes gradually blur into one another [Wesson78].

In Fig. 4.3.(a) we see the growth-rate of various modes for different positions of the conductive shell, increasingly close to the plasma. The stabilising effect is dramatic especially for low m modes, which, otherwise, are the most unstable (especially mode $m = 1$): both growth-rates and stability regions change rapidly as $b \to a$.

Recalling what we said about $m = 1$ external mode, that solely depends on the total current q_a rather than its profile, since this model cannot display any effect relating to current profiling, we could expect it to replicate the $m = 1$ stability behaviour also for higher m modes. This is in fact what happens and it is visible in panel (b) of Fig. 4.3, where $\gamma\tau_A/\varepsilon_a$ is further normalised over the total current value $(1/J_{0,z}) \propto q_a$.

   Figure 4.4 reports the normalised eigenfunctions of the Shafranov's flat-current model for $n = 1$ and three different values of m.
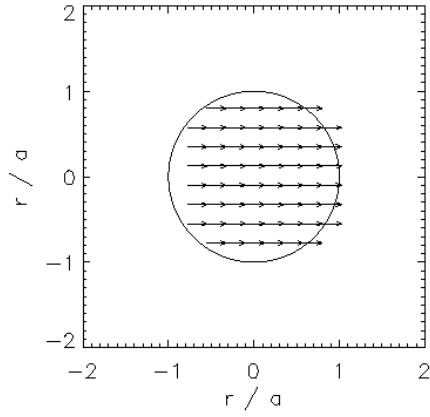
(a) displacement for $m=1$
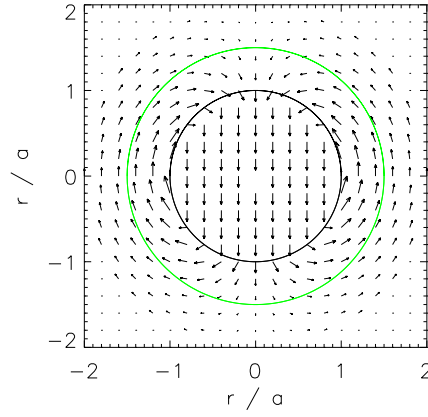
(b) magnetic perturbation for $m=1$
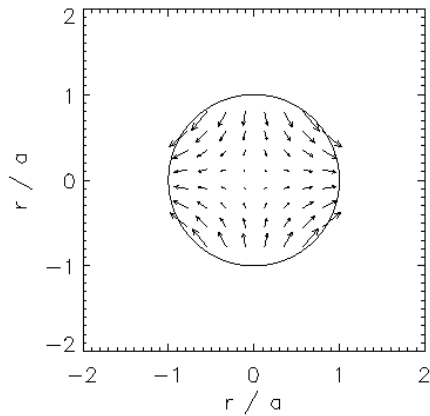
(c) displacement for $m=2$
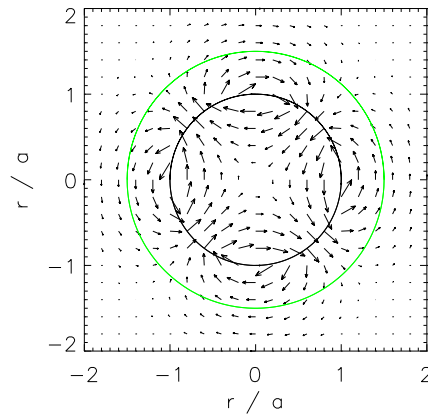
(d) magnetic perturbation for $m=2$
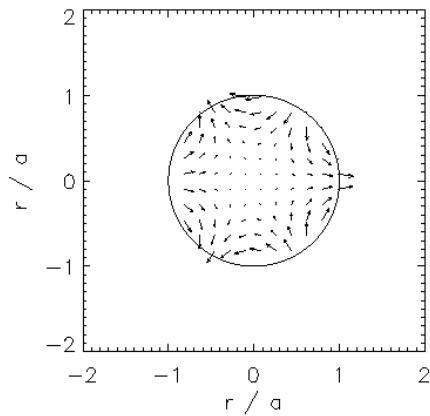
(e) displacement for $m=3$
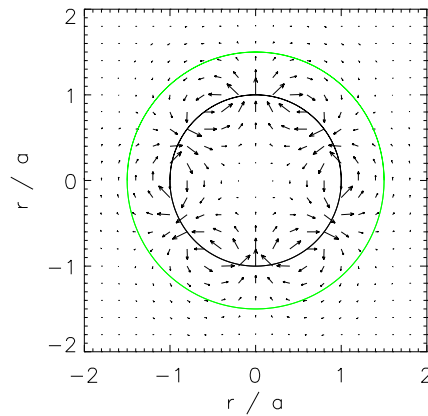
(f) magnetic perturbation for $m=3$

Figure 4.2: Poloidal cross section at $z = 0$. Both the flow and the magnetic field perturbation are represented for the linear phase of some external kink modes, using a flat profile for both mass and current densities. A black contour marks the plasma edge and a green one shows the resonance radius.

(a)

(b)
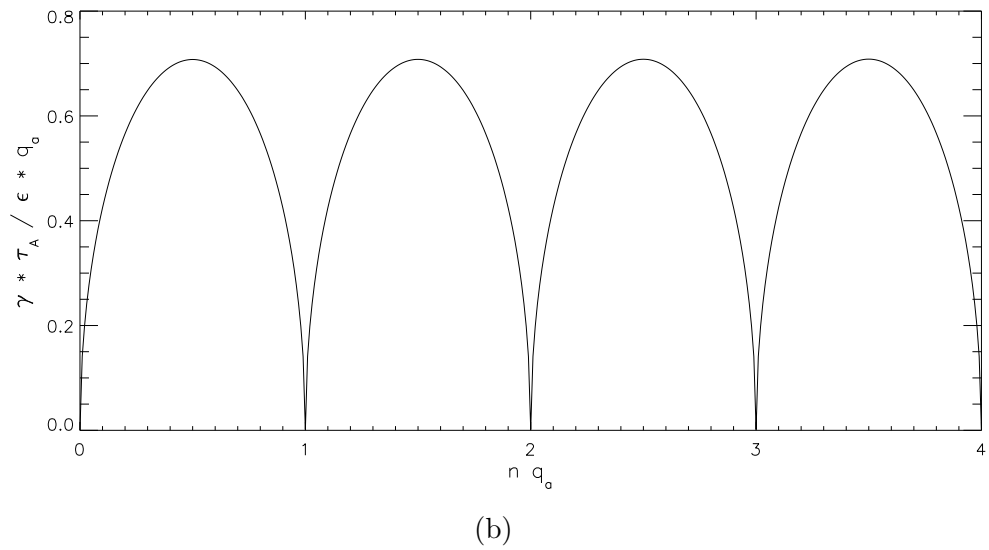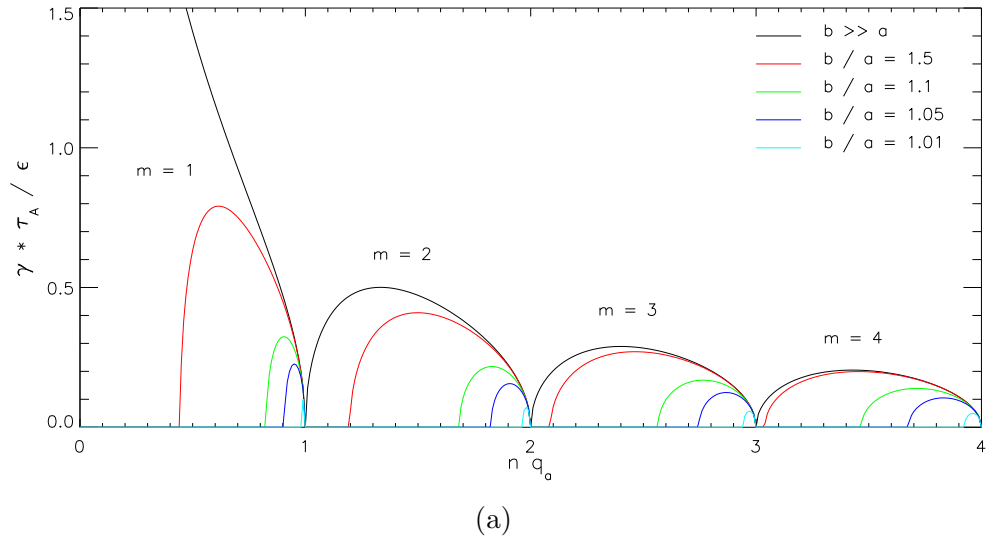
Figure 4.3: Flat current density and mass density profiles: growth rate achieved by different modes plotted against the total current nq_a. Subfigure (a) shows the actual growth-rates, normalised to the Alfvénic time and for various ideal-wall proximities; (b) shows for the case of $b \gg a$ that all modes behave the same way, up to a factor q_a.
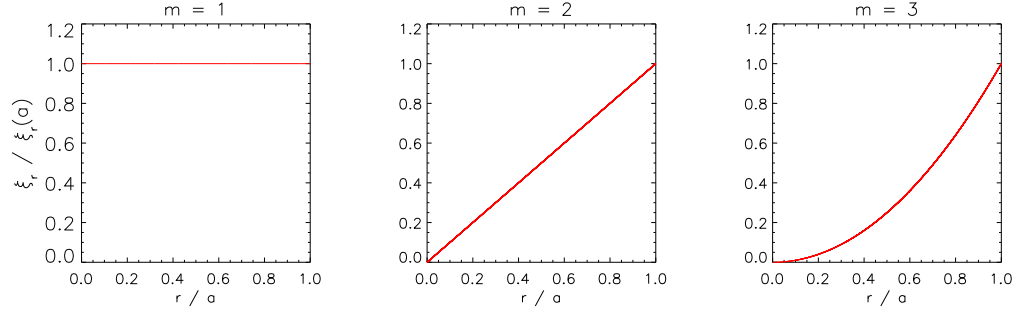
Figure 4.4: Normalised eigenfunctions of the flat-current model for $n = 1$ and three values of m.

Step-current profile: when we introduced the energy principle, we made the claim that its description of ideal modes stability is more complete than the amount of information contained in Newcomb's equation. Albeit Euler's equation has been proven to contain the same batch of information as the Newcomb's counterpart (describing the magnetic drive and neglecting plasma inertia), we may ask what happens if we take our current-channel of Eq. 4.2 a bit thinner than the actual plasma radius.

This leaves us with a step-profile for the current density inside our still homogeneous plasma:

$$J_z(r) = J_{0,z} \, \Theta(r_0 - r) \tag{4.7}$$

$$\rho_0(r) = \rho_0 \, \Theta(a - r) \tag{4.8}$$

$$q(r) = \begin{cases} q_0 & \text{if } r \leq r_0 \\ q_0 \left(\frac{r}{r_0}\right)^2 & \text{if } r > r_0 \end{cases} \tag{4.9}$$

being $r_0 < a$. Despite being very similar to the previous case (q_0 is still the same quantity we used to call q_a in Eq. 4.4 and everything is identical up to $r \leq r_0$), there is one striking difference: the plasma extends to a region of so-called *pseudo-vacuum*, where the electromagnetic part of our equations sees nothing but perfect vacuum but we still have mass and flow.

This means that the term q_a in the energy variation is now $q_a = q_0(a/r_0)^2$, and, more importantly, that ξ_a and the kinetic term are now completely

different. From [Shafranov70] we can get:

$$
\xi_r(r) =
\begin{cases}
\xi_r(r_0) \left(\dfrac{r}{r_0} \right)^{m-1} & \text{if } r \le r_0 \\[3ex]
\dfrac{\xi_r(r_0)}{m - nq_0 \left(r/r_0 \right)^2} \left[\left(\dfrac{r_0}{r} \right)^{m-1} + \left(\dfrac{r}{r_0} \right)^{m+1} (m - 1 - nq_0) \right] & \text{if } r_0 < r \le a
\end{cases}
\tag{4.10}
$$

The new value of γ is represented in Fig. 4.5 for different values of the ratio of the plasma radius to the current-channel width. It is seen that the introduction of finite shear in the magnetic field configuration has a strongly stabilizing effect, as instability regions get narrower and the instability growth-rate is reduced. External $m = 1$ mode is once more unaffected, since it does not depend on the current profile.
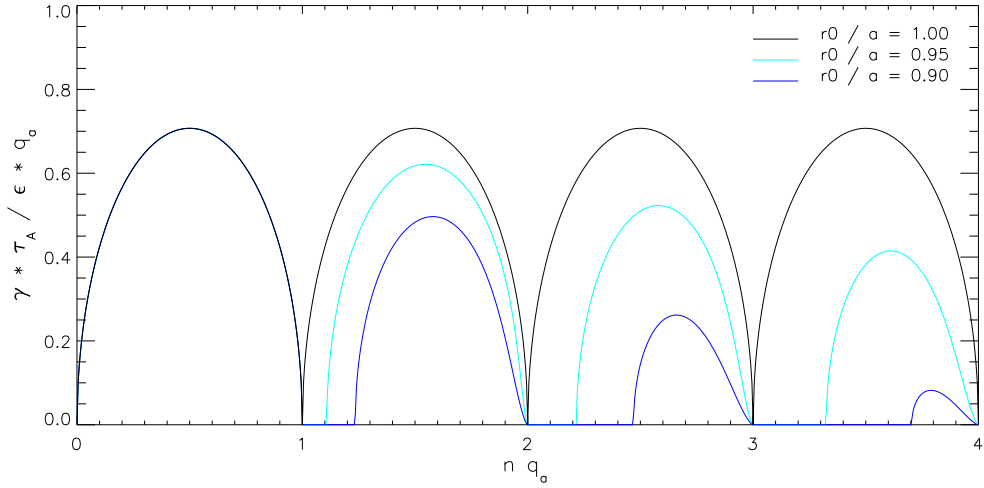
Figure 4.5: Shafranov's step-current model for different values of r_0/a.

Wesson's current model: A more realistic current profile was proposed by Wesson [Wesson78]:

$$
J_z(r) =
\begin{cases}
J_{0,z} \left[1 - \left(\dfrac{r}{a} \right)^2 \right]^\nu & \text{if } r \le a \\[2ex]
0 & \text{if } r > a
\end{cases}
\tag{4.11}
$$

$$q(r) = \begin{cases} q_a \dfrac{(r/a)^2}{1 - \left[1 - (r/a)^2\right]^{\nu+1}} & \text{if } r \le a \\[2ex] q_a \left(\dfrac{r}{a}\right)^2 & \text{if } r > a \end{cases} \qquad (4.12)$$

with constant axial field $B_{0,z}$. One relevant property of this model is that:

$$\frac{q_a}{q_0} = \nu + 1\,, \qquad q_0 \equiv q(0) = \frac{2B_{0,z}}{J_{0,z}R}\,.$$

For this model there is no analytical solution to the Euler's equation. Nonetheless, it is easy to prove that for any value of ν and $J_{0,z} \ne 0$, in the proximity of the cylinder axis ($r \approx 0$) we recover the flat-current model, since $J_z \approx J_{0,z}$ and $q \approx q_0$.

Hence, we can solve numerically with LENS the Euler's equation with our usual initial conditions:

$$\xi_r(r \to 0) \sim r^{m-1}\,; \qquad \xi_r'(r \to 0) \sim (m-1)\,r^{m-2}\,.$$

The eigenfunctions for modes $m = 1, 2, 3$ were already presented for a specific set of parameters in fig. 3.8.

Concerning the growth rates, they are obtained by substituting the eigenfunction found by the solver into the energy balance equation. If on the one hand we can avoid computing the integral in the definition of the potential energy variation by making use of the minimised form in Eq. 3.50, we must deal with the integral in the kinetic term. This is dealt with in LENS using a fourth-order precision Cavalieri-Simpson algorithm, that has been positively verified on several trial functions, yielding the expected rate of convergence.

Figure 4.6.(a) reports the normalised growth-rates predicted for some values of the model parameter ν. Direct comparison with Fig. 4.3 and 4.5 shows that the Shafranov's flat-current model coincides with the $\nu = 0$ limit case for Wesson's model. We see that the effect of finite shear on stability closely resembles what we already saw in Fig. 4.5, with higher-m modes being strongly damped and stability regions broadening, starting from the left-hand side of instability "bells": this means that the mode can be destabilised only if the resonance happens just outside the plasma edge ($nq_a \approx m$), while we recover stability as soon as it enters the plasma (as nq_a grows larger than m).

Panel (b) shows a more general picture including stability of all modes against every possible profile corresponding to Eqs. 4.11 and 4.12. Despite the incomplete picture in Panel (a), we see that below $\nu = 1$ there is no stability region, when also higher-m modes are considered, while above $\nu = 3$ only the profile-insensitive $m = 1$ mode is still unstable.
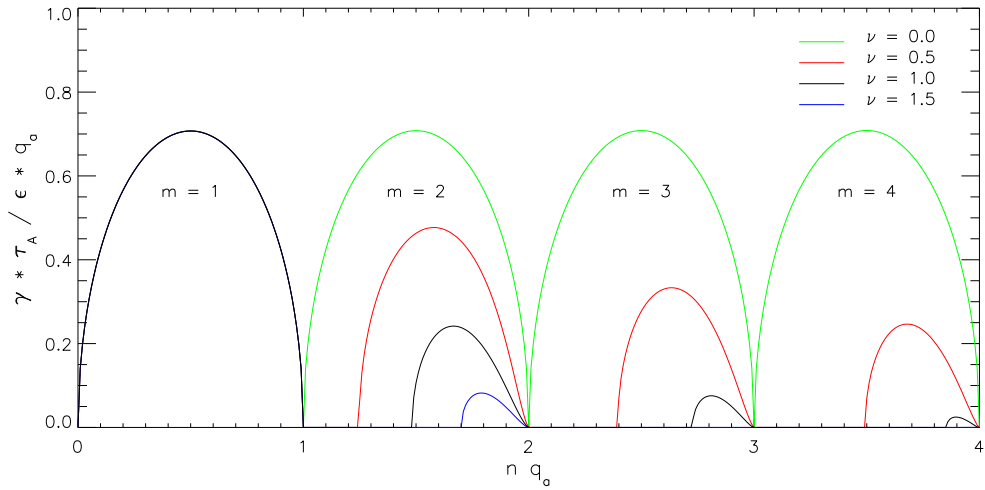
(a) Normalized growth-rates for several values of model parameter
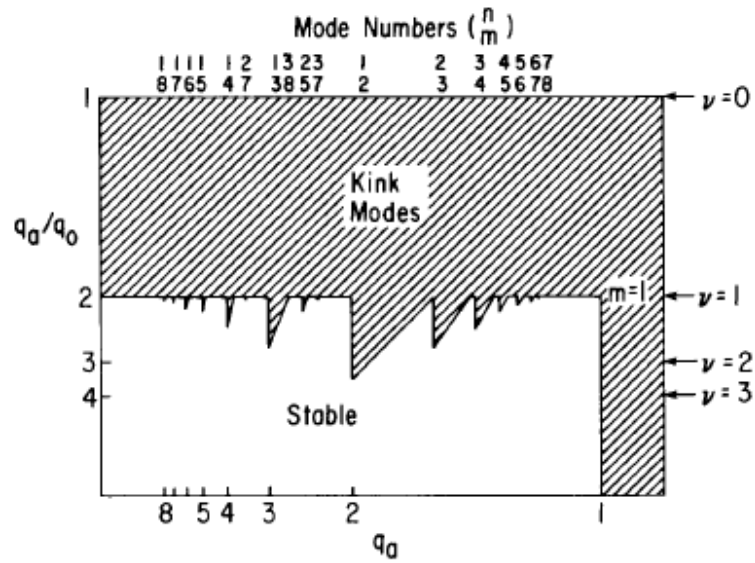
(b) Stability diagram for all possible modes and profiles (taken from [Wesson78]).

Figure 4.6: Stability of the Wesson's current model, for different modes and values of ν.
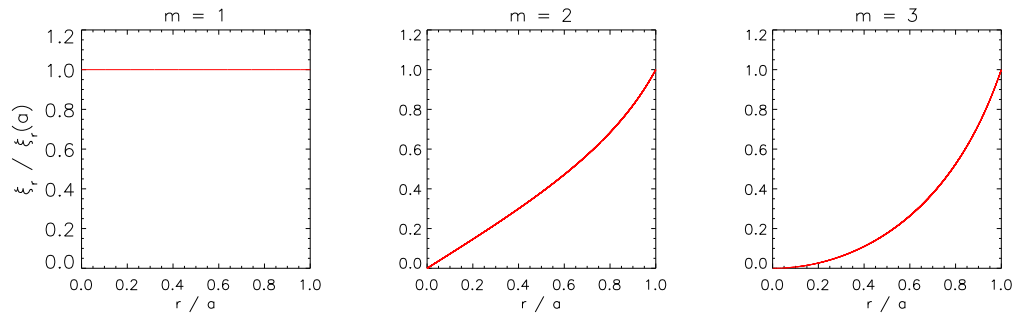
Figure 4.7: Normalised eigenfunctions of the Wesson's current model for $\nu = 1$, $n = 1$ and three values of m.

Figure 4.7 reports the normalised eigenfunctions of the Shafranov's flat-current model for $n = 1$ and three different values of m, obtained using LENS. The case for $m = 1$ still yields the same eigenvalue, in compliance with the requirement that this case is insensitive to the current profile.

4.2 Tearing modes

When a resonant layer falls inside the plasma region, it may separate two plasma domains with different (discontinuous) magnetic field components along the azimuthal and axial directions, sustained by intense currents in a narrow channel enclosing the layer, known as current sheet.

In presence of finite resistivity, magnetic diffusion may arise to compensate the imbalance. Assuming a layer width of $\lambda \ll a$, the local Lundquist value $S = \tau_A / \tau_R \propto 1/\lambda$ is expected to be relatively high. The plasma is then broken in two large domains where ideality conditions apply and a narrow, resistive layer.

Resistive diffusion of **B** yields non-linearly to tearing and reconnection of magnetic field lines into the formation of a chain of islands along the resonant layer, with the same periodicity of the resonant mode (m, n). Nonetheless, our focus here is only on the linear tearing mode instability, in the simplified case of the straight tokamak geometry.

4.2.1 Linear tearing mode stability in the straight toka-mak

As we said, the plasma region is effectively split into three domains: one narrow and resistive band enclosing the resonant layer and two outer ideal

plasmas where Newcomb equation applies. The drive for diffusion is in the imbalance of b_θ and b_z across the resonance, while b_r should be regarded as continuous, as we assume a vanishing layer width λ. From before, we know that the large aspect-ratio dynamics is mainly set in the $r - \theta$ plane, and from Eq. 3.11-3.13 we get:

$$b_\theta^{m,n} \propto \frac{\mathrm{d}\psi}{\mathrm{d}r}\,, \qquad b_r^{m,n} \propto \psi\,.$$

Hence, one very representative quantity will be

$$\Delta' = \frac{1}{\psi_s}\left[\frac{\mathrm{d}\psi}{\mathrm{d}r}\right]_{r_s-\lambda/2}^{r_s+\lambda/2} \tag{4.13}$$

where r_s is the resonance radius and $\psi_s \equiv \psi(r_s)$. From the matching of this quantity between outer ideal and inner resistive regions we can indeed derive the mode stability analysis.

In this, we will mainly follow [Wesson04] (but alternative derivations can be found on [FRS73, Militello04]). The main assumptions in the following derivation descend from the narrowness of the layer ($\lambda \ll a$): $\psi \approx \psi_s$ and $r \approx r_s$ within the layer. Also, we assume our usual ordering of a perturbed axi-symmetric and stationary equilibrium.

External domain

In the ideally conductive region outside can be treated according to the large aspect-ratio Newcomb's equation (Eq. 3.33), since diffusion processes are slow enough to neglect the inertial term in momentum balance equation [Wesson04].

To compute the transverse-field jump across the resistive layer, one must independently integrate two Newcomb solutions, with suitable initial conditions, such that they match with ψ_s in r_s: ψ_- from axis to $r_s - \lambda/2$ and ψ_+ from outside to $r_s + \lambda/2$, so that

$$\Delta' = \frac{1}{\psi_s}\left[\frac{\mathrm{d}\psi_+}{dr}(r_s + \lambda/2) - \frac{\mathrm{d}\psi_-}{dr}(r_s - \lambda/2)\right] \tag{4.14}$$

Resistive layer

In the resistive domain enclosing the resonance, plasma dynamics is described by the resistive Ohm's law, along with the linearised momentum balance equation without viscosity:

$$-\frac{\partial \mathbf{B}}{\partial t} + \nabla \times (\boldsymbol{v} \times \mathbf{B}) = \frac{\eta}{\mu_0}\nabla \times \nabla \times \mathbf{B}\,,$$

$$\rho \frac{\partial \boldsymbol{v}}{\partial t} = \mathbf{J} \times \mathbf{B} - \nabla p \,.$$

A thorough derivation of a dispersion relation for the tearing modes in this relevant case with negligible viscosity is reported in Appendix A.4. In the following, we just wish to list the main assumptions implied in the derivation, along with the final results.

The main assumptions enforced through the derivation are

1) large aspect ratio limit ($\varepsilon \to 0$) and circular poloidal cross-section,

2) incompressible flow ($\nabla \cdot \boldsymbol{v} = 0$),

3) resistive layer much thinner than macroscopic length-scales ($\lambda \ll a$),

4) resistive layer much larger than the characteristic space-variation scale h, which is defined below ($\lambda \gg h$).

In particular, the third assumption implies has two implications: the first one concerns the gradient and the Laplacian operator and implies that

$$\nabla \approx \frac{\partial}{\partial r}\,, \qquad \nabla^2 \approx \frac{\partial^2}{\partial r^2}\,;$$

the second is the so-called "constant-ψ" approximation, which consists in assuming that ψ does not vary across the layer. Along with ψ, we also assume the constancy of ρ.

Concerning the fourth assumption, the space-variation scale is found to be

$$h = \left[\left(\frac{\rho \eta \gamma r^2 q^2}{B_{0,\theta} m^2 q'^2} \right)^{1/4} \right]_{r=r_s} \ll \lambda \,, \tag{4.15}$$

as reported in Eq. A.6.

After the long manipulation reported in Appendix A.4 we finally get to

$$\Delta'_{in} = 2.12 \frac{\mu_0 \gamma\, h}{\eta_s} \tag{4.16}$$

and making h explicit and matching Eq. 4.16 with 4.14 we get

$$\gamma = 0.5474 \left[\left(\frac{\eta}{\mu_0} \right)^{3/5} \left(\frac{m B_{0,\theta}\, q'}{\sqrt{\mu_0 \rho}\, r q} \right)^{2/5} \right]_{r=r_s} \cdot \left(\Delta' \right)^{4/5} . \tag{4.17}$$

Instability requires $\gamma \geq 0$, so that

- $\Delta' < 0$ yields mode stability

- $\Delta' = 0$ yields marginal mode stability

- $\Delta' > 0$ yields mode instability

Figure 4.8 illustrates the geometrical interpretation of such a condition. Panel (a) reports the radial profile of the two branches of the magnetic flux, obtained by solving Newcomb's equation with a very large aspect ratio and for the specific case of mode $(2,1)$. The equilibrium fed to LENS is once more given by a Wesson's current profile with $\nu = 1$. Solver's solutions are matched at the given resonance radius, which is different for every plotted eigenfunction and for each is marked by a grey dotted line. By looking at the graph, we can immediately tell which are the unstable cases: since we require for instability that

$$\frac{1}{\psi(r_s)} \frac{\mathrm{d}\psi}{\mathrm{d}r} \left(r_s^+ \right) > \frac{1}{\psi(r_s)} \frac{\mathrm{d}\psi}{\mathrm{d}r} \left(r_s^- \right) ,$$

we can guess that all the reported eigenfunctions are relative to unstable tearing modes, apart from the one in red.
Panels (b) and (c) illustrate the magnetic perturbation projected onto the poloidal cross-section of the plasma and correspond to the eigenfunctions in blue and red, respectively, of panel (a). Also in this case, there is a precise graphical meaning of the instability condition. Since, as we know,

$$\frac{\mathrm{d}\psi}{\mathrm{d}r} = -imb_\theta \,,$$

instability in the large aspect ratio limit coincides with the geometrical property that $b_\theta \left(r_s^+ \right) < b_\theta \left(r_s^- \right)$. Again, since the resonance is indicated on the polodal plots as a green circle, we can safely guess that the tearing mode in panel (b) is going to be unstable, while panel (c) shows a stable case. Note in panels (b-c) that already in the linear onset of the instability there is atready present the initial seed of a magnetic island across the resonance radius.

4.2.2 Numerical solution for Δ'

In the previous Subsection we derived a geometrical condition that binds the magnetic flux derivative across the resonance to the stability of the associated tearing mode. This resulted by solving the resistive momentum balance equation in a vanishingly narrow layer across the resonance radius and the ideal Newcomb's equation outside it, assuming a very large aspect
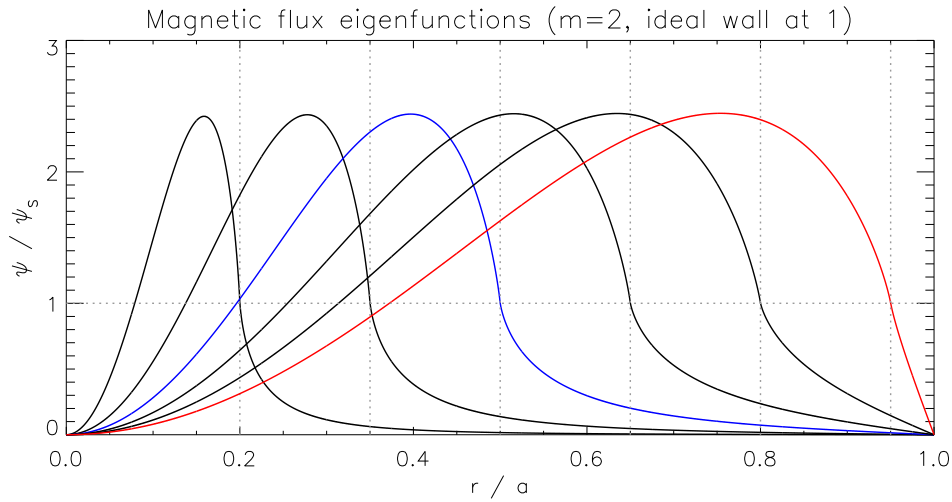
(a) Magnetic flux eigenfunction for $m = 2$: several alternative cases, relative to various resonance radii (grey dotted lines).
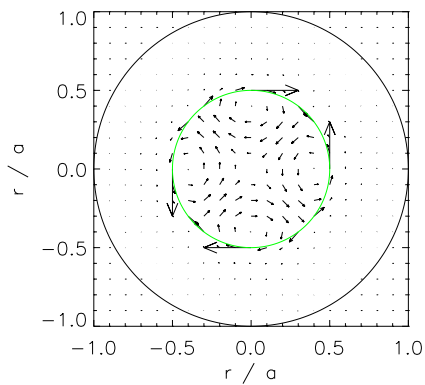
(b) Unstable $(2, 1)$ mode: $r_s/a = 0.5$. Blue eigenfunction in the upper plot.
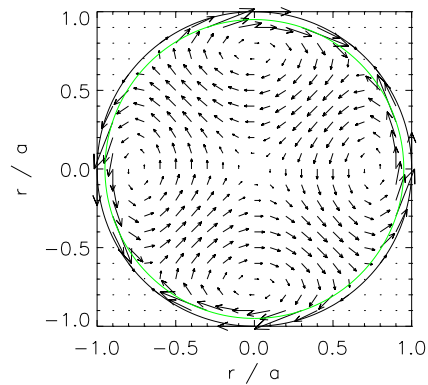
(c) Stable $(2, 1)$ mode: $r_s/a = 1$. Red eigenfunction in the upper plot.

Figure 4.8: Graphical interpretation of $\Delta' < 0$ condition for stability: mode $(2, 1)$, ideal wall at $r = a$, large aspect-ratio limit.

ratio.

Let us start again from the large aspect ratio form of Newcomb's equation:

$$\frac{1}{r}\frac{\mathrm{d}}{\mathrm{d}r}\left(r\frac{\mathrm{d}\psi}{\mathrm{d}r}\right) = \left[\frac{m^2}{r^2} + \frac{m}{F}\mu_0\frac{\mathrm{d}J_{0,z}}{\mathrm{d}r}\right]\psi \,.$$

Since we need to define very precisely the derivative of its solution in the immediate proximity of the resonant layer, it is convenient to study its expected behaviour in such a critical domain.

Recalling the definition of F, its first order approximation around resonance radius r_s is

$$F(r) = mB_{0,\theta}(r_s)\left(1 - \frac{nq(r)}{m}\right)$$

$$\approx -mB_{0,\theta}(r_s)\frac{n}{m}q'(r_s)\cdot(r - r_s) = \left[-\frac{mB_{0,\theta}\,q'}{q}\right]_{r_s}(r - r_s)\,,$$

since $q(r_s) = m/n$ by definition. Taking an interval small enough such that $|r - r_s| \ll r_s$, we isolate the leading order terms and find

$$\frac{\mathrm{d}^2\psi}{\mathrm{d}r^2} = \left[-\frac{\mu_0 q}{B_{0,\theta}\,q'}\frac{\mathrm{d}J_{0,z}}{\mathrm{d}r}\right]_{r_s}\frac{\psi}{r - r_s}\,, \tag{4.18}$$

or

$$\frac{\mathrm{d}^2\psi}{\mathrm{d}s^2} = \frac{\kappa}{s}\psi\,, \tag{4.19}$$

where $s = r - r_s$ and κ is the term in square brackets in Eq. 4.18. The general solution to this equation is thus

$$\psi_- = 1 + \kappa s \ln|s| + A_- s + \mathcal{O}\left(s^2\right)\,, \quad \text{if } s < 0\,,$$
$$\psi_+ = 1 + \kappa s \ln|s| + A_+ s + \mathcal{O}\left(s^2\right)\,, \quad \text{if } s > 0\,. \tag{4.20}$$

so that

$$\psi'_- = \kappa\left(\ln|s| + 1\right) + A_- + \mathcal{O}\left(s\right)\,, \quad \text{if } s < 0\,,$$
$$\psi'_+ = \kappa\left(\ln|s| + 1\right) + A_+ + \mathcal{O}\left(s^2\right)\,, \quad \text{if } s > 0\,. \tag{4.21}$$

The resulting expression for Δ' is

$$\Delta' = A_+ - A_-\,,$$

which is very palatable for a numerical solution. In fact, in the LENS code, after producing and matching the two branches of the solution, integrating

Table 4.1: Validation of the numeric tool for the computation of Δ' against reference values of $x_s \Delta'$, in the limit of $x_s \to 0$ (p. 326 of [Wesson04]). Numeric results obtained with an equally spaced mesh of 10^7 points in plasma region $0 \leq x \leq 1$.

m	$\{x_s \Delta'\}_{\text{ref}}$	$\{x_s \Delta'\}_{\text{tool}}$
2	11.22	11.219
3	2.46	2.457
4	-2.01	-2.015

from axis and from an ideal wall at arbitrary distance from the plasma edge, we leverage the local problem solutions in Eqs. 4.20-4.21 to get a more precise estimate of the coefficients A_+ and A_-. This is done by taking a space average over the last 20 radial mesh points of each solution branch:

$$(A_\pm)^{\text{LENS}} := \left\langle \left(\psi'_\pm\right)^{\text{LENS}} - \kappa \left(\ln|s| + 1\right) \right\rangle_{|s| \in [\, 0\,,\, 20 \cdot \Delta r\,]}.$$

Nonetheless, the choice of this procedure over *e.g.* a linear fit based on Eq. 4.20 (or really many other chances) is arbitrary and must thus be tested to verify its accuracy.

Fortunately, Wesson provides a very accurate test in [Wesson04] (p. 325-326): fig. 4.9 reports a study on the stability of modes $m = 2, 3, 4$, $n = 1$, as a function of both resonance position and ideal wall displacement from the edge of the plasma. This completes Fig. 6.9.1 of [Wesson04], which is only relative to $m = 2$, and presents no visible difference with the red curve in our one. A similar study on the ideal shell proximity effect on tearing modes stability can also be found in [FRS73].

We see that the presence of an ideal wall has an important impact on modes stability only if the resonance is close to the plasma edge, whereas core-resonant modes are almost completely unaffected. Also, we see that $m = 2, 3$ (along with the far more unstable $m = 1$, which is out of scale for the plot) are pretty much unavoidably present in the straight tokamak, whereas $m = 4$ can be simply avoided even with a loosely fitting ideal wall.

Table 4.1 reports the asymptotic values on axis for the three curves of Fig. 4.9. The Table shows very good agreement between the reference values obtained by Wesson and by our numerical tool. It should however be highlighted that this is just meant as an exercise, since real fusion plasmas generally have way too high conductivity in their hot core for a tearing mode to develop there.
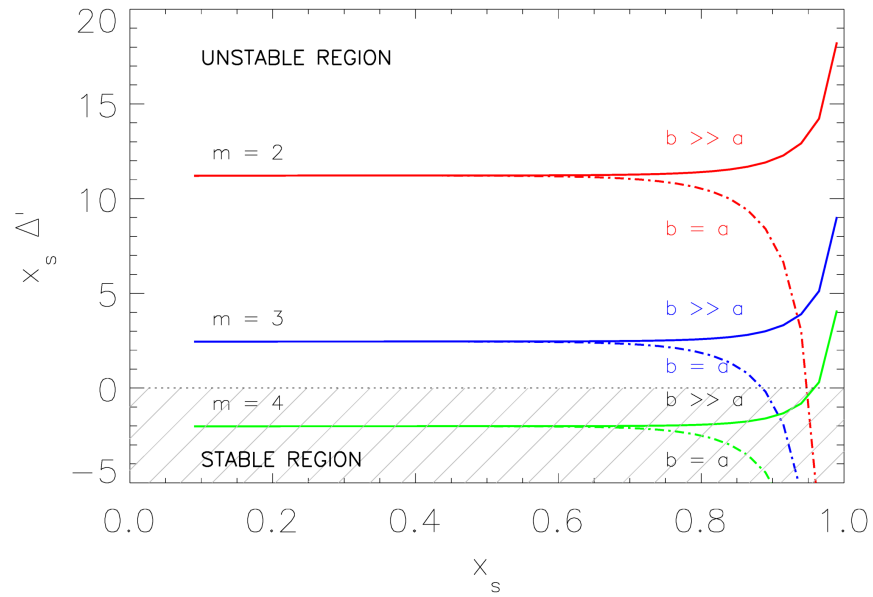
Figure 4.9: Study on the stability of $m = 2, 3, 4,\ n = 1$ linear tearing modes in the straight-tokamak limit, also in relation to the ideal-wall proximity, with the Wesson's current model. Tearing instability ($\Delta' > 0$) can be greatly reduced or eliminated with a close-fitting ideal wall, but only if the resonance radius $x_s = r_s/a$ is close to the plasma edge: internally resonating modes are not influenced by external walls. Modes $m = 2, 3$ (and, not framed, $m = 1$) are mostly unstable, whereas $m \geq 4$ can be easily prevented through adding an ideal wall. [Solver information: equally-spaced radial mesh ($\delta x = 2 \cdot 10^{-7}$)].

4.2.3 Bondeson-Sobel's visco-resistive dispersion relation

In view of our simulations, it will sometimes be convenient to introduce some viscosity to damp unwanted oscillations and bring SpeCyl to a more sound convergence. Luckily, there is an easy generalization of the resistive tearing mode dispersion relation in Eq. 4.17 [Bondeson84, Porcelli87].
We saw how tearing modes can develop in a conductive plasma relying on the fact that within a very narrow layer around the resonance small spacial scales may reduce locally the resistive diffusion time-scales. However, the same mechanism does also enhance viscous processes within the resistive layer.
For this case, a slightly more general (visco-resistive) derivation is needed than what we did for Eq. 4.17, later specialised to the opposite case of dominant viscosity rather than resistivity (see Appendix A.5). The final dispersion relation for dominant viscosity inside the resonant layer is

$$\gamma = 0.4754 \left[\left(\frac{\eta}{\mu_0} \right)^{5/6} \nu^{-1/6} \left(\frac{m B_{0,\theta} \, q'}{\sqrt{\mu_0 \rho} \, rq} \right)^{1/3} \right]_{r_s} \Delta' . \qquad (4.22)$$

The control parameter that defines which regime we are in is the critical viscosity (found by equating the two dispersion relations)

$$\nu_{\text{crit}} = 0.4291 \left[\eta^{7/5} \left(\frac{\sqrt{\rho} \, rq}{m B_{0,\theta} \, q'} \right)^{2/5} \right]_{r_s} \left(\Delta' \right)^{6/5} . \qquad (4.23)$$

When $\nu(r_s) > \nu_{\text{crit}}$ we are in a viscosity dominated regime, vice versa we should stick to the old dispersion relation.
Bondeson's dispersion relation has been implemented along with the resistive one LENS. ν_{crit} is computed as well as both growth rates, so as to provide the user with freedom of choice.

4.2.4 Bertin-Militello correction to the resistive dispersion relation

In [Bertin82] a first attempt to extend the resistive tearing mode dispersion relation beyond the constant-ψ approximation is presented, studying the effect of current gradients inside the resistive layer. Later work [Militello04] has extended the analysis to include also the local current curvature inside the layer. Here we present just the final result.

The dispersion relation is found to be:

$$2.12 \frac{\mu_0 \gamma h}{\eta_s} = \Delta' + 2.12 \, h \left[a \frac{A_+ + A_-}{2} + a^2 \left(\log h + 1.304 \right) - b \right], \qquad (4.24)$$

where h is still the length-scale of spatial variation across the resistive layer (see Eq. 4.15), and $A_\pm$ are defined as in Eq. 4.20 (even if now many more terms in the development of $\psi_\pm$ must be considered). The other coefficients are defined as follows:

$$a \equiv \left[\left(\frac{m}{r_s} \frac{\mathrm{d}J_{0,z}}{\mathrm{d}r} \right) \Big/ \left(\frac{n}{R} \frac{q'}{q} \right) \right]_{r=r_s} \qquad \text{local current gradient,}$$

$$b \equiv \left[\left(a \frac{q''n}{2qR} - \frac{\mathrm{d}}{\mathrm{d}r} \left(\frac{m}{r} \frac{\mathrm{d}J_{0,z}}{\mathrm{d}r} \right) \right) \Big/ \left(\frac{n}{R} \frac{q'}{q} \right) \right]_{r=r_s} \qquad \text{local current curvature.}$$

Numerical studies reported in [Militello04] prove Eq. 4.24 to provide an important correction when the resonant layer has relatively high resistivity, and to fall reliably into analogous predictions with respect to Eq. 4.17 when $S(r_s) \gtrsim \mathcal{O}(10^7)$. A milder dependence is also observed on Δ': the "standard" dispersion relation Eq. 4.17 resents less of the correction when Δ' is larger.

The complete resistive dispersion relation Eq. 4.24 has not been included in our LENS's analysis. Therefore in the next Chapters we will limit our benchmark studies to relatively large values of Lundquist number, where the "standard" resistive relation can still be trusted.

Conclusive summary of Part II

Linear MHD perturbative theory has been the object of this part of our dissertation. We started from a very elegant linearised toy model introducing in the large aspect ratio limit the physical meaning of the curl of the momentum balance equation. An effective geometrical interpretation has been given of how a non-uniform current density can provide the drive for a relaxation of the axi-symmetric initial magnetic equilibrium.

Consequently, we derived two alternative ways to write the linearised momentum balance equation in convenient variables, namely the Newcomb's equation for the magnetic flux and the Euler's variational equation for plasma displacement. Both have been analytically derived and specialised to some of the most relevant limit cases, namely the straight tokamak limit and the vacuum limit for the Newcomb's equation, yielding Poisson's problem.

Their analytical derivation has been paired with the progressive report of the implementation of a linear-instability solver, dubbed LENS (Linear Euler-Newcomb Solver). This numeric tool will be instrumental to the linear benchmark of the new boundary conditions of the 3D nonlinear simulations code SpeCyl. Convergence studies on both limit cases and manufactured solutions successfully verified solver robustness and sufficient accuracy.

The Euler's equation has been derived in the frame of the Energy Principle, that grants a powerful tool to investigate those instabilities for which the inertial term in momentum balance equation should not be neglected (*e.g.* the ideal kink modes). Despite the drive to the instabilities has an electromagnetic nature, the inclusion of the inertial term (and thus of fluid effects) is a fundamental complement to the magnetic-flux description. This is however not visible from Euler's equation alone, which is derived from the Energy Principle in the assumption that the inertial term $K(\boldsymbol{\xi}, \boldsymbol{\xi}^*)$ brings negligible

99

contribution to the overall variational principle.

In fact, in the simplified limit of the straight tokamak we proved both analytically and numerically that Newcomb's and Euler's equations do actually coincide upon suitable change of variables.

Wide literature on the theory of the ideal external kink in the straight tokamak has been condensed in Sec. 4.1, dealing with three alternative current density profiles: the flat current, the step-function and a more realistic class of profiles studied in [Wesson04]. The step-function profile has been instrumental in highlighting and quantifying the important role of the inertial effects:

- Either Newcomb's or Euler's equation cannot distinguish between a plasma and a current channel.

- Their purely electro-magnetic description should suffice to draw gross stability analysis ($\delta W(\boldsymbol{\xi}, \boldsymbol{\xi}^*) \gtrless 0$), provided that the edge of the plasma is identified with the current-channel width $r_0 < a$.

- Without a correct inclusion of the inertial term, no meaningful quantitative estimate can be given of the eigenvalue ω.

Finally, the tearing modes have been presented. We have derived their dispersion relation almost from first principles in the simplified large aspect ratio limit. This has been done in two operative regimes: one characterised by resistivity dominated dynamics inside the resonant layer, and one considering dominant viscosity. A stability condition has been identified and numerically implemented: its straightforward geometrical meaning has been investigated, also with the aid of our numeric tool.

Part III

Nonlinear MHD simulations with preparatory magnetic boundary formulations

This part of my thesis aims at presenting the state of art of the three-dimensional (3D) MHD nonlinear simulations code SpeCyl [Cappello08].
In Chap. 5 we start with an overview of the work-flow of this code. In particular, Fig. 5.2 presents a very useful flow-chart representing the main loop of SpeCyl's.
Subsequently, we introduce the traditional set of boundary conditions, featuring an ideally conducting wall in direct contact with the plasma edge. The rest of the Chapter presents a benchmark against the linear theory of MHD instabilities, as it was derived in Part II: this is not intended as a validation of an already well established set of BCs, but rather as a first application of the concept we explored throughout Part II in some sort of a "friendly environment".

Chapter 6 presents the first step towards a more realistic formulation of SpeCyl's BCs. This was implemented by Daniele Bonfiglio in 2017 and features a thin resistive shell in direct contact with the plasma. The outer ideal wall is still present, even if displaced at finite distance from the shell: the region between the two shells is treated analytically as vacuum.
We begin this Chapter with a derivation of the well established matching conditions across a thin resistive shell, and by deriving a solution for the magnetic field in the vacuum, complementary to the one we drew from Newcomb's equation in Part II.
Consequently, we present the model equations of this new set of BCs. In doing so, we try to highlight its originality with respect to most of the analogous implementations reported in dedicated literature.
The rest of the Chapter is devoted to a benchmark verification against the linear MHD theory presented in Part II. Unfortunately, we argument that the agreement is quite unsatisfactory and will motivate a major reformulation of the fluid part of the BCs, as is going to be described in Part IV.

5

The SpeCyl code and simulations with a pseudo-vacuum enclosed by an ideal wall

5.1 Main features of the SpeCyl code

SpeCyl is a 3D nonlinear self-consistent MHD simulations tool [Cappello08].
It relies on momentum balance equation and Faraday's and Ohm's laws to
progress the flow and the magnetic field in time, according to a visco-resistive
scheme. In its main version, it assumes no pressure gradients, so that

$$\rho \frac{\partial \boldsymbol{v}}{\partial t} + \rho \boldsymbol{v} \cdot \nabla \boldsymbol{v} = \mathbf{J} \times \mathbf{B} + \rho \nu \nabla^2 v \tag{5.1}$$

$$\frac{\partial \mathbf{B}}{\partial t} = \nabla \times (\boldsymbol{v} \times \mathbf{B} - \eta \mathbf{J}) \, , \tag{5.2}$$

where ρ is the (generally uniform and constant) mass density, $\mathbf{J}$ is self-
consistently obtained as the curl of $\mathbf{B}$, and $\nabla \cdot \mathbf{B} = 0$. All quantities are
normalised and appear in adimensional units. In particular, lengths are
normalised to the plasma minor radius a, the plasma density to the initial
ion density on axis $f_0 m_i$ (f_0 being the initial number density), the mag-
netic field to its initial value on axis B_0, the velocity to the Alfvèn veloc-
ity $v_A = B_0/(\mu_0 f_0 m_i)^{1/2}$, and time to the Alfvèn time $\tau_A = a/v_A$, respec-
tively. In these units, resistivity η corresponds to the inverse Lundquist
number $S^{-1} = \tau_A/\tau_R$ ($\tau_R = \mu_0 a^2/\eta$ being the resistive time-scale) as much
as kinematic viscosity corresponds to the inverse viscous Lundquist number
$M^{-1} = \tau_A/\tau_\nu$ ($\tau_\nu = a^2/\nu$ being the viscous time-scale).
SpeCyl operates in cylindrical geometry, neglecting thus any curvature ef-
fect.
Furthermore it presents a spectral formulation in the periodic coordinates

$\theta \in [0, 2\pi]$ and $z \in [0, 2\pi R]$, meaning that it treats the dependence of physical quantities on poloidal and axial directions in a Fourier space.

During my PhD I had the need to go through the code implementation much more than what would be required for this first Chapter. However, for the sake of avoiding future repetitions, we start with an overview of SpeCyl's work-flow. This is mandatory for the understanding of the next Chapters, that will present the the steps in the implementation of the new set of magneto-fluid boundary conditions (BCs), extending the already present ones.

Moreover, such a long lived code was initially thoroughly documented [Merlin89, Cappello96, Cappello04, Viterbo99], but cumulated many further additions that still lack of a single comprehensive and up to date manual. Far from completing such endeavour, this Chapter and the ones that will follow aim at a first structured reorganization.

5.2   Work-flow of the SpeCyl code

In this section we present the main technical aspects of the implementation of the SpeCyl code. We start from the initial equilibrium, descried in Sec. 5.2.1, then we illustrate the work-flow of the code's main loop in Sec. 5.2.2, and we conclude with the presentation of the ideal-wall formulation of the boundary conditions in Sec. 5.2.3.

5.2.1   Paramagnetic pinch equilibrium

Before starting the main loop, the initial equilibrium is computed from the simulations inputs. The equilibrium assumed is that of a zero-β paramagnetic pinch [Delzanno08], where the following relations hold:

$$\mathbf{J}_0 \times \mathbf{B}_0 = 0 \qquad \text{static equilibrium,}$$
$$\mathbf{E}_0 + \boldsymbol{v}_0 \times \mathbf{B}_0 = \eta \mathbf{J}_0 \qquad \text{Ohm's law,}$$
$$\mathbf{E}_0 = E_0 \, \hat{\mathbf{z}} \qquad \text{axisymmetric loop tension,}$$

being E_0 the loop field, accounting for the presence of toroidal current. Assuming axial symmetry, we recover a one dimensional dependence on the radial coordinate r.

As we saw for Newcomb's equation, excluding pressure from equations implies that there exists some $\lambda = \lambda(r)$, such that $\mathbf{J}_0(r) = \lambda(r)\mathbf{B}_0(r)$.

Applying the scalar product with $\mathbf{B}_0$ onto the Ohm's law and using Faraday's

(a) RFP equilibrium   (b) tokamak equilibrium
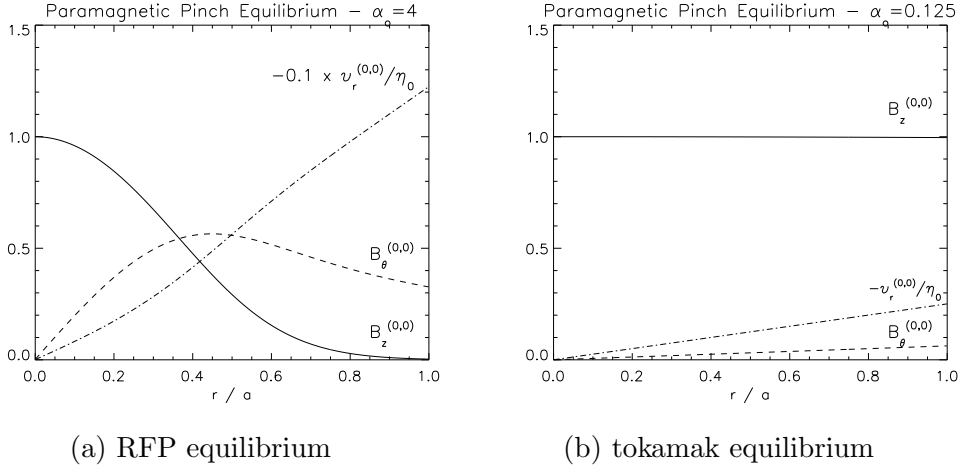
Figure 5.1: Paramagnetic pinch equilibrium main quantities, for $\alpha_0 = E_0/\eta_0 = 4$ (panel (a)), and $\alpha_0 = 0.125$ (panel (b)). Pinch velocity in panel (a) is rescaled by -0.1 for graphical purposes.

law yields

$$\mathbf{B}_0 \cdot \mathbf{E}_0 = B_{0,z}E_0 \equiv \eta \left[-B_{0,\theta}\frac{\mathrm{d}B_{0,z}}{\mathrm{d}r} + B_{0,z}J_{0,z} \right]$$

so that:

$$\frac{\mathrm{d}B_{0,z}}{\mathrm{d}r} = \frac{B_{0,z}}{B_{0,\theta}} \left[-\frac{E_0}{\eta} + \lambda B_{0,z} \right] .$$

We can find λ from $\lambda|B_0|^2 = \mathbf{J}_0 \cdot \mathbf{B}_0 = \mathbf{E}_0 \cdot \mathbf{B}_0$, thus

$$\lambda = \frac{E_0}{\eta} \frac{B_{0,z}}{B_{0,z}^2 + B_{0,\theta}^2} ,$$

whence

$$\frac{\mathrm{d}B_{0,z}}{\mathrm{d}r} = -\frac{E_0}{\eta} \frac{B_{0,\theta}B_{0,z}}{B_{0,\theta}^2 + B_{0,z}^2} , \qquad (5.3)$$

which is a defining condition for the equilibrium toroidal field.

The poloidal magnetic field instead can found from the radial projection of the static equilibrium condition $\mathbf{J}_0 \times \mathbf{B}_0 \cdot \hat{\mathbf{r}} = 0$, and thus

$$B_{0,\theta}^2 = -B_{0,z}^2 + \frac{2}{r^2} \int_0^r r' B_{0,z}^2(r') \, \mathrm{d}r' . \qquad (5.4)$$

By integrating iteratively equations 5.3 and 5.4, for a given value of parameter $\alpha_0 = E_0/\eta$ the equilibrium field is constructed.

Finally, the pinch flow velocity is determined via Ohm's law to be:

$$\boldsymbol{v}_0 = -\frac{\eta J_{0,\theta}}{B_{0,z}}\,\hat{\mathbf{r}}\,. \qquad (5.5)$$

Figure 5.1 shows the three main pinch quantities, achieved through numerical integration of eqs. 5.3-5.5 with appropriate initial conditions, derived in [Delzanno08]:

$$B_{0,z} \sim 1 - \left(\frac{E_0}{2\eta}\right)^2 r^2\,,$$

$$B_{0,\theta} \sim \frac{E_0}{2\eta}r$$

$$v_{0,r} \sim \left(\frac{E_0}{\eta}\right)^2 \frac{\eta r}{2}\,.$$

This equilibrium is also suitable to reproduce the straight tokamak case, since, if we make the usual assumptions that $\varepsilon \to 0$ while $q \sim 1$, since q_0 ends up being

$$q_0 = \frac{2}{R \cdot \alpha_0}\,,$$

the larger R, the smaller α_0 must be. Fig. 5.1.(b) shows a straight tokamak equilibrium in the case of $\alpha_0 = 0.125$: we recover uniform axial magnetic field and vanishing poloidal field and radial velocity.

In simulations, the equilibrium represents the mode $(m, n) = (0, 0)$ since it has no angular modulation.

Before entering the main loop, the initial equilibrium is perturbed with an ad hoc small initial perturbation on some modes of radial velocity, according to user's choice. The perturbation is typically in the shape of

$$\delta\boldsymbol{v} = \sum_{m,n} \frac{\varepsilon}{r} \sin\left(\pi r\right)^{m+2} \cos\left(m\theta + nz/R\right)\hat{\mathbf{r}}\,, \qquad (5.6)$$

where the initial perturbation amplitude ε is given in input.

5.2.2 SpeCyl's main loop

A general working-flow of the SpeCyl's main loop is now presented, also relying on [Merlin89, Viterbo99, Cappello04] and on unpublished notes by Susanna Cappello and Daniele Bonfiglio. A synthetic flow chart is reported in Fig. 5.2. To keep this section as general as possible, we will not discuss here any detail concerning the boundary conditions, which will be the object
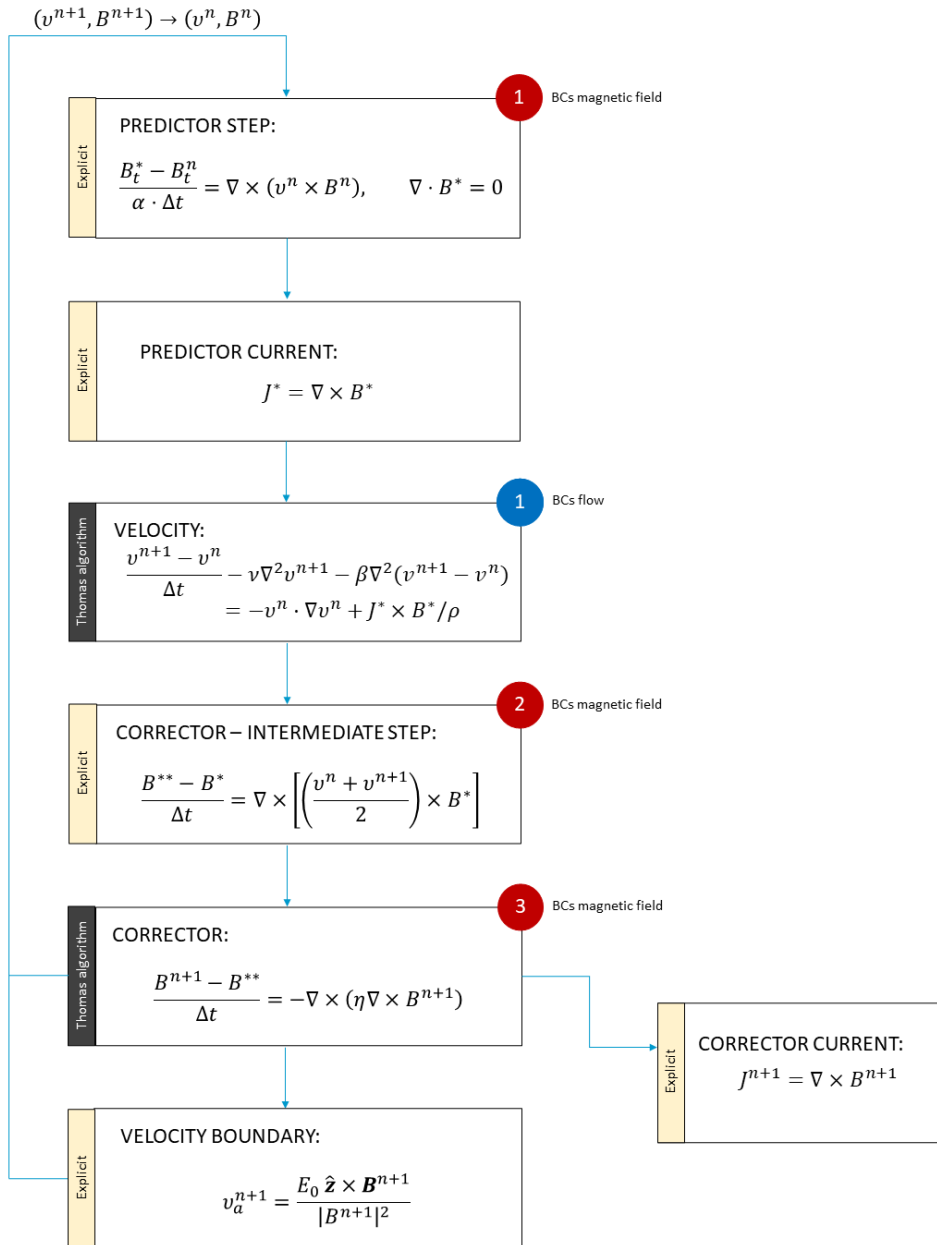
Figure 5.2: Flow chart of SpeCyl working scheme. Numbered circles highlight where boundary conditions are enforced: purple relates to magnetic BCs, whereas blue relates to the flow. The steps in SpeCyl's main loop that are solve explicitly are marked with a yellow band a the tag "explicit", conversely, the steps that are solved implicitly are marked with dark-grey band and the tag "Thomas algorithm".

of Sec. 5.2.3.

The code advances velocity $\boldsymbol{v}$ and magnetic $\mathbf{B}$ fields in time according to a predictor-corrector scheme. The explicit predictor semi-step advances the fields from the preceding time-step t_n to a given fraction of the simulation time resolution Δt (usually, $t^* = t^n + \alpha \cdot \Delta t$, with $0.4 \leq \alpha \leq 0.6$). At this level, resistivity is neglected and the predictor tangential (to the wall) magnetic field $\mathbf{B}_t^* = B_\theta^* \hat{\boldsymbol{\theta}} + B_z^* \hat{\mathbf{z}}$ for each Fourier mode is obtained via the ideal Ohm's law, coupled with the Faraday's law:

$$\begin{cases} \dfrac{\partial \mathbf{B}_t}{\partial t} = -\nabla \times \mathbf{E} \\ \mathbf{E} = -\boldsymbol{v} \times \mathbf{B} \end{cases} \implies \boxed{\dfrac{\mathbf{B}_t^* - \mathbf{B}_t^n}{t^* - t^n} = \nabla \times (\boldsymbol{v}^n \times \mathbf{B}^n)},$$

while the B_r^* is explicitly set so as to fulfil the solenoidal property of the magnetic field:

$$\boxed{\dfrac{\partial(r B_r^*)}{\partial r} = -r \nabla \cdot \mathbf{B}_t^*},$$

where the radial derivative is written as an incremental ratio and an explicit integration of $B_r^*|_r$ is performed using the values of $B_r^*|_{r-\Delta r}$ and $\mathbf{B}_t^*$. Predictor current is also computed for later use, as

$$\boxed{\mathbf{J}^* = \nabla \times \mathbf{B}^*}.$$

Regularity conditions are imposed on axis on both $\mathbf{B}^*$ and $\mathbf{J}^*$ (see [Merlin89]) and the first call of magnetic boundary conditions is made for $\mathbf{B}^*$. It is worth noting that the predictor radial profiles are computed from axis to edge, so that the boundary conditions play no role at this step, if not by setting the outermost value of $\mathbf{B}^*$ and $\mathbf{J}^*$.

Predictor fields are then employed for the implicit computation of the advanced velocity field $\boldsymbol{v}^{n+1}$, enforcing the momentum balance equation:

$$\boxed{\dfrac{\boldsymbol{v}^{n+1} - \boldsymbol{v}^n}{\Delta t} - \nu \nabla^2 \boldsymbol{v}^{n+1} = -\boldsymbol{v}^n \cdot \nabla \boldsymbol{v}^n + \dfrac{1}{\rho} \mathbf{J}^* \times \mathbf{B}^* + \beta \Delta t \nabla^2 \dfrac{\boldsymbol{v}^{n+1} - \boldsymbol{v}^n}{\Delta t}}$$

where ν is intended as the kinematic viscosity and ρ is time-constant mass density. The last term at second member, known as "semi-implicit term", is meant for numerical stability and acts as some kind of an artificial viscosity, affecting acceleration rather than flow: this way, stationary equilibria are unchanged, allowing more freedom in the choice of the time-step [Schnack86]. Unless the previous cases, this equation is quite tougher to write in such a way to highlight the unknown $\boldsymbol{v}^{n+1}$ at one side of the equality: in particular,

the presence of a second order derivative in space, enclosed in the laplacian, introduces a mixed dependence on $\boldsymbol{v}^{n+1}(r)$ evaluated at three different radial positions, separated by the radial mesh resolution of the simulation: $r - \Delta r$, r, $r + \Delta r$.

The implicit resolution of this step is thus linked to the inversion of a three-diagonal matrix of coefficients for each of the three dimentions of cylindrical space. Furthermore, due to the peculiar shape of the cylindrical laplacian, only the axial problem is actually independent from the others, while the radial and the poloidal ones have to be solved together.

Three-diagonal problems can be efficiently solved in terms of the Thomas algorithm. Let us suppose having a simple three-diagonal system of equations:

$$\begin{bmatrix} b_1 & a_1 & 0 & 0 \\ c_2 & b_2 & a_2 & 0 \\ 0 & c_3 & b_3 & a_3 \\ 0 & 0 & c_4 & b_4 \end{bmatrix} \cdot \begin{bmatrix} u_1 \\ u_2 \\ u_3 \\ u_4 \end{bmatrix} = \begin{bmatrix} d_1 \\ d_2 \\ d_3 \\ d_4 \end{bmatrix}$$

where vector $\underline{u}$ in the decoupled case of the axial direction coincides sequentially with each mode of $\boldsymbol{v}_z$, evaluated at time t^{n+1}: various components $\{u_i\}_{i=1,2...}$ identify with progressive radial evaluation, from axis position to plasma edge. The coupled radial-poloidal problem is formally similar, if not that each component of $\underline{u}$ is a two dimensional array, whose components relate to $\boldsymbol{v}_r$ and $\boldsymbol{v}_\theta$, and a_i, b_i, c_i and d_i are also array quantities.

The Thomas approach consists of two steps: the forward and the backward steps. Within forward one, a formal inversion of all equations is performed, from axis to edge, so to highlight $u_1(u_2)$ from the first one, $u_2(u_3)$ from the second one and so on. Inverted matrix coefficients are computed.

By the end of the forward step, the system is such that knowing the last component of vector $\underline{u}$, all the others can be readily computed: this is what happens in the backward step. The edge value of the velocity field components is enforced here and backward propagation ensures that it influences the whole radial profile.

After the predictor and the velocity field computation, the implicit corrector step kicks in, producing a magnetic field time advancement of a whole step Δt from previous time t^n to subsequent time t^{n+1}. This is done via the resistive Ohm's law, again coupled with the Faraday's law:

$$\frac{\mathbf{B}^{n+1} - \mathbf{B}^n}{\Delta t} = \nabla \times \left[\left(\frac{\boldsymbol{v}^{n+1} + \boldsymbol{v}^n}{2} \right) \times \mathbf{B}^* \right] - \nabla \times \left(\eta \nabla \times \mathbf{B}^{n+1} \right)$$

where η stands for plasma resistivity.

Practically, this relation is broken into two parts, relying onto an intermediate

magnetic field $\mathbf{B}^{**}$ which is still evaluated at time t^{n+1} but only considers the first addend of the above formula:

$$\boxed{\frac{\mathbf{B}_t^{**} - \mathbf{B}_t^n}{\Delta t} = \nabla \times \left[\left(\frac{\boldsymbol{v}^{n+1} + \boldsymbol{v}^n}{2} \right) \times \mathbf{B}^* \right]},$$

while the solenoidal property is ensured again by computing $\boxed{B_r^{**} \text{ from } \nabla \cdot \mathbf{B}^{**} = 0}$. As before, on-axis regularity conditions and boundary conditions at edge are enforced for $\mathbf{B}^{**}$. This first corrector intermediate step is solved explicitly, again from axis to boundary.

Then, the corrector step is completed by involving also the second addend of the resistive Ohm's law:

$$\boxed{\frac{\mathbf{B}^{n+1} - \mathbf{B}^{**}}{\Delta t} = - (\nabla \eta) \times \left(\nabla \times \mathbf{B}^{n+1} \right) + \eta \nabla^2 \mathbf{B}^{n+1}}$$

As we can see from the presence of the Laplacian operator, also this step will involve a three-diagonal system and thus the Thomas algorithm again. Hence, in view of the next chapters, it is worth noting that this is the step at which the magnetic boundary conditions can really penetrate into the plasma, throughout the backward solution.

Along with the magnetic field, the corrected value of the current density is computed by means of Ampère's law:

$$\mathbf{J}^{n+1} = \nabla \times \mathbf{B}^{n+1}.$$

This value is not really used in the loop, but is available for possible use. Finally, the edge value of the radial velocity field is computed, as an $E \times B$ drift, as we are about to discuss as soon as we present the boundary conditions, and made ready for the next iteration.

Despite this section presents the equations in the physical space, as mentioned before SpeCyl is indeed a spectral code. This means that each block of the flow-chart in Fig. 5.2 is solved serially for each Fourier mode. The Fourier transform is defined in line with the general notation of the RFP community, which differs from the tokamak community notation (used up to this point in this Thesis, Eq. 3.5) in the sign of n:

$$\mathbf{Q}(r, \theta, z, t) = \sum_{m,n} \mathbf{Q}^{m,n}(r, t) \cdot e^{im\theta + inz/R}. \tag{5.7}$$

From now on we will have to switch to this new convention, for consistency with the code notation.

variable	mesh	
B_r	X_1	
B_θ	X_2	
B_z	X_2	
υ_r	X_1	
$\upsilon\theta$	X_2	
υ	X_2	
J_r	X_2	
J_θ	X_1	
J_z	X_1	
E_r	X_2	(not explicitly computed in SpeCyl)
E_θ	X_1	(not explicitly computed in SpeCyl)
E_z	X_1	(not explicitly computed in SpeCyl)

Table 5.1: Variables relevant to the BCs and associated radial mesh

One last anticipation needs to be done before we can discuss the actual BCs implementation and it regards the radial mesh: in SpeCyl, along with the main mesh X_1, there is an auxiliary mesh X_2 which is staggered with respect to the first one. In other words, while X_1 runs from the axis $(X_1(0) = 0)$ to the plasma edge $(X_1(L_X) = 1)$ in L_X equally spaced points $(\Delta r = 1/L_X)$, X_2 is made of $L_X + 1$ equally spaced points from $X_2(-1) = -\Delta r/2$ to $X_2(L_X) = 1 + \Delta r/2$.

This is convenient for the computation of radial derivatives, since the incremental ratio between $X_1 = \bar{r}$ and $X_1 = r + \Delta r$ is twice as a good an estimate of the derivative in $X_2 = \bar{r} + \Delta r/2$ than it is in $X_1 = \bar{r}$, and vice versa. However, this means that some quantities will be defined on X_1 and some others on X_2: tab. 5.1 reports a short list of the main physical quantities. The electric fields that are not computed in SpeCyl implementation are yet listed, along with the radial mesh they would correspond to.

To confront quantities living on different meshes, they must of course be reported to a same grid. The solution adopted is the linear interpolation: hence, to evaluate *e.g.* $B_z(0)$, we will take it as the average between $B_z(-\Delta r/2)$ and $B_z(\Delta r/2)$.

5.2.3 Ideal wall boundary conditions

The traditional formulation of boundary conditions (BCs) pictured the plasma as in direct contact with an ideal conductor, as reported in Fig. 5.3. In this Thesis we will always refer to them as to "SpeCyl.1" BCs, due to the
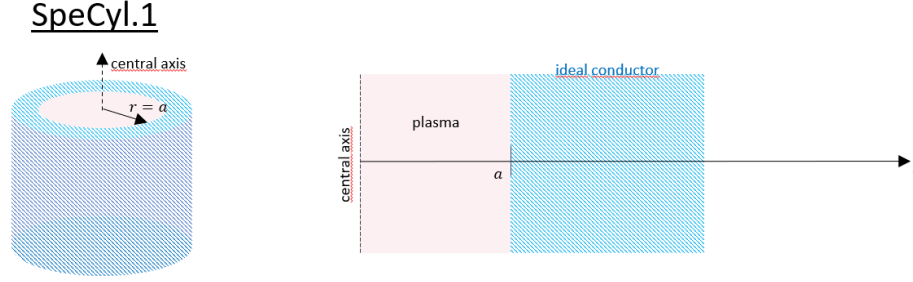
SpeCyl.1

Figure 5.3: SpeCyl.1 Boundary conditions: plasma in direct contact with an ideally conducting wall.

presence of one single (ideal) wall, directly facing the plasma surface. This version of the code was the subject of a nonlinear verification benchmark reported in [Bonfiglio10].

Regarding the flow, the stiffness of the wall along with the no-slip assumption should prevent any edge flow. Anyway, there is the exception of the pinch velocity (Eq. 5.5) which is set to a finite value:

$$v_r^{0,0}(a)\, \hat{\mathbf{r}} = \frac{\left[E_0 \hat{\mathbf{z}} \times \mathbf{B}_\theta^{0,0}\right]_{r=a}}{|B(a)|^2} \ , \tag{5.8}$$

being

$$|B(a)|^2 = \sum_{m,n} \left\{ (B_\theta^{m,n})^2 + (B_z^{m,n})^2 \right\}_{r=a},$$

where the sum is intended over all the simulation's modes. Eq. 5.8 generalises Eq. 5.5 to the case where non-axisymmetric modes of the **B** field are finite and in presence of an ideal wall at a.

Equation 5.8 is computed at the end of the main loop and is fed to the Thomas algorithm for the flow at the beginning of its backwards step. Note that this term is generally negative throughout the simulation, so as to "pinch" axisymmetrically the flow away from the wall.

For the electro-magnetic fields, the BCs are diversified between the equilibrium and the generic mode $(m,n) \neq (0,0)$. In fact, ideal wall conductivity

implies:

$$(m,n) = (0,0) \longleftrightarrow \begin{cases} E_\theta^{0,0}(a) & = 0 \\ E_z^{0,0}(a) & = E_0 \\ B_r^{0,0}(a) & = 0 \end{cases} \tag{5.9}$$

$$(m,n) \neq (0,0) \longleftrightarrow \begin{cases} E_\theta^{m,n}(a) & = 0 \\ E_z^{m,n}(a) & = 0 \\ B_r^{m,n}(a) & = (b_r^{m,n})^{\text{ext}} \end{cases} \tag{5.10}$$

where $(b_r^{m,n})^{\text{ext}}$ accounts for any possible externally applied seed magnetic perturbation (MP), aimed at triggering a specific mode. For what concerns the simulations reported in this chapter, this magnetic perturbation is always set to null.

For what concerns the axisymmetric constraints in Eqs. 5.9, the condition on $E_\theta^{0,0}(a) = 0$ implies the conservation of the toroidal magnetic flux (the ideal wall is hence an effective flux-preserver). Furthermore, it should be highlighted that the condition on the axial electric field is the yield of a recent reformulation, in substitution of the previous condition of $\partial_r B_\theta^{0,0}(a) = 0$ (and thus: $J_z^{0,0}(a) = J_0$, with J_0 assigned and constant throughout the simulation). Apart from the radial edge magnetic field, explicitly assigned in Eqs. 5.9-5.10, all the other components of the magnetic field and of current density are obtained indirectly from the equations above, by matching the electric field components of the plasma to the ones on the wall:

$$0 = E_\theta^{m,n}(a) = \eta J_\theta^{m,n}(a) - v_r^{0,0}(a) B_z^{m,n}(a)\,,$$
$$E_0 = E_z^{m,n}(a) = \eta J_z^{m,n}(a) + v_r^{0,0}(a) B_\theta^{m,n}(a)\,.$$

Expressing the current densities in terms of magnetic field components, via the Ampère's law, we can in fact obtain suitable conditions for the outermost values of each mode of B_θ and B_z.

We report below the example of how the first of this two equations may be rendered in SpeCyl. Writing derivatives as finite differences and interpolating all quantities on the main mesh X_1 we get

$$\eta(a)\frac{B_z^{m,n}(a + \frac{\Delta r}{2}) - B_z^{m,n}(a - \frac{\Delta r}{2})}{\Delta r} = -v_r^{0,0}(a)\frac{B_z^{m,n}(a + \frac{\Delta r}{2}) + B_z^{m,n}(a - \frac{\Delta r}{2})}{2}\,,$$

from which, rearranging terms so as to isolate $B_z^{m,n}(a + \frac{\Delta r}{2})$, we obtain the desired relation, in the shape of

$$\{B_z^{m,n}\}_{a+\frac{\Delta r}{2}} = \mathbb{A}_z \{B_z^{m,n}\}_{a-\frac{\Delta r}{2}} + \mathbb{B}_z$$

for suitable linear coefficients $\mathbb{A}_z$ and $\mathbb{B}_z$. A similar procedure applies for the other equation, with analogous outcome.

These are enforced twice to fix the outermost value of the magnetic field (at predictor step and corrector intermediate step) and once in a much less trivial way, when interfacing with Thomas algorithm. In that case, the inversion of the three-diagonal matrix, performed during forwards step, produces some other linear relations in the form of

$$
\left\{ \begin{matrix} B_r^{m,n} \\ B_\theta^{m,n} \end{matrix} \right\}_{a-\frac{\Delta r}{2}} = \underline{\underline{\mathbb{E}}}_{r,\theta} \cdot \left\{ \begin{matrix} B_r^{m,n} \\ B_\theta^{m,n} \end{matrix} \right\}_{a+\frac{\Delta r}{2}} + \underline{\mathbb{F}}_{r,\theta}
$$

$$
\left\{ B_z^{m,n} \right\}_{a-\frac{\Delta r}{2}} = \mathbb{E}_z \cdot \left\{ B_z^{m,n} \right\}_{a+\frac{\Delta r}{2}} + \mathbb{F}_z
$$

for suitable matrices and arrays of constants. By combining in a system these relations with our BCs for magnetic field components (including the radial one), we can obtain magnetic field evaluation at both $a + \frac{\Delta r}{2}$ and $a - \frac{\Delta r}{2}$, for all modes and all field components. These values are then fed to the backwards Thomas algorithm.

5.3 Benchmark of SpeCyl simulations against linear theory

For the rest of this Chapter, we will present a benchmark study of SpeCyl simulations against linear theory predictions produced through LENS. This is intended as a preliminary study to test on a familiar ground the numerical methods that we must use to approximate the assumptions of the ideal analytical theory. Among them, the absolute lack of viscosity and resistivity cannot be reproduced in the code for numerical stability reasons and needs of course some approximation. Moreover, as seen, SpeCyl model does not explicitly contain the continuity equation, so that the general assumption we made in part II of incompressibility is not to be given for granted, even if $\partial_t \rho = 0$.

Finally, this will be useful to define a starting point, before developing new boundary conditions. We will see in this Chapter what the traditional set of boundary conditions SpeCyl.1 can achieve, also to define its limitations that we wish to overcome with the new set of BCs that we will present starting from the next Chapter.

5.3.1 Numerical set-up for the linear benchmark

Since mass density plays a crucial role in kink stability analysis, we took advantage from the possibility of SpeCyl.1 to be operated with non-homogeneous - yet fixed in time - density profile $\rho(r)$. To render the step-profile in mass density, we imposed a smooth-step radial dependence of the kind:

$$\rho(r) = \left[1 - \alpha_\rho\right] \cdot \left\{\frac{1}{2} - \frac{1}{\pi} \arctan\left[\beta_\rho \cdot (r - a)\right]\right\} + \alpha_\rho, \qquad (5.11)$$

being a the plasma radius and α_ρ, β_ρ profile parameters expressing how tall and how sharp the step is, respectively. Resulting density on axis is $\rho(0) = 1$, while edge density yields $\rho(a) = \alpha_\rho$. Usual values in simulations are $\alpha_\rho = 0.1$ and $10^2 \leq \beta_\rho \leq 10^3$.

Hence, edge density is not null, in contrast with model hypotheses: this results from a trade-off between the requirement of an ideal-MHD (inviscid) plasma and the finite surface tension required to prevent fluid diffusion across the step-like interface. Also, numerical stability prevents density from being exactly zero, since the momentum balance equation contains a term proportional to $1/\rho$.

Step-current profiles instead have been approximated by tailoring the SpeCyl resistivity profile parameters in such a way to produce a central channel of low η, surrounded by a high-resistivity domain, where almost no current flows:

$$\eta(r) = \eta_0 \cdot \left[1 + (\texttt{ALET} - 1)\, r^{\texttt{BEET}}\right]^{\texttt{GAET}}. \qquad (5.12)$$

Profile parameters $\eta(0) \equiv \eta_0$, $\texttt{ALET,}$ $\texttt{BEET}$ and $\texttt{GAET}$ have been adjusted to recreate a current profile like that of [FRS73]:

$$\eta^{\text{FRS}}(r) = \eta_0 \left[1 + \left(\frac{r}{r_0}\right)^{2\lambda}\right]^{1+\frac{1}{\lambda}} \qquad (5.13)$$

that produces a step-profile across $r = r_0 \equiv (\texttt{ALET} - 1)^{2\lambda}$ that is sharper for larger $\lambda \equiv \texttt{BEET}/2$, being $\texttt{GAET} \equiv 1 + 2/\texttt{BEET}$. In the simulations we present hereafter, we have used $\lambda = 40$, thus $\texttt{ALET} = r_0^{-80} + 1$, $\texttt{BEET} = 80$, and $\texttt{GAET} = 1.025$. Different values of r_0 and a have been used to scan on a range of plasma-wall proximities. For numerical requirements, the resulting resistivity profile is cut when it reaches a maximum value, defined arbitrarily as $\eta^{\text{max}} = 100 \times \eta_0$, as represented in the upper half of Fig. 5.4.

Figure 5.4 illustrates for the specific case of $r_0/b = a/b = 0.6$ and $q_0 = 1.3$ the initial equilibrium in SpeCyl.1, as compared to the Shafranov flat-current
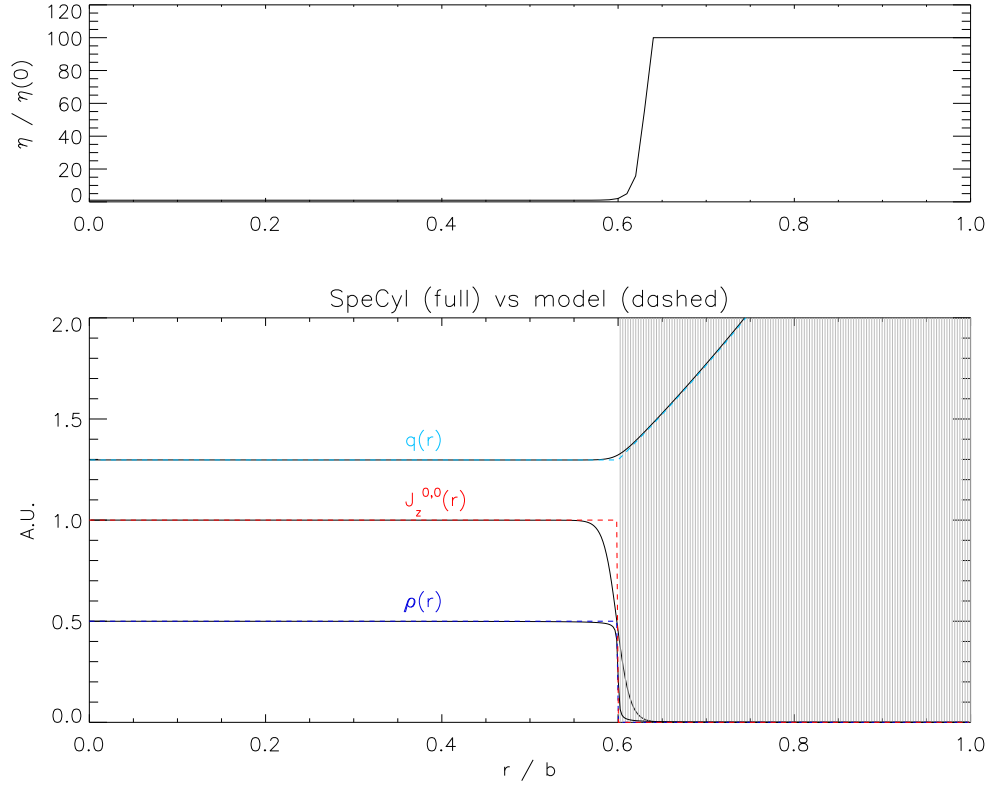
Figure 5.4: Radial profiles of the main equilibrium quantities in SpeCyl and in the flat-current model, according to the chosen numerical set-up: in the upper plot the SpeCyl's resistivity profile is reported. In the lower plot, we report the equilibrium axial current density, the safety factor and the mass density. The shaded region indicates the pseudo-vacuum.

model. There is overall excellent agreement between them, with the exception of a thin transition layer around $r = a$. There, both mass density and (more visibly) current density have a smoother step than what the model prescribes: on the bright side, the relatively smoother current density profile does not spoil the safety factor transition across the plasma edge.

For the study of the external kink, we focused on a single mode, to speed up simulations. This has been chosen as the mode $(m, n) = (2, 1)$, which is the most unstable that also depends on the choice of current profiles. Moreover, the $(2, 1)$ external kink mode has been widely studied experimentally in RFX-mod, operated as a tokamak: its high potential disruptiveness could indeed be suppressed by means of the active magnetic control in this device [Baruzzo11, Marchiori12, Baruzzo12, Zanca12]. Simulations have been
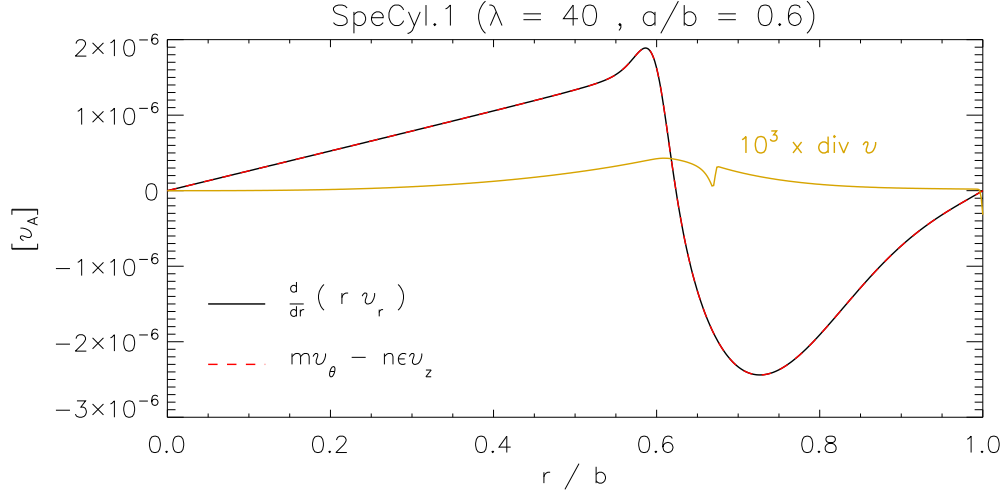
Figure 5.5: Incompressibility of $(m,n) = (2,1)$ external kink mode for the flat current model: the full superposition of the two curves proves that $\nabla \cdot \boldsymbol{v}^{2,1} \approx 0$. For reference, the value of $\nabla \cdot \boldsymbol{v} \sim \mathcal{O}(10^{-10})$ obtained by SpeCyl is reported in orange, magnified by a factor 10^3 to make it visible. Simulation profile parameters are: $\lambda = 40$, $r_0/b = a/b = 0.6$, $\alpha_\rho = 0.1$, $\beta_\rho = 10^2$, $\eta_0 = \nu = 10^{-6}$. Velocities are expressed in units of the Alfvénic velocity v_A.

performed with a superposition of the $(m,n) = (0,0)$ equilibrium state and at least the first two harmonics of the desired mode: $(m,n) = (2,1)$ and $(m,n) = (4,2)$, so that at a certain point a non-linear interaction between resonant modes could kick-in, giving some realistic flavour to the outcome.

5.3.2 Preliminary test of incompressibility

The first test we show is in Fig. 5.5, where the incompressibility of the flow is proved by confronting the real parts of the radial and the angular components of the divergence of the flow. Incompressibility involves the equality:

$$\nabla \cdot v^{2,1} = \frac{1}{r}\frac{\mathrm{d}}{\mathrm{d}r}(rv_r^{2,1}) + \frac{i}{r}\left(2v_\theta - \varepsilon v_z^{2,1}\right) = 0,$$

whence, taking only real parts of both addends (since $\{v_r, iv_\theta, iv_z\} \in \mathbb{R}^3$),

$$\frac{\mathrm{d}}{\mathrm{d}r}(rv_r^{2,1}) = \left[2 \cdot v_\theta^{2,1} - 1 \cdot \varepsilon \cdot v_z^{2,1}\right].$$

In fact, by individually plotting each side of the above equation, for the particular case of the flat current profile, as in Fig. 5.5, it can be seen that they

fully overlap, proving that the theoretical assumption of incompressibility is respected by SpeCyl's simulations. This should not be given for granted, since this condition is not imposed *a priori* in the code's equations.

In fact, the divergence of $\boldsymbol{v}$ is not exactly null in SpeCyl, as seen from the orange curve on the same plot (which is magnified by a factor 10^3 to make it visible), and is in fact a very small term $\sim \mathcal{O}(10^{-10})$. The discontinuity in the orange profile is motivated by the crossing of the resonance radius, where v_r has a vertical asymptote (to linear order).

The driving numerical mechanism that forces SpeCyl's flow to be mostly incompressible in this case-study is unclear for us and should be sought for in an attentive analysis of the model equations in the linear approximation. Anyway, this property seems always verified through the rest of our Benchmark studies against the external kinks and tearing modes, for the rest of this Thesis. This is of course a very convenient result for us, since it motivates the theoretical assumption made, *e.g.*, in the formulation of the Energy Principle, that the flow can be considered as incompressible.

5.3.3 Benchmark of SpeCyl.1 against the external kink (2,1)

Next, we focus on eigenvectors profiles. To do so, we will compare the flow velocity $v^{2,1}$ produced by SpeCyl's simulations with the displacement $\xi^{2,1}$ predicted by theory, as they are in fact expected to be proportional, up to a factor γ.

Figure 5.6 shows the radial eigenfunction ξ_r compared to three radial velocity profiles obtained with SpeCyl, for different values of the Lundquist number S and for large aspect ratio: $R/a = 20$. All quantities are normalised to their values at plasma edge: $\xi_a \equiv \xi_r(a)$ and $v_a \equiv v_r(a)$.

The expected profile is a straight line, which is null at axis and maximum at edge (as given by Eq. 4.5). By confronting the four simulations, we see that the higher the value of Lundquist number S (having fixed $P = 1$), the better the matching to the theoretical expectation inside the plasma region: $0 \leq r \leq a$. This is motivated by the increasing ideal conditions of SpeCyl MHD, as $\eta_0 = \nu \to 0$.

We are not able to make perfect vacuum in SpeCyl.1 simulations, but rather a very low-density, high-resistivity plasma. This is why simulations retain a finite velocity also in the shaded region beyond a, where the theoretical eigenvalue ξ_r would be ill-defined.

It should be noticed that:
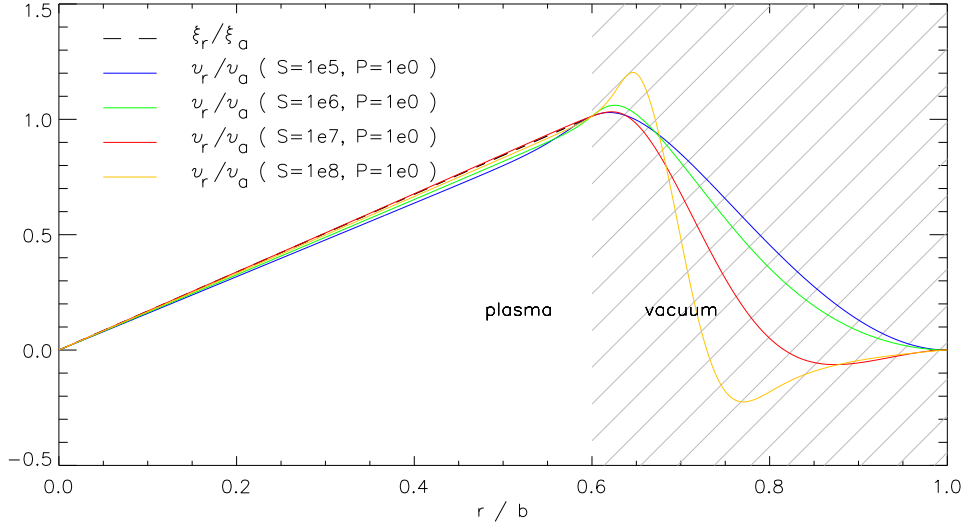
Figure 5.6: Radial eigenfunction for the $(m, n) = (2, 1)$ external mode for the flat-current model, against three different radial velocity profiles produced by SpeCyl with different $S = 1/\eta_0$ and $P = \nu/\eta_0$ values. In all simulations: $R/a = 20$, $q_a = 1.5$, $\lambda = 40$, $r_0/b = a/b = 0.6$, $\alpha_\rho = 0.01$, $\beta_\rho = 10^2$.

a) The sudden drop of current density **J** at plasma edge bends the radial flow profile upwards. This is poorly visible for $S = 10^7$, $P = 1$ (yet present) and stronger in all other cases. It is probably due to the unavoidable smoothness of $\rho(r)$, allowing finite magnetic shear inside a thin layer where density is still present.

b) However, there is a substantial difference between the first two curves, where profile bending spoils the accuracy inside the plasma region, and the latter, where the bending happens outside $r = a$.

c) As stated, SpeCyl vacuum is not perfect, so that the flow retains physical meaning also in this region. It is seen that we pay a price as we enhance core-conductivity: also vacuum conductivity raises. Hence, the two best-fitting solutions for the plasma region come at the cost of a partial flux-freezing in the vacuum region. In fig. 4.2.(d) we saw that mode $(2, 1)$ has finite b_r at resonance, so that flux-freezing condition would imply $\xi_r = -irb_r/F \to \infty$ as F vanishes at resonance. We see that the higher conductivity profiles ($S = 10^7$ and $S = 10^8$) progressively bend towards a vertical asymptote at resonant radius $r_s/b \approx 0.7$.

The consequence of point (c) is that - despite providing a better fit to the
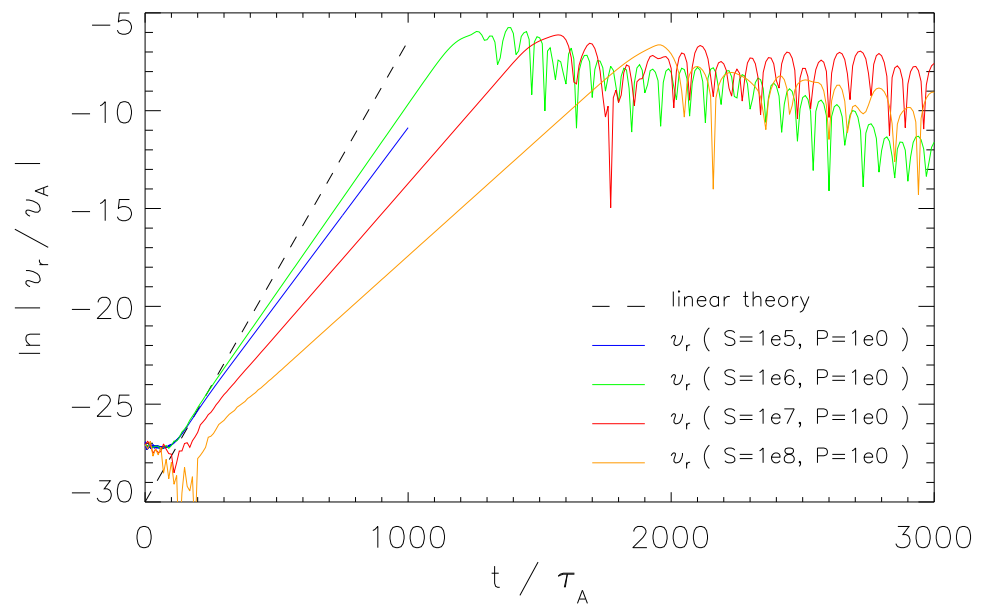
Figure 5.7: Time evolution of mode $(m, n) = (2, 1)$ of various radial velocity profiles produced by SpeCyl with different $S = 1/\eta_0$ and $P = \nu/\eta_0$ values. In all simulations: $R/a = 20$, $q_a = 1.5$, $\lambda = 40$, $r_0/b = a/b = 0.6$, $\alpha_\rho = 0.01$, $\beta_\rho = 10^2$. Velocities are expressed in units of the Alfvénic velocity v_A.

theoretical eigenvalue inside the plasma - the last two cases are not suitable for a benchmark against growth-rates, as the dynamics at resonance radius does now happen on an intermediate time-scale between Alfvèn time and the plasma resistive scale.

In fact, Fig. 5.7 displays clearly that our best shot for a study on growth-rates is the case $S = 10^6$, $P = 1$. The figure shows the exponential growth of $v_r \sim e^{\gamma t}$ for the same values of S and P as in the previous case. We may recognise for each curve the same dynamical pattern in time: the initial perturbation triggers some transient oscillations that are damped on the viscous time-scale. Then, the rapid linear growth brings the mode up to a saturation level (here around $|v_r| \approx 10^{-7}$), where its magnitude matches the same order as the equilibrium velocity (not shown) and that of secondary modes (also not plotted), whose growth has been dragged by the main one through weak non-linear couplings.

For the study of exponential growth-rates of mode $(m, n) = (2, 1)$, we performed a scan over the value of q_a in various SpeCyl.1 simulations. For each of them a fit of $|v_r|$ over the linear-growth time window was performed. It should be highlighted that this procedure involves some freedom, as the fitting domain should be chosen large enough to neglect small noise, but still small enough to cut out nonlinear phases. Nonetheless, good robustness upon small time-domain choice variations was generally achieved, for all unstable cases.

For those values of q_a that are deep in the stable region, many small-amplitude oscillations make the system very sensitive to both fitting-domain span and position in time. Such oscillations are probably related to the purely imaginary eigenvalue ω of simulation modes[1], along with some numerical noise: only in these cases, we arbitrarily decided to put the growth-rate to null, which is what we would reasonably see if we could rid off all observed disturbances.

Figure 5.8 illustrates the result of three sets of SpeCyl.1's simulations, for various ideal wall displacements from the edge of the plasma: the black curve sees almost no wall, so that theory predicts $\gamma \cdot \tau_A / \varepsilon_a \cdot q_a$ to closely resemble the second black curve in Fig. 4.5.(b), while the red and green ones see a much stronger stabilizing effect. On the bright side, we can observe that stability boundaries of our simulations perfectly match the theoretical predictions: this is particularly good news, since energy principle has exact validity only in constraining linear stability. On the dark side, SpeCyl growth rates significantly underestimate the theoretical value, due to the reasons already

---

[1]Reminiscent of one corollary of self-adjointness of δW, yielding that the problem eigenvalue must be either purely real or purely imaginary
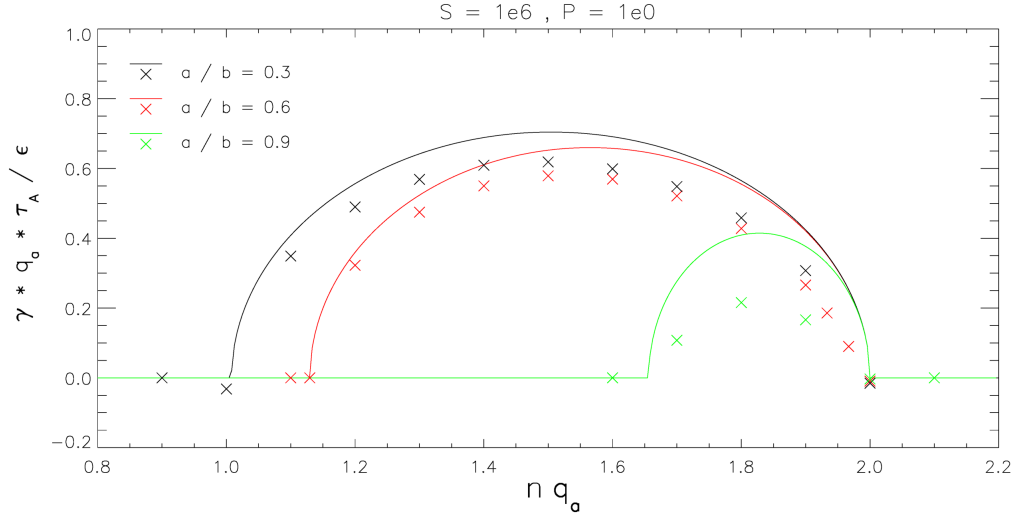
Figure 5.8: Exponential growth-rate of mode $(m, n) = (2, 1)$ predicted by theory (full line) and resulting from single SpeCyl.1 simulations (each marked with an "x"). Colours mark three wall positions b, with respect to density-step radius a. In all simulations: $R/a = 20$, $S = 10^6$, $P = 1$, $\lambda = 40$, $\alpha_\rho = 0.01$, $\beta_\rho = 10^2$.

discussed. It can also be seen that growth rates as a function of $q(a)$ obtained from SpeCyl draw slightly asymmetrical curves, much resembling the effect displayed in Figure 4.5 in presence of finite magnetic shear inside the plasma region: due to density and current profiles Eq. 5.11-5.13 not being perfectly step-function like, there is some unavoidable transition layer in which both quantities shrink but are still finite. In Fig. 4.5 we highlighted how a very small discrepancy between current-channel width and plasma radius may produce relevant effects on the growth-rate predictions.

A final remark should go on the case of $a/b = 0.9$, which shows comparatively larger discrepancy between SpeCyl.1 and theory. This is probably due to the current and mass-density steps being too close the the edge of the integration domain, preventing the required space for an actual vacuum region between plasma-edge and wall.

5.3.4   Benchmark of SpeCyl.1 against tearing modes

Mass density does not play any important role in tearing modes dynamics, hence for the linear benchmark against these instabilities we assumed uniform $\rho = 1$. Also, unlike the external kink, tearing modes cannot be observed with a flat current profile, since no resonance can be intercepted

within plasma region by a flat safety factor profile. Unfortunately, Wesson's profile results particularly cumbersome in this set of boundary conditions, since the relatively flatter decrease of the current profile it prescribes could blur the plasma edge definition if we must keep a small (but finite) current also in the pseudo-vacuum region beyond it.

For this reason, we used another class of current profiles, as in [FRS73]:

$$J_z(r) = \frac{2 r_0 B_{0,z}}{\mu_0} \frac{1}{\left(1 + x^{2\lambda}\right)^{1 + \frac{1}{\lambda}}} \, , \qquad (5.14)$$

$$q(r) = \frac{m}{n} \left(\frac{1 + x^{2\lambda}}{1 + x_s^{2\lambda}} \right)^{1/\lambda} \, , \qquad (5.15)$$

where r_0 is the current-channel width, $B_{0,z} = 1$, $x = r/r_0$, and $x_s = r_s/r_0$ (with $q(x_s) = m/n$).

This is the same profile already used to recreate in the limit of very large λ a step-like current profile in the past section. For the sake of this section, we used a much smoother profile, for $r_0 = 0.81$ and $\lambda = 1$. This roughly coincides with the "peaked" profile of [FRS73] in the case of ideal wall proximity $b/a = 1.2$, explicitly studied on that paper. This is quite a closely-fitting ideal-wall proximity that is expected to produce visible damping on the modes resonating near edge, with respect to the no-wall case. We have nonetheless decided to present it on the basis of two considerations: on the one hand, we know from part II that linear $m = 2$ tearing stability is widely unaffected by a closely fitting ideal shell, if not for modes resonating near the plasma edge; on the other hand, pushing the wall far away from the plasma is quite onerous and wasteful in SpeCyl.1, since the (pseudo-)vacuum region is still included in the simulation domain, yielding the requirement of very large radial meshes, a significant part of which serves to model the uninteresting vacuum region.

For the case of the tearing modes, no significant improvement in the benchmark is found for smaller inverse aspect ratio than $\varepsilon_a = 0.1$. Figure 5.9 shows the good level of achieved compliance to the desired equilibrium.

Figure 5.10.(a) shows the radial profile of the tearing modes eigenfunction as a function of resonance position inside the plasma region. The quantity represented is actually $B_r^{2,1}$, as a proxy for $\psi^{2,1} = -ir B_r^{2,1}$: the full curves are SpeCyl's profiles as taken from the linear growth phase of each simulation and normalised to the value at resonance; the dashed curves are the Newcomb's solver outcomes for the same input parameters. The overall matching we observe is excellent.

In this case, unlike what seen for the external kinks, monotonic improve-
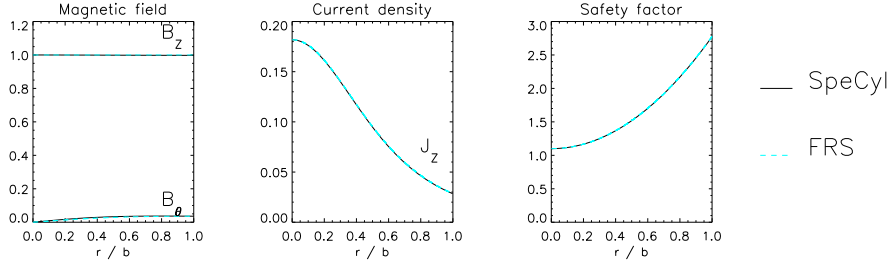
Figure 5.9:   Good compliance between SpeCyl initial equilibrium and the "flat profile" of [FRS73]: $\lambda = 1$, current-channel width $r_0 = 0.81$.

ment of both profiles and growth rates was found with decreasing plasma resistivity and viscosity. This would seemingly confirm that the limit we had in that case was related to the presence of vacuum: in the case of an internal mode, instead, the vacuum region finite conductivity is not so important.

Unfortunately, we still cannot dare pushing the plasma resistivity too low to faithfully model the resistive layer around resonance (since SpeCyl's resistivity is not self-consistent through the simulation, but rather a time-invariant input profile). Also, numerical instabilities produce increasing noise as viscosity is decreased.

The best case study we could achieve is the one reported, with Lundquist number on axis $S = 10^8$ and homogeneous viscous Lundquist number $M = 10^8$ (Prandtl number $P = 1$).

Figure 5.10.(b) reports the growth rates for the same set of simulations as a function of the safety factor at edge. It is seen that modes resonating close by the edge ($q_a \gtrsim 2$) are the least unstable, in agreement to the theoretical prescription. For comparison, the plot includes also the expected theoretical growth rates, coming from both the standard (purely resistive) dispersion relation Eq. 4.17 and the Bondeson-Sobel's visco-resistive one, Eq. 4.22. The latter appears to approximate much more reliably the simulations growth rates: in fact, the critical viscosity defining the range transition between the purely resistive and the visco-resistive regimes ranges for the considered cases from 10^{-11} to $5 \cdot 10^{-11}$. Since $\nu_{\mathrm{SpeCyl}} = 10^{-8}$, we are well inside the domain of application of Bondeson-Sobel's formula.

5.4   Conclusive summary

In this Chapter we initially introduced the 3D nonlinear self-consistent MHD simulations code SpeCyl, which is the main protagonist of this Thesis. The traditional set of BCs used in the code version, here dubbed SpeCyl.1,
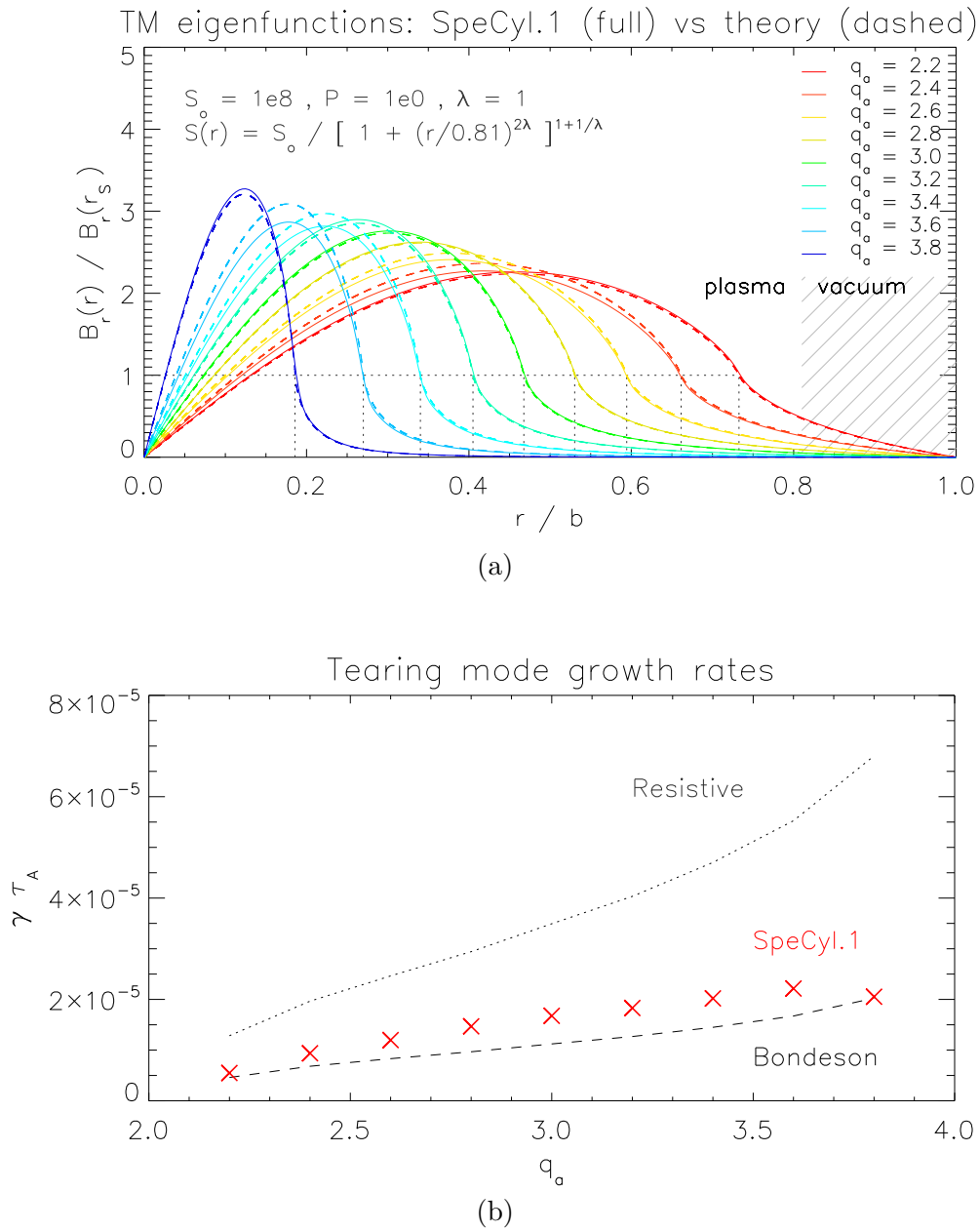
Figure 5.10: Linear benchmark against the predictions of LENS for the tearing mode: (a) SpeCyl.1's $B_r^{2,1}$ against the LENS code eigenvalue $b_r = i\psi/r$ (all quantities are normalised to their value at resonance); (b) SpeCyl.1's growth rates for the same case as in panel (a). Bondeson-Sobel's formula fits better than the resistive one, reported for comparison. Model parameters: $\lambda = 1$, $r_0 = 0.81$, $S_0 = 10^8$, and $P = 1$. $\nu_{crit} \sim 10^{-11} \ll \nu_{SpeCyl} = 10^{-8}$. Solver parameters: $\Delta r = 2 \cdot 10^{-6}$.

features an ideally conducting wall in direct contact with the plasma edge. Nonetheless, ideal wall displacement can be modelled by tailoring the resistivity profile along with the density profile, in giving a variable-size low-current low-density "vacuum" region, whose physical interpretation can be associated to a cold halo surrounding the plasma core.

It is therefore possible to test this set of BCs against external modes, like the external kinks, and internal ones, like the tearing modes. The agreement with theoretical expectations is overall good, even if numerical constraints make difficult to fully reproduce the analytical assumptions usually made in models. Among these, the most impactful is probably the inability of producing an actual vacuum between the plasma edge and the wall. For large "vacuum" regions, the presence of a uniform cold halo - despite its low density - could contribute non-negligibly to radially integrated quantities, like total plasma current or mass, due to its larger radial weight, being more external. For instance, in the flat-current case, with $a/b = 0.3$ and $\rho_{\mathrm{pl}} = 100\rho_{\mathrm{vac}}$ as in our simulations. The mass of the plasma is

$$m_{\mathrm{pl}} = 2\pi R \int_0^{0.3 \cdot b} 100\rho_{\mathrm{vac}} r \, dr = 2\pi R b^2 \cdot 4.5\rho_{\mathrm{vac}} \,.$$

The halo mass is

$$m_{\mathrm{vac}} = 2\pi R \int_{0.3 \cdot b}^{b} \rho_{\mathrm{vac}} r \, dr = 2\pi R b^2 \cdot 0.45\rho_{\mathrm{vac}} \,,$$

which is reliably negligible, but not vanishing.

The other side of the coin is also an important numerical cost in performing distant-wall simulations: since the vacuum region is indeed a cold halo, its computational cost is the same as the plasma region. Its time evolution is still dealt with via the code's equations, yielding a wasteful usage of computing resources. Also, SpeCyl is only equipped with an equally-spaced radial mesh, leading to the requirement of very refined meshes to gain the required resolution in the actual plasma region, while unavoidably refining it also in the halo region.

6

Simulations with a thin resistive shell but axisymmetric boundary flow

In this Chapter we present the first step towards a more realistic set of boundary conditions, consisting in a thin resistive shell in contact with the plasma and an ideal wall placed at finite distance, separated from the resistive shell by a vacuum region. This layout was implemented by Daniele Bonfiglio in 2017, before the beginning of my PhD programme, and the corresponding version of SpeCyl is here dubbed "SpeCyl.2.V00", since the BCs feature two separate walls (the resistive one, facing the plasma, and the ideal one, at finite and tunable distance). The "V00" in the name of this set of BCs, as we will see more in detail, signifies that the boundary conditions are mainly thought in terms of the magnetic field diffusion through the resistive shell, while keeping the same axisymmetric formulation for the fluid part of the edge-plasma behaviour $(v_r(a) = v_r^{0,0}(a))$.

The diffusion of the magnetic field through the resistive shell happens on a time-scale τ_W which is given as an input. $\tau_W \to \infty$ defines the diffusionless case of an ideal wall (thus effectively falling into SpeCyl.1 conditions); $\tau_W \lesssim \tau_A$ gives instant-diffusion and thus a *vacuum-wall*, transparent to the magnetic fields; and every finite τ_W determines the intermediate regime of a plasma-facing resistive wall.

After presenting SpeCyl.2.V00, we will show the outcome of a linear benchmark, which was initially intended as a verification. By setting $\tau_W \lesssim \tau_A$, the resistive wall (RW) can be employed to mimic a free plasma-vacuum interface: external kinks could provide an extremely challenging test to verify the reliability of these BCs, while tearing modes could allow a backup test. In this Chapter we argument how insufficient agreement with the theoretical expectations proves that SpeCyl.2.V00 description was still incomplete and
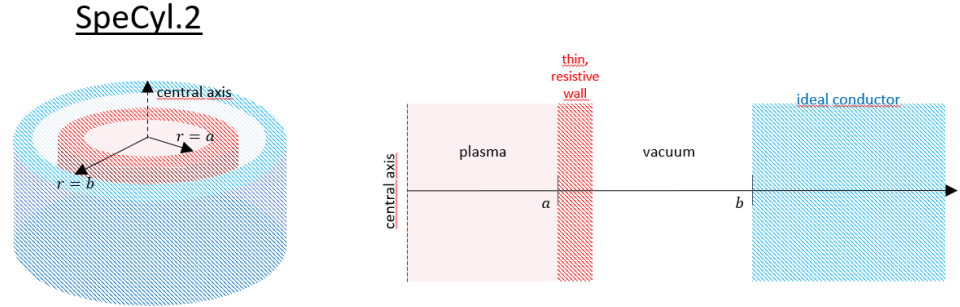
Figure 6.1: RW boundary conditions: a thin resistive shell directly faces the cylindrical plasma in $r = a$, separating it from a vacuum region and an ideal wall at finite, tunable distance, in $r = b$.

motivates a substantial reformulation of the fluid boundary conditions.

6.1 The Resistive-Wall boundary conditions

We present in this section the resistive wall (RW) boundary conditions. A schematic representation of their layout can be seen in Fig. 6.1: SpeCyl's cylindrical plasma is in direct contact with a thin resistive shell at plasma radius $r = a$. The outer ideal wall is displaced at finite, tunable distance, in $r = b$. The region between the two shells is treated as vacuum, analytically solving the Poisson's problem in the domain $a < r < b$.

The idea is to describe the plasma edge as a thin resistive shell [Hender89, Gimblett86, Haines13, Nalesso80] allowing resistive penetration of the magnetic field, on the time-scale defined by the RW time constant τ_W. The magnetic field matching conditions across the resistive shell are presented in subsection 6.1.1, where also τ_W is defined.

Next, in subsection 6.1.2 we present the analytical solution to the vacuum magnetic problem.

In subsection 6.1.3 we present the model equations of SpeCyl.2.V00 BCs.

Indeed, there are many examples in literature of the implementation of similar boundary conditions, leveraging the thin resistive shell approximation. Subsection 6.1.4 gives a quick review of the dedicated literature, also trying to highlight the originality of the SpeCyl's formulation.

6.1.1 Matching conditions across a thin shell

We seek to define a well posed set of boundary conditions for the magnetic field across an infinitely thin resistive shell.

It should be clear that the problem is not resistivity, but rather finite conductivity, allowing for surface currents and thus tangential magnetic field variation across the interface. In contrast, owing to the solenoidal property of $\mathbf{B}$, the normal component must be conserved across the shell

$$[B_r]_-^+ = 0 \,. \tag{6.1}$$

Let the dimensions of our cylindrical shell be the shell radius r_w (which in our case would be plasma radius, a), its radial thickness $2\delta_w$ and its axial length L_w. The thin shell approximation consists in the ordering:

$$\delta_w \ll r_w \ll L_w = 2\pi R \,.$$

Poloidal field matching conditions

The matching condition for the poloidal field component is due to the presence of finite toroidal current on the shell, so that:

$$\mu_0 j_z^{m,n} = (\nabla \times \mathbf{B}^{m,n})_z = \frac{1}{r}\frac{\mathrm{d}}{\mathrm{d}r}\left(rB_\theta^{m,n}\right) - \frac{im}{r}B_r^{m,n} \,.$$

Integration over the poloidal cross section of our thin shell gives the required condition:

$$\int_0^{2\pi} \mathrm{d}\theta \int_{r_w-\delta_w}^{r_w+\delta_w} \mu_0 j_z^{m,n} r \, \mathrm{d}r = \int_0^{2\pi} \mathrm{d}\theta \int_{r_w-\delta_w}^{r_w+\delta_w} \left[\frac{\mathrm{d}}{\mathrm{d}r}(rB_\theta^{m,n}) - imB_r^{m,n}\right] \mathrm{d}r$$

whence, assuming for a thin wall that $B_r^{m,n}(r_w - \delta_w) \approx B_r^{m,n}(r_w + \delta_w) \approx B_r^{m,n}(r_w)$ (Eq. 6.1):

$$2\pi\mu_0 j_z^{m,n} r_w \cdot 2\delta_w = 2\pi\left([rB_\theta^{m,n}]_{r_w-\delta_w}^{r_w+\delta_w} - imB_r^{m,n}(r_w) \cdot 2\delta_w\right) \,.$$

Finally, enforcing thin wall ordering to make the last term vanish and approximating $[rB_\theta^{m,n}]_{r_w-\delta_w}^{r_w+\delta_w} \approx r_w [B_\theta^{m,n}]_{r_w-\delta_w}^{r_w+\delta_w}$ yields:

$$\eta_w j_z^{m,n} = \frac{r_w}{\tau_w}[B_\theta^{m,n}]_{r_w-\delta_w}^{r_w+\delta_w} \,, \tag{6.2}$$

with

$$\tau_w = \frac{\mu_0 \cdot r_w \cdot 2\delta_w}{\eta_w}, \tag{6.3}$$

being η_w the wall resistivity and τ_w the wall resistive-diffusion time constant. In Eq. 6.2, the LHS can be identified with the axial electric field $E_z^{m,n}$ on wall, via the Ohm's law.

Toroidal field matching conditions

For the toroidal field jump, a similar argument holds:

$$\mu_0 j_\theta^{m,n} = (\nabla \times \mathbf{B}^{m,n})_\theta = \frac{in}{R} B_r^{m,n} - \frac{\mathrm{d}}{\mathrm{d}r} B_z^{m,n},$$

yielding

$$2\pi R \mu_0 j_\theta \cdot r_w \cdot 2\delta_w = \int_{r_w - \delta_w}^{r_w + \delta_w} [B_r^{m,n}]_0^{2\pi R} \, \mathrm{d}r - \int_0^{2\pi R} [B_z^{m,n}]_{r_w - \delta_w}^{r_w + \delta_w} \, \mathrm{d}z.$$

Enforcing periodic boundary conditions in the axial direction and rearranging terms, we get:

$$\eta_w j_\theta^{m,n} = -\frac{r_w}{\tau_w} [B_z^{m,n}]_{r_w - \delta_w}^{r_w + \delta_w}, \tag{6.4}$$

where τ_w is still the same of Eq. 6.3. Again, the LHS can be identified with $E_z^{m,n}$ via the Ohm's law.

Together, Eq. 6.2 and 6.4 may be written in a compact form as:

$$\mathbf{E}_{t,w}^{m,n} = \hat{\mathbf{r}} \times [\mathbf{B}_t^{m,n}]_-^+, \tag{6.5}$$

where the subscript "t" refers to the tangential components θ and z.

Radial field time evolution

To complete the analysis, there is still one quantity to be evaluated, which is the time decay of surface currents, on the wall resistive timescale. Faraday's law implies:

$$-\frac{\partial B_r^{m,n}}{\partial t} = \hat{\mathbf{r}} \cdot (\nabla \times \mathbf{E}^{m,n}) = \nabla \cdot (\mathbf{E}^{m,n} \times \hat{\mathbf{r}})$$

Using now equations 6.2 and 6.4 for E_z and E_θ, respectively, yields

$$\nabla \cdot (\mathbf{E}^{m,n} \times \hat{\mathbf{r}}) = \nabla \cdot \left[\left(\underline{\underline{\mathbb{I}}} - \hat{\mathbf{r}}\hat{\mathbf{r}} \right) \cdot \frac{r_w}{\tau_w} [\mathbf{B}^{m,n}]_{r_w - \delta_w}^{r_w + \delta_w} \right]$$

$$= -\frac{r_w}{\tau_w} \left[\frac{1}{r_w} \frac{\mathrm{d}}{\mathrm{d}r} (r B_r^{m,n}) \right]_{r_w - \delta_w}^{r_w + \delta_w}$$

Thus, putting all together,

$$\frac{\partial B_r^{m,n}}{\partial t} = \frac{1}{\tau_w} \left[\frac{\mathrm{d}}{\mathrm{d}r} (r B_r^{m,n}) \right]_{r_w - \delta_w}^{r_w + \delta_w} \tag{6.6}$$

6.1.2   Magnetic fields in the vacuum region

In Part II we once derived the solutions to the cylindrical Poisson's equation for the magneto-static problem in vacuum as a limit case of Newcomb's equation (Eq. 3.21).

We also mentioned that there is yet another way to solve the same problem, using an alternative scalar function. Indeed, the absence of currents in the vacuum region requires (through the Faraday's law) that $\nabla \times \mathbf{B} = 0$, *i.e.* the magnetic field admits a scalar potential ϕ such that $\mathbf{B} = \nabla \phi$. In cylindrical coordinates the Poisson's problem assumes the form of a modified Bessel's equation for each Fourier mode separately (we report below Eqs. 3.29, 3.30):

$$\nabla \cdot \mathbf{B}_0 = \nabla^2 \phi^{0,0} = \frac{1}{r}\frac{\mathrm{d}}{\mathrm{d}r}\left(r\frac{\mathrm{d}\phi^{0,0}}{\mathrm{d}r}\right) = 0\,,$$

$$\nabla \cdot \mathbf{b}^{m,n} = \nabla^2 \phi^{m,n} = \frac{1}{r^2}\left[r\frac{\mathrm{d}}{\mathrm{d}r}\left(r\frac{\mathrm{d}\phi^{m,n}}{\mathrm{d}r}\right) - \left(m^2 + k_n^2 r^2\right)\phi^{m,n}\right] = 0\,,$$

where $k_n = n/R$.

This is a class of differential problem in $\phi^{m,n}$, $\forall\, m, n$, associated to Von Neumann conditions in $r = a$ and $r = b$ (enforcing B_r continuity across the shell, Eq. 6.1):

$$\frac{\partial \phi}{\partial r}\Big|_{r=a} = B_r^{m,n}\big|_a \qquad \text{at plasma edge,} \tag{6.7}$$

$$\frac{\partial \phi}{\partial r}\Big|_{r=a} = 0 \qquad \text{on the ideal wall.} \tag{6.8}$$

We can now discuss three cases:

General case: $(m, k_n) \neq 0$

The general solution is a linear combination of the Bessel functions of the second kind:

$$\phi^{m,n} = \mathcal{A}\,I_m(|k_n|r) + \mathcal{B}K_m(|k_n|r)\,.$$

Complex coefficients $\mathcal{A}$ and $\mathcal{B}$ are determined from Eqs. 6.7-6.8:

$$\mathcal{A}\,|k_n|I_m'(|k_n|) \;+\; \mathcal{B}\,|k_n|K_m'(|k_n|) = B_a^{m,n}\,,$$
$$\mathcal{A}\,|k_n|I_m'(|k_n|b) \;+\; \mathcal{B}\,|k_n|K_m'(|k_n|b) = 0\,,$$

where $B_a^{m,n} \equiv B_r^{m,n}|_a$. Solving for $\mathcal{A}$ and $\mathcal{B}$ then we find:

$$\phi^{m,n} = B_a^{m,n} g_{m,n}(r)\,, \tag{6.9}$$

$$g_{m,n}(r) = \frac{1}{|k_n|}\frac{I_m'(|k_n|b)K_m(|k_n|r) - K_m'(|k_n|b)I_m(|k_n|r)}{I_m'(|k_n|b)K_m'(|k_n|a) - K_m'(|k_n|b)I_m'(|k_n|a)}\,.$$

Hence, the vacuum magnetic field just outside the RW in this case reads (using the RFP community sign convention for the Fourier transform, Eq. 5.7):

$$B_r^{m,n}|_+ = B_a^{m,n}\,,$$

$$B_\theta^{m,n}|_+ = \frac{1}{a}\frac{\partial \phi^{m,n}}{\partial \theta}|_a = B_a^{m,n}\,img_{m,n}(a)\,,$$

$$B_z^{m,n}|_+ = \frac{\partial \phi^{m,n}}{\partial z}|_a = B_a^{m,n}\,ik_ng_{m,n}(a)\,.$$

We compute now, for later use, the tangential magnetic field Fourier components with respect to the radial ones:

$$\Theta_{m,n} \equiv \left[\frac{B_\theta^{m,n}}{iB_r^{m,n}}\right]_+ = mg_{m,n}(a)\,, \tag{6.10}$$

$$Z_{m,n} \equiv \left[\frac{B_z^{m,n}}{iB_r^{m,n}}\right]_+ = k_ng_{m,n}(a)\,, \tag{6.11}$$

and the radial derivative of $rB_r^{m,n}|_+$ just outside the RW:

$$\Delta_{m,n} \equiv \left[\frac{\partial(rB_r^{m,n})}{\partial r}\right]_+ = B_a^{m,n}\left(a|k_n|^2g_{m,n}''(a) - |k_n|g_{m,n}'(a)\right)\,. \tag{6.12}$$

Large aspect ratio (or $n = 0$): $k_n = 0$, $\forall m \neq 0$

As we already discussed in Part II, in the large aspect ratio limit we can approximate the Bessel's functions with the first term in their series expansion: $I_m(x) \approx x^m$ and $K_m(x) \approx x^{-m}$. In fact, our differential equation becomes now

$$r\frac{\mathrm{d}}{\mathrm{d}r}\left(r\frac{\mathrm{d}\phi^{m,0}}{\mathrm{d}r}\right) - m^2\phi^{m,0} = 0\,,$$

whose solution is of

$$\phi^{m,0} = \mathcal{A}r^m + \mathcal{B}r^{-m}\,.$$

Solving again Eqs. 6.7-6.8 for the complex amplitudes $\mathcal{A}$ and $\mathcal{B}$ we get

$$\phi^{m,0} = B_a^{m,0}\,g_{m,0}(r)\,, \qquad g_{m,0}(r) = \frac{a}{m}\frac{(b/a)^m}{1 - (b/a)^{2m}}\left[\left(\frac{r}{b}\right)^m + \left(\frac{b}{r}\right)^m\right]. \tag{6.13}$$

Equations 6.10-6.12 specialise to

$$\Theta_{m,0} = m\,g_{m,0}(a)\,, \tag{6.14}$$

$$Z_{m,0} = 0\,, \tag{6.15}$$

$$\Delta_{m,0} = B_a^{m,0}\left(ag_{m,0}''(a) - g_{m,0}'(a)\right)\,. \tag{6.16}$$

Axi-symmetric (equilibrium) mode: $m = k_n = 0$

Recall from Eq. 3.31 that this case must be treated somewhat more carefully:

$$\phi^{0,0}(r, \theta, z) = \Phi^{0,0}(r) + B_\theta^{0,0}(a) \cdot a\theta + B_z^{0,0}(a) \cdot z \,,$$

so that $\mathbf{B}^{0,0} = \nabla\phi^{0,0}$ complies for $a \leq r \leq b$ with the magnetic equilibrium produced by a cylindrical current distribution (the plasma), immersed in a uniform axial magnetic field (produced by the external coils in all magnetic-confinement devices). On the top of this field, $\Phi^{0,0}(r)$ provides the RW magnetic response for the axi-symmetric mode that we are about to determine.

The Poisson's equation simply reduces to

$$\frac{1}{r}\frac{\mathrm{d}}{\mathrm{d}r}\left(r\frac{\mathrm{d}\phi^{0,0}}{\mathrm{d}r}\right) \equiv \frac{1}{r}\frac{\mathrm{d}}{\mathrm{d}r}\left(r\frac{\mathrm{d}\Phi^{0,0}}{\mathrm{d}r}\right) = 0 \,.$$

Integrating across the vacuum region we get

$$\int_a^b \frac{1}{r}\frac{\mathrm{d}}{\mathrm{d}r}\left(r\frac{\mathrm{d}\Phi^{0,0}}{\mathrm{d}r}\right)r\,dr = 0 \qquad \Rightarrow \qquad b\frac{\mathrm{d}\Phi^{0,0}}{\mathrm{d}r}\Big|_b = a\frac{\mathrm{d}\Phi^{0,0}}{\mathrm{d}r}\Big|_a.$$

However, since at the perfect conductor $B_r^{0,0}(b) = \partial_r\Phi^{0,0}|_b = 0$, this implies $\partial_r\Phi^{0,0}|_a = 0$, *i.e.*, no penetration.
This also implies that $\Phi^{0,0}(r) = 0$ in the vacuum region. Therefore:

$$\Theta_{0,0} \text{ and } Z_{0,0} \text{ are not well defined,} \qquad \Delta_{0,0} = 0. \qquad (6.17)$$

We have thus found out that the axi-symmetric case is not influenced by the resistive shell and will need to be treated separately from the other modes when RW BCs will be defined.

6.1.3 SpeCyl.2.V00 model equations

We are now ready to introduce the SpeCyl.2.V00 boundary conditions. The overall work-flow already presented in the previous chapter is mostly preserved, with some additions.

We start from the fluid BCs since they are the easiest. As for SpeCyl.1 a purely radial, purely axisymmetric "pinch" flow is retained at the edge of the plasma. This is still unchanged from the ideal wall case of SpeCyl.1 (Eq. 5.8):

$$v_r^{0,0}(a)\,\hat{\mathbf{r}} = \left[\frac{E_0\hat{\mathbf{z}} \times \mathbf{B}_\theta^{0,0}}{\sum_{m,n}\left(B_\theta^{m,n}\right)^2 + \left(B_z^{m,n}\right)^2}\right]_{r=a},$$

where the sum is intended over all simulation's modes. This formula involves some deal of approximation: despite the presence of resistive-wall magnetic boundary conditions, the flow does not see any wall electric field but the axisymmetric loop-field E_0, and no radial magnetic field component is considered (as if the flow did still see an ideal-wall boundary). The general assumption is that the flow may play a minor role in the evolution of current-driven instabilities.

Referring to the flow-chart of SpeCyl's main loop (Fig. 5.2), the updated value of the edge velocity is still computed after the corrector step and assigned to the Thomas algorithm for the velocity at the subsequent iteration.

For the electro-magnetic fields, the BCs are still separated between the equilibrium and the non-axisymmetric modes $(m, n) \neq (0, 0)$. In fact, making use of Eqs. 6.1-6.6 for the thin-shell conditions and of Eqs. 6.10-6.17 to relate the vacuum fields outside the RW to $B_a^{m,n} \equiv B_r^{m,n}(a)$, we get

$$(m, n) = (0, 0) \longleftrightarrow \begin{cases} E_{\theta,w}^{0,0} &= 0 \\ E_{z,w}^{0,0} &= E_0 \\ B_r^{0,0}|_a &= 0 \end{cases} \tag{6.18}$$

$$(m, n) \neq (0, 0) \longleftrightarrow \begin{cases} E_{\theta,w}^{m,n} &= -\dfrac{a}{\tau_W}\left[\Theta_{m,n} i B_a^{m,n} - (B_\theta^{m,n})_-\right] \\ E_{z,w}^{m,n} &= \dfrac{a}{\tau_W}\left[Z_{m,n} i B_a^{m,n} - (B_z^{m,n})_-\right] \\ \dfrac{\partial B_r^{m,n}}{\partial t}\Big|_a &= \dfrac{1}{\tau_W}\left[\Delta_{m,n} B_a^{m,n} - \dfrac{\partial(r B_r^{m,n})}{\partial r}\right] \end{cases} \tag{6.19}$$

As a consequence of $B_r^{0,0}(a) = 0$, the axi-symmetric mode sees no resistive penetration of the magnetic field, and thus its magnetic BCs are still the same as before, with the ideal wall facing the plasma.

As it was already in SpeCyl.1, for the tangential magnetic field components we impose that the tangential plasma electric field at boundary (obtained through the resistive Ohm's law) matches the electric field on the wall:

$$E_{\theta,w}^{m,n} = E_\theta^{m,n}(a) = \eta J_\theta^{m,n}(a) - \upsilon_r^{0,0}(a) B_z^{m,n}(a) \,,$$
$$E_{z,w}^{m,n} = E_z^{m,n}(a) = \eta J_z^{m,n}(a) + \upsilon_r^{0,0}(a) B_\theta^{m,n}(a) \,.$$

Expressing the current densities in terms of magnetic field components, via the Ampère's law, we can in fact obtain suitable conditions for the outermost values of each mode of B_θ and B_z, except that this time also $E_{\theta,w}^{m,n}$ and $E_{z,w}^{m,n}$ depend on the magnetic field (both tangential and radial).

The adopted scheme leverages the already present predictor-corrector time-stepping. Recall from Fig. 5.2 that the magnetic BCs are enforced three

times throughout the main loop: the first time to fix the edge values of the predictor field; then to fix the edge value of the corrector intermediate step; finally to set the initial conditions for the backwards integration of the Thomas algorithm in the corrector step.

1&2) At predictor step and corrector intermediate step, the edge value of the radial-**B** is not evolved and its prior-step value is used to determine the tangential components through

$$\eta \nabla \times (B_r^{m,n}\hat{\mathbf{r}} + \mathbf{B}_t^{m,n}) - \upsilon_r^{0,0}\hat{\mathbf{r}} \times \mathbf{B}_t^{m,n} = \frac{a}{\tau_W}\hat{\mathbf{r}} \times [\mathbf{B}_t^{m,n}]_-^+,$$

where the term at second member is alternatively $\left[\Theta_{m,n} i B_r^{m,n} - (B_\theta^{m,n})_-\right]$ or $\left[Z_{m,n} i B_r^{m,n} - (B_z^{m,n})_-\right]$, $B_r^{m,n}$ being evaluated a the prior time-step.

3) At corrector step the full magnetic BCs are enforced, starting from the one for B_r. The updated value of this component is then used to compute the corrector-step values of the tangential components, in the way just shown.

6.1.4 The originality of SpeCyl's RW BCs

Similar boundary conditions have already been implemented on several MHD numeric codes, such as DEBS [Paccagnella07], NIMROD [Becerra16], XTOR-2F [Marx17], and M3D [Strauss04]. In all these, the resistive shell is typically intended as a physical wall having finite conductivity: in most cases the edge radial flow velocity is set to null, since the wall is impenetrable, with the exception of NIMROD, where a physically informed finite radial "wall velocity" is also present.

In the coupling of the code JOREK with the linear stability code STARWALL [Merkel15, McAdams14], in the vacuum region between the plasma surface (S_1) and an outer ideal conductor (S_3), a multiply-connected thin resistive shell (S_2) is implemented. STARWALL provides the magnetic response of resistive/conductive structures outside the plasma, generating a boundary condition for JOREK at plasma-vacuum interface S_1. There, a purely radial flow velocity is assigned either in the form of a Dirichlet condition or of a von Neumann condition.

A significantly different approach is pursued in M3D-C1 [Ferraro16], where the (finite-thickness) resistive wall and external vacuum region are included in the computational domain, enforcing $\boldsymbol{\upsilon} = 0$ BCs on the outer ideal conductor.

In the above mentioned studies, when dealing with free-boundary instabilities, a pseudo-vacuum region is typically enforced at the edge of the plasma, either to simulate a "cold and sparse plasma" region between the hot core and an impenetrable wall, or to mitigate possible numerical issues arising from some mild inconsistencies in the "free interface" boundary conditions. Despite achieving good performance in linear and nonlinear benchmarks, this looks like an unsatisfactory solution from both the numerical and the conceptual points of view.

The implementation in SpeCyl, on the other hand aims at reproducing a fully self-consistent description of a free interface, both penetrable by the magnetic field and by the flow velocity. The resistive shell in thus not only intended as a physical wall, but possibly also as the boundary of the plasma domain. This implementation would bring the twofold advantage of greater simulations speed and of decoupling some relevant physical quantities, such as the edge value of mass and current density from numerical requirements of BCs consistency.

Despite the natural choice of the time constant of such an interface is that of a instantly penetrable "vacuum-wall" [Hender89] $\tau_W \lesssim \tau_A$, larger values could also be used to account for a closely-fitting resistive (or even ideal, for $\tau_W \to \infty$) structure.

Finally, it is important to mention that an independent implementation of analogous boundary conditions is being developed in the 3D nonlinear MHD code Pixie3D [Chacón04, Bonfiglio10].

6.2   Limit cases for evolution time much longer and much shorter than τ_W

A first test for our new set of boundary conditions is presented in this section. In fact, Eq. 6.6 conceals a geometric property which is much alike to the tearing mode stability. After all, the quantity Δ' is indeed very similar to the second member of Eq. 6.6. This condition says that the magnetic field across the thin layer will evolve in such a way to minimise its slope imbalance between the two regions.

The physical reason for this is of course that this slope imbalance in the radial magnetic field translates into a discontinuity of $\mathbf{B}_t^{m,n} \propto (rB_r^{m,n})'/r$ (owing to the solenoidal property) across the RW, that needs being sustained by the image currents on the shell. The finite resistivity will then slowly damp these currents, on the resistive-penetration time-scale τ_W.
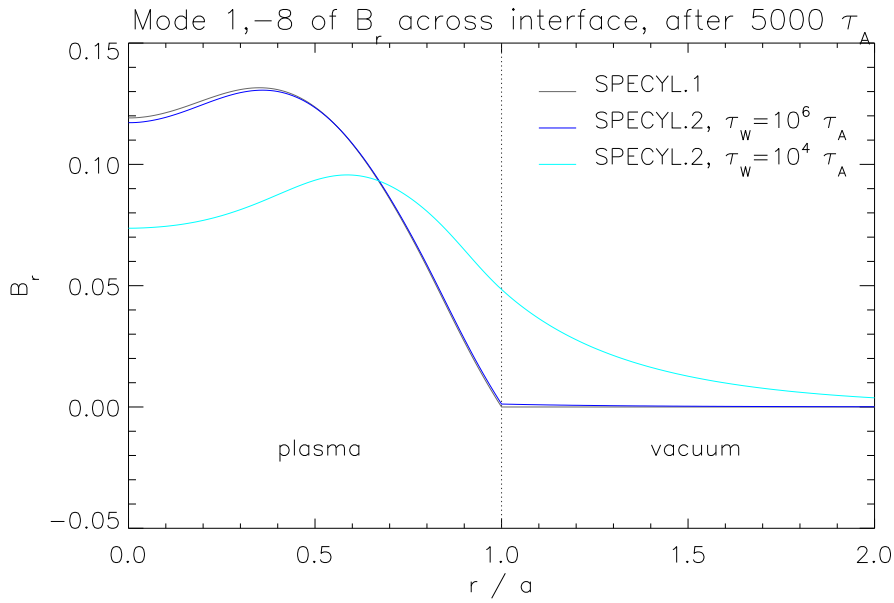
Figure 6.2: Radial magnetic field $B_r^{1,-8}$ for the marginally resonant kink mode $(1, -8)$, plotted across the plasma interface: SpeCyl.2.V00 gives the solution in the plasma region, while the vacuum counterpart is computed analytically with IDL built-in Bessel's functions. If the simulation time Δt_{sim} is much longer than τ_W, B_r is smooth across the RW. The ideal wall case of SpeCyl.1 is retrieved for $\Delta t_{\text{sim}} \ll \tau_W$.

Figure 6.2 illustrates this property: it reports three different simulations the final saturation of a marginally resonating kink mode in reversed-field pinch geometry. This case study will be explored in depth in Chap. 9. The first simulation is obtained with an ideal wall at plasma interface, through SpeCyl.1; the other two simulations are produced with SpeCyl.2.V00, with a very far-displaced ideal wall ($b/a = 10$), and for two different values of τ_W. For the first case (blue in the figure) the evolution time of the simulation is quite smaller than the resistive-shell time-constant: $\Delta t_{\mathrm{sim}} \ll \tau_W$. For the second case (cyan in the figure), $\Delta t_{\mathrm{sim}} > \tau_W$, but still not too much, so that the final saturated state of the simulation is still quite similar.

The radial profile across the interface is rendered by matching the processed simulation profile of $B_r^{1,-8}$ with the analytical solution for the radial component of the magnetic field (see Sec. 6.1.1).

Indeed we observe that when the simulation is long enough to see several characteristic times (here, $\Delta t_{\mathrm{sim}} = 50 \, \tau_W$), the radial profile of $B_r^{1,-8}$ across the interface (dotted vertical line) gets actually smooth, whereas if $\Delta t_{\mathrm{sim}} \ll \tau_W$ we almost retrieve the limit case of an ideal wall at plasma edge.

6.3 Numerical benchmark against the ideal kink

We present in this section the outcomes of the benchmark of SpeCyl.2.V00 against the ideal MHD external kink $(2,1)$, in tokamak geometry. As we will see, this resulted in poor agreement with the analytical theory, mainly because of the remaining constraint on the velocity boundary response. However, before presenting our results, we start with the numerical set-up.

6.3.1 Numerical set-up

Since we aim at describing the plasma-vacuum interface with our RW, we assume here and for the rest of this Chapter a short time constant for the RW wall ($\tau_W = \tau_A$), and a uniform profile for the mass density: $\rho(r) \equiv \rho_0$. A scan was performed on the value of τ_W, finding no macroscopic difference between $\tau_W \approx \tau_A$ and $\tau_W \ll \tau_A$. Also, to keep low complexity, the stabilising ideal wall was set to a very distant radius $b = 10$, large enough to neglect completely its action.

We could successfully reproduce both the flat-current profile (Eq. 4.2-4.4) and the more realistic Wesson's profile (Eq. 4.11-4.12), as described for SpeCyl.1,
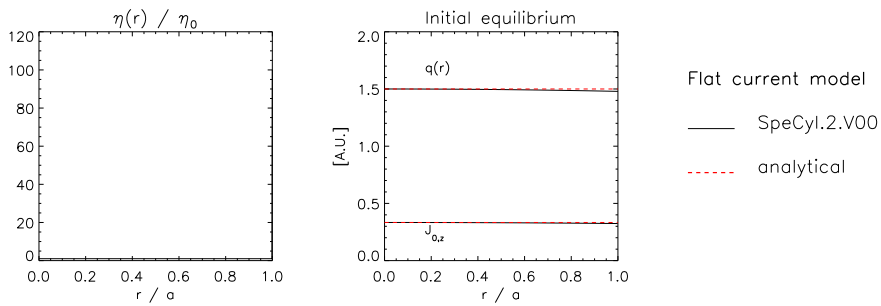
(a) Shafranov's flat-current equilibrium.
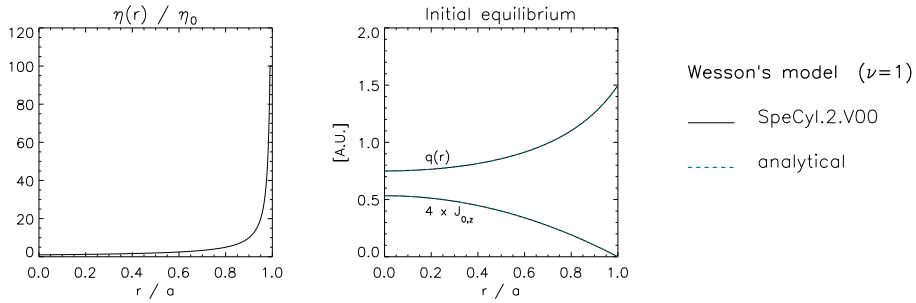
(b) Wesson's equilibrium for $\nu = 1$

Figure 6.3:   Initial equilibria for the numerical benchmark.

by shaping the resistivity profile. Recall from Eq. 5.12 that

$$\eta(r) = \texttt{ETA0} \cdot \left[1 + (\texttt{ALET} - 1)\, r^{\texttt{BEET}} \right]^{\texttt{GAET}}.$$

To obtain the flat current profile, we set $\texttt{ALET} = 1$ and $\texttt{GAET} = 0$, while, for the Wesson's profile:

$$\eta^{\text{Wess}}(r) = \eta_0 \left[1 - \left(\frac{r}{a} \right)^2 \right]^{-\nu}, \tag{6.20}$$

with $a = 1$, is rendered by setting $\texttt{ALET} = 0$, $\texttt{BEET} = 2$, and $\texttt{GAET} = -1$. This poses some numerical issues, since such a resistivity profile should be singular in $r = 1$. This problem is overcome by setting a maximum value for edge resistivity $\eta_{\max}$, and redefine η such that:

$$\begin{cases} \eta(r) = \eta^{\text{Wess}}(r) & \text{if } \eta^{\text{Wess}}(r) \leq \eta_{\max}, \\ \eta(r) = \eta_{\max} & \text{if } \eta^{\text{Wess}}(r) > \eta_{\max}. \end{cases}$$

The value of $\eta_{\max}$ is empirically set at $\eta_0 \times 100$.

Apart from this, the initial equilibrium and the general set-up is the same as the one presented in Sec. 5.3.1.
Figure 6.3 reports the initial equilibria for our numerical benchmark and their relative resistivity profile. The agreement with the equilibria prescribed by the models is completely satisfying.

6.3.2 Numerical results

The linear benchmark against the external kink mode $(2, 1)$ could not produce but very unsatisfactory results.

We started from the Shafranov's flat-current model, which is predicted to be the most unstable by the linear theory. Yet, SpeCyl's simulations could not find it unstable at all, for any initial equilibrium with $1 \leq q_a \leq 2$.
The direct observation of $v_r^{2,1}$ and $B_r^{2,1}$ radial profiles in Fig. 6.4 suggests that the strong simplification in the fluid boundary conditions has important drawbacks on the global shape of the eigenfunction. While the magnetic field linear perturbation follows quite well the theoretical profile (small detachment at the edge is probably motivated by finite resistivity effects), the radial flow perturbation departs significantly from the expectations in a transition layer that roughly spans over the outermost $10\,\%$ of the radial domain. This is a symptom of a competition between the dynamics in the hot core of
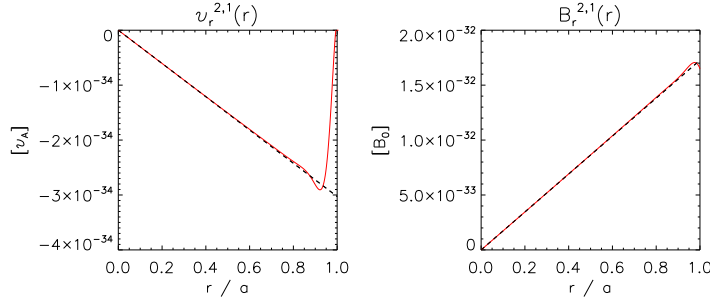
Figure 6.4: Shafranov's flat-current eigenfunctions: SpeCyl (solid red) is almost indistinguishable from the model prediction (dashed black) concerning the radial magnetic field perturbation $B_r^{2,1}$ and most of the velocity perturbation $v_r^{2,1}$ profile. Some inconsistency in the fluid boundary conditions reveals in $0.9 < r/a < 1$. Velocity and magnetic field are expressed in SpeCyl's units: $v_A = a/\tau_A$ and $B_0 = |\mathbf{B}|_{t=0}$.

the plasma (that seems to behave in accordance with the linear theory) and the fluid BCs that seem to inhibit the mode's growth.

The linear benchmark against Wesson's current model produced little more promising results, at first. In fact, stability analysis found a narrow unstable domain for $q_a \lesssim 2$.
Figure 6.5 reports the radial profile of the flow perturbation $v_r^{2,1}$ of one of such unstable simulations. Once more we can observe the formation of a transition layer (shaded in the figure) between the hot core of the plasma, where the theoretical profile visibly emerges, and the BCs that once more act as a "braking force".
A full stability analysis is reported in Fig. 6.6.(a). We see that modes keep being unstable even for $q_a > 2$, suggesting that the unstable mode has in fact a partially resistive nature (since it can get unstable even with an internal resonance). Also the growth rate, much lower than theoretically expected, seems to suggest that the time-scale is not Alfvènic.
It appears that the instability domain is globally shifted to higher values of q_a. Panel (b) shows the safety-factor profile of the first unstable mode ($q_a \approx 1.8$): it is interesting to notice that the theoretical value for the lower instability boundary is intersected by $q(r)$ at the entrance of the transition layer. Similar considerations apply also to the higher instability boundary.
The transition-layer at boundary seems thus to produce an effect similar to pseudo-vacuum. Indeed, the deviation of $v_r^{2,1}$ from the ideal MHD profile breaks locally the linearised flux-freezing relation (Eq. 3.35): $-irB_r^{2,1} \propto$
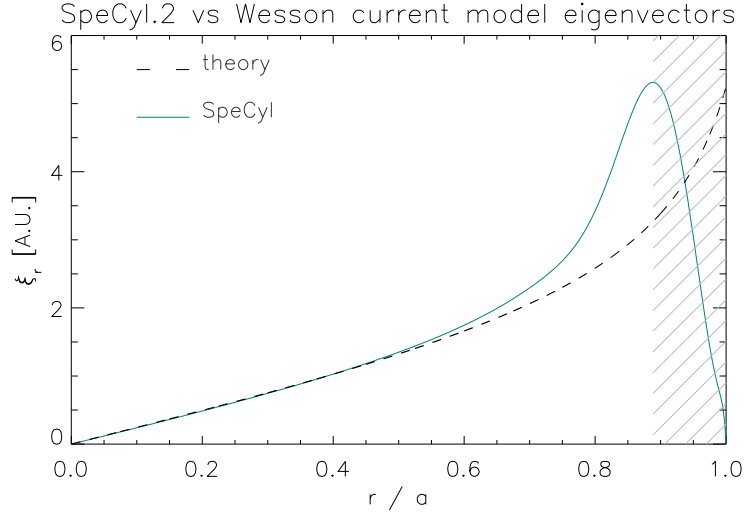
Figure 6.5: Benchmark of SpeCyl.2.V00's radial velocity profile to the theoretical eigenvector ξ_r, for $q_a = 1.9$, $R/a = 4$, $S = 10^5$, $P = 1$. We find a "resisitive" boundary region where SpeCyl.2 departs significantly from the expected eigenfunction.

$Fv_r^{2,1}$. Thus, it effectively acts as a "resistive-layer" produced by the boundary conditions, as discussed in [Hender89].

As a matter of fact, all the unstable simulations presented here have relatively low plasma conductivity: $S = 10^5$, $P = 1$. The attempt of raising the conductivity to $S = 10^8$ produced no unstable modes for $q_a \leq 2$.

6.4   Numerical benchmark against tearing modes

For the numerical benchmark against the tearing mode $(2,1)$ we enforced the same numerical set-up as for the kink mode $(2,1)$ with the Wesson's current model.

Figure 6.7 reports our results: it is visible that the magnetic field penetration through the RW is producing finite $B_r^{m,n}|_a$ in fair agreement with the linear eigenvalue produced by the Newcomb's solver. As for the case of SpeCyl.1, we found increasingly good agreement between SpeCyl.2.V00 and the linear theory as we increase S and P. For the simulations presented here, $S = 10^8$ and $P = 10^4$. Smaller values for the Prandtl number were also attempted, but are not reported as simulations tend to be very noisy for such small viscosities.

Panel (b) presents the growth rates: once more, as for SpeCyl.1, the Bondeson-
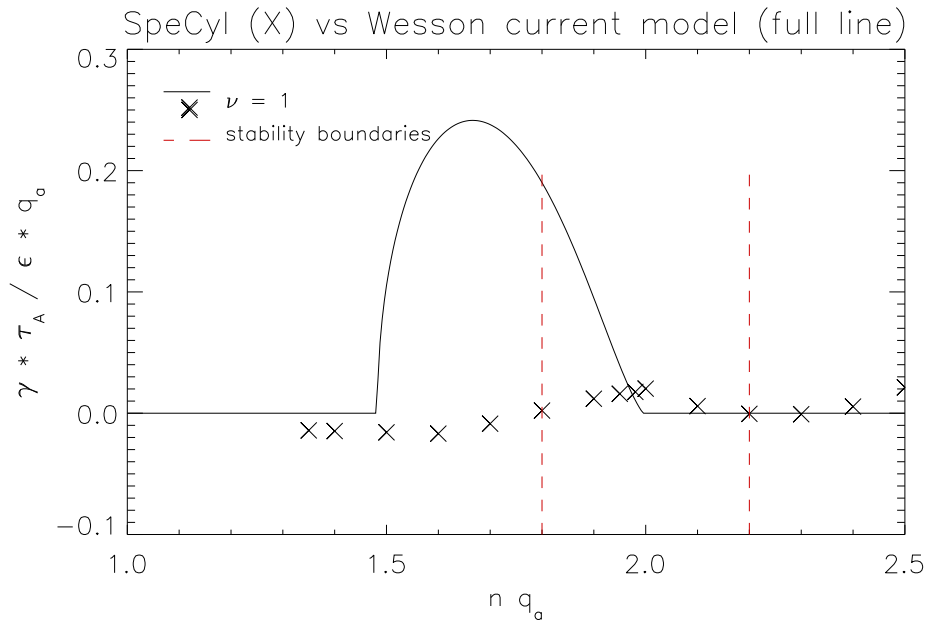
(a) Growth rates of SpeCyl.2.V00 against theoretical prediction. Two vertical lines mark the empirical instability region, which appears to be shifted with respect to the expectation. SpeCyl's growth rates greatly underestimate the theoretical predictions.
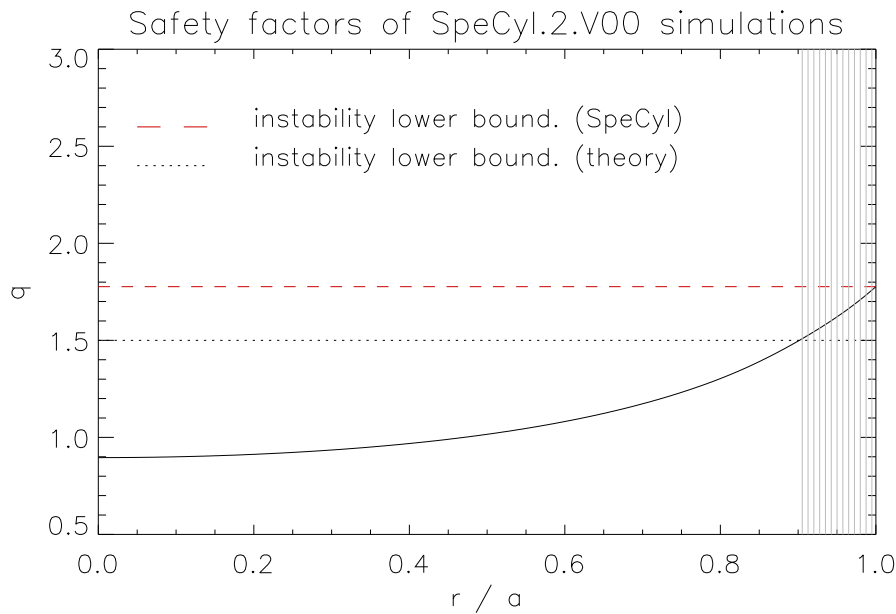
(b) Safety factor profile for the first unstable kink mode (left-side red dashed line in panel (a)). The shift from SpeCyl's lower instability boundary and the theoretical one roughly corresponds to the radial span of the resistive boundary in Fig. 6.5.

Figure 6.6: Benchmark of SpeCyl.2 against the linear theory of the external kink $1, 2$, with a Wesson's current distribution ($\nu = 1$) and for $R/a = 4$, $S = 10^5$, $P = 1$, and $\tau_W = \tau_A$.

Sobel dispersion relation seems to describe more accurately the SpeCyl.2.V00's behaviour (in fact $\nu_{\text{SpeCyl}} \approx 10^{-4} \ggg \nu_{\text{crit}} \approx 10^{-11}$). However this time the numerical growth rates are more poorly captured by either dispersion relation, despite their general trend is correct, plummeting as the resonance sinks inside the plasma.

6.5   Conclusive summary

We have presented the resistive wall boundary conditions, that are a first valuable step in the direction of a more realistic description of the plasma boundary. To do this, we preliminarily reviewed the well known analytical theory of the thin shell approximation and solved the Poisson's magneto-static problem in vacuum.

An overview of the specific implementation of SpeCyl.2.V00 boundary condition was given, to document for the first time this set of boundary conditions in a structured way.

We also produced a quick overview of the literature dedicated to similar implementations in other codes. In doing this, we highlighted the original and ambitious aim set by my supervisors for these new boundary conditions. In fact, unlike most of the dedicated literature, the resistive shell is not only intended as an impenetrable wall, but also possibly as a free interface between the plasma and the surrounding vacuum. The main advantages of this approach, if successful, would be twofold: on the one hand we would not need enforcing a computationally unfavourable pseudo-vacuum region at plasma edge; on the other hand, avoiding the pseudo-vacuum region could be more instructive, in the view of "doing things well". In fact, the pseudo-vacuum has the effect of displacing the BCs enforcement to a position where the flow has no impact. This means that the small inconsistencies in the implemented model lose relevance, are concealed rather than corrected.

The benchmark against the linear MHD instabilities resulted in insufficient agreement, and yet produced some promising results: in particular, we have shown the good agreement between SpeCyl and the two initial classes of equilibria mainly used throughout this Thesis, and the overall reliability of SpeCyl.2.V00 in reproducing the magnetic boundary conditions. The latter was evident from the radial profile of $B_r^{2,1}$, displayed in Fig. 6.4, and from the good agreement between SpeCyl and the Newcomb's eigenfunctions, especially at plasma edge, for the case of the tearing mode $(2,1)$.

The mismatch in the growth rates, particularly stressed in the external kink case study, is the symptom of some major inconsistency in this set of boundary conditions and it seems natural to ascribe it to the strong assumptions
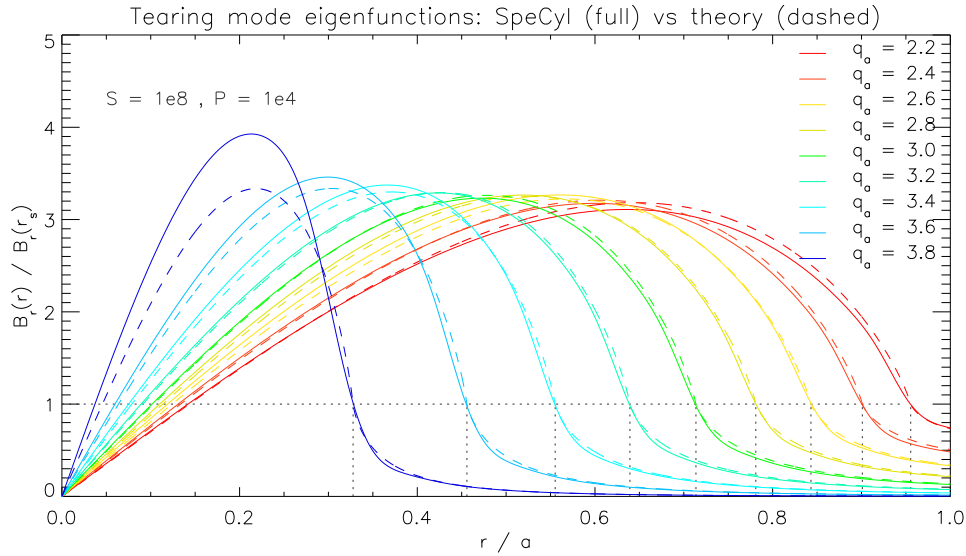
(a) Benchmark of SpeCyl.2.V00's $B_r^{2,1}$ against the linear instability code eigenvalue $b_r = i\psi/r$. All quantities are normalised to their value at resonance.
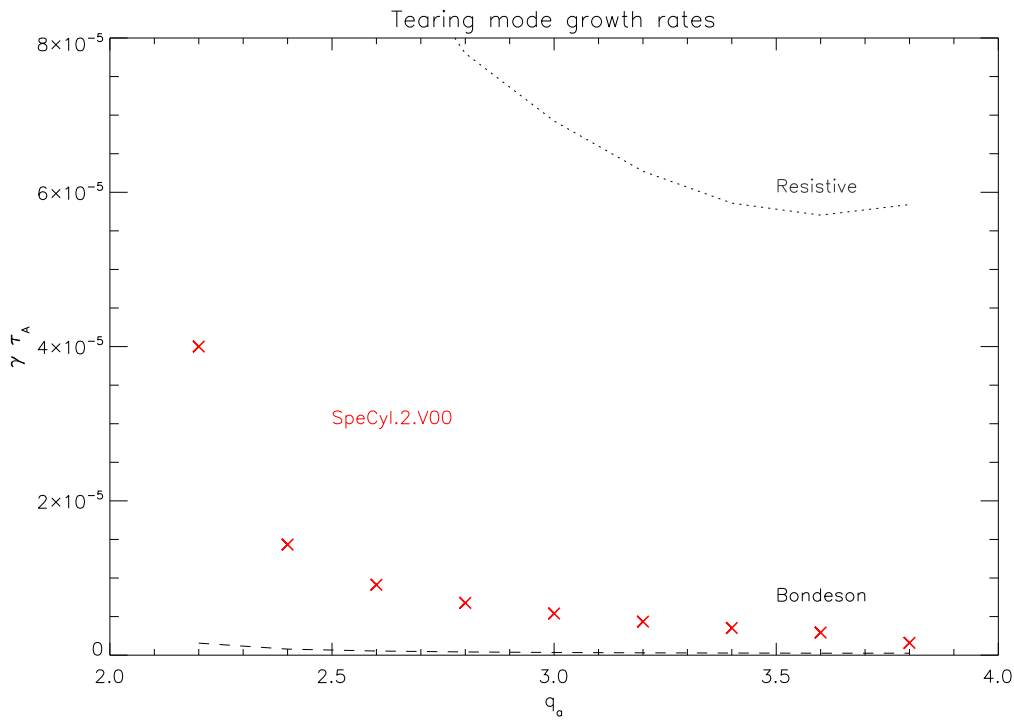
(b) Benchmark of SpeCyl.2.V00's growth rates for the same case as in panel (a). Bondeson-Sobel's formula fits better than the resistive one, reported for comparison.

Figure 6.7: Linear benchmark against the Newcomb's solver for the tearing mode. Model parameters: $\nu = 1$, $R/a = 20$, $\tau_W = \tau_A$, $b = 10$, $S_0 = 10^8$, and $P = 1$. $\nu_{\text{crit}} \sim 10^{-11} \ll \nu_{\text{SpeCyl}} = 10^{-4}$. Solver parameters: $\Delta r = 2 \cdot 10^{-6}$.

that this model makes on the flow velocity. Among these assumptions the main ones are that the edge flow is purely radial and axi-symmetric, and that it does not see the finite resistivity of the wall.

Conclusive summary of Part III

Part III has introduced the state of art of the code SpeCyl when I started my PhD, in 2019. In particular, two alternative sets of boundary conditions were present: SpeCyl.1, featuring a single ideal wall in direct contact with the plasma, and SpeCyl.2.V00, where the plasma faces a thin resistive shell and is surrounded by vacuum and by an outer ideal wall at tunable distance. In Chap. 5 we gave a rich overview of the work-flow of the SpeCyl code. If on the one hand this is instrumental to the comprehension of all the next Chapters, it is also a valuable starting point in the reorganisation of various sparse notes into a well-structured and updated user guide into this code.

Consequently, SpeCyl.1 BCs have been presented. A nonlinear benchmark against the linearised theory of MHD current-driven instabilities has been proposed, to test preliminarily the needed numerical approximations on a safer ground, before repeating the same verification with the SpeCyl.2.V00 BCs. Indeed, both the external kink mode and the tearing mode case-studies produced reasonably good agreement with the theoretical models, both concerning the shape of the problem eigenfunctions and concerning the growth rates.

For the external kink we studied a flat-current profile, enforcing a high-resistivity, low-density region (dubbed pseudo-vacuum) between the hot core of the plasma and the wall. By tuning the width of this region, we could also operate a scan on the ideal wall proximity. However, finite resistivity and mass-density in the pseudo-vacuum region, due to computational requirements, marginally spoiled the agreement in the stability analysis. Furthermore, the pseudo-vacuum approach results particularly cumbersome when the wall position is far from plasma edge.

Tearing modes were reproduced using a smooth equilibrium current distri-

bution, as in [FRS73]. Also in this case, a good agreement was achieved, both concerning eigenvectors and stability analysis, particularly when using the Bondeson-Sobel dispersion relation.

In Chapter 6, we have introduced the resistive wall formalism, widely present in literature. All model equations have been derived from first principles. A solution of the Poisson's magneto-static problem has been presented, complementary to the one already derived from Newcomb's equation in Part II.

Consequently, we have presented SpeCyl.2.V00 BCs, the first step towards a self-consistent and realistic description of the plasma boundary. This is a flexible set-up that aims at reproducing either a physical resistive wall at plasma boundary or a free plasma-vacuum interface, leveraging the thin-shell matching conditions.

The nonlinear benchmark against linear theory of MHD current-driven instabilities has produced unsatisfactory results: in particular, in the modelling of a free interface we assist to the formation of a resistive boundary domain in the outermost $10\,\%$ of the radial coordinate, in which the plasma velocity fluctuations shrink to zero, to meet the axi-symmetric assumption on the edge flow, also departing from the theoretically frozen-in magnetic flux.

Such a behaviour is the symptom of an inconsistency in the formulation of SpeCyl.2.V00 BCs that needs to be addressed. From a review of the main critical assumptions in the model behind the present formulation, it emerges that the major ones are related to the purely axi-symmetric condition on the edge flow and the approximation that the velocity boundary does not depend on the non-axisymmetric electric field fluctuations that are present on the thin resistive shell, in direct contact with the plasma.

This motivates a major reformulation of the fluid boundary conditions, which will be the subject of the next two Chapters.

Part IV

New magneto-fluid BCs: formulation and implementation

Part IV and Part V together present the bulk of my research activity. In this Part IV we describe the formulation and implementation of the new set of boundary conditions. In the next Part V a rigorous nonlinear verification will follow.

In quest for the formulation of a three-dimensional edge flow, inclusive of non-axisymmetric edge fluctuations, the first difficulty to be faced results from the spectral implementation of the SpeCyl code in the periodic variables θ and z. In particular, all the products in the physical space are mapped by the Fourier transform into highly nonlinear convolutions of modes along both the azimuthal and the axial coordinate. This is already dealt with in SpeCyl, where several equations already contain products to be evaluated explicitly.

The real complication however arises when our model equations contain the inverse operation of the product, as in the case of the $(\mathbf{E} \times \mathbf{B})/B^2$ drift equation that we leverage for the velocity boundary. In the real space, this is simply sorted as a fraction between real numbers: in the Fourier space, we need a deconvolution technique to isolate the unknown terms in the equations and evaluate them implicitly.

This problem was totally absent in the previous axi-symmetric implementation of the edge flow and is the topic of Chap. 7. In this first Chapter, an original deconvolution technique, allowing semi-implicit evaluation of the velocity boundary terms, is presented and tested. In order to reduce the problem complexity, the implementation in Chap. 7 considers the simplified ideal-wall boundary conditions for the magnetic part. A final nonlinear verification benchmark is presented between this formulation of SpeCyl and the independent (non-spectral) 3D MHD code Pixie3D [Chacón04, Chacón06, Chacón08], in the common ideal-wall limit of their boundary conditions.

The full implementation, comprehensive of both the realistic thin-shell magnetic description and of the 3D edge flow is presented in Chap. 8. The result is a flexible and self-consistent set of boundary conditions that constitutes a synthesis of all the previous implementations (which are retrieved as limit cases).

The key to the final excellent verification presented through Part. V is the strong attention paid to ensuring complete self-consistency in its formulation: this is fostered by a preliminary analytical re-derivation of all the hidden assumptions contained in the model and by some additional numeric devices that are also presented at the end of Chap. 8.

7

Preliminary study with ideal wall and non-axisymmetric boundary flow

7.1 The newly implemented deconvolution technique

The fist step towards the implementation of a full-spectrum magneto-fluid set of boundary conditions is to understand and face the problem presented by convolutions of modes in SpeCyl code. This section aims at presenting this problem, along with the solution we found to it, and the final implementation of a new and more complete set of boundary conditions for the ideal-wall case.

As already mentioned, SpeCyl's fully spectral implementation maps every product into a nonlinear convolution of modes. This renders highly nontrivial isolating one specific mode of, *e.g.*, the magnetic field from one of the $\boldsymbol{v} \times \mathbf{B}$ products contained in the model of our BCs. On the other hand, separating the unknowns of an equation is essential for the semi-implicit resolution approach described through all Part III.

This problem is completely absent in the case of a purely axi-symmetric edge velocity since, as we will see, in that case the convolution in $\boldsymbol{v} \times \mathbf{B}$ at the boundary collapses into a trivial single term, which is linear in $\mathbf{B}$.

For the same reasons, also the edge value for the velocity field gets very intricate when a full-spectrum edge flow is considered.

We start this section with an introduction to the convolutions theorem, to explain how is it that Fourier transform maps physical-space products into convolutions. Next, we suggest a matrix-based reformulation of convolutions, which we think is particularly effective to visualise the problem. This reformulation constituted the key to the implementation of the new deconvolution

technique.

We conclude illustrating the actual formulation and implementation of the resulting new set of BCs in the case of the ideal wall directly facing the plasma.

7.1.1 Convolution theorem

One fundamental property of the Fourier transform is the so-called convolution theorem, which states the following:

Theorem 1. Every product in the real space is mapped into a convolution in the Fourier space.

Proof. We are interested in the case of discrete Fourier transform, mapping the dependence on a continuously varying angle θ into a discrete wavenumber m, such that:

$$A(\theta) = \sum_{m=-\infty}^{+\infty} \hat{A}_m \, e^{im\theta} \qquad , \qquad B(\theta) = \sum_{m=-\infty}^{+\infty} \hat{B}_m \, e^{im\theta}$$

$$\hat{A}_m = \frac{1}{2\pi} \int_0^{2\pi} A(\theta) \, e^{-im\theta} \mathrm{d}\theta \qquad , \qquad \hat{B}_m = \frac{1}{2\pi} \int_0^{2\pi} B(\theta) \, e^{-im\theta} \mathrm{d}\theta$$

where the hatted quantities signify the Fourier transform of the unhatted ones.

It is now easy to show that a convolution in the Fourier space is indeed a product in the physical one:

$$\sum_{m_s=-\infty}^{+\infty} \hat{A}_{m-m_s} \, \hat{B}_{m_s} = \sum_{m_s=-\infty}^{+\infty} \frac{1}{2\pi} \int_0^{2\pi} A(\theta) \, e^{-im\theta+im_s\theta} \, \hat{B}_{m_s} \mathrm{d}\theta$$

$$= \frac{1}{2\pi} \int_0^{2\pi} A(\theta) \left[\sum_{m_s=-\infty}^{+\infty} \hat{B}_{m_s} \, e^{im_s\theta} \right] e^{-im\theta} \, \mathrm{d}\theta$$

$$= \frac{1}{2\pi} \int_0^{2\pi} A(\theta) B(\theta) \, e^{-im\theta} \, \mathrm{d}\theta$$

$$\equiv \mathcal{F}\left[A(\theta) \cdot B(\theta) \right]$$

$\square$

The generalization to the case where the angles are more than one is quite straightforward.

7.1.2 The matrix formulation of discrete convolutions

Let us now pay a closer look to the convolution product in the case of discrete Fourier transform of a single angle θ. As we said:

$$\mathcal{F}\left[A(\theta) \cdot B(\theta)\right] = \sum_{m_s=-\infty}^{+\infty} \hat{A}_{m-m_s} \hat{B}_{m_s} = \hat{C}_m \qquad (7.1)$$

where $\hat{C}_m$ is just a convenient name for result of the convolution product. A very good way to visualize this product is to settle in the space of wavenumbers and consider the above as the usual row-by-column scalar product between the square matrix $A(m_s, m)$ and the column vector $B(m_s)$. For the sake of simplicity, let us fix an upper and lower bound to our space: $-M \leq m \leq M$, so that, computing the value of $m - m_s$ for each (m_s, m) component of A, we get

$$\underline{\underline{A}} \cdot \underline{B} = \underline{C}$$

with

$$\underline{\underline{A}} = \begin{bmatrix}
\hat{A}_0 & \hat{A}_{-1} & \dots & \dots & \hat{A}_{-M+1} & \hat{A}_{-M} & 0 & \dots & \dots & 0 & 0 \\
\hat{A}_1 & \hat{A}_0 & \hat{A}_{-1} & \dots & \dots & \hat{A}_{-M+1} & \hat{A}_{-M} & 0 & \dots & \dots & 0 \\
\hat{A}_2 & \hat{A}_1 & \hat{A}_0 & \hat{A}_{-1} & \dots & \dots & \hat{A}_{-M+1} & \hat{A}_{-M} & 0 & \dots & 0 \\
\dots & \dots & \dots & \dots & \dots & \dots & \dots & \dots & \dots & \dots & \dots \\
\hat{A}_{M-1} & \dots & \dots & \hat{A}_1 & \hat{A}_0 & \hat{A}_{-1} & \hat{A}_{-2} & \dots & \dots & \hat{A}_{-M} & 0 \\
\hat{A}_M & \hat{A}_{M-1} & \dots & \dots & \hat{A}_1 & \hat{A}_0 & \hat{A}_{-1} & \dots & \dots & \hat{A}_{-M+1} & \hat{A}_{-M} \\
0 & \hat{A}_M & \hat{A}_{M-1} & \dots & \dots & \hat{A}_1 & \hat{A}_0 & \hat{A}_{-1} & \dots & \dots & \hat{A}_{-M+1} \\
\dots & \dots & \dots & \dots & \dots & \dots & \dots & \dots & \dots & \dots & \dots \\
0 & \dots & 0 & \hat{A}_M & \hat{A}_{M-1} & \dots & \dots & \hat{A}_1 & \hat{A}_0 & \hat{A}_{-1} & \hat{A}_{-2} \\
0 & \dots & \dots & 0 & \hat{A}_M & \hat{A}_{M-1} & \dots & \dots & \hat{A}_1 & \hat{A}_0 & \hat{A}_{-1} \\
0 & 0 & \dots & \dots & 0 & \hat{A}_M & \hat{A}_{M-1} & \dots & \dots & \hat{A}_1 & \hat{A}_0
\end{bmatrix}$$

$$(7.2)$$

and

$$\underline{B} = \begin{bmatrix}
\hat{B}_{-M} \\
\hat{B}_{-M+1} \\
\dots \\
\dots \\
\hat{B}_{-1} \\
\hat{B}_0 \\
\hat{B}_1 \\
\dots \\
\dots \\
\hat{B}_{M-1} \\
\hat{B}_M
\end{bmatrix} \quad , \quad \underline{C} = \begin{bmatrix}
\hat{C}_{-M} \\
\hat{C}_{-M+1} \\
\dots \\
\dots \\
\hat{C}_{-1} \\
\hat{C}_0 \\
\hat{C}_1 \\
\dots \\
\dots \\
\hat{C}_{M-1} \\
\hat{C}_M
\end{bmatrix}$$

Even if SpeCyl implementation uses the explicit summation formula of Eq. 7.1 to evaluate convolutions, this compact matrix form on modes space will become a very handy formalism in understanding their general properties, in view of producing the new set of BCs. From the explicit calculation of the *convolution matrix* $\underline{\underline{A}}$ coefficients reported above, we can draw some fundamental considerations:

Property 3 (Band matrix). $\underline{\underline{A}}$ is a band matrix, the central diagonal assuming only the value A_0. Also, it presents two "sidebands" of zeros, such that $\hat{C}_m$ is the sum of $2 \times M + 1 - m$ finite addends, $\forall$ allowed m.

Property 4 (Decomposition). The convolution matrix can always be decomposed in two parts having different roles:

$$\underline{\underline{A}} = \hat{A}_0\,\underline{\underline{\mathbb{I}}} + \underline{\underline{\langle A \rangle}}$$

$\underline{\underline{\mathbb{I}}}$ being the identity matrix on modes space.

a) $\hat{A}_0\,\underline{\underline{\mathbb{I}}}$ has a *non-shuffling* effect on Fourier modes, that linearly maps each m-th mode of $\underline{B}$ into the corresponding m-th mode of $\underline{C}$ through a scaling factor $\hat{A}_0$: $\hat{C}_m = \hat{A}_0\hat{B}_m$.

b) $\underline{\underline{\langle A \rangle}}$ has a *shuffling* effect on Fourier modes, that maps a linear combination of all the modes $\hat{B}_{p \neq m}$ into $\hat{C}_m$, for all m.

Property 5 (axi-symmetric velocity case). In the limit case in which only the axi-symmetric part of $\hat{A}$ is finite, the convolution matrix reduces to its "non-shuffling" part and the convolution product becomes:

$$\underline{C} = \hat{A}_0\,\underline{\underline{\mathbb{I}}} \cdot \underline{B} = \hat{A}_0\,\underline{B}$$

$\underline{\underline{\mathbb{I}}}$ being the identity matrix on modes space.

This is the case of, *e.g.*, the boundary $\boldsymbol{v} \times \mathbf{B}$ products in the assumption of purely axi-symmetric velocity: in this analogy, $\boldsymbol{v} = \boldsymbol{v}^{0,0}\underline{\underline{\mathbb{I}}}$ and $\mathbf{B}^{m,n} = \underline{B}$.

The generalization of this matrix formalism to the case with two continuously varying angles $(\theta, \phi = z/R)$, mapped into two discrete wavenumbers (m, n) by the Fourier transform (as it is in SpeCyl), is achieved by establishing an ordering rule, such to map the two dimensional set of modes into a one dimensional variable j. The convolution product would now read

$$\mathcal{F}\left[A(\theta, \phi) \cdot B(\theta, \phi)\right] = \lim_{M \to \infty} \lim_{N \to \infty} \sum_{m_s=-M}^{+M} \sum_{n_s=-N}^{+N} \hat{A}_{(m-m_s),(n-n_s)}\hat{B}_{m_s,n_s} \quad (7.3)$$

and we may thus set such an ordering rule that:

$$
\begin{aligned}
\left\{ \hat{A}_{0,0} \ldots \hat{A}_{0,N} \right\} &\rightarrow \left\{ \hat{A}_{j=0} \ldots \hat{A}_{j=N} \right\} \\
\left\{ \hat{A}_{1,-N} \ldots \hat{A}_{1,+N} \right\} &\rightarrow \left\{ \hat{A}_{j=N+1} \ldots \hat{A}_{j=3N+2} \right\} \\
&\ldots \\
\left\{ \hat{A}_{M,-N} \ldots \hat{A}_{M,+N} \right\} &\rightarrow \left\{ \hat{A}_{j=N(2M-1)+M} \ldots \hat{A}_{j=M(2N+1)+N+1} \right\}
\end{aligned}
\tag{7.4}
$$

with the additional property that the simultaneous change of sign of both m and n flips the sign of index j:

$$
j(-m,-n) = -j(m,n)
\tag{7.5}
$$

As a matter of fact, this same ordering rule is already implemented in SpeCyl and is dubbed `JANZ`. The only difference from the notation we use here is that `JANZ`$(0,n) > 0$ when $n < 0$, and vice versa, for historic reasons. In this section we stick to the notation just presented in Eqs. 7.4-7.5.
This way, retaining finite (though arbitrarily large) M and N, the two summations in Eq. 7.3 collapse into one:

$$
\sum_{j_s=-J}^{+J} \hat{A}_{j-j_s} \hat{B}_{j_s} = \hat{C}_j \quad \leftrightarrow \quad \underline{\underline{A}} \cdot \underline{B} = \underline{C}
\tag{7.6}
$$

and the problem can be effectively treated as one-dimensional, with a convolution matrix in the form given before.
It must be added that this dimensional reduction is a purely formal trick, made possible by the fact that we are considering a finite range of modes m, n and j and by no means can it be considered a substantial change of problem dimensionality[1]. The only case in which Eq. 7.6 is formally accurate are the already two-dimensional simulations in helical geometry, where $(m,n) = (m, h \times m)$ for some winding constant h.

7.1.3   Definition of the deconvolution technique

We are finally ready to introduce the deconvolution method. Albeit Eq. 7.2 suggests that we should be facing a formal inversion problem for

---

[1]This is why no practical use is made in SpeCyl of the convolution matrix: to keep it well-defined in the most general three-dimensional case, it would require many caveats and cumbersome handling of exceptions. We present it here only as a valid theoretical tool.

a multi-diagonal matrix to pursue a fully consistent implicit approach, this solution appears largely infeasible, owing to SpeCyl's main loop architecture. In fact, each step of this code code - the predictor step, the Thomas algorithm for velocity, and the two corrector steps - is implemented serially for the various modes. In other words, without an extremely undesirable reformulation of the entire main loop structure, each j-th equation of our matrix problem needs to be inverted individually to isolate the j-th unknown, before even computing the matrix coefficients of the $(j + 1)$-th equation.

It is far more convenient to pursue a semi-implicit approach, where some terms in the convolutions are evaluated explicitly, using their value at prior time-step as an approximant for their present value. More explicitly, we always face a set of $2 \times J + 1$ equations in $2 \times J + 1$ unknowns, which we intend to solve serially. In each of them, convolutions can be written in the form

$$\left[\underline{\underline{A}} \cdot \underline{x}\right]_j = \hat{A}_0\, x_j + \left[\underline{\underline{\langle A \rangle}} \cdot \underline{x}^{\text{old}}\right]_j ,\qquad(7.7)$$

where $\underline{x}$ is an array of unknowns, the superscript "old" signifies evaluation at the prior time-step, and the subscript j numerates the MHD modes. In second member of Eq. 7.7, the first term is treated implicitly, while the second term gives an explicit contribution through prior step evaluation.

This is the kernel of the approximated deconvolution technique.

7.1.4 Formulation of magneto-fluid boundary conditions

The implementation of our new set or BCs through the application of Eq. 7.7 needs to face two challenges: the generalisation to non-axi-symmetric modes of the edge value for the radial flow, and the $\boldsymbol{v} \times \mathbf{B}$ products in the BCs for the magnetic field.

Concerning the fluid boundary, we must generalise to non-axisymmetric components the pinch velocity $\boldsymbol{v}(a) = v_{r,a}\,\hat{\mathbf{r}}$, expressed by Eq. 5.8 that we report here:

$$v_{r,a}^{0,0} = \frac{\left[E_0\hat{\mathbf{z}} \times \mathbf{B}_\theta^{0,0}\right]_{r=a}}{|B(a)|^2} \cdot \hat{\mathbf{r}} .$$

For the time being, we still consider a purely radial flow at plasma edge: transverse components will be added in a second moment. Equation 5.8 can be conveniently re-written in the modes space as

$$\underline{\underline{B_a^2}} \cdot \underline{v_{r,a}} = \underline{\underline{E_{\theta,a}}} \cdot \underline{B_{z,a}} - \underline{\underline{E_{z,a}}} \cdot \underline{B_{\theta,a}} \qquad(7.8)$$

where all quantities are evaluated at plasma edge. $\underline{\underline{B_a^2}}$, $\underline{\underline{E_{\theta,a}}}$ and $\underline{\underline{E_{z,a}}}$ are the usual convolution matrices, formally similar to the one in Eq. 7.2 and the components of the array $\underline{v_{r,a}}$ are the unknowns of this equation.

The implementation is SpeCyl features thee subsequent passages to solve this equation. The first step must be to compute the squared Cartesian amplitude of the magnetic field as the sum of three convolutions:

$$\underline{B_a^2} = \underline{\underline{B_{r,a}}} \cdot \underline{B_{r,a}} + \underline{\underline{B_{\theta,a}}} \cdot \underline{B_{\theta,a}} + \underline{\underline{B_{z,a}}} \cdot \underline{B_{z,a}} \tag{7.9}$$

this can be subsequently turned into the corresponding convolution matrix, according to the definition of the convolution product. For the ideal wall case, of course $\underline{B_{r,a}} = 0$.

It is worth noticing that $\underline{B_a^2}$ is generally a complex vector, being the magnetic field components complex numbers themselves: this is due to the fact that this is not the norm of a physical field but rather its complex Fourier transform.

The second step is the evaluation of the right-hand side of Eq. 7.8: albeit $\underline{E_{\theta,a}} = \underline{0}$ in the ideal wall case, the implementation accounts also for it, to allow future changes.

Finally, the third step is the inversion of the left-hand side of Eq. 7.8, to find the components of $\underline{v_{r,a}}$. This is done by leveraging the deconvolution technique just developed:

$$\underline{\underline{B_a^2}} \cdot \underline{v_{r,a}} = \left(B_a^2\right)^0 \underline{v_{r,a}} + \underline{\underline{\left\langle B_a^2 \right\rangle}} \cdot \underline{v_{r,a}^{\text{old}}}$$

where $(B_a^2)^0$ is the axi-symmetric component of $\underline{B_a^2}$. Finally, we can assign the boundary value to the modes of velocity (including the axi-symmetric one) as

$$\underline{v_{r,a}} = \frac{1}{\left(B_a^2\right)^0} \left[\underline{\underline{E_{\theta,a}}} \cdot \underline{B_{z,a}} - \underline{\underline{E_{z,a}}} \cdot \underline{B_{\theta,a}} - \underline{\underline{\left\langle B_a^2 \right\rangle}} \cdot \underline{v_{r,a}^{\text{old}}} \right], \tag{7.10}$$

where $\underline{v_{r,a}^{\text{old}}}$ at the RHS is evaluated at the previous time step. Note that in the purely axi-symmetric case this formula specialises to the previous Eq. 5.8:

$$v_{r,a}^{0,0} = -\frac{E_0 B_{\theta,a}^{0,0}}{\left(B_a^2\right)^0}.$$

Referring to SpeCyl's work-flow, represented in Fig. 5.2, the computation of the edge value for the radial flow in Eq. 7.10 is still located at the end of the corrector step. The obtained values are fed to the Thomas algorithm for the

flow, at the subsequent time-step.

Concerning the magnetic field, the application of our deconvolution technique is pretty straightforward, and the real complexity lies in the already present predictor-corrector approach.
The general structure of the transverse magnetic field components is preserved, with the only addition of the non-axisymmetric modes in the $\boldsymbol{v} \times \mathbf{B_t}$ product:

$$\eta_a \nabla \times \left(\underline{B_{r,a}} \, \hat{\mathbf{r}} + \underline{\mathbf{B}_{t,a}} \right) - v_{r,a}^{0,0} \, \hat{\mathbf{r}} \times \underline{\mathbf{B}_{t,a}} - \underline{\left\langle v_{r,a} \right\rangle} \hat{\mathbf{r}} \times \underline{\mathbf{B}_{t,a}^{\mathrm{old}}} = \underline{\mathbf{E}_{t,a}} \,, \qquad (7.11)$$

where $\underline{\mathbf{E}_{t,a}} = E_{z,a}^{0,0} \, \hat{\mathbf{z}}$ for the ideal wall case. Thus also in this case, as for the velocity case, for each Fourier mode such that $-J \leq j \leq J$, we serially isolate the j-th MHD mode of B_θ and B_z from the j-th equation, using an explicit prior-step evaluation of all the other MHD modes having $j' \neq j$.

Since this new version of our boundary conditions is a generalisation of SpeCyl.1 to a full-spectrum radial velocity, $v_r^{m,n}$, in the following we will refer to it as to "SpeCyl.1.Vmn".

7.2   Verification against Pixie3D code

A very valuable test for our deconvolution method can be achieved by comparing its predictions with a non-spectral numeric tool. In this section we present a verification benchmark between SpeCyl and the independent 3D nonlinear MHD code Pixie3D, enforcing similar assumptions at plasma edge (ideal wall and full-spectrum radial flow velocity). The term "verification" defines a specific endeavour aimed at ensuring the mathematical correctness of numeric tools.
One such verification had already been performed in 2010 between SpeCyl and Pixie3D [Bonfiglio10], enforcing ideal wall boundary conditions and purely radial edge flow. In that case, of course, only Pixie3D could produce a full spectrum radial flow at plasma edge, since the generalisation of SpeCyl's boundary flow was not yet implemented. Nonetheless, the two codes achieved excellent linear and nonlinear agreement on several case-studies, in one-, two-, and three-dimensional MHD simulations.
For this reason, we do not expect our modification to produce any macroscopic variation in simulations outcomes, at least in the ideal wall case (while we strongly hope it to make a relevant difference in the resistive wall case, discussed in the next chapters). Also, as we discussed in Part II, the presence of an ideal wall directly at plasma edge is expected to stabilise all the

free-interface modes, allowing thus only small velocity fluctuations at the boundary.

We start this section with a brief presentation of the Pixie3D code. Then we present the verification results, comparing SpeCyl.1.Vmn both to Pixie3D and to the previous version, SpeCyl.1. As we will see, even the small and unimportant differences between the two codes at the plasma boundary, present in [Bonfiglio10], are totally removed with this new formulation, confirming thus the correctness of its implementations.

7.2.1 Pixie3D

The conservative, fully implicit, finite-difference code Pixie3D [Chacón04, Chacón06] enforces a self-consistent visco-resistive and compressive MHD model to propagate in time the magnetic field $\mathbf{B}$, the flow velocity $\boldsymbol{v}$, the plasma temperature T, mass density ρ and pressure p:

$$\partial_t \rho + \nabla \cdot (\rho \boldsymbol{v}) = 0, \tag{7.12}$$

$$\partial_t(\rho \boldsymbol{v}) + \nabla \cdot \left[\rho \boldsymbol{v} \boldsymbol{v} - \mathbf{B}\mathbf{B} - \rho \nu(T) \nabla \boldsymbol{v} + \mathbb{I}\left(p + \frac{B^2}{2\mu_0} \right) \right] = 0, \tag{7.13}$$

$$\partial_t \mathbf{B} = -\nabla \times \mathbf{E}, \tag{7.14}$$

$$\mathbf{E} = \eta(T)\mathbf{J} - \boldsymbol{v} \times \mathbf{B} - \frac{d_i}{\rho}(\mathbf{J} \times \mathbf{B}\nabla p), \tag{7.15}$$

$$\mathbf{J} = \nabla \times \mathbf{B}, \tag{7.16}$$

$$\nabla \cdot \mathbf{B} = 0, \tag{7.17}$$

$$\partial_t T_e + \boldsymbol{v} \cdot \nabla T_e + (\gamma - 1)\left[T_e \nabla \cdot \boldsymbol{v}_e + \frac{\nabla \cdot \mathbf{q} - \mathbf{Q}}{\rho} \right] = 0, \tag{7.18}$$

$$p = (1 + \alpha_T)\rho T_e \ ; \ \ \boldsymbol{v}_e = \boldsymbol{v} - \frac{d_i}{\rho}\mathbf{J}, \tag{7.19}$$

where $d_i = c/\omega_{pi}$ is the ion skin depth, T_e is plasma temperature, $\alpha_T = T_i/T_e$ is the ratio of ion to electron temperatures, and $\mathbb{I}$ is the identity tensor. The electric field is determined by resistive Ohm's law [Fitzpartick22] plus a Hall term, accounting for the interaction between the two plasma species [Chacón08].
Resistivity and viscosity are in general function of the temperature profile, which evolves according the the heat equations 7.18, with $\mathbf{q}$ and $\mathbf{Q}$ heat flux and heat source, respectively. γ is the polytropic constant ($p \propto \rho^\gamma$).

As for SpeCyl, Eqs. 7.12-7.19 are normalised to physical constants: lengths to the minor radius a, time and velocities to the Alfvén time and Alfvén velocity $v_A = a/\tau_A$, respectively, the magnetic field and the temperature to their respective initial value on axis, and the same holds for pressure and density. As already seen for SpeCyl, in this units the resistivity is the inverse-Lundquist number $S = 1/\eta$ and the viscosity is the inverse-Reynolds number $Re = 1/\nu$.

Pixie3D adopts a conservative, finite-difference scheme to discretize the equations [Chacón04]: a Cartesian logical mesh $\boldsymbol{\xi}$ is used, along with a coordinates transformation $\mathbf{x}[\boldsymbol{\xi}]$ for the embedding in the physical space geometry. This ability of treating a generalised curvilinear coordinates allows Pixie3D to operated in many different geometries relevant to fusion, among which the toroidal, the cylindrical and the helical. All quantities are thus evaluated in the physical space, in opposition to the spectral implementation of SpeCyl.

The temporal discretisation is fully implicit, generally relying on a Crank-Nicholson method. The resulting set of algebraic equations is dealt with a preconditioned Newton-Krylov solver [Chacón04, Chacón06].

For the verification in [Bonfiglio10], a reduction in the models of both codes was operated to find a common regime of applicability: constant and uniform mass density ρ, no artificial viscosity β in the momentum balance equation of SpeCyl, uniform and constant temperature and pressure in Pixie3D, uniform and constant kinematic viscosity ν in both codes and no heat sources neither Hall effect in Pixie3D.

7.2.2 Nonlinear results

In our verification we focused on the single case study of a marginally resonant (on axis) mode $(1, -8)$ in RFP geometry, among those present in [Bonfiglio10]. This is a 2D helical case-study, where an initial perturbation $1, -8$ is excited on the top of our usual Ohmic pinch equilibrium. The resistivity profile is $\eta = 3.33 \cdot 10^{-5} [1 + 20\, r^{10}]$, while the uniform viscosity is $\nu = 10^{-2}$. The safety-factor on axis is $q_0 = 1/8$, with $\alpha_0 = 4$ and $R/a = 4$ as in Fig. 5.1.(a). This case and the relative set-up will be discussed much more in deep in Chap. 9.
As foreseen, the overall predictions are mostly unchanged between SpeCyl.1 and SpeCyl.1.Vmn. In fact, the only visible difference is in a narrow layer close to the plasma edge, in the radial profiles of two physical quantities: the radial flow velocity (of course), and the current density. Figure 7.1 represents the detail in the boundary region of three plasma quantities: the axial

electric field, the radial flow velocity, and the axial current density. For each quantity, the first three harmonics of mode $(1, -8)$ are represented, along with the axi-symmetric mode.

In the first panel, the electric field results from enforcing the resistive Ohm's law on the processed simulation data: $\mathbf{E} = \eta\mathbf{J} - \boldsymbol{v} \times \mathbf{B}$. The fact that its value at plasma edge is the one prescribed by the boundary conditions - finite axi-symmetric loop-field $E_z^{0,0} = E_0$ and null non-axisymmetric modes - certifies that the self-consistency of the code has been preserved by our modification. This is a first and promising hint, suggesting that the implementation is correct. Analogous considerations hold for E_θ, whose modes all vanish at plasma boundary, in accordance with the prescription of the ideal wall BCs.

Paying now a closer look the the radial velocity, we see that the non-axisymmetric components that SpeCyl.1 profiles plummet rapidly near plasma edge, to meet the purely axi-symmetric condition in $r = a$. This is not the case for SpeCyl.1.Vmn, which rather sticks quite perfectly onto Pixie3D's solutions. It is comforting to observe that the last few outermost radial steps seem to continue the same trajectory suggested by the rest of the radial profile, unlike SpeCyl.1's profiles. More important is however the outstanding agreement with a code that, like Pixie3D, can completely avoid the convolutions complexity by operating in the physical space.

Concerning the axi-symmetric mode, a very small (still visible) difference in the edge value is also present between SpeCyl.1 and the other two (mutually agreeing) profiles, that are slightly more negative at plasma edge. This is due to the last term at second member in Eq. 7.10, accounting for the presence of other modes in the spectrum of radial velocity at edge. This term is here quantitatively very small, but it is reasonable to assume that it may become important for free-edge instabilities where the velocity fluctuations at plasma edge are expected to grow larger.

Finally, we can see how the axi-symmetric velocity assumption in SpeCyl.1 is mirrored in the presence of little unphysical current spikes at plasma edge. This owes to the fact that SpeCyl's BCs simultaneously enforce the resistive Ohm's law and assign a fixed edge value to the tangential electric field. This implies that for all the non- modes

$$E_{z,a}^{m,n} = \eta_a J_{z,a}^{m,n} - v_a^{0,0} B_{\theta,a}^{m,n} = 0 \,,$$

so that $J_{z,a}^{m,n} \propto v_a^{m,n}$. This implies that the abrupt change of direction in the velocity profiles near the plasma edge must be reflected also on the modes of current density. Also in this case the problem is avoided with the new implementation, in excellent agreement with Pixie3D.

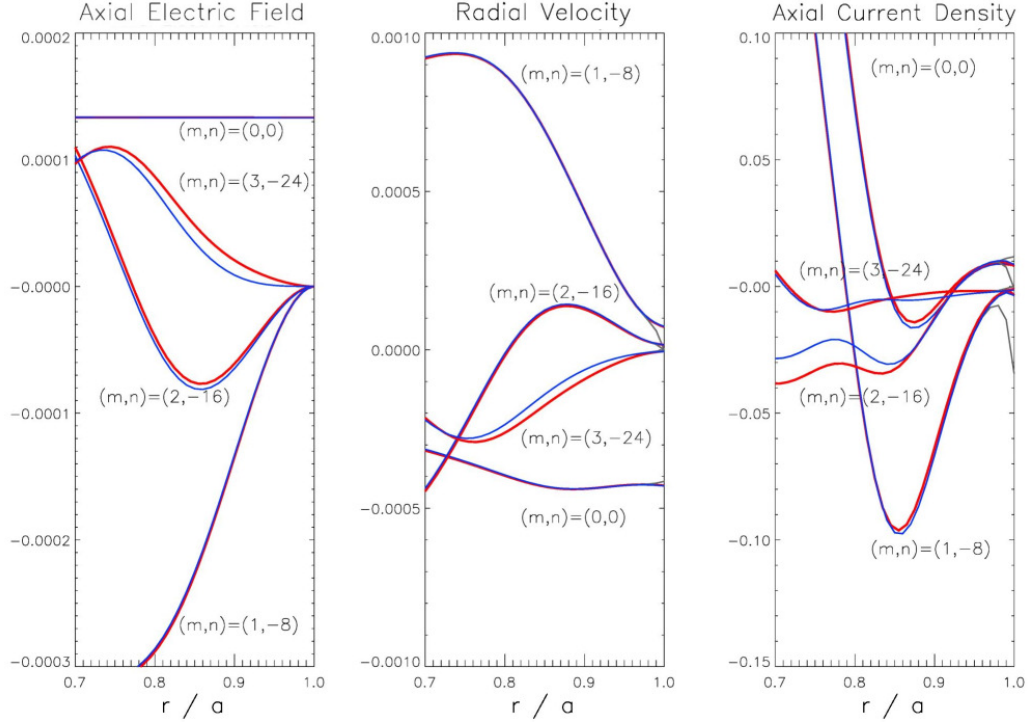The remaining small inconsistencies between the two codes in the bulk of

Figure 7.1: Detail of the radial profile of three physical quantities, in the stationary nonlinear saturation of the marginally resonant kink mode $(1, -8)$, after $5000\,\tau_A$ of evolution. **SpeCyl.1.Vmn** (in blue), **SpeCyl.1** (in gray), and **Pixie3D** (in red) are in excellent agreement everywhere but in a narrow layer at plasma edge, where SpeCyl.1's v_r and J_z exhibit a small unphysical drop.

the plasma, away from the boundary, were already present in [Bonfiglio10] and are indeed very small when they are viewed in the full scale of the image (here we only present a magnified detail of the boundary region). They may originate from a number of causes, including small intrinsic differences between the architectures of the two codes, or a slightly insufficient azimuthal mesh in Pixie3D's simulation (here: 64 mesh points along θ in Pixie3D, against 32 helical harmonics in SpeCyl).

7.3   Conclusive summary

This chapter started presenting the main challenge that needed to be overcome in order to formulate a new set of boundary conditions, comprehensive of finite non-axisymmetric edge velocity fluctuations. This originates

from the fact that a simple product in the physical space is mapped into a nonlinear convolution of modes, according the the convolutions theorem 1, in the Fourier base in which SpeCyl operates.

The problem assumes some interesting symmetry in terms of an original and convenient matrix-array formalism, whose main advantage is to help visualising the problem. This way, three useful general properties of the convolution products emerge quite naturally. We defined an ordering rule that leverages the already present numeration of the modes in SpeCyl, to lower the problem dimensionality in the case of a finite number of modes, which is the case relevant to the implementation.

From all this we could finally derive an approximated deconvolution technique, whose implementation allows to extend SpeCyl's boundary conditions to non-axisymmetric edge velocities.

A preliminary study was conducted for the simpler case of an ideal wall facing the plasma, extending SpeCyl.1 BCs to a new set, featuring full-spectrum edge flow and dubbed SpeCyl.1.Vmn. This has been tested against SpeCyl.1 and Pixie3D on the case study of a marginally resonant kink mode in the RFP.

The results of the verification benchmark suggest that the deconvolution technique is effective and its implementation is correct. Also, some aspects in the edge flow and current density suggest a slight enhancement in the self-consistency of the code.

Altogether the results presented in this chapter allow us to switch to the implementation of the full set of boundary conditions, including both a three-dimensional edge flow velocity and a thin-shell like magnetic boundary.

8

New magneto-fluid boundary conditions with 3D edge flow

This Chapter is dedicated to the new set of boundary conditions: its physical hypotheses and implications, its formulation, and its implementation in SpeCyl.

We start by re-deriving in Sec. 8.1 the model equations, also using the mathematical tools already presented in Chap. 6. This step is mandatory to highlight all the hidden assumptions and finally achieve a fully self-consistent formulation. Indeed, some previous exploratory attempts to get to a comprehensive magneto-fluid set of BCs had been formulated and tested without going through this formal step. These are documented in [Spinicci22] and thoroughly presented in Appendix B. In that case - formally very similar to the final set-up we present in this chapter - the incomplete self-consistency of the BCs forced us to leverage a narrow pseudo-vacuum region at plasma edge. The nonlinear benchmark study against the ideal external kink, featuring also a qualitative comparison with the JOREK-STARWALL code, obtained acceptable but still unsatisfactory agreement with the linear theory predictions.

In Sec. 8.2 we illustrate the final implementation of our new and comprehensive set of boundary conditions, dubbed "SpeCyl.2". The thin resistive shell formulation of the magnetic boundary is here self-consistently coupled with two alternative formulations for a three-dimensional edge flow. This is a flexible set-up that aims at containing all the other sets of BCs hitherto described as a particular case: SpeCyl.2.V00 would be the radial-axisymmetric limit for the edge velocity, SpeCyl.1.Vmn must be retrieved as the ideal wall limit (for $\tau_W \ggg 1$) and SpeCyl.1 by enforcing the two limits simultaneously. Sec. 8.3 presents the conclusive summary of this chapter.

The work contained in this chapter was partially produced during my stay at Los Alamos National Laboratory, USA, under the guidance of Dr. Luis Chacón.

8.1   Re-derivation of the physical model

We seek to define a fully self consistent set of boundary conditions, featuring a thin resistive shell at plasma boundary, surrounded by vacuum and by an outer ideal wall at finite distance, and a three-dimensional flow at plasma edge.

The magnetic boundary conditions enforce the continuity of the electric field components in the direction tangential to the shell surface. This is computed according to the thin-shell relations Eq. 6.1-6.6 already derived in Chap. 8, which we report below in a compact form:

$$[B_r]_-^+ = 0 \,, \qquad \mathbf{E}_{t,W} = \frac{a}{\tau_W}\,[\hat{\mathbf{r}} \times \mathbf{B}_t]_-^+ \,, \qquad \frac{\partial B_{r,a}}{\partial t} = \frac{1}{\tau_W}\left[\frac{\mathrm{d}(rB_r)}{\mathrm{d}r}\right]_-^+ \,,$$

where $\tau_W = (\mu_0\, a\, \Delta_W)/\eta_W$ is the resistive diffusion time through the thin shell, $\Delta_W \ll a$ the shell thickness, and η_W its resistivity. The vacuum fields just outside the resistive wall and their derivatives have already been analytically obtained in Chap. 6 by solving analytically the Poisson's problem with assigned boundary conditions on the resistive shell ($B_r = B_{r,a}$) and on the outer conductor ($B_r = 0$). Suitable coefficients ($\Theta_{m,n}$, $Z_{m,n}$, $\Delta_{m,n}$, Eqs. 6.10-6.17) can be obtained such that, for every mode (m,n),

$$B_{\theta,a}^{m,n}|_+ = \Theta_{m,n}iB_{r,a}^{m,n} \,, \qquad\qquad B_{z,a}^{m,n}|_+ = Z_{m,n}iB_{r,a}^{m,n} \,,$$

$$\frac{\mathrm{d}}{\mathrm{d}r}(rB_r^{m,n})|_+ = \Delta_{m,n}B_{r,a}^{m,n} \,.$$

The boundary condition for the velocity requires some further assumption, needed to close the set of equations of our model. In this section we generalise the already presented $\mathbf{E} \times \mathbf{B}$-like edge flow in two alternative ways. In the ideal wall case, the last magnetic flux surface was parallel to the surface of the wall: from the properties of the vector product, it was manifest that the pinch flow, inherently orthogonal to the magnetic field, had to be purely radial.

Once we allow finite resistive diffusion through our boundary, we can close

our model equations based on two alternative assumptions. The first is to retain all the three spatial components (r, θ, z) of the perpendicular flow. The second is perhaps the most direct and consists in considering again a purely radial velocity: this means taking only the radial projection of the perpendicular flow.

As we will see in the following, both these assumptions are totally legitimate, since they both lead to a self-consistent closure of our magneto-fluid model equations. As a matter of fact, our implementation allows them both, as we will discuss more in deep in Sec. 8.2. In particular, the purely radial assumption for the edge flow is preferentially used when the thin-shell is interpreted as a physical wall, that can brake the mode rotation and fix its angular velocity at boundary. On the other hand, the purely perpendicular constraint is typically adopted for this Thesis in the vacuum-wall limit.

In the next two subsections we derive the two alternative formulations for the boundary flow. All the results we will find are summarised in Fig. 8.1.

Before we start with our derivation it is useful to introduce some formalism. In Fig. 8.1.(a) we see the representation of the "entrance" (*i.e.*, the inner side) of the thin-shell: the plasma is the region beneath the gray surface, while the region above it is the RW. The red arrow named $\mathbf{B}_a$ is magnetic field at the surface of the plasma (and not the vacuum field), which is penetrating the shell. We want to define a set of local coordinates on the plane of the plasma surface, perpendicular to the radial unit vector $\hat{\mathbf{r}}$. This is defined as follows:

$$\hat{\mathbf{s}}_1 \equiv \frac{\mathbf{B}_{t,a}}{|\mathbf{B}_{t,a}|}, \qquad \hat{\mathbf{s}}_2 \equiv \hat{\mathbf{r}} \times \hat{\mathbf{s}}_1, \tag{8.1}$$

where $\mathbf{B}_{t,a} = \mathbf{B}_a - B_{r,a}\,\hat{\mathbf{r}}$, as usual. Along with the radial direction, $(\hat{\mathbf{r}}, \hat{\mathbf{s}}_1, \hat{\mathbf{s}}_2)$ constitutes a right-handed local system of coordinates at the plasma interface. Also, we recall here two properties of the vector product, which will have large application in the next few pages:

$$(\mathbf{A} \times \mathbf{B}) \times \mathbf{C} = (\mathbf{A} \cdot \mathbf{C})\mathbf{B} - (\mathbf{B} \cdot \mathbf{C})\mathbf{A}, \tag{8.2}$$

$$\mathbf{A} \times \mathbf{B} \cdot \mathbf{C} = \mathbf{A} \cdot (\mathbf{B} \times \mathbf{C}), \tag{8.3}$$
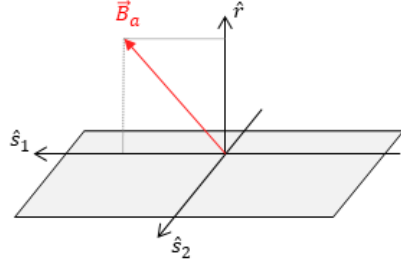
for any three vectors $\mathbf{A}$, $\mathbf{B}$, and $\mathbf{C}$.

8.1.1 Self-consistent formulation with $v_{\parallel,a} = 0$

We start from the case of purely perpendicular velocity, since it is the easiest. In fact, in this case we simply have a scalar constraint on the edge flow:

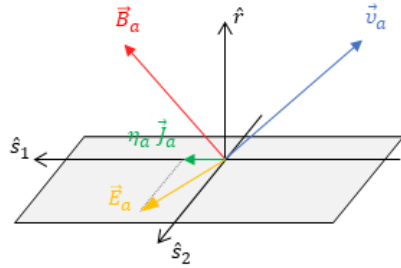$$v_{\parallel,a} = (\boldsymbol{v}_a \cdot \mathbf{B}_a) = 0. \tag{8.4}$$

(*a*) **Entrance of the thin shell**

$$\mathbf{B}_{t,a} = \mathbf{B}_a - B_{r,a}\,\hat{r}$$

$$\hat{s}_1 = \frac{\mathbf{B}_{t,a}}{|\mathbf{B}_{t,a}|}$$

$$\hat{s}_2 = \hat{r} \times \hat{s}_1$$

(*b*) **Purely perpendicular velocity** → **vacuum wall limit**

$$v_{\parallel,a} = \boldsymbol{v}_a \cdot \mathbf{B}_a = 0$$

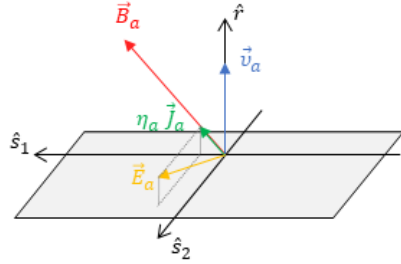$$\boldsymbol{v}_a = \frac{\mathbf{E}_a \times \mathbf{B}_a}{|\mathbf{B}_a|^2}$$

$$\boldsymbol{J}_a = J_{r,a}\,\hat{r} + J_{1,a}\,\hat{s}_1$$

$$\mathbf{E}_a = \eta_a \boldsymbol{J}_a + E_{2,a}\,\hat{s}_2$$

Assumptions:

$$|\mathbf{B}_a|^2 \boldsymbol{v}_a \gg \eta_a \boldsymbol{J}_a \times \mathbf{B}_a$$

$$E_{r,a} = \eta_a J_{r,a} = 0$$

(*c*) **Purely radial velocity** → **physical resistive shell**

$$\boldsymbol{v}_{t,a} = \boldsymbol{v}_a - v_{r,a}\,\hat{r} = 0$$

$$\boldsymbol{v}_a = \frac{\mathbf{E}_a \times \mathbf{B}_a \cdot \hat{r}}{|\mathbf{B}_{t,a}|^2}\,\hat{r}$$

$$\boldsymbol{J}_a = J_{r,a}\,\hat{r} + J_{1,a}\,\hat{s}_1$$

$$\mathbf{E}_a = \eta_a \boldsymbol{J}_a + E_{2,a}\,\hat{s}_2$$

Assumption:

$$|\mathbf{B}_{t,a}|^2 \boldsymbol{v}_a \gg \eta_a \boldsymbol{J}_a \times \mathbf{B}_a \cdot \hat{r}$$

Figure 8.1:   Graphical representation of the two formulations of the fluid boundary. Panel (*a*) introduces the local coordinates $(\hat{r}, \hat{s}_1, \hat{s}_2)$: $\mathbf{B}_a$ is the plasma magnetic field at boundary, the grey surface is the inner side of the shell (below it there is the plasma, above it is the shell itself). Panel (*b*) presents the $v_{\parallel,a} = 0$ formulation, preferentially used for the vacuum-wall limit ($\tau_W \lesssim \tau_A$). Panel (*c*) illustrates the $\boldsymbol{v}_{t,a} = 0$ formulation, typically used to model a physical resistive shell. In panels (*b-c*) the amplitude of $\eta_a \mathbf{J}_a$ is strongly exaggerated to make it visible.

If we now write the resistive Ohm's law, we find

$$\mathbf{E}_a + \boldsymbol{v}_{\perp,a} \times \mathbf{B}_a = \eta_a \mathbf{J}_a \,.$$

Taking the vector product with $\mathbf{B}_a$ of both members of the relation above and making use of Eq. 8.2 produces

$$|\mathbf{B}_a|^2 \boldsymbol{v}_{\perp,a} = (\mathbf{E}_a - \eta_a \mathbf{J}_a) \times \mathbf{B}_a \,.$$

This reveals our first implicit assumption: in order to get an $\mathbf{E} \times \mathbf{B}$-like velocity, we need to require that

$$\boldsymbol{v}_{\perp,a} = \frac{\mathbf{E}_a \times \mathbf{B}_a}{|\mathbf{B}_a|^2} \qquad \Longrightarrow \qquad \boxed{\mathbf{E}_a \times \mathbf{B}_a \gg \eta_a \mathbf{J}_a \times \mathbf{B}_a}, \qquad (8.5)$$

where $\boldsymbol{v}_{\perp,a} = v_{r,a}^{\perp}\, \hat{\mathbf{r}} + v_{1,a}^{\perp}\, \hat{\mathbf{s}}_1 + v_{2,a}^{\perp}\, \hat{\mathbf{s}}_2$, and

$$|\mathbf{B}_a|^2 = B_{r,a}^2 + B_{1,a}^2 \,.$$

The assumption contained in Eq. 8.5 is a force-free condition for our plasma boundary, since it requests that $\mathbf{J} \times \mathbf{B}$ forces are negligible on the scale of the $\mathbf{E} \times \mathbf{B}$ flow.

The direct substitution of $\boldsymbol{v}_{\perp,a}$ back into the Ohm's law gives us is revealing of the consequences of our assumption:

$$\mathbf{E}_a + \frac{\mathbf{E}_a \times \mathbf{B}_a}{|\mathbf{B}_a|^2} \times \mathbf{B}_a = \eta_a \mathbf{J}_a$$

or, making use of Eq. 8.2,

$$\mathbf{E}_a \cdot \left[\underline{\underline{\mathbb{I}}} + \hat{\mathbf{b}}\hat{\mathbf{b}} - \underline{\underline{\mathbb{I}}} \right] = \eta_a \mathbf{J}_a \,, \qquad \text{with } \hat{\mathbf{b}} = \frac{\mathbf{B}_a}{|\mathbf{B}_a|} \,,$$

implying that self-consistency needs that

$$E_{\parallel,a}\hat{\mathbf{b}} = \eta_a \mathbf{J}_a \,. \qquad (8.6)$$

Equation 8.6 implies that $\mathbf{J}_a \times \mathbf{B}_a = 0$, as a natural consequence of Eq. 8.5. The resulting current density and electric field at plasma edge are then

$$\mathbf{J}_a = J_{r,a}\, \hat{\mathbf{r}} + J_{1,a}\, \hat{\mathbf{s}}_1 \,, \qquad (8.7)$$
$$\mathbf{E}_a = \eta_a \mathbf{J}_a + E_{2,a}\, \hat{\mathbf{s}}_2 \,. \qquad (8.8)$$

There is yet another assumption we need to make, in order to close our set of equations. In fact, the tangential components of $\boldsymbol{v}_{\perp,a}$ depend on the radial

electric field, which we cannot determine from the above analysis (recall that $\mathbf{E}_{t,a} = \frac{a}{\tau_W}\hat{\mathbf{r}} \times [\mathbf{B}_t]_-^+$).
The easiest assumption we can opt for is the following:

$$\boxed{E_{r,a} = \eta_a J_{r,a} = 0}\,. \tag{8.9}$$

The rationale for this is to enforce a "continuity" property between the plasma edge and the resistive wall, whose vanishing radial thickness does not allow radial currents or electric fields. Concerning the current density, the physical meaning of Eq. 8.9 is to ensure that the plasma interface with the shell does not behave as a source/sink of electric charge, thus motivating a discontinuity from a finite $J_{r,a}$, just inside the plasma, to no charge flux just outside. This would be conceptually problematic since we plan to use this formulation in the the vacuum-wall limit, when we treat the RW as a free interface between plasma and vacuum: of course no currents can come from outside.
As a consequence, $\mathbf{J}_a \times \mathbf{B}_a$ is not any more null, since $B_{r,a} \neq 0$, and this partially contradicts our first assumption Eq. 8.5. The problem is however only apparent, since both the assumption and the edge-velocity constraint keep valid, up to $\mathcal{O}(\eta_a)$.

Figure 8.1.(b) shows the geometry of this case, along with the relative assumptions.

8.1.2 Self-consistent formulation with $v_{t,a} = 0$

This second case implies imposing "no-slip" (Dirichlet) boundary conditions on the flow components tangential to the RW:

$$\boldsymbol{v}_{t,a} = \boldsymbol{v}_a - v_{r,a}\,\hat{\mathbf{r}} = 0\,. \tag{8.10}$$

The resistive Ohm's law becomes

$$\mathbf{E}_a + v_{r,a}\,\hat{\mathbf{r}} \times \mathbf{B}_a = \eta_a \mathbf{J}_a\,.$$

Taking the vector product with $\mathbf{B}_a$ and relying on Eq. 8.2 yields

$$v_{r,a}\left(B_{r,a}\mathbf{B}_a - |\mathbf{B}_a|^2\,\hat{\mathbf{r}}\right) = -\mathbf{E}_a \times \mathbf{B}_a + \eta_a\mathbf{J}_a \times \mathbf{B}_a\,.$$

Taking the radial component of the above equality we get

$$|\mathbf{B}_{t,a}|^2 v_{r,a} = [(\mathbf{E}_a - \eta_a\mathbf{J}_a) \times \mathbf{B}_a] \cdot \hat{\mathbf{r}}\,.$$

To get to an $\mathbf{E} \times \mathbf{B}$-like velocity, our first implicit assumption must be (as for the other case):

$$v_{r,a} = \frac{\mathbf{E}_a \times \mathbf{B}_a}{|\mathbf{B}_{t,a}|^2} \cdot \hat{\mathbf{r}} \qquad \Longrightarrow \qquad \boxed{\mathbf{E}_a \times \mathbf{B}_a \cdot \hat{\mathbf{r}} \gg \eta_a \mathbf{J}_a \times \mathbf{B}_a \cdot \hat{\mathbf{r}}}. \qquad (8.11)$$

Please note that the two important differences with respect to Eq. 8.5:

- our assumption only concerns the radial direction;

- our purely radial velocity has $|\mathbf{B}_{t,a}|^2 = B_{1,a}^2$ at the denominator, instead of the full $|\mathbf{B}_a|^2$.

Substituting this term back into the resistive Ohm's law, we obtain:

$$\mathbf{E}_a + \frac{\mathbf{E}_a \times \mathbf{B}_a \cdot \hat{\mathbf{r}}}{|\mathbf{B}_{t,a}|^2} \, \hat{\mathbf{r}} \times \mathbf{B}_a = \eta_a \mathbf{J}_a \,.$$

Making use of Eq. 8.3 we get

$$\mathbf{E}_a \cdot \left[\underline{\underline{\mathbb{I}}} - \frac{(\hat{\mathbf{r}} \times \mathbf{B}_{t,a})(\hat{\mathbf{r}} \times \mathbf{B}_{t,a})}{|\mathbf{B}_{t,a}|^2} \right] = \eta_a \mathbf{J}_a \,,$$

or, leveraging Eq. 8.1,

$$\mathbf{E}_a \cdot \left[\underline{\underline{\mathbb{I}}} - \hat{\mathbf{s}}_2 \hat{\mathbf{s}}_2 \right] = \eta_a \mathbf{J}_a \,.$$

If we project this equation along $\hat{\mathbf{r}}$ and along $\hat{\mathbf{s}}_1$ we get

$$\mathbf{E}_{r,a} = \eta_a \mathbf{J}_{1,a}, \qquad (8.12)$$
$$\mathbf{E}_{1,a} = \eta_a \mathbf{J}_{1,a}, \qquad (8.13)$$

whereas projecting along the $\hat{\mathbf{s}}_2$ we get

$$E_{2,a}[1 - 1] = \eta_a J_{2,a} \qquad \Longrightarrow \qquad J_{2,a} = 0 \,. \qquad (8.14)$$

All along, Eqs. 8.12-8.14 imply

$$\mathbf{J}_a = J_{r,a} \, \hat{\mathbf{r}} + J_{1,a} \, \hat{\mathbf{s}}_1 \,,$$
$$\mathbf{E}_a = \eta_a \mathbf{J}_a + E_{2,a} \, \hat{\mathbf{s}}_2 \,.$$

This time, since no explicit reference is made of $E_{r,a}$ and $J_{r,a}$ in our model equations, we do not need to enforce Eq. 8.9, hence $\mathbf{J}_a \times \mathbf{B}_a \cdot \hat{\mathbf{r}} = 0$ and we should expect Eq. 8.11 to hold exactly.

The geometry of this case, along with its assumptions, is reported in Fig. 8.1.(c).

8.1.3 Remark on the role of the hidden assumptions in the implementation

In the next section we illustrate the implementation of this new set of boundary conditions. As we will see, none of the hidden assumptions that we have highlighted in the previous sections will be explicitly enforced: they will rather "emerge" from the implementation itself, when, for instance, we will not consider the contribution of $\mathbf{J} \times \mathbf{B}$ terms in determining the edge flow.

The reason why it is fundamental to keep track of them, however, is that we can use them as a metric of the self-consistency of our implementation.

Suppose that we find that a simulation has produced very intense radial $\mathbf{J} \times \mathbf{B}$ radial forces at plasma edge. With our present implementation, this is a sign that something is producing an inconsistency, that needs to be tackled and corrected in the implementation.

Of course there may be some inconsistency in the code which is not probed by these metrics. Nonetheless, the attentive study of these valid tools is ultimately one of the main reasons why in the end we are able to present a fully operative set of BCs.

8.2 Implementation

Let us put all parts together. Figure 8.2 shows the general features of the implementation of SpeCyl.2. It is manifest that this is a flexible and comprehensive set of boundary conditions that contains all the previous implementations as limit cases. Their combination in one complete formulation bring the code to advanced capabilities in modelling the plasma boundary, also fixing some inconsistencies of the previous version, and it can be considered a major upgrade for the SpeCyl code.

In SpeCyl.1, the geometry features an ideal wall in direct contact with the plasma and a purely one-dimensional edge flow. By keeping the same formulation for the flow, while displacing the ideal wall at finite distance and modelling a thin resistive shell facing the plasma, we get to SpeCyl.2.V00. We have shown that by setting the resistive wall time to a very large value it is possible to retrieve SpeCyl.1 as a particular case of SpeCyl.2.V00.

On the other hand, modelling a three-dimensional boundary flow we could advance SpeCyl.1 into SpeCyl.1.Vmn. Of course, by switching off the non-axisymmetric modes of the boundary flow, SpeCyl.1 is fully retrieved.

This final step, dubbed SpeCyl.2, is the merging of the more realistic magnetic modelling of SpeCyl.2.V00 and of the more complete modelling of
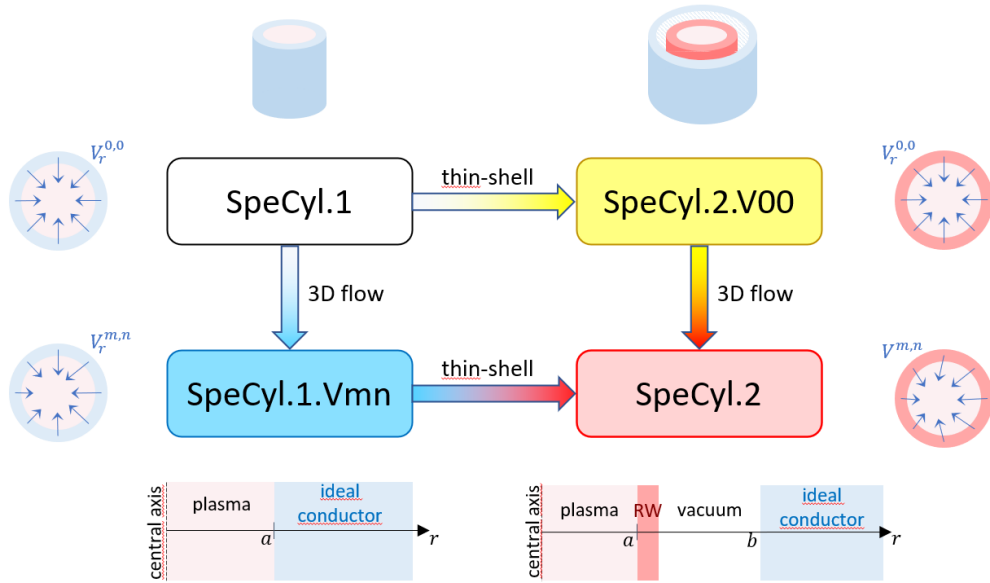
Figure 8.2: General scheme of the evolution of SpeCyl's BCs. SpeCyl.2 contains all the other formulations as limit cases: SpeCyl.1.Vmn is re-obtained for $\tau_W \gg 1$; SpeCyl.2.V00 by setting an axisymmetric radial edge flow as in Eq. 5.8; SpeCyl.1 descends from the simultaneous application of both limits.

boundary flow in SpeCyl.1.Vmn. Indeed, both intermediate versions can be retrieved by substituting our new and articulate modelling of the edge flow with Eq. 5.8, and by setting $\tau_W \gg \tau_A$, respectively.

In this section, we report the three main parts that constitute the upgrade from the previous versions:

- the generalisation of SpeCyl.2.V00 magnetic boundary equations to a three-dimensional flow;

- the implementation of the two alternative formulations for the edge flow;

- a rearrangement of the structure of SpeCyl's corrector step, to provide enhanced self-consistency.

8.2.1 Generalisation of the thin-shell magnetic boundary to 3D edge flow

The overall structure of SpeCyl.2 is very similar to SpeCyl.2.V00, apart from the fluid conditions and some details in the implementation. For this reason, we report here Eqs. 6.18-6.19 that are formally still valid:

$$(m,n) = (0,0) \longleftrightarrow \begin{cases} E_{\theta,w}^{0,0} &= 0 \\ E_{z,w}^{0,0} &= E_0 \\ B_{r,a}^{0,0} &= 0 \end{cases} \tag{8.15}$$

$$(m,n) \neq (0,0) \longleftrightarrow \begin{cases} E_{\theta,w}^{m,n} &= -\dfrac{a}{\tau_W} \left[\Theta_{m,n} i B_{r,a}^{m,n} - (B_{\theta,a}^{m,n})_- \right] \\ E_{z,w}^{m,n} &= \dfrac{a}{\tau_W} \left[Z_{m,n} i B_{r,a}^{m,n} - (B_{z,a}^{m,n})_- \right] \\ \dfrac{\partial B_{r,a}^{m,n}}{\partial t} &= \dfrac{1}{\tau_W} \left[\Delta_{m,n} B_{r,a}^{m,n} - \dfrac{\partial (r B_r^{m,n})}{\partial r} \right] \end{cases} \tag{8.16}$$

The tangential components of the magnetic field are still updated by enforcing the continuity of the tangential electric field between the plasma edge and the resistive wall:

$$\underline{\mathbf{E}}_{t,a} = \underline{\mathbf{E}}_W = \underline{E}_0 \, \hat{\mathbf{z}} + \frac{a}{\tau_W} \hat{\mathbf{r}} \times [\underline{\mathbf{B}}_t]_-^+ \, , \tag{8.17}$$

where we have restored our compact array-like notation for SpeCyl's modes, already introduced in Chap. 7, and $\underline{E}_0 \equiv (E_{z,a})^{0,0}$.
For a non-axisymmetric, three dimensional flow and in presence of a thin resistive shell at plasma edge, Eq. 8.17 reads:

$$\begin{aligned} \underline{E}_0 \, \hat{\mathbf{z}} + \frac{a}{\tau_W} \hat{\mathbf{r}} \times [\underline{\mathbf{B}}_t]_-^+ = & \, \eta \nabla \times \left(\underline{B}_{r,a} \, \hat{\mathbf{r}} + \underline{\mathbf{B}}_{t.a} \right) \\ & + \left(\boldsymbol{v}_{t,a}^{0,0} \, \underline{\underline{\mathbb{I}}} + \underline{\langle \underline{\boldsymbol{v}}_{t,a} \rangle} \right) \times \underline{B}_{r,a} \, \hat{\mathbf{r}} \\ & - v_{r,a}^{0,0} \, \hat{\mathbf{r}} \times \underline{\mathbf{B}}_{t,a} - \underline{\langle v_{r,a} \rangle} \, \hat{\mathbf{r}} \times \mathbf{B}_{t,a}^{\text{old}} \, , \end{aligned} \tag{8.18}$$

Note that, unlike the product $\boldsymbol{v}_r \times \mathbf{B}_t$ in the third line of Eq. 8.18 (already discussed in Chap. 7), the new term $\boldsymbol{v}_t \times \mathbf{B}_r$ in the second line of Eq. 8.18 gives only an explicit contribution. Referring again to Fig. 5.2 for the visual representation of SpeCyl's work-flow, Eq. 8.18 is enforced three times throughout the main loop of the code: at predictor step, corrector intermediate step and final corrector step. The first two times, the radial magnetic field $\underline{B}_{r,a}$ is not updated by the code (as discussed in Chap. 6) and thus

Eq. 8.18 uses its prior step evaluation explicitly. For the final corrector step, $\underline{B_{r,a}}$ evolves according to

$$\frac{\partial B_{r,a}^{m,n}}{\partial t} = \frac{1}{\tau_W} \left[\Delta_{m,n} B_{r,a}^{m,n} - \frac{\partial (r B_r^{~m,n})}{\partial r} \right] , \qquad (8.19)$$

and its updated value is explicitly used in Eq. 8.18.

Equation 8.19 does not depend on the flow velocity, so it is formally unchanged in the generalised case. Unfortunately, this is not the case for its implementation, since this equation is used in SpeCyl so as to constrain the initial value for the inwards integration, from edge to axis, that constitutes the backwards step of the Thomas algorithm. As anticipated in Chap. 5, the forward Thomas algorithm produces a set of linear equations like

$$\left\{ \begin{matrix} B_r^{m,n} \\ B_\theta^{m,n} \end{matrix} \right\}_{r-\Delta r} = \left\{ \begin{matrix} \mathbb{E}_{r,r} & \mathbb{E}_{r,\theta} \\ \mathbb{E}_{\theta,r} & \mathbb{E}_{\theta,\theta} \end{matrix} \right\} \cdot \left\{ \begin{matrix} B_r^{m,n} \\ B_\theta^{m,n} \end{matrix} \right\}_r + \left\{ \begin{matrix} \mathbb{F}_r \\ \mathbb{F}_\theta \end{matrix} \right\} ,$$

$$\left\{ B_z^{m,n} \right\}_{r-\Delta r} = \mathbb{E}_z \cdot \left\{ B_z^{m,n} \right\}_r + \mathbb{F}_z ,$$

such that by assigning the boundary values to all the magnetic field components we can start the inwards integration.

Crucially, Eq. 8.19 depends on $B_r^{m,n}(a - \Delta r)$, which is still formally an unknown (we have not started the backwards step yet), through the radial derivative of $r B_r^{m,n}$ in the plasma region. SpeCyl's implementation deals with this issue by leveraging the set of linear equations produced by the Thomas algorithm, writing

$$B_r^{m,n}|_{a-\Delta r} = \mathbb{E}_{r,r} B_{r,a}^{m,n} + \mathbb{E}_{r,\theta} B_{\theta,a}^{m,n} .$$

Unfortunately, also $B_{\theta,a}^{m,n}$ is still an unknown. This is finally overcome by enforcing Eq. 8.18 along with

$$B_\theta^{m,n}|_{a-\Delta r} = \mathbb{E}_{\theta,r} B_{r,a}^{m,n} + \mathbb{E}_{\theta,\theta} B_{\theta,a}^{m,n}$$

to obtain a final equation that only depends on the single unknown $B_{r,a}^{m,n}$. This brings a rather complex manipulation that was initially dealt with by Daniele Bonfiglio for the implementation of SpeCyl.2.V00, but had to be generalised to keep track of the new terms in Eq. 8.18. We report below the snippet corresponding in concrete to what we have been discussing about: we do not want to explore the meaning of each term, but just to provide the idea of the involved complexity:

```
      UU(1,LX) =
   .    ( ( FFJ(1,LX-1,Jmn)
   .         + TAUW/DT*BR(LX,J)/X(LX-1)/LX
   .        ) / EEJ(1,2,LX-1,Jmn)
   .       + ( FFJ(2,LX-1,Jmn)
   .          +( SUM1(LX) - 2.*SUM3(LX) ) /
   .           ( 2.*ETAA(LX)*X2(LX-1)*LX
   .              + ( VRLX(0) - X(LX)/TAUW ) )
   .         )/( 1./RRADMN - EEJ(2,2,LX-1,Jmn) )
   .     ) / ( ( ( X(LX) - (CDRBR(J)-TAUW/DT)/LX )/X(LX-1)
   .              - EEJ(1,1,LX-1,Jmn)
   .            ) / EEJ(1,2,LX-1,Jmn)
   .        - ( I*2.*X(LX)/LX
   .             *( ETAA(LX)*M/X(LX) + X(LX)/TAUW*CBT(J) )
   .             /(2.*ETAA(LX)*X2(LX-1)
   .                +(VRLX(0)-X(LX)/TAUW)*X(LX)/LX )
   .            + EEJ(2,1,LX-1,Jmn)
   .           ) / ( 1./RRADMN-EEJ(2,2,LX-1,Jmn) )
   .          )
```

Nonetheless, this manipulation allows a mostly implicit evaluation of the most important equation of our set of BCs. This is in fact the only constraint that determines the time evolution of our magnetic field at boundary (and flow velocity), whence the crucial need for all the affordable mutual consistency of all the involved terms.

8.2.2   A fully self-consistent condition for the edge flow

We come now to the implementation of the fluid boundary conditions. Since we have two alternative formulations, already discussed in Sec. 8.1, we need to treat the two cases separately.

(I)   The $v_{\parallel,a} = 0$ constraint

For the case of $v_{\parallel,a} = 0$, we have a three-dimensional edge flow, in the direction perpendicular to the magnetic field. The implementation makes use of the deconvolution technique described in Chapter 7 and is a generalisation of Eq. 7.10, where instead of the axisymmetric loop electric field, we leverage

the full electric field response of the resistive shell:

$$\underline{v_{r,a}^{\perp}} = \frac{1}{\left(B_a^2\right)^0} \left[\underline{\underline{E_{\theta,a}}} \cdot \underline{B_{z,a}} - \underline{\underline{E_{z,a}}} \cdot \underline{B_{\theta,a}} - \underline{\underline{\langle B_a^2 \rangle}} \cdot \underline{v_{r,a}^{\perp,\text{old}}} \right], \tag{8.20}$$

$$\underline{v_{\theta,a}^{\perp}} = \frac{1}{\left(B_a^2\right)^0} \left[\underline{\underline{E_{z,a}}} \cdot \underline{B_{r,a}} - \underline{\underline{\langle B_a^2 \rangle}} \cdot \underline{v_{\theta,a}^{\perp,\text{old}}} \right], \tag{8.21}$$

$$\underline{v_{z,a}^{\perp}} = \frac{1}{\left(B_a^2\right)^0} \left[-\underline{\underline{E_{\theta,a}}} \cdot \underline{B_{r,a}} - \underline{\underline{\langle B_a^2 \rangle}} \cdot \underline{v_{z,a}^{\perp,\text{old}}} \right]. \tag{8.22}$$

Recall here our compact matrix-vector notation in the space of SpeCyl's modes to signify that the equation is computed sequentially for each simulation mode. Also recall that (see Property 4)

$$\underline{\underline{\langle A \rangle}} \cdot \underline{B} = \sum_{(\mu,\nu) \neq (m.n)} \hat{A}^{m-\mu,\,n-\nu} \, \hat{B}^{\mu,\nu}.$$

The squared Cartesian amplitude of the magnetic field

$$\underline{B_a^2} = \underline{\underline{B_{r,a}}} \cdot \underline{B_{r,a}} + \underline{\underline{B_{\theta,a}}} \cdot \underline{B_{\theta,a}} + \underline{\underline{B_{z,a}}} \cdot \underline{B_{z,a}},$$

and the resistive wall response (Eq. 8.17)

$$\underline{\mathbf{E}_W} = \underline{E_0}\,\hat{\mathbf{z}} + \frac{a}{\tau_W}\hat{\mathbf{r}} \times [\underline{\mathbf{B}_t}]_-^+$$

are computed right before Eqs. 8.20-8.22, using the most updated values for the magnetic field.

Note that both the implicit assumptions, Eqs. 8.5-8.5, are not explicitly enforced: on the one hand, no term containing $\eta_a \mathbf{J}_a \times \mathbf{B}_a$ is present; on the other hand, Eqs. 8.21-8.22 do not contain $\mathbf{E}_{r,a}$, since this is null by assumption.
Also note that in the ideal wall limit the resistive wall response reduces to

$$\underline{\mathbf{E}_{t,a}} \to E_0\,\hat{\mathbf{z}}\,,$$

while $\underline{B_{r,a}} \to 0$, and we retrieve the purely radial velocity of Eq. 7.10:

$$\underline{v_{r,a}^{\perp}} = \frac{1}{\left(B_{t,a}^2\right)^0} \left[-E_0 \underline{B_{\theta,a}} - \underline{\underline{\langle B_{t,a}^2 \rangle}} \cdot \underline{v_{r,a}^{\perp,\text{old}}} \right],$$

$$\underline{v_{\theta,a}^{\perp}} = 0\,,$$

$$\underline{v_{z,a}^{\perp}} = 0\,.$$

(II) The $v_{t,a} = 0$ constraint

For the case of $\boldsymbol{v}_{t,a} = 0$, we have a full-spectrum but solely radial velocity, as in Eq. 8.11:

$$\underline{v_{r,a}} = \frac{1}{\left(B_{t,a}^2\right)^0} \left[\underline{\underline{E_{\theta,a}}} \cdot \underline{B_{z,a}} - \underline{\underline{E_{z,a}}} \cdot \underline{B_{\theta,a}} - \underline{\underline{\left\langle B_a^2 \right\rangle}} \cdot \underline{v_{r,a}^{\text{old}}}\right]. \qquad (8.23)$$

Also in this case, the squared Cartesian amplitude of $\mathbf{B}_{t,a}$ and the wall response are computed immediately before Eq. 8.23, using the most updated values of the magnetic field.

The same inexplicit enforcement of the implicit assumptions is operated also here, since no term containing $\eta_a \underline{\underline{\mathbf{J}_a}} \times \underline{\mathbf{B}_a} \cdot \hat{\mathbf{r}}$ appears in Eq. 8.23. As anticipated, this formulation foresees no terms containing $\mathbf{E}_{r,a}$ and thus no assumption is made on it, in this case.
Finally, also Eq. 8.23, as Eqs. 8.20-8.22, converge to Eq. 7.10 in the ideal wall limit.

8.2.3 The new arrangement of the corrector step for the SpeCyl code

The hidden assumptions of our model can be inspected to quantify the effectiveness of various implementations in terms of overall self-consistency. A possible source of inconsistency is the unavoidable presence of some "lag" due to our deconvolution technique, which uses the prior time-step evaluation of some quantities as an approximate estimator for their actual values.
During the nonlinear verification benchmark against Pixie3D, which will be the object of the next chapter, this issue was studied in depth. It emerges that there are in fact two passages whose convolutions accuracy is crucial for the time evolution in SpeCyl: the one that determines the edge flow (Eqs. 8.20-8.22 or Eq. 8.23), and - especially - the one that provides the edge values of the magnetic field to be fed to the inwards integration of Thomas algorithm.
It is no wonder why these two passages are so delicate, since they produce the only two sets of edge values - for the flow and for the magnetic field, respectively - that have a direct impact on the whole bulk of the plasma, owing to the inwards integrations performed by the two calls of the Thomas algorithm (see Fig. 8.3). Also, it should not surprise that the single most important equation in the boundary conditions is the evolutionary rule for $\mathbf{B}_{r,a}$ (Eq. 8.19), as it is the only one that contains a time derivative. As a

matter of fact, this equation is enforced only once, during the corrector step, and determining crucially the initial conditions for the inwards integration. This same equation depends on a large number of $\boldsymbol{v} \times \mathbf{B}$ convolutions, in that cumbersome way that was already presented in Sec. 8.2.1.

To face this problem, a small but substantial reformulation of the corrector step was performed, whose scope is marked in Fig. 8.3 with a red rectangle. Aside from this rectangle, Fig. 8.3 is an almost exact replica of Fig. 5.2, which we duplicate here for reader's convenience. Note however that this time, for SpeCyl.2, the velocity boundary computation is not anymore explicit, but rather semi-implicit, thanks to the deconvolution technique.
The corrector step, along with the final computation of the edge flow are rearranged as represented in Fig. 8.4. The previous layout of the last two sections of SpeCyl's main loop was the following:

1) the forwards step of Thomas algorithm would produce a set of linear coefficients, such that the whole magnetic field profile could be derived by assigning the edge values of $\underline{\mathbf{B}}$;

2) the values of $\mathbf{B}_a$ would be computed, according to the most recent estimate of $\underline{\mathbf{B}_a^{\text{old}}}$ (from the intermediate step of the corrector) and of the edge flow $\underline{\boldsymbol{v}_a^{\text{old}}}$ (last section of the previous iteration of the main loop, *i.e.*, evaluated at prior time-step);

3) these edge magnetic values would be fed to the inwards integration of Thomas algorithm;

4) finally, the new velocity boundary would be obtained, using the corrector magnetic field $\underline{\mathbf{B}_a}$ and the most recent evaluation of $\underline{\boldsymbol{v}_a^{\text{old}}}$ (computed at the same point, during the prior iteration of SpeCyl's main loop).

The new rearrangement moves the computation of the velocity boundary before the inwards integration by the Thomas algorithm for the magnetic field. By doing so, it gives the option to iterate the enforcement of the magnetic and fluid boundary conditions, in order to bring them to better mutual consistency, before feeding $\underline{\mathbf{B}_a}$ to the inwards integration.
The new scheme foresees:

1) the Thomas forwards step;

2) the initial computation of $\underline{\mathbf{B}_a}$ from $\underline{\mathbf{B}_a^{\text{old}}} \equiv \underline{\mathbf{B}_a^{**}}$, and from $\underline{\boldsymbol{v}_a^{\text{old}}}$, just as before;
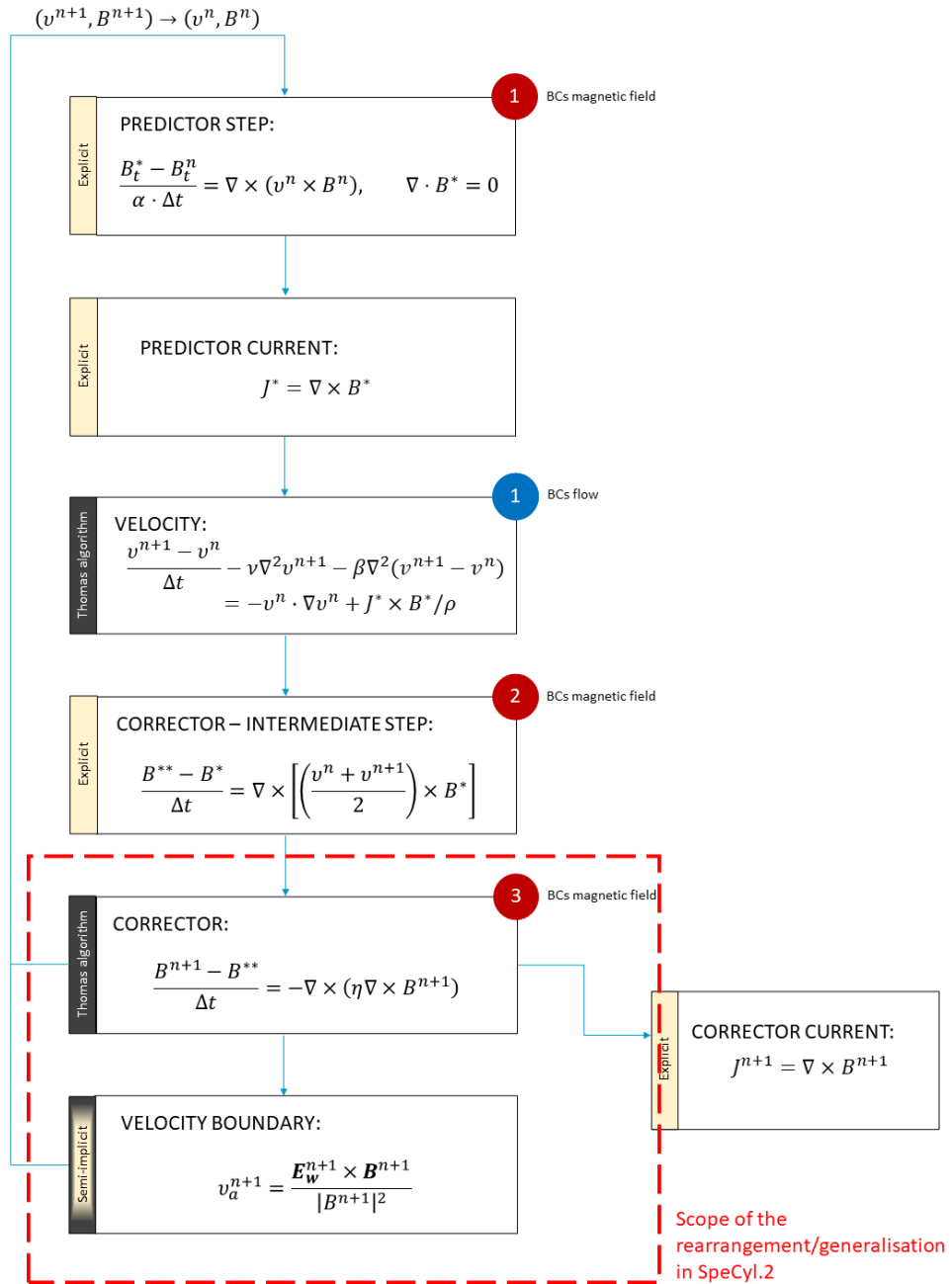
Figure 8.3: On the top of the same work-flow already presented in Fig. 5.2, a red rectangle marks the section of the code whose structure has been rearranged in SpeCyl.2. Note that this time the velocity boundary computation is semi-implicit, owing to the deconvolution technique.
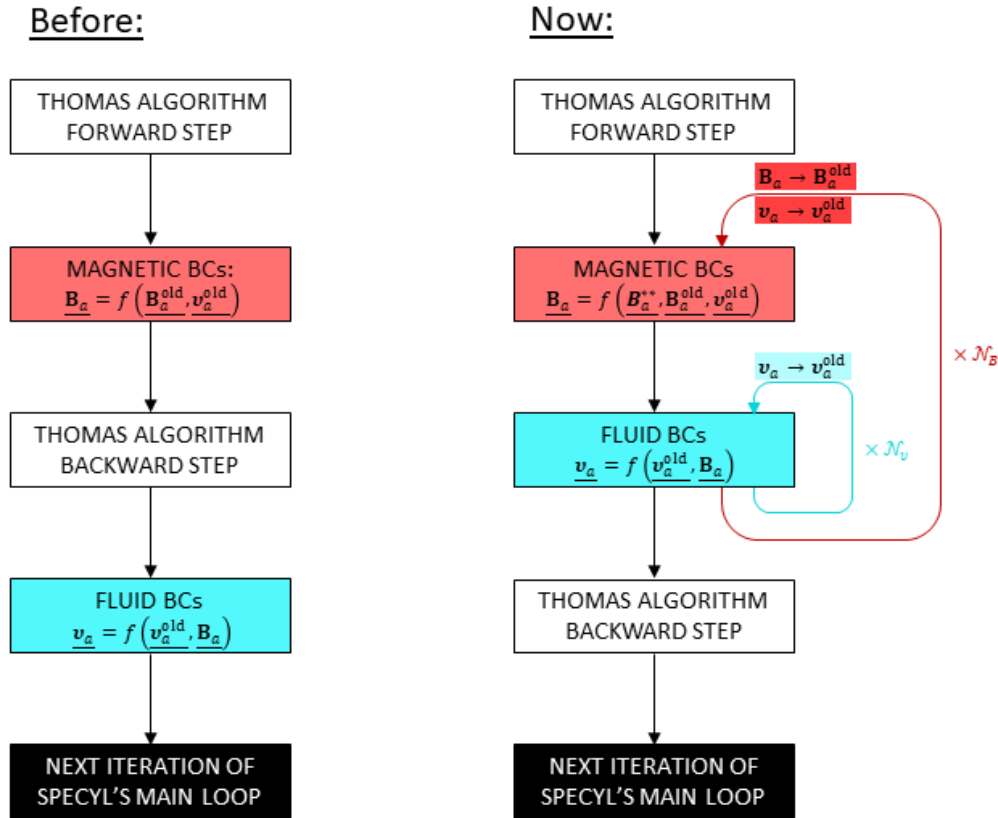
Figure 8.4: New formulation of the magnetic field corrector step: the edge flow is now computed right after the edge values of the magnetic field. It is now possible to cycle $\mathcal{N}_v$ times per time-step the enforcement of the fluid BCs, to minimise the lag between the prior evaluation and the current value. The resulting edge flow can be fed back $\mathcal{N}_B$ times per time-step to recompute $\mathbf{B}_a$ in agreement with the most updated velocity boundary. This ensures better self-consistency at the boundary, in the case of demanding numerical parameters, before starting the inwards integration. Anyway, for most practical cases it is sufficient to operate with $\mathcal{N}_v = \mathcal{N}_B = 1$.

3) the computation of the velocity boundary, using the corrector $\underline{\mathbf{B}}_a$ and the prior time-step evaluation for $\underline{\boldsymbol{v}}_a^{\mathrm{old}}$;

3bis) the repetition of bullet [3], using the corrector $\underline{\mathbf{B}}_a$ and the modes of the edge flow just obtained in [3] as $\underline{\boldsymbol{v}}_a^{\mathrm{old}}$, for the deconvolution technique ([3bis] is repeated $\mathcal{N}_v \geq 1$ times per time-step);

2bis) re-computation of $\underline{\mathbf{B}}_a$, using the corrector magnetic field obtained in [2] as $\underline{\mathbf{B}}_a^{\mathrm{old}}$, the edge flow from [3bis] as $\underline{\boldsymbol{v}}_a^{\mathrm{old}}$, and $\underline{\mathbf{B}}_a^{**}$ only in the evaluation of $\partial_t \underline{\mathbf{B}}_{r,a} = (\underline{\mathbf{B}}_{r,a}^{n+1} - \underline{\mathbf{B}}_{r,a}^{**})/\Delta t$;

2↔3) this outer loop is repeated $\mathcal{N}_B \geq 1$ times per time-step, yielding enhanced self-consistency;

4) final call of the backwards step of the Thomas algorithm and reinitialisation of variables for the new iteration of the main loop.

For most practical applications, $\mathcal{N}_v = \mathcal{N}_B = 1$ and the loop works as before (the displacement of the computation of the fluid boundary inside the magnetic corrector step has no effect if $\mathcal{N}_B = 1$). However there are some cases, typically in extreme numerical conditions (very large radial meshes, very low viscosity and resistivity, as in Chap. 10), in which this modification has indeed a quantitative relevance.

From the verification studies, it seems like $\mathcal{N}_v$ has a relatively low importance and in most cases it can be just set to 1. Nonetheless, it is also true that SpeCyl.2 has still been tested on a few case studies with a very large spectrum of MHD modes (having much longer computational times). Since the error generated by our deconvolution technique scales positively with the number of modes, there is some chance that this term may result having some relevance, after all.

Already with fewer modes, the role of $\mathcal{N}_B > 1$ is much more visible in presence of fast plasma dynamics (or, vice-versa, when relatively large time-steps are used), when the prior time-step evaluation may not be an accurate estimate of the present value.

8.3 Conclusive summary

This Chapter has presented our new set of boundary conditions. Dubbed SpeCyl.2, they accurately model a thin resistive shell facing the plasma, surrounded by a vacuum region (modelled analytically) and by an outer, coaxial conductor at finite and tunable distance.

As already for SpeCyl.2.V00, the shell resistive time-scale τ_W can be set to different values, to reproduce various experimental conditions:

- $\tau_W \gg \Delta t_{\text{sim}}$ (where Δt_{sim} is the simulation time length) identifies the ideal wall limit, where the same assumptions and implications of SpeCyl.1.Vmn are retrieved;

- $\tau_W \lesssim \tau_A$ is the so-called vacuum-wall limit, where the resistive wall formalism acts as an artefact to model a plasma-vacuum free interface;

- $\tau_A \ll \tau_W \ll \Delta t_{\text{sim}}$ aims at reproducing the case of a finitely-resistive physical wall at plasma boundary.

A fully self-consistent edge flow has been formulated and implemented: as for the magnetic part, the implementation has been made flexible to meet specifically the requirements of the modelling of different experimental conditions:

- a three-dimensional velocity $\boldsymbol{v}_{\perp,a}$, perpendicular to the magnetic field at boundary, is preferentially used to model the vacuum wall limit. This choice relies on the absence of friction terms with the resistive shell, so that finite azimuthal and axial velocities can freely set and grow, and on the explicit assumption that the boundary does not behave as a sink/source of electric charge;

- a purely radial velocity $\boldsymbol{v}_{r,a}$ is typically used along with higher values of τ_W, to reproduce a finitely-resistive physical wall. SpeCyl's model equations do not allow the evolution of mass density, so that the physical interpretation of such a velocity does not involve the penetration of mass inside the wall, but rather the local velocity field that can guide impinging particles or suck the wall sputtering inside the plasma. On a wider note, our simplified MHD model is totally insufficient to describe the plasma-wall interaction from a microscopic viewpoint, hence even a slightly controversial assumption on boundary flow can be accepted, if it consistently closes our set of equations (while providing more freedom to the MHD modes);

- in the ideal wall case, both formulations of our fluid boundary collapse in the same purely radial condition, already valid for SpeCyl.1.Vmn.

Not only does SpeCyl.2 generalise all the previous implementations - that can all be retrieved as limit cases - but it amends several small inconsistencies of the previous implementations and even provides some metrics to evaluate the overall grade of consistency throughout each simulation.

This is only possible by tracking the model implicit assumptions and using them to provide a quantitative metric, simulation by simulation. These have been highlighted in Sec. 8.1, along with the reformulation of the fluid boundary.

The implementation is discussed in Sec. 8.2 and involves three important changes from the previous versions: namely, the generalisation of the magnetic boundary conditions to a three-dimensional (unlike ever before) and full-spectrum edge flow, the implementation of a flexible module to compute either $\boldsymbol{v}_{r,a}$ or $\boldsymbol{v}_{\perp,a}$, upon user's request, and a rearrangement of the corrector step in the SpeCyl code, leading to enhanced mutual consistency between the magnetic and the fluid boundary, resulting in augmented self-consistency of the whole simulations code. The opportunity of this last modification is motivated by extreme numerical cases, even if it is normally sufficient to rely on the other modifications to achieve reliable results.

All along, SpeCyl.2 is an articulate reformulation of SpeCyl's boundary conditions and can be defined as a major step towards a more realistic description of the plasma edge in this code.

Part V

New magneto-fluid BCs: nonlinear verification

9

Nonlinear verification benchmark against Pixie3D

With the increasing relevance of advanced numerical tools in modern science [Tang02], a crucial role is played by the verification and validation procedure. The term "verification" refers to the specific effort of ensuring the mathematical correctness of a numeric tool in solving its model equations, whereas "validation" signifies the endeavour of assessing to which extent a numerical model can capture the experimental phenomena [Greenwald10]. Many recent examples of verification studies regarding the external kink and resistive wall modes can be found in literature, *e.g.*, here: [Ramasamy22, Artola18].

We present in this Chapter the cross-verification benchmark between SpeCyl and Pixie3D, both enforcing a thin resistive shell module at their boundary. This comes as a substantial extension of a previous successful verification study between the same two codes [Bonfiglio10] and focuses specifically on the verification of resistive-wall boundary conditions, recently implemented in both codes.

SpeCyl.2 boundary conditions have already been widely presented in Chap. 8. As for Pixie3D, Sec. 9.1 gives a synthetic overview of the two alternative implementations: dubbed "Pixie3D-A" and "Pixie3D-B", respectively.

Section 9.2 illustrates the set-up of this verification, that includes several case-studies, both in the reversed field pinch and in the tokamak. Consequently, Sec. 9.3 constitutes the attempt of deriving a general method from the nonlinear verification of these two codes, highlighting the most useful tests and practices. In Sec. 9.4 we present the diagnostic tools we used to look into our codes, to compare them with one another and to assess their mutual- and self-consistency.

After these preliminary Sections, we start to present our numeric results, in

Secs. 9.5, 9.6, and 9.7. The aim of these three Sections is twofold: on the one hand, the robust results we present will ensure the mathematical correctness of both codes, on the other hand, we present some decisive tests that have motivated some of the choices in the final implementation of SpeCyl.2 (whose final layout has already been presented in Chap. 8).

We start from Sec. 9.5: here two interesting limit case-studies are used to test the magnetic boundary specifically (damping the edge flow to negligible values with high viscosity) and the fluid boundary (in the ideal wall limit, where the magnetic BCs are greatly simplified). The main focus in this Section is on the excellent final agreement on these preliminary tests and on its implications about the correctness of the implementations of the two codes. Section 9.6 reports some of the most relevant tests we made in the general case of both resistive boundary and full plasma response. In particular, this section motivates the great attention that we dedicated, already in Chap. 8, to ensuring full self-consistency of our codes, both by tracking the implicit model assumptions and by rearranging the structure of the corrector step in SpeCyl. In this case, the emphasis is on the motivations that led us to the reorganisation of the corrector step in SpeCyl.2, as it has been presented in Chap. 8.

Sec. 9.7 illustrates our final results on three physically relevant case studies: a marginally resonant kink mode in the RFP, the effect of the ideal-wall proximity in stabilising a non-resonant kink mode in the RFP, and an external kink mode $m = 1$ in the tokamak. In this Section, the accent is on the excellent agreement of the two codes in all the case studies, and on its strong implications for their correctness and reliability.

Finally, Sec. 9.8 contains the usual conclusive summary.

The work presented in this chapter was produced in collaboration with Dr. Luis Chacón and part of it was performed during my stay at Los Alamos National Laboratory, in the USA. Most of the arguments of this chapter have been gathered in an article, soon to be submitted to Physics of Plasmas: along with the numerical verification outcomes, it will also contain an analytical derivation of our model equations in general curvilinear geometry, to comply with Pixie3D's implementation.

9.1   Pixie3D and its boundary conditions

We have already presented the main characteristics of the Pixie3D code in Sec. 7.2.1, so we will not repeat the full introduction. Anyways, both SpeCyl and Pixie3D work here with the same simplified set of model equa-

Table 9.1: Major structural differences between the two codes.

SpeCyl	Pixie3D
Single implementation in variables $\{\mathbf{v}, \mathbf{B}\}$	Two alternative implementations: • Pixie3D-A in $\{\mathbf{v}, \mathbf{A}\}$ • Pixie3D-B in $\{\mathbf{v}, \mathbf{B}\}$
Semi-implicit time-stepping	Fully implicit time-stepping
Cylindrical geometry	Arbitrary curvilinear geometry
Fully spectral	Pseudo-spectral resistive-wall BCs

tions already enforced in [Bonfiglio10], to find a common ground of applicability: uniform and constant mass density ρ, uniform plasma viscosity ν, zero-β regime and no Hall effect in Pixie3D. Moreover, two fluid effects are switched off in PIXIE3D, as well as the artificial viscosity in SpeCyl's momentum equation.

Table 9.1 presents the main differences between SpeCyl and Pixie3D: some of them were already mentioned in Sec. 7.2.1, some other will be evident as we keep going. For now, it is enough to remark the two, quite different, numerical approaches to solve the same model of equations.

This is for instance the case of our deconvolution technique, which has hitherto only been verified in the ideal wall limit: this is a complex solution to a problem that in Pixie, where model equations are set in the physical space, can be simply dealt with a product or a ratio between real numbers.

On the other hand, the fully spectral implementation of SpeCyl is an advantage with respect to the pseudo-spectral implementation of Pixie3D, since the FFT algorithm embedded in Pixie3D's main loop must be tested to be held reliable.

Among these differences, a very important one is the fact that Pixie3D comes in two alternative implementations: Pixie3D-A and Pixie3D-B, leveragin a vector potential formalism and a magnetic field formalism, respectively. The rest of this section briefly presents the implementation of Pixie3D's BCs in this two formulations.

The content of the rest of this section is reported for completeness of information and in no way contains my original contribution. I record here Pixie3D's formulation with the consent of Dr. Luis Chacón.

9.1.1   Magnetic boundary in vector potential formalism: Pixie3D-A

As a first thing, the electric field at the resistive shell is computed with an explicit step, using the values of $\mathbf{B}_{t,a}$ evaluated at prior time-step and the coefficients $\Theta_{m,n}$ and $Z_{m,n}$ already defined to treat the vacuum magnetic field (Eqs. 6.10-6.17). This is done in a pseudo-spectral approach, relying on an FFT algorithm, and anti-transforming to the physical space the updated result $\mathbf{E}_W$. This is update features an explicit stability time-step limit, which in cylindrical coordinates takes the form of

$$\Delta t \lesssim 0.5\,\tau_W\,\Delta r\,. \tag{9.1}$$

The temporal evolution of the tangential components of $\mathbf{A}$ at the resistive wall can be found from the equation (in the Weyl gauge $\varphi = 0$):

$$\partial_t(\mathbf{n} \times \mathbf{A}_a) + (\mathbf{n} \times \mathbf{E}_W) = 0, \tag{9.2}$$

where $\mathbf{n}$ is the normal vector to the plasma surface, which is in Pixie3D a general curvilinear surface. As already discussed in Sec. 7.2.1, Pixie3D works on a logical mesh $\boldsymbol{\xi}$, which is transformed to the coordinates system of interest by a transformation $\mathbf{x}(\boldsymbol{\xi})$, so that $\mathbf{n} = \nabla_{\mathbf{x}}\boldsymbol{\xi}$ [Chacón04]. Throughout this chapter we will always refer to cylindrical geometry, so that $\hat{\mathbf{n}} = \mathbf{n}/|\mathbf{n}| \equiv \hat{\mathbf{r}}$. Therefore, Eq. 9.2 gives:

$$\partial_t(\mathbf{n} \times \mathbf{A})_a + \frac{1}{\tau_W}[\mathbf{n} \times \mathbf{n} \times \mathbf{B}_{t,a}]_-^+ \tag{9.3}$$

$$= \partial_t(\mathbf{n} \times \mathbf{A})_a - \frac{|\mathbf{n}|}{\tau_W}[\mathbf{B}_{t,a}]_-^+ = 0,$$

since $(\mathbf{n} \times \delta\mathbf{B}_{t,a}) \times \mathbf{n} = |\mathbf{n}|\,[\mathbf{B}_{t,a}]_-^+$ because $\mathbf{n} \cdot [\mathbf{B}_{t,a}]_-^+ = 0$. This equation provides all required temporal evolution information for the vector potential. In practice, the tangential components of the vector potential at the wall are advanced at the beginning of the time-step with an explicit update as:

$$\mathbf{n} \times \mathbf{A}_a^{n+1} = \mathbf{n} \times \mathbf{A}_a^n - \Delta t(\mathbf{n} \times \mathbf{E}_a^n). \tag{9.4}$$

The normal $\mathbf{A}$-component is determined from the tangential ones using the solenoidal condition in Weyl gauge.

The evolution eq. 8.19 is particularly cumbersome in Pixie3D, since the normal $\mathbf{B}$-component descends from the solenoidal property. Instead, an approach is pursued that leverages the divergence cleaning step already performed. The idea is to use the tangential $\mathbf{A}$-components boundary update

in Eq. 9.4 and incorporate it in the divergence cleaning step. This is done as follows. Let us start again from the Pixie3D divergence cleaning procedure:

$$\nabla^2 \delta \mathbf{A}_a = \nabla \times (\mathbf{B}_a^{n+1} - \mathbf{B}_a^n). \tag{9.5}$$

The resulting magnetic field update is

$$\mathbf{B}_a^{n+1} = \mathbf{B}_a^n + \nabla \times \delta \mathbf{A}_a.$$

In the previous implementation [Chacón04, Bonfiglio10], with an ideal wall facing the plasma, Eq. 9.7 is solved with $\mathbf{A}_{t,a} = 0$, and enforcing $\nabla \cdot \mathbf{A} = 0$ for the normal component. With a resistive wall, the homogeneous Dirichlet BCs become inhomogeneous, as:

$$\mathbf{n} \times \delta \mathbf{A}_a = -\Delta t(\mathbf{n} \times \mathbf{E}_a^n).$$

The new vector potential update (which includes the RW update) is found from eq. 9.7 with these new BCs.

9.1.2 Magnetic boundary in magnetic field formalism: Pixie3D-B

The implementation of Pixie3D-B has been subject to major modifications throughout this verification study. We report here its final layout.

The first step is again to compute the resistive wall response from the magnetic field components at prior time-step and leveraging the already defined coefficients $\Theta_{m,n}$ and $Z_{m,n}$ with a pseudo-spectral approach. This is done in the same way as for Pixie3D-A, with the same resulting limit on the time-step width, already expressed in Eq. 9.1.

In line of principle, eq. 8.19 could be used to update the normal component of the magnetic field, as it is done in most codes [Paccagnella07, Becerra16, Kruger04, Schnack86], including SpeCyl.2. However, this is infeasible for Pixie3D's implementation, since it conflicts with the enforcement of the solenoidal property. Instead, the pursued approach leverages the already present divergence-cleaning step of Pixie3D's main loop. Such a technique is needed in this code to remove the non-solenoidal pollution introduced by the pre-conditioner for the Newton-Krylov implicit solver [Chacón04, Chacón06]. The divergence cleaning step aims to find a divergence-clean updated magnetic field in the form of

$$\mathbf{B}^{k+1} = \mathbf{B}^k + \nabla \times \delta \mathbf{A}, \tag{9.6}$$

where $\delta \mathbf{A}$ is an *ad-hoc* potential correction. Since we assume that the prior evaluation of the magnetic field is already solenoidal, adding a correction in

the form of a curl cannot alter its divergence[1].

$\delta\mathbf{A}$ is obtained from

$$\nabla^2\delta\mathbf{A} = \nabla \times (\mathbf{B}^{k+1} - \mathbf{B}^k), \tag{9.7}$$

which is solved with the same boundary conditions as for the analogous problem in the implementation of Pixie3D-A: $\delta\mathbf{A}_{t,a} = 0$ and $\nabla \cdot \delta\mathbf{A}_a = 0$ for the ideal wall case, and

$$\mathbf{n} \times \delta\mathbf{A}_a = -\Delta t\ \mathbf{n} \times \mathbf{E}_W^k,$$

for the resistive wall case.

The new vector potential update found from Eq. 9.7 with this boundary condition includes the RW response, and is then used in Eq. 9.6 to find the new-time magnetic field, which is automatically solenoidal.

For the tangential field components, Pixie3D-B enforces the *force-free* assumption $\mathbf{J} \times \mathbf{B} = 0$. The resulting constraint reads:

$$\mathbf{J}_{t,a} = \lambda\mathbf{B}_{t,a}, \qquad \text{with } \lambda = \frac{\mathbf{E}_w \cdot \mathbf{B}_{t,a}}{\eta|\mathbf{B}_a|^2}. \tag{9.8}$$

9.1.3   Velocity boundary conditions

Concerning the velocity boundary conditions, not much should be said, since they are totally equivalent to their counterpart in SpeCyl.2.

Also for Pixie3D (both implementations) there are two alternative formulations for the velocity boundary:

- A purely perpendicular edge velocity, in the form of:

$$v_{\parallel,a} = 0\ ;\quad \boldsymbol{v}_a = \boldsymbol{v}_{\perp,a} = \frac{\mathbf{E}_W \times \mathbf{B}_a}{|\mathbf{B}_a|^2}.$$

  preferentially used for the modelling of a plasma-vacuum free interface.

- A purely normal (radial) edge velocity, in the form of:

$$v_{n,a} = \frac{(\mathbf{E}_W \times \mathbf{B}_a) \cdot \hat{\mathbf{n}}}{|\mathbf{B}_{t,a}|^2}, \qquad \boldsymbol{v}_{t,a} = 0,$$

  typically used for modelling a physical resistive shell.

Unlike the case of SpeCyl.2, it must be remarked that the implementation in Pixie3D works in the physical space, allowing to treat the products and (especially) the ratios as common operations between real numbers.

---

[1]The divergence of a curl is always null, since it is the product of a symmetric tensor ($[\nabla\cdot]_i \equiv \delta_i^j\partial_j$) with an anti-symmetric one ($[\nabla \times \mathbf{A}]_i \equiv \varepsilon_i^{\ell,m}\partial_\ell A_m$)

9.2   Numerical set-up

For the present verification study, the usual paramagnetic pinch initial equilibrium is enforced, as presented in Sec. 5.2.1. The resistivity profile is rendered in both codes with the usual Eq 5.12:

$$\eta(r) = \eta_0 \left[1 - (\texttt{ALET} - 1)\ r^{\texttt{BEET}}\right]^{\texttt{GAET}},$$

while the viscosity and the mass density have a uniform profile.
In this verification study we both explored case-studies in RFP geometry and in the tokamak. Table 9.2 reports the most important parameters defining the RFP and tokamak reference initial equilibria, always valid unless specified.
  The resulting plot of equilibrium quantities is reported in Fig. 9.1.

Table 9.2: General plasma and RW parameters chosen for the RFP (first line) and tokamak (second line) verification cases.

$\alpha(0)$	R/a	η_0	ALET	BEET	GAET	ν	τ_w/τ_A	b/a	ρ
4	4	$3.33 \cdot 10^{-5}$	21	10	1	10^{-2}	100	1.5	1
0.5	10	10^{-5}	1.01	2	-1	10^{-5}	$10^{-6} \to 1$	100	1

On the top of this equilibrium, at the first time-step in both codes, a velocity perturbation in the form of Eq. 5.6 is excited for the dominant mode (m, n) of the specific simulation:

$$\delta\boldsymbol{v} = \frac{\varepsilon}{r} \sin\left(\pi r\right)^{m+2} \cos\left(m\theta + nz/R\right) \hat{\mathbf{r}},$$

with $\varepsilon = 10^{-6}$. Throughout this work, $m = 1$ and n will be specified case by case.

All the simulations presented here are in 2D helical geometry: in SpeCyl, this means taking several harmonics of the same dominant mode (the one that gets excited initially), plus the axisymmetric equilibrium represented in Fig. 9.1. For Pixie3D, a change of coordinates from the logical Cartesian-like $\boldsymbol{\xi}$ is set, such that $\mathbf{x}(\boldsymbol{\xi}) : \{r,\ u,\ z\} \to \{r\cos\left((u - kz)/m\right), r\sin\left((u - kz)/m\right), z\}$, with $u = m\theta + kz$ (where m and $k = n/R$ define the helical pitch).
Finally, Table 9.3 presents all the simulations that compose this verification benchmark study in two-dimensional RFP geometry for both codes. For each, some of the relevant input parameters are reported, such as the time-step length, the radial mesh refinement, the number of modes (in SpeCyl), and the refinement of the azimuthal mesh (in Pixie3D).

Table 9.3: Numeric parameters used in simulations: 2D helical pitch, normalized time-step, number of points in the radial or azimuthal mesh, and number of modes.

SPECYL: Simulation nick-name	m/n	$\Delta t/\tau_A$	N_r	$N_{\text{modes}}{}^*$
Double_vac_kn0 $\to 4^{**}$	-1	10^{-2}	128	32
PP.m1n8.tW1e10	-8	10^{-3}	100	32
PP.m1n8.tW1e2.Vt	-8	10^{-3}	100	32
PP.m1n8.tW1e2.Vp	-8	10^{-3}	100	32
PP.m1n6.tW1e0.b/a0 $\to 2$	-6	$10^{-3\,\to\,-5}$	100	10
PP.m1n6.tW1e2.b/a0 $\to 2$	-6	$10^{-3\,\to\,-5}$	100	10
TK.m1n1.tW1e-2$\to$-6.S1e4	-1	10^{-5}	256	10
TK.m1n1.tW1e-2$\to$-6.S1e5	-1	10^{-5}	256	10
TK.m1n1.tW1e-2$\to$-6.S1e6	-1	10^{-5}	300	10
TK.m1n1.tW1e-2$\to$-6.S1e7	-1	10^{-5}	1000	10
TK.m1n1.tW1e-8.S1e7.qa0.4$\to$1	-1	10^{-5}	1000	10

PIXIE3D: versions A and B Simulation nick-name	m/n	$\Delta t/\tau_A$	N_r	N_θ
Double_vac.pixA.kn0 $\to 4$	-1	10^{-2}	128	32
Double_vac.pixB.kn0 $\to 4$	-1	10^{-2}	128	32
PP.m1n8.tW1e10.pixB	-8	1.0	128	64
PP.m1n8.tW1e2.pixA.Vt	-8	1.0	128	32
PP.m1n8.tW1e2.pixA.Vp	-8	1.0	128	32
PP.m1n8.tW1e2.pixB.Vt	-8	1.0	128	64
PP.m1n8.tW1e2.pixB.Vp	-8	1.0	128	64
PP.m1n6.pixA.tW1e0.b/a0 $\to 2$	-6	10^{-2}	256	64
PP.m1n6.pixB.tW1e0.b/a0 $\to 2$	-6	10^{-2}	256	64
PP.m1n6.pixA.tW1e2.b/a0 $\to 2$	-6	10^{-2}	256	64
PP.m1n6.pixB.tW1e2.b/a0 $\to 2$	-6	10^{-2}	256	64
TK.m1n1.tW1e-2$\to$-6.S1e5.pixB	-1	10^{-5}	$0.5\tau_W/N_r$	64

Legend of colours:	Fig. 9.2;	Fig. 9.3-9.5;	Fig. 9.13-9.15;
	Fig. 9.16;	Fig. 9.17;	Fig. 9.18-9.19.

$*$ The number of modes only refers to $m \geq 0$, since in helical geometry all modes with the same $|m|$ are complex conjugate of one another. The full spectrum hence counts $2 \times N_{\text{modes}} + 1$ modes.

$**$ Here and elsewhere we use an arrow to condense in one line a group of simulations whose names are diversified only by a numerical value: in this case, this are as follows: Double_vac_kn0, Double_vac_kn0.5, Double_vac_kn1, Double_vac_kn2, Double_vac_kn4.
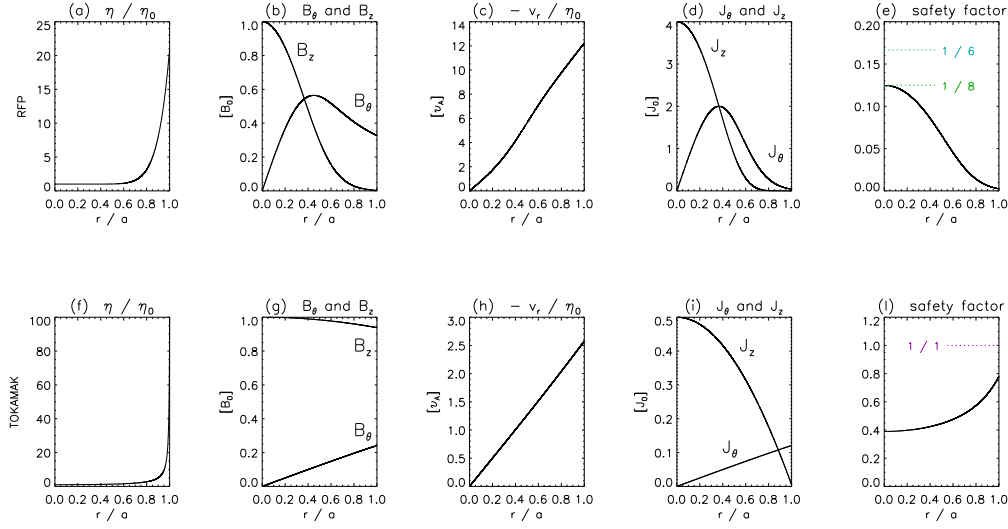
Figure 9.1: Initial equilibrium profiles for the verification in RFP configuration (a-e) and in the straight tokamak (g-l). All units are normalised up to SpeCyl's convention: $v_A = a/\tau_A$, $B_0 = |\mathbf{B}(0)||_{t=0}$, $J_0 = v_A B_0$, and $\eta = 1/S$.

9.3 Definition of the verification procedure

Before illustrating our results, we summarize the employed verification procedure.

For a better understanding of modes dynamics we performed all tests in Fourier space. We have used in particular three diagnostic tools to analyse the simulation results with a high level of detail:

D1. Time plot of normalised Kinetic and Magnetic energies of modes, defined as:

$$E_{kin}^{m,n} \equiv \int_0^a |\boldsymbol{v}^{m,n}|^2 r\, dr, \qquad E_{mag}^{m,n} \equiv \int_0^a |\mathbf{B}^{m,n}|^2 r\, dr.$$

They give a space-averaged overlook on the evolution of the two main fields.

D2. Radial profiles of $\boldsymbol{v}$, $\mathbf{B}$, $\mathbf{J}$, $\mathbf{E}$ components at fixed time-snapshots.

D3. Magnetic helical flux projection onto the $z = 0$ plane, which will be more properly defined later. The agreement between Pixie3D and SpeCyl concerning the 2D plots of this quantity at different time-snapshots produces a very challenging final test for the magnetic field evolution.

Along with them, we defined two fundamental and quick-read figures of merit:

F1. Linear growth rate (exponential fit of early growth of the dominant mode of either E_{kin} or E_{mag}) is a quantitative and direct estimator of codes agreement.

F2. $\eta_a \mathbf{J}_a \times \mathbf{B}_a$ smallness in time with respect to $\mathbf{E}_a \times \mathbf{B}_a$: it is a metric of self-consistency in BCs implementation.

The diagnostics and figures of merit will be defined more in detail in Sec. 9.4.

Before verifying of the full set, the fluid and the magnetic BCs can be tested separately in suitable limit cases:

L1. Effective vacuum behaviour for the plasma can be obtained by setting instant resistive and viscous diffusion ($S = P = 1$, *i.e.* $\eta = \nu = 1$). We can thus produce a double-vacuum case-study, where the RW has effective vacuum on both sides: the fluid response of such a viscous plasma shrinks quickly, while the edge magnetic field is slowly damped on the RW time-scale.

L2. The ideal wall limit for $\tau_w \gg \tau_A$ reduces the magnetic part of the BCs to be equivalent to their original formulation, still retaining some complexity in its fluid counterpart.

Only after that, the final and longest step of the verification can take place: single blocks of the two codes are isolated and tested against one another, until full agreement is found. Among the (many) tests we set, we found some very useful methods:

M1. Check first those parts that produce a simple output, *e.g.*, lists of parameters, such as $\Theta_{m,n}$ and $Z_{m,n}$.

M2. Re-derive the model of both codes using a white board and check for self- and mutual-consistency. Look for easy metrics, such as F2. As a matter of fact, the careful re-derivation of the model behind our boundary conditions, already presented in Chap. 8, originates from this verification endeavour.

M3. Make single time-step evolution tests to isolate the onset of discrepancies. Combining this method with a sudden change of simulation parameters (*e.g.*, by changing within the time-step τ_W by several orders of magnitude) helps identify and correct intrinsic lags of either code.

The rest of this chapter will be organised as follows: Sec. 9.4 explores more in depth the diagnostics (D1-D3) and figures of merit (F1-F2), providing the specific formulae and implementations used throughout the verification; Sec. 9.5 presents the two limit cases (L1-L2) and their final verification results; Sec. 9.6 reports some of the most interesting tests performed in the full nonlinear verification (M1-M3), and aims to provide a synthetic overview of the main steps of the verification; Sec. 9.7 presents the final outcomes of this work, obtained in RFP geometry; Sec. 9.8 provides the usual conclusive summary to this Chapter.

9.4 Suitable diagnostics and figures of merit

We define in this section the diagnostic tools D1-D3 and the figures of merit F1-F2, used throughout the verification procedure. The concepts introduced in this Section are quite standard and are only presented for completeness, apart from the $\mathbf{J}_a \times \mathbf{B}_a \cdot \hat{\mathbf{r}}$ diagnostics, presented in Sec. 9.4.3.

The time-snapshots of radial profiles do not need any further introduction: the raw data at the end of SpeCyl's simulations are analysed with post-processing routines that were already available before the beginning of my PhD and have already been used throughout my Thesis. On the other hand, corresponding profiles for Pixie3D are obtained via a Fourier transform of fields in real space.

Concerning the growth rates, to comply with what is done in Pixie3D, an alternative but equivalent approach is used in this chapter: instead of fitting the linear growth of the dominant mode of one quantity (typically, $v_{r,a}^{m,n}(t)$ or $B_{r,a}^{m,n}(t)$) the fit is performed on the linear growth of the magnetic or kinetic energy of the dominant mode. This can be done either directly, as an exponential fit on the time history, or indirectly, by averaging the value of its time-derivative, which is flat throughout the linear-growth regime.
All the three methods are always used together, to get redundancy of information: in general they all agree within a few percents. In any case, all the growth rates reported in this chapter are computed as a numeric fit on the linear growth of the magnetic energy of the dominant MHD mode of the simulation.

We define in the next subsections the remaining three diagnostic tools, that we implemented from scratch, and possibly require some analytical background.

9.4.1 Normalised Kinetic and magnetic energies of modes

We define the normalised kinetic and magnetic energies of modes as the $L2$ norms of the corresponding velocity and magnetic field, respectively:

$$E_{kin}^{m,n} \equiv \int_0^a |\boldsymbol{v}^{m,n}|^2 r \, dr, \qquad \text{kinetic energy of mode } (m,n), \qquad (9.9)$$

$$E_{mag}^{m,n} \equiv \int_0^a |\mathbf{B}^{m,n}|^2 r \, dr, \qquad \text{magnetic energy of mode } (m,n). \qquad (9.10)$$

These are of course not the Fourier modes of the global kinetic or magnetic energy of the plasma, but rather the energy contributions provided by each MHD mode.

In fact, the $L2$ norm in cylindrical space of, *e.g.*, velocity reads:

$$||\boldsymbol{v}||_2 \equiv \int_0^{2\pi} \mathrm{d}\theta \int_0^{2\pi R} \mathrm{d}z \int_0^a r\mathrm{d}r \left(\sum_{m,n} \boldsymbol{v}^{m,n}(r)\, e^{im\theta + i\frac{n}{R}z} \right) \left(\sum_{p,q} (\boldsymbol{v}^*)^{p,q}(r)\, e^{-ip\theta - i\frac{p}{R}z} \right)$$

$$= \mathcal{K} \int_0^a r\mathrm{d}r \sum_{m,n} |\boldsymbol{v}^{m,n}|^2,$$

where $\mathcal{K}$ is a normalisation constant (in dimensional units it would be $\mathcal{K}_{kin} = 4\pi^2 R\rho/2$ for Kinetic energy and $\mathcal{K}_{mag} = 4\pi^2 R/2\mu_0$ for Magnetic energy). In the second line, the two integrals on θ and z get simplified, producing Kroneker's deltas like $\delta^{m,p}$ and $\delta^{n,q}$, owing to the orthogonal property of the Fourier base. A formally identical argument holds for the magnetic energy and the $L2$ norm of the magnetic field. In Eqs. 9.9 and 9.10 the normalisation constants are set to $\mathcal{K} = 1$.

In other words, it results that the relation they have to the global plasma kinetic and magnetic energies are the following:

$$E_{kin}^{\text{tot}} = \sum_{m,n} E_{kin}^{m,n}, \qquad\qquad E_{mag}^{\text{tot}} = \sum_{m,n} E_{mag}^{m,n}.$$

For the implementation of this diagnostic tool, the easiest strategy would be to sum the energies of SpeCyl's modes, to compare them with Pixie3D's total energies. Nonetheless we pursue the more useful and instructive approach of Fourier-transforming Pixie3D's outputs (leveraging the built-in FFT algorithm of the IDL coding language) and plotting the energy of each mode separately.

9.4.2 Helical flux function

The helical flux function χ is a convenient scalar function that can be used to study the geometrical properties of a two-dimensional magnetic field, that

winds into a helix around the z-axis. Its re-derivation has constituted a theoretical exercise during my month at Los Alamos National Laboratory, under the guidance of Dr. Luis Chacón.

With respect to the full 3D cylindrical geometry in which we usually work, the helix defines a new constraint that lowers the dimensionality of our problem:

$$\zeta = m^*\theta + k_n^* z \,, \tag{9.11}$$

where m^* and $k_n^* = n^*/R$ define the helical pitch. Lines of constant ζ wind around the helical axis z, with a given azimuthal periodicity of $2\pi m^*/k_n^*$. We seek to write now the helical flux χ in an explicit way, starting from its defining property:

$$\mathbf{B} = \nabla\chi \times \hat{\mathbf{z}} + B_z\,\hat{\mathbf{z}} \,. \tag{9.12}$$

Let us move to a helical set of coordinates (r', ζ, z'): this is defined from the cylindrical coordinates by leveraging Eq. 9.11:

$$\begin{cases} r' = r \,, \\ \zeta = m^*\theta + k_n^* z \,, \\ z' = z \,. \end{cases} \qquad \text{with} \qquad \begin{cases} r = \sqrt{x^2 + y^2} \,, \\ \theta = \arctan\frac{y}{x} \,, \\ z = z \,. \end{cases}$$

It is useful to define immediately the Jacobian of the transformation from Cartesian coordinates to helical coordinates. The most convenient way to do this is to pass through the cylindrical coordinates, as the two transformations become much more immediate. From helical to cylindrical coordinates the Jacobian determinant is

$$\left| \frac{\partial\{r', \zeta, z'\}}{\partial\{r, \theta, z\}} \right| = \begin{vmatrix} 1 & 0 & 0 \\ 0 & m^* & k_n^* \\ 0 & 0 & 1 \end{vmatrix} = m^*$$

while from cylindrical to Cartesian, as known, it is $1/r$. The Jacobian determinant of the whole transformation thus reads:

$$\left| \frac{\partial\{r', \zeta, z'\}}{\partial\{x, y, z\}} \right| = \frac{m^*}{r} \qquad \Longleftrightarrow \qquad \left| \frac{\partial\{x, y, z\}}{\partial\{r', \zeta, z'\}} \right| = \frac{r}{m^*} \tag{9.13}$$

Let us now restrict our interest to a plane of constant z: the helical components of the magnetic field on it are

$$B_{r'} = \mathbf{B} \cdot \nabla_{\{x,y,z\}} r' = \frac{r}{m^*} B_r \,,$$

and

$$B_\zeta = \mathbf{B} \cdot \nabla_{\{x,y,z\}} \zeta = \frac{r}{m^*} \mathbf{B} \cdot \hat{\boldsymbol{\zeta}} \,,$$

where $\hat{\boldsymbol{\zeta}}$ can be readily written in cylindrical coordinates as

$$\hat{\boldsymbol{\zeta}} = \frac{m^*}{r} \hat{\boldsymbol{\theta}} + k_n^* \hat{\mathbf{z}} \,.$$

We are now ready to deal with the projection of Eq. 9.12 in the transversal plane to the z-axis. We may write:

$$\frac{r}{m^*} B_r = \partial_\zeta \chi \,, \qquad B_\zeta = B_\theta + \frac{k_n^* r}{m^*} B_z = -\partial_r \chi \,. \qquad (9.14)$$

These two relations extend the result in [Petrie07] to the case of $m^* \neq 1$. We can turn Eqs. 9.14 into integral form, finding

$$\chi(r,\zeta) = \int_0^\zeta \frac{rB_r}{m^*} \mathrm{d}\zeta + \mathcal{A}(r)$$

$$\chi(r,\zeta) = -\int_0^r \left(B_\theta + \frac{rk_n^*}{m^*} B_z \right) \mathrm{d}r + \mathcal{B}(\zeta)$$

where $\mathcal{A}(r)$ and $\mathcal{B}(\zeta)$ are unknown scalar functions. We can constrain them by looking at two instructive cases:

$$\chi(0,\zeta) = \mathcal{A}(0) = \mathcal{B}(\zeta), \qquad \forall\, \zeta \,,$$

$$\chi(r,0) = -\int_0^r \left(B_\theta + \frac{rk_n^*}{m^*} B_z \right)_{\zeta=0} \mathrm{d}r + \mathcal{B}(0) = \mathcal{A}(r), \qquad \forall\, r \,.$$

Since χ appears in Eq. 9.12 only through its gradient, it is defined up to an additive constant: this can be used to set $\mathcal{A}(0) = 0$, and thus also $\mathcal{B}(\zeta) = 0$, $\forall\, \zeta$, as a consequence of the first constraint.
The second constraint yields the final result we are looking for:

$$\chi(r,\zeta) = \int_0^\zeta \frac{rB_r}{m^*} \mathrm{d}\zeta - \int_0^r \left(B_\theta + \frac{rk_n^*}{m^*} B_z \right)_{\zeta=0} \mathrm{d}r \,. \qquad (9.15)$$

Finally, we shall make one further step and write Eq. 9.15 also in the Fourier space, as well as all the other diagnostic tools. For this, it is convenient to settle on the plane $z = 0$, so that $\zeta = m^*\theta$:

$$\chi(r,\theta) = \sum_{m,n} \chi^{m,n}(r,\theta)$$

$$\text{with } \chi^{m,n}(r,\theta) = -irB_r^{m,n}(r)\frac{e^{im\theta}-1}{m} - \int_0^r \left(B_\theta^{m,n}(r) + \frac{rk_n^*}{m^*} B_z^{m,n}(r) \right) \mathrm{d}r \,.$$

$$(9.16)$$

As for the magnetic energy, please note that $\chi^{m,n}$ is not a Fourier mode of χ. Throughout the verification study, Eq. 9.16 is solved numerically for the MHD modes of SpeCyl and for the Fourier decomposition of Pixie3D's results.

9.4.3 The $\mathbf{J}_a \times \mathbf{B}_a \cdot \hat{\mathbf{r}}$ diagnostics

Finally, the $\mathbf{J} \times \mathbf{B}_a \cdot \hat{\mathbf{r}}$ diagnostics is a metric of self-consistency in the implementation of the code. Its theoretical background has already been presented in the detail in Chap. 8: the formulation of both our sets of boundary conditions implicitly require that

$$(\eta_a \mathbf{J}_a \times \mathbf{B}_a \cdot \hat{\mathbf{r}})^{m,n} \ll (\mathbf{E}_a \times \mathbf{B}_a \cdot \hat{\mathbf{r}})^{m,n} \, .$$

This assumption extends also to the $\hat{\boldsymbol{\theta}}$ and $\hat{\mathbf{z}}$ directions when enforcing $v_{\parallel,a} = 0$ BCs.

This property is thus a possible quantifier of the implementation self-consistency. We define a safety parameter

$$X^r \equiv \left(X^r_{0,0} \ldots X^r_{M_{\max},N_{\max}} \right)^T \, , \qquad \text{with } X^r_{m,n} = \frac{(\eta_a \mathbf{J}_a \times \mathbf{B}_a \cdot \hat{\mathbf{r}})^{m,n}}{(\mathbf{E}_a \times \mathbf{B}_a \cdot \hat{\mathbf{r}})^{m,n}} \, , \quad (9.17)$$

to keep track of the implementation self-consistency:

- $X^r \geq 1$ defines the "inconsistency domain", where the model assumption is not fulfilled.

- $X^r < 1$ defines the "self-consistency domain", where we should expect our simulation to stay, throughout its temporal evolution.

Also in this case, as for the energies of modes and for the helical potential of various modes, $X^r_{m,n}$ is not the Fourier component of any relevant quantity. This means that both in SpeCyl and in Pixie3D we will always need to compute the Fourier spectrum of numerator and denominator preliminarily. In Pixie3D, the products are performed in the physical space and subsequently transformed with the built in FFT of IDL, while SpeCyl uses either a direct approach, based on convolutions, or an indirect one, relying on the built-in FFT method of IDL to perform the products in the physical space. The two alternative approaches for SpeCyl provide perfectly compatible outcomes.

Since each component of X^r ultimately contains the convolutions of several modes of three different plasma quantities, some discrepancy between SpeCyl's and Pixie3D's outcomes is generally tolerated, provided that the

Table 9.4: Adjustments made on the two codes in order to achieve the good agreement on the limit cases L1-L2.

SPECYL	PIXIE3D
general de-bugging	revision of the pre-conditioner for the solver revision of the divergence-cleaning scheme general de-bugging

both keep in the self-consistency domain.

As we will motivate in Sec. 9.6, this diagnostic tool had a central role in the rearrangement of the corrector step in SpeCyl (see Sec. 8.2).

9.5   Limit case studies

The full set of boundary conditions can be preliminarily tested in two limit cases, where the magnetic part of the BCs or their fluid part have a dominant role, respectively. These two cases (L1-L2, following Sec. 9.3) are presented through this section.
Despite we present here just the final results, there is of course a long work behind them. When we started our verification benchmark, evident qualitative agreement between the two codes was definitely present, however spoiled by various quantitative discrepancies, both in radial profiles and (especially) in their time-evolution.
Table 9.4 summarises the main adjustments that the two codes needed to achieve the results presented through this section.

9.5.1   The double vacuum test

This test was invented and proposed by Dr. Luis Chacón. The idea is to reproduce effective vacuum behaviour in the plasma domain by setting extremely high values for the plasma resistivity and viscosity ($\eta = \nu = 1$, corresponding in codes' normalised units to instant visco-resistive diffusion: $\tau_R = \tau_V = \tau_A$). We can thus set an effective vacuum in plasma region, similar to the actual vacuum outside the resistive wall. High plasma viscosity will act fast damping of any flow, leaving us with almost pure magnetic BCs. This is much alike to the "current-ring" case study, already presented in Chap. 3 for the verification of the Newcomb's equation numeric solver.
For a generic $k_n = n/R \neq 0$ the "vacuum" solution of the Poisson's problem

in the plasma region must be (see Eq. 3.29-3.30):

$$\phi_P^{m,n} = a_P^m \, I_m(|k_n|r) + b_P^m K_m(|k_n|r) \,.$$

By regularity on axis, we find

$$\phi_P^{m,n}(|k_n|\hat{r}) = a_P^m(t) I_m(|k_n|r),$$

where we have made apparent that the coefficient will be time dependent (decaying). Assuming $a_P^m(t = 0) = 1$, the corresponding initial condition for the magnetic field in the plasma domain is:

$$
\begin{aligned}
\{B_r^{m,n}\}^P &= \frac{\partial \phi_P^{m,n}}{\partial r} = a_P^m(t)|k_n|I_m'(|k_n|r), \\
\{B_\theta^{m,n}\}^P &= \frac{1}{r}\frac{\partial \phi_P^{m,n}}{\partial \theta} = a_P^m(t)\frac{im}{r}I_m(|k_n|r), \\
\{B_z^{m,n}\}^P &= \frac{\partial \phi_P^{m,n}}{\partial z} = 0.
\end{aligned}
$$

The vacuum solution for the actual vacuum region, beyond the thin shell, is must comply with Eq. 6.9:

$$\phi_V^{m,n} = B_{r,a}^{m,n} g_{m,n}(r)\,, \qquad g_{m,n}(r) = \frac{1}{|k_n|}\left[\frac{I_m'(|k_n|b)K_m(|k_n|r) - K_m'(|k_n|b)I_m(|k_n|r)}{I_m'(|k_n|b)K_m'(|k_n|a) - K_m'(|k_n|b)I_m'(|k_n|a)}\right],$$

where $B_{r,a}^{m,n} = a_P^m(t)\,|k_n|I_m'(|k_n|a)$, by continuity of the normal component of the magnetic field across the RW (Eq. 6.1). The resulting initial condition for the magnetic field in the external vacuum region is then

$$\{B_r^{m,n}\}^V = a_P^m(t) I_m'(|k_n|a) \cdot g_{m,n}'(r)\,.$$

We look now for the an analytical solution for the time evolution of the radial magnetic field on the RW. This is the same as finding the temporal evolution of the coefficient $a_P(t)$, via Eq. 8.19,

$$\frac{\partial_t a_P^m}{a_P^m} = \frac{1}{\tau_W}\left[g_{m,n}''(a) - |k_n|\frac{I_m''(|k_n|a)}{I_m'(|k_n|a)}\right] = \frac{1}{\tau_W}f(m,|k_n|,b), \qquad (9.18)$$

where

$$g_{m,n}''(a) = |k_n|\frac{I_m'(|k_n|b)K_m''(|k_na|) - K_m'(|k_n|b)I_m''(|k_n|a)}{I_m'(|k_n|b)K_m'(|k_n|a) - K_m'(|k_n|b)I_m'(|k_n|a)}.$$
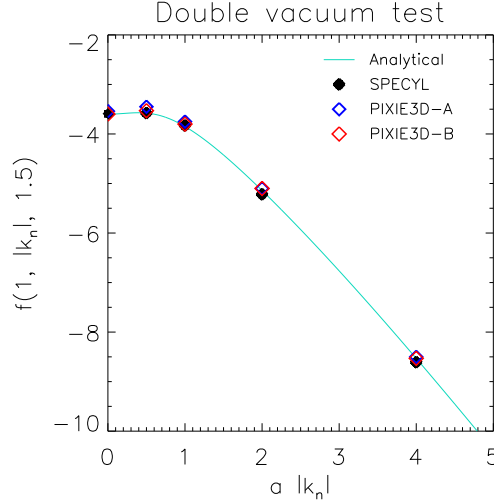
Figure 9.2:   Comparison of decay rates for the double-vacuum test (with $m = 1$, $b/a = 1.5$).

The case of $k_n = 0$ (large aspect ratio, or $n = 0$) can be easily found by approximating both Bessel's functions to their first term in their series development: $K_m(x) \approx x^{-m}$ and $I_m(x) \approx x^m$. This way, equation 9.18 reduces to

$$\frac{\partial_t a_P^m}{a_P^m} = -\frac{1}{\tau_W} \frac{2}{a} \frac{2(b/a)^{2m}}{(b/a)^{2m} - 1} = \frac{1}{\tau_W} f(m, 0, b). \qquad (9.19)$$

In both Eq. 9.18 and 9.19 the l.h.s. is negative and does not depend on time, hence our analysis predicts a linear decay.

Figure 9.2 illustrates the remarkable agreement between the two codes and with the analytical results. Each symbol corresponds to a simulation (referring to Tab. 9.3, the nicknames of the represented simulations are associated to the light-blue colour, both for SpeCyl and for the two implementations of Pixie3D).For the general set-up, we used the same parameters as in Tab. 9.2. In each simulation, the decay rate was computed numerically (as a fit) and divided by τ_W: different values of τ_W were explored, giving compatible results.

9.5.2   The ideal wall limit

Complementary to the double vacuum test, we present here the ideal wall limit case, obtained for $\tau_w = 10^{10}\,\tau_A$. The simulations presented here are the ones referenced in Tab. 9.3 with the nicknames: *PP.m1n8.tW1e10* for SpeCyl and *PP.m1n8.tW1e10.pixB* for Pixie3D-B (associated to the lighter

green colour in the Table).

In this limit, in the absence of non-axisymmetric $\mathbf{E}_W$ shell response at plasma boundary, there is no relevant difference between the two formulations of our fluid BCs, nor are there actual reasons to distinguish between Pixie3D-A and Pixie3D-B. For this reason, we only display here a study between Pixie3D-B and SpeCyl, with no-slip ($\boldsymbol{v}_{t,a} = 0$) BCs.

We examine the stability of a marginally resonant kink mode $(1, -8)$ in the RFP, in presence of a tightly fitting ideal wall at plasma edge. This case was also analysed in [Bonfiglio10], obtaining a remarkable agreement between the two codes, still enforcing an ideal-wall module at plasma boundary. In that case, already briefly discussed in Sec. 7.2, linear growth rate compatibility within a 0.3% tolerance was obtained, and both codes predicted a very similar nonlinear temporal evolution, up to $5000\,\tau_A$.

As was already anticipated in Sec. 7.2, some small differences were yet present, all depending on the simplified assumption of a purely axisymmetric boundary flow in SpeCyl.1. These were corrected in SpeCyl.1.Vmn, thanks to the implementation of the deconvolution method.

What this test aims to prove is thus ultimately the capability of SpeCyl.2 to fall back to the same predictions of SpeCyl.1.Vmn, in the limit case of an ideally conducting shell (along with an analogous test for Pixie3D-B).

Figure 9.3 displays the radial, azimuthal and axial components of the first three Fourier modes of some relevant plasma quantities, at the final, nonlinearly saturated state produced after $5000\,\tau_A$ from the initial perturbation. Not only this is very similar to the original verification study presented in [Bonfiglio10] (see Fig. 10 in the Reference), but the agreement in the edge radial flow between the two codes presents no visible differences. A separate comparison with SpeCyl.1.Vmn (not shown here) proves the perfect overlapping of profiles, ensuring once more that the new implementation of SpeCyl's boundary can reliably substitute the ideal-wall implementations in the limit of large τ_W.

From the second line of plots, we see that even after such a long evolution time, the magnetic field penetration in the (almost) ideal wall is still negligible, in accordance with the physical expectations. This can be better observed in Fig. 9.4, which presents the helical flux projection on a cylindrical cross-section $z = 0$ for both codes at selected times. As already apparent in fig. 9.3, there is a remarkable similarity between the outcomes of the two codes: the progress in the radial drift of the helical axis from the centre to a saturated $m = 1$ final configuration is almost identically reproduced.

Figure 9.5 reports the first $500\,\tau_A$ of temporal evolution for the normalised kinetic and magnetic energies of modes. Also in this case, the agreement

is excellent, even if slightly better for the magnetic energy modes: this is probably due for the low-m modes to some difference in the radial profiles of the components of $\boldsymbol{v}^{m,n}$ away from the boundary, as can be seen in the first line of plots in Fig. 9.3. Some more visible (in log-scale) discrepancy in the kinetic energy of high-m modes is not concerning, since it happens on extremely small scales ($E_{kin}^{m,n} \lesssim 10^{-12}$).

Fitting the linear growth of the magnetic (or kinetic) energy of mode $(1, -8)$ we find $\gamma\,\tau_A = 7.797 \cdot 10^{-2}$ for SpeCyl and $\gamma\,\tau_A = 7.821 \cdot 10^{-2}$ for Pixie3D-B, compatible within $0.3\,\%$. Apart from confirming overall excellent match in this limit-case, this will also set the aim for the comparison with the full BCs set-up, presented in Sec. 9.7.

The linear growth saturates around $\sim 120\,\tau_A$, when two kinetic energy modes have reached comparable magnitude with the axisymmetric mode. From $\sim 400\,\tau_A$ the simulation enters a stationary saturated equilibrium, very similarly reproduced by both codes. It is interesting to notice from the fourth line of plots in Fig. 9.3 that the flat radial profiles of both $E_\theta^{0,0}$ and $E_z^{0,0}$ is physically compatible with a stationary conditions, since it implies that the axisymmetric mode is not evolving. This follows from the Faraday's law:

$$-\partial_t B_z^{0,0} = \partial_r E_\theta^{0,0} = 0\,,$$

and

$$\partial_t B_\theta^{0,0} = \partial_r E_z^{0,0} = 0\,.$$

This seems to suggest preliminarily some good physical consistency in reproducing the plasma dynamics.

9.6   General test-cases with both RW and full flow response: preliminary numerical checks

This Section preludes to the final results of our verification benchmark, presented in Sec. 9.7. We present here some of the most interesting tests that eventually brought us to the excellent final agreement.

This is an important part, since it accounts for a very long endeavour: if it took us not more than three weeks to get to an agreement on the limit case studies, we needed more than five months to reach the positive situation that the next section will present.

Figure 9.6 reports for reference the starting point of this journey: we present the comparison between SpeCyl and Pixie3D-B, concerning the temporal evolution of the energies of modes and of the helical flux projection onto the plane $z = 0$. The case study constitutes a small variation on the one
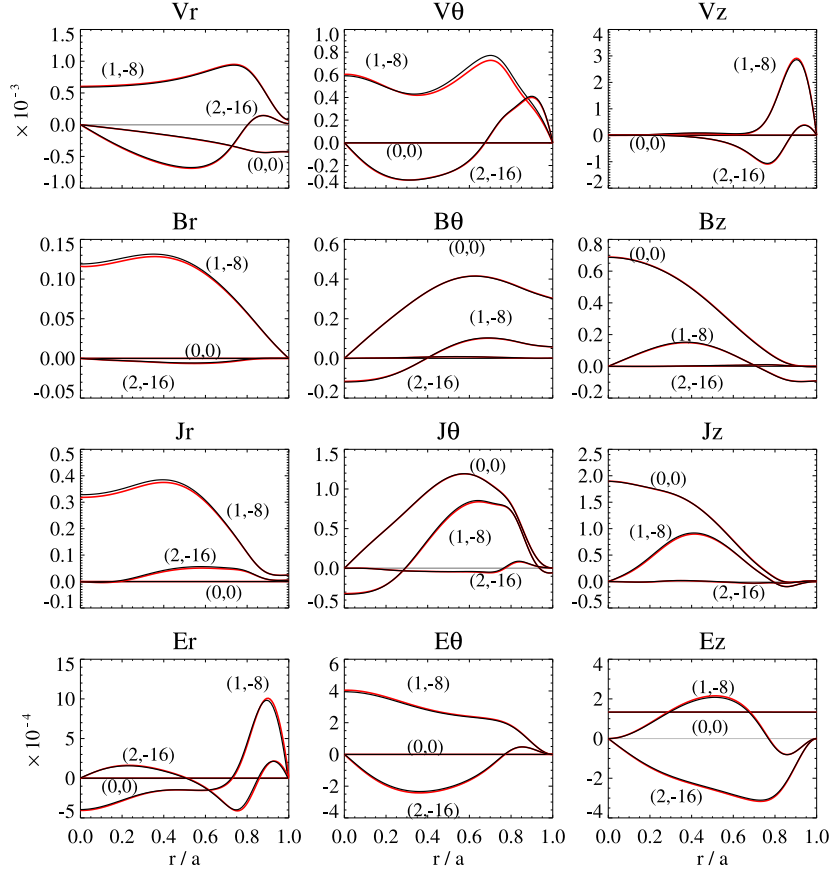
Figure 9.3: *Ideal wall limit test case.* Radial plot of the main plasma quantities, defining the nonlinearly saturated helical equilibrium after $5000\,\tau_A$ in the ideal-wall limit ($\tau_w = 10^{10} \times \tau_A$. Fourier modes $m = 0, 1, 2$ are represented for both Pixie3D-B (**red**) and SpeCyl (**black**). Units are normalised according to SpeCyl's conventions: velocities to $v_A = a/\tau_A$, magnetic fields to $B_0 = |\mathbf{B}(0)|_{t=0}$, currents and electric fields to $v_A B_0$ ($\eta = 1/S$).
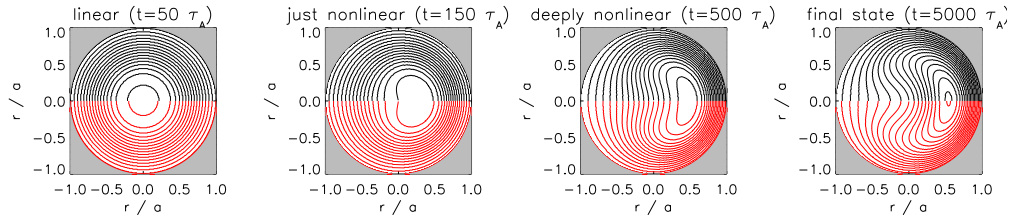
Figure 9.4: *Ideal wall limit test case.* Evolution of the helical flux projection on the cylinder cross-section for Pixie3D-B (lower **red** half) and SpeCyl (upper **black** half). Increasing dominance and saturation of mode $m = 1$ is visible. $\chi = const$ curves must not penetrate the ideal wall.
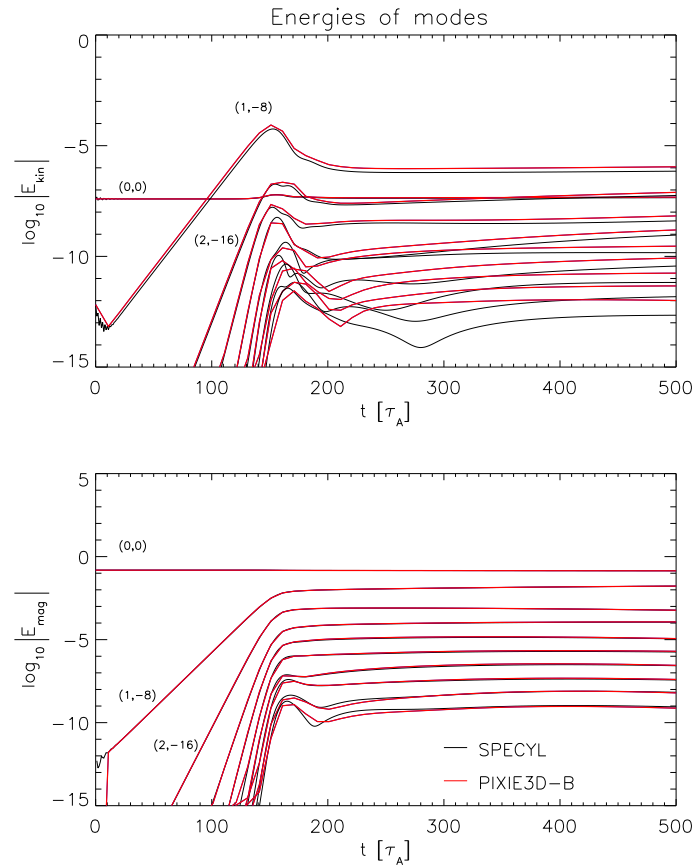
Figure 9.5: *Ideal wall limit test case.* First $500\,\tau_A$ of temporal evolution for the normalised kinetic and magnetic energies of modes, for the ideal wall limit case $(\tau_W = 10^{10}\,\tau_A)$.

already discussed: this is a marginally resonant kink $(1, -8)$ for the same RFP equilibrium, with a resistive shell at plasma boundary $(\tau_W = 100 \, \tau_A)$ and a finitely displaced ideal wall $(b/a = 1.5)$.

As we can see, there is some general and qualitative agreement between the codes, which is however quantitatively unsatisfactory, if compared to the previous agreement in the ideal wall case.

In particular, in Fig. 9.6.(a) Pixie3D has a visibly slower linear-growth (by approximately 3%), anticipated by some important noise in the early phases of the simulation. The agreement is quite poor also concerning the final state, largely dominated in SpeCyl by an $m = 1$ component in the velocity spectrum, while Pixie3D obtains a much more relevant $m = 2$ component. Figure 9.6.(b) confirms that also the magnetic field geometry follows a slightly different evolution.

Despite all these discrepancies, there are of course mostly similarities, which testify that the general agreement between the two codes is not off by far and that there must be something very subtle in the two implementations that cumulates an increasing discrepancy, which is small during the linear phase and gets larger with time.

In the rest of this Section, we organised our work in three phases: a rich and long study on the velocity boundary conditions is reported in Sec: 9.6.1, a schematic list of tests of single modules is to be found in Sec. 9.6.2, while Sec. 9.6.3 presents a decisive final test, concerning the overall structure of the main loop of both codes, that finally led to remarkable agreement.

9.6.1 Single-timestep check

Starting from a discrepancy as the one displayed in Fig. 9.6, the first part of our BCs modules to be tested was the one concerning the velocity: in fact, this is still the least tested part, at least in SpeCyl, where it also involves a high complexity level. We present in this section a very challenging test we set for the velocity boundary, which eventually led to a partial reformulation of its implementation is SpeCyl.

In general, it is a good practice to evolve both codes for a single timestep, and carefully analysing the outcome to isolate those quantities that are found to be already different after such a short time.

In our case, it seems like the source of the discrepancy, albeit present already from the beginning of the simulation, could become more visible in the nonlinearly saturated phase. In other words, for the test to be more instructive, we should start our one-step simulation from an already nonlinear initial
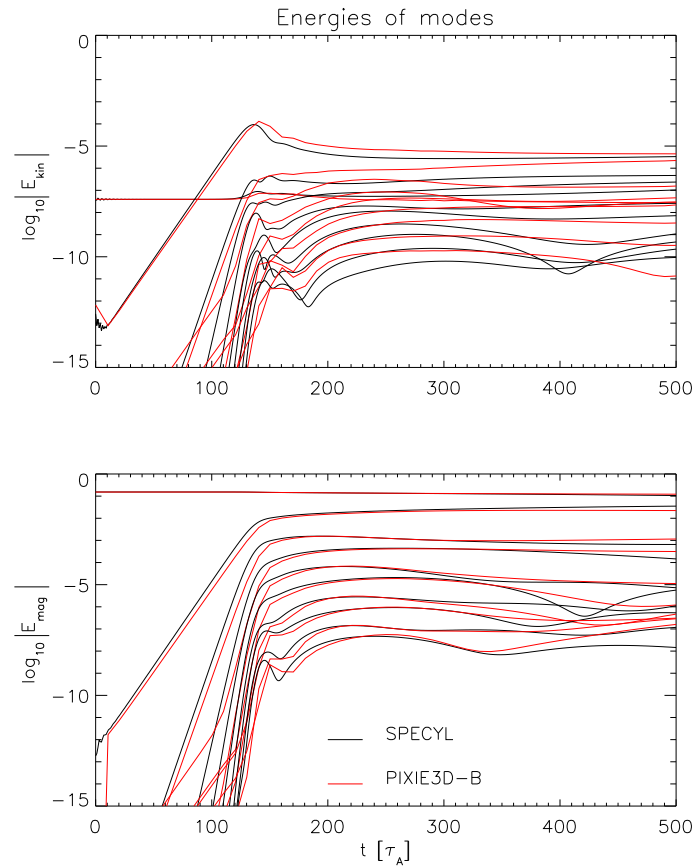
(a) Temporal evolution of the energy of modes.
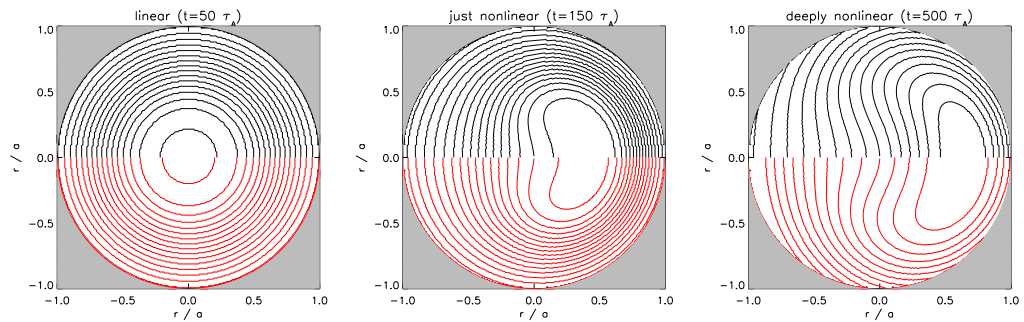
(b) Helical flux projection on the $z = 0$ cross-section.

Figure 9.6: *Full magneto-fluid BCs, marginally resonant kink* $1, -8$. Starting point for our verification study with the full set-up for the magneto-fluid resistive shell module. The case study is a marginally resonant kink mode $(1, -8)$ in the RFP, with a resistive shell at boundary $(\tau_W = 100 \, \tau_A)$ and an ideal wall at finite distance $b/a = 1.5$. For these plots, $\boldsymbol{v}_{t,a} = 0$ BCs are enforced.
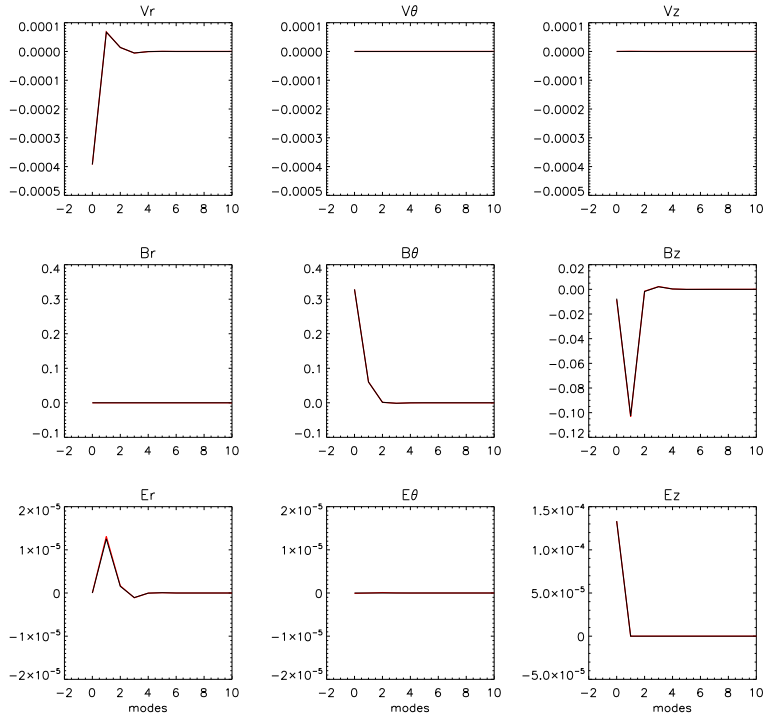
Figure 9.7: *Ideal wall limit case.* Edge spectrum of plasma quantities, for SpeCyl (black) and Pixie3D-B (red), at the final time of the ideal-wall limit case study. Only the first eleven modes are displayed: $(0,0)$, $(1,-8)$, $(2,-16)\ldots(10,-80)$.

state.

However, neither Pixie3D nor SpeCyl is equipped for this, since they are both designed to start from the axisymmetric, paramagnetic pinch equilibrium.

The strategy we pursue leverages the excellent agreement already found in the ideal wall limit case: we start from the nonlinearly saturated final state presented in Fig. 9.3 and restart the simulation with a much lower resistive shell time-constant, from $\tau_W = 10^{10}\,\tau_A$ to $\tau_W = 100\,\tau_A$.

Figure 9.7 stands to confirm - if still needed - that the nonlinear equilibrium we start from is indeed almost equivalent, concerning the plasma edge. It shows the comparison between the boundary values of some plasma quantities, for the first eleven simulation modes of SpeCyl and of the Fourier decomposition of Pixie3D-B's results.

The instantaneous change in the geometry of the system, determined by an abrupt substitution of the ideal wall at plasma boundary with a much more resistive thin shell, is of course a very unphysical situation and only serves for the purpose of this test. We expect that the magnetic configuration with

no radial penetration and very intense discontinuity of $\mathbf{B}_{t,a}$ across the (previously ideal) wall should quickly relax, giving rise to an intense burst in all plasma quantities.

As a first thing, as soon as τ_W shrinks, a very intense electric field should build up on the shell, since Eq. 8.17 prescribes

$$\mathbf{E}_W = \frac{a}{\tau_W}[\hat{\mathbf{r}} \times \mathbf{B}_{t,a}]^+_- ,$$

and $[\hat{\mathbf{r}} \times \mathbf{B}_{t,a}]^+_-$ is quite large. This should immediately determine a strong variation in the edge flow, which is proportional to the electric field response of the shell. The magnetic field should follow, through the $\boldsymbol{v} \times \mathbf{B}$ products, and rapidly bring the simulation to a global and probably violent relaxation. From what we just said, it appears how this study can constitute a very stringent test for the implementation of the fluid boundary conditions. In practice, we decided to keep the magnetic evolution from evolving (by manually substituting its boundary conditions with trivial Dirichlet constraints, to fix them at their prior value) and just focused on the evolution in the edge electric field and edge flow. Figure 9.8 presents the result of this test. We immediately see that, according to our predictions, the radial edge flow (no-slip boundary conditions are enforced throughout this study) and the electric field components have changed drastically from Fig. 9.7, in both codes. However, while the electric field is still in perfect agreement between the two codes (the discrepancy in $E^{0,0}_{z,a}$ depends only on the fact that Pixie3D uses a separate variable for the loop-field E_0), the radial velocity spectrum presents indeed some differences.

In Fig. 9.8 we also report the spectra for the edge magnetic field components that, by direct imposition, do not vary from Fig. 9.7 and are thus still in perfect agreement.

Since both $\mathbf{E}_a$ and $\mathbf{B}_a$ are in excellent agreement between the two codes, there is no apparent justification for the discrepancy in $v_{r,a}$, unless it is the deconvolution technique that is not working properly.

Recall from Chap. 7 that our technique solves for $v^{m,n}_{r,a}$ the equation:

$$\sum_{\mu,\nu}(|\mathbf{B}_{t,a}|^2)^{m-\mu,n-\nu}v^{\mu,\nu}_{r,a} = \sum_{\mu,\nu}(\mathbf{E}^{m-\mu,n-\nu}_W \times \mathbf{B}^{\mu,\nu}_a)$$

by splitting the first member into

$$(|\mathbf{B}_{t,a}|^2)^{0,0}v^{m,n}_{r,a} + \sum_{\mu \neq m,\nu \neq n}(|\mathbf{B}_{t,a}|^2)^{m-\mu,n-\nu}v^{\mu,\nu}_{r,a} ,$$

and evaluating explicitly the second addend at the prior time-step. In our

convenient matrix formalism (Eq. 8.23):

$$\underline{v_{r,a}} = \frac{1}{\left(B_{t,a}^2\right)^0} \left[\underline{\underline{E_{\theta,a}}} \cdot \underline{B_{z,a}} - \underline{\underline{E_{z,a}}} \cdot \underline{B_{\theta,a}} - \underline{\underline{\left\langle B_a^2 \right\rangle}} \cdot \underline{v_{r,a}^{\text{old}}}\right] ,$$

where

$$\underline{\underline{\left\langle B_a^2 \right\rangle}} \cdot \underline{v_{r,a}^{\text{old}}} \equiv \sum_{\mu \neq m, \nu \neq n} (|\mathbf{B}_{t,a}|^2)^{m-\mu, n-\nu} v_{r,a}^{\mu,\nu}|_{t-dt}$$

takes care of the "off-diagonal" modes of our system of equations.
It is possible that this retarded evaluation introduces some lag in the equations, which is particularly evident in this case of extremely violent and fast relaxation.

This initial suspect is confirmed by some further experiments. The most decisive is assigning to the "off-diagonal" modes the values of the corresponding modes of the Fourier spectrum of the edge flow obtained by Pixie3D for the same time-step. This way, not only there is no lag in the deconvolution, but we must expect to find the same $v_{r,a}^{m,n}$ as Pixie3D, for all m, n, since all the second member in Eq. 8.23 is now compatible or identical to Pixie3D. Since this expectancy is met, then we know there is some weakness in the prior time-step evaluation, which is at the base of our deconvolution technique.

Figure 9.9 shows however that it suffices to iterate the enforcement of the fluid BCs in SpeCyl.2 to recover from the effect of the lag in the deconvolution. This technique relies on the idea of evaluating a trial $v_{r,a}^{m,n}$ via Eq. 8.11, to be subsequently used in place of the prior time-step evaluation in a second enforcement of the same BCs, and so on. The convergence of this method is not granted in principle, and relies on a general property of well-posedness that however seems to hold in all the cases ever explored so far.
As we see from Fig. 9.9.(a), 3 to 5 iterations of this method bring the whole velocity spectrum to convergence to a compatible value with what also Pixie3D-B finds. Fig. 9.9.(b) confirms that the small residual inconsistencies between the two codes are now perfectly compatible with the small differences in all the other quantities.

This important test convinced us in the opportunity of implementing the iterative method for the fluid BCs permanently in SpeCyl.2, as already described in Sec. 8.2.
It must be also said that the case study presented in this Section represents an extreme challenge for the deconvolution method, as normal cases of interest
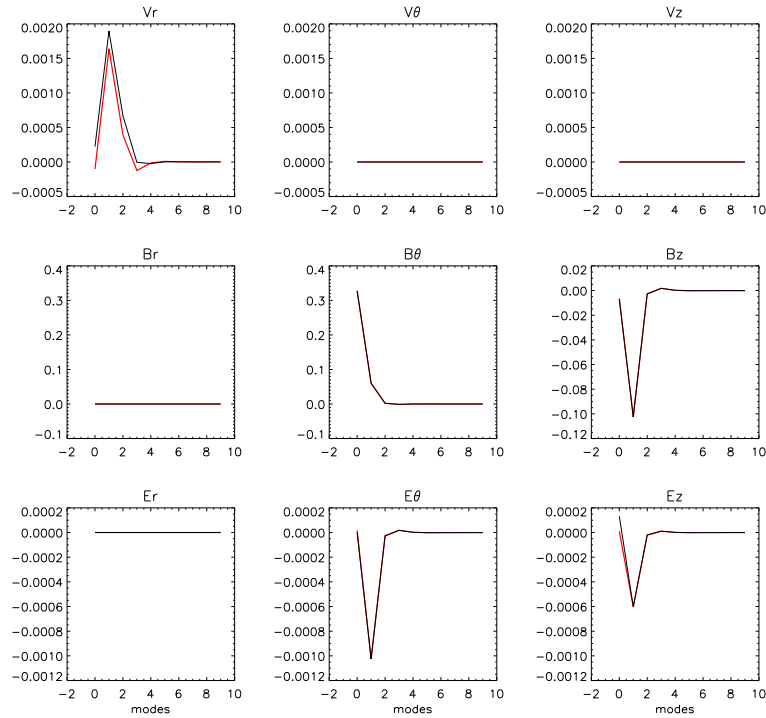
Figure 9.8: *Full magneto-fluid BCs, marginally resonant kink* $1, -8$. Edge spectrum of plasma quantities in the single-timestep test: the final saturated equilibrium of an ideal wall simulation is evolved for a single time-step after replacing the ideal wall with a much more resistive one. The magnetic field components are kept artificially constant. The electric field thin-shell response reacts the same way in the two codes to the sudden change in the BCs, while the edge radial flow in SpeCyl (black) is subject to some lag, owing to the prior-timestep evaluation leveraged in the deconvolution technique.

(a) Convergence study.

(b) Final outcome.
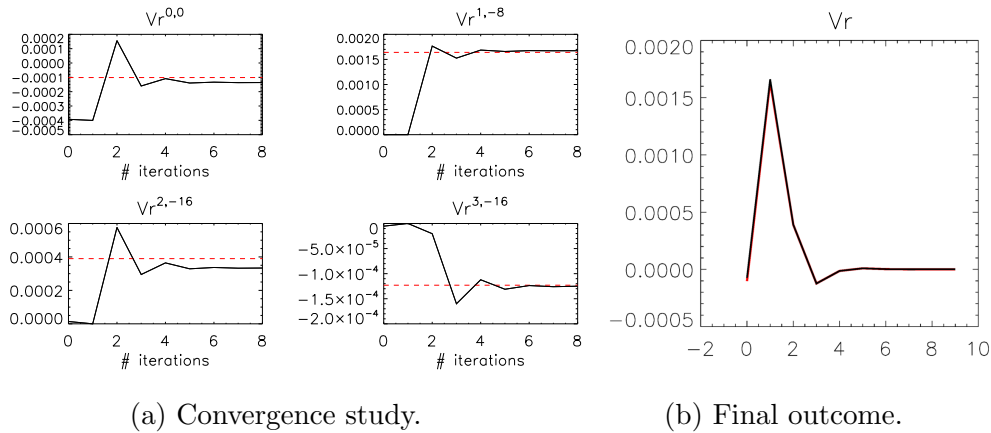
Figure 9.9: *Full magneto-fluid BCs, marginally resonant kink* $1, -8$. The iteration of the enforcement of fluid BCs can effectively overcome the lag introduced by the deconvolution technique. (a) Convergence in $3 - 5$ iterations of SpeCyl's fluid BCs to a compatible value with respect to Pixie3D-B (red line). (b) Edge radial velocity spectra in comparison, after iterating SpeCyl's fluid BCs 5 times.

can rarely exhibit such a fast variation of the entire spectrum of the edge flow (in this case 65 modes, symmetric across $(0,0)$).

9.6.2 Intermediate tests and codes modifications

After we had already implemented the correction for the lag in the deconvolution technique, just presented in the previous subsection, some marginal improvement in the agreement between the codes was achieved, but the overall situation was far from being solved.

Furthermore, some explorative tests with a purely axisymmetric edge radial velocity, kept constant at a pre-assigned value, still retained almost the same level of discrepancy between SpeCyl and either implementation of Pixie3D, proving that some other module in either code was faulted, apart from the fluid BCs.

We performed a long series of tests in collaboration with Dr. Luis Chacón, leading to the correction of several aspects in both codes. The main ones are listed here:

- Test of the electric field response produced by the thin shell: we started by feeding some dummy magnetic field signals to the resistive shell module and comparing the answers. In the end it was more practical

to directly compare the list of values of the shell coefficients $\Theta_{m,n}$ and $Z_{m,n}$. This made evident a bug in the embedding of Pixie3D's logical mesh into 2D helical coordinates.

- Test of the FFT algorithm in Pixie3D against the independent built-in FFT of IDL. The conversion of some outputs from single to double precision achieved a considerable step forward in the matching with SpeCyl.

- Analytical re-derivation of wide parts of the model for the evolution of the flow in SpeCyl. Some minor inconsistency was found and corrected, with no visible effect on simulations outcome.

- General and reiterate debugging.

In the end, almost all modules of each code had been tested and found in agreement with its counterpart in the other code, and yet the matching was still unsatisfactory, if compared to the excellent previous agreement, documented in [Bonfiglio10] and found in the two limit cases.
The last possible place to look into was either a very well hidden mistake in either implementation, or a general "time-stepping" error in either code, *i.e.*, relative to the way that individually working units are put together to form the whole of a time-step advancement.
As Sec. 9.6.3 will argument, it was both.

9.6.3 The self-consistency test and the rearrangement of predictor step in SpeCyl

We present here another test, that represented a turning point in our verification benchmark study. This consisted in the implementation of a quantifier of algorithm self-consistency as the $\mathbf{J}_a \times \mathbf{B}_a \cdot \hat{\mathbf{r}}$ diagnostics (see Eq. 9.17):

$$X^r \equiv \left(X^r_{0,0} \ldots X^r_{M_{\max},N_{\max}} \right)^T , \qquad \text{with } X^r_{m,n} = \frac{(\eta_a \mathbf{J}_a \times \mathbf{B}_a \cdot \hat{\mathbf{r}})^{m,n}}{(\mathbf{E}_a \times \mathbf{B}_a \cdot \hat{\mathbf{r}})^{m,n}} .$$

Figure 9.10 presents the first application of this diagnostic tool on for the usual case study of a marginally resonant $(1, -8)$ kink mode in the RFP with a resistive wall at plasma edge ($\tau_W = 100\,\tau_A$, $b/a = 1.5$), enforcing no-slip BCs. A simulation of SpeCyl (in black) is compared with one performed with Pixie3D-A (in blue), for two different time-snapshots, representing the linear phase ($t = 50\,\tau_A$, see Fig. 9.6) and the beginning of the nonlinear phase

Figure 9.10: *Full magneto-fluid BCs, marginally resonant kink* $1, -8$. Self-consistency test on SpeCyl (black) and Pixie3D-A (blue): it must be that $(\eta_a \mathbf{J}_a \times \mathbf{B}_a \cdot \hat{\mathbf{r}})^{m,n} \ll (\mathbf{E}_a \times \mathbf{B}_a \cdot \hat{\mathbf{r}})^{m,n}$ for all modes. This is represented as a ratio between the two quantities and plot for the various modes $(0, 0) \dots (32, -256)$ at two time snapshots, one linear and one nonlinear. SpeCyl modes stay dangerously closer to the "inconsistency" domain, for $X^r \geq 1$.

$(t = 200\,\tau_A)$, respectively. The shaded region in brown represents the condition $X^r \geq 1$, which was previously (in Sec. 9.4.3) dubbed the "inconsistency domain". Only the $m \geq 0$ modes are represented, since in a 2D simulation the rest of the spectrum is just their complex conjugate.

Since early linear evolution, it appears that SpeCyl's modes get dangerously closer the inconsistency domain, with respect to Pixie3D's ones. This concern is widely confirmed by the later evolution, where one mode (and its conjugate) even presents $X^r > 10$. This initially appeared as a signal that the individually tested modules of SpeCyl's implementation were not communicating correctly.

This led to the rearrangement of the predictor step in this code, which has been already described at the end of Chap. 8. The key idea is that the magnetic boundary conditions may be affected by some lag, owing both to the prior-step evaluation in the deconvolutions of the $\boldsymbol{v}_a \times \mathbf{B}_a$ products and to the fact that $\boldsymbol{v}_a$ itself has never been updated since the end of the previous time-step. The adopted scheme, as already explained (refer to Figs. 8.3-8.4), features a first tentative evaluation of the magnetic BCs, whose result is then used to compute a tentative $\mathbf{E} \times \mathbf{B}$ velocity, which is subsequently used for a second tentative evaluation of the magnetic boundary conditions and so on. The described loop iterates $\mathcal{N}_B$ times per time-step. On the top of this, if the iterative method for the correction of the lag in the fluid BCs (refer to Sec. 9.6.1) is active, the velocity boundary gets now updated $\mathcal{N}_B \times \mathcal{N}_v$ times per time-step.
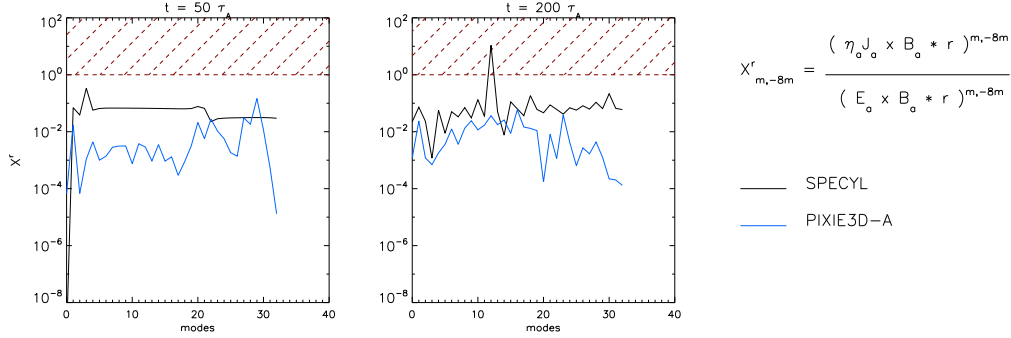
Figure 9.11: *Full magneto-fluid BCs, marginally resonant kink* $1, -8$. Self-consistency test on SpeCyl (black) and Pixie3D-A (blue), enforcing the iterative method in the boundary conditions, $\mathcal{N}_B = 3$ times per time-step, each time iterating also the enforcement of the fluid BCs $\mathcal{N}_v = 5$ times. This time SpeCyl self-consistency is comparable to Pixie3D's, and both codes stay well within the "self-consistency" domain, for $X^r \ll 1$.

Figure 9.11 presents the same analysis as in Fig. 9.10, repeated for an identical SpeCyl's simulation that however enforces $\mathcal{N}_B = 3$ times per time-step the magnetic boundary conditions, with a fluid deconvolution lag correction that iterates $\mathcal{N}_v = 5$ times per $\mathcal{N}_B$ (15 times per time-step, complexively).
A much improved self consistency is now achieved by SpeCyl, whose X^r profile is now very well compatible with Pixie3D (recall that we are not interested in that the two curves overlap, but only that they both stay well within the consistency domain: $X^r_{m,n} \ll 1$, for all m and n). As a result of this iterative correction, the linear growth rate is now raised by approximately 7 % and the fluid velocities, including the axisymmetric one, display a much more reactive dynamics. A full analysis of these results is presented in Sec. 9.7.
 The iterative method has shown great robustness and the ability converge within a limited number of iterations. Also, the coupling with the $\mathbf{J} \times \mathbf{B} \cdot \hat{\mathbf{r}}$ diagnostics produces a valuable test of the implementation, possibly relevant also for future usage of SpeCyl.2 for realistic physics applications.
Faster dynamics and more challenging simulation parameters could however raise the number of needed iterations before getting to a safe value of X^r.

   Luckily, we found and corrected a very small but very impactful typo in the name of a variable, in the implementation of SpeCyl.2. Basically, we were mixing one component of the axisymmetric magnetic field computed at the predictor step in a context where all other magnetic field components were
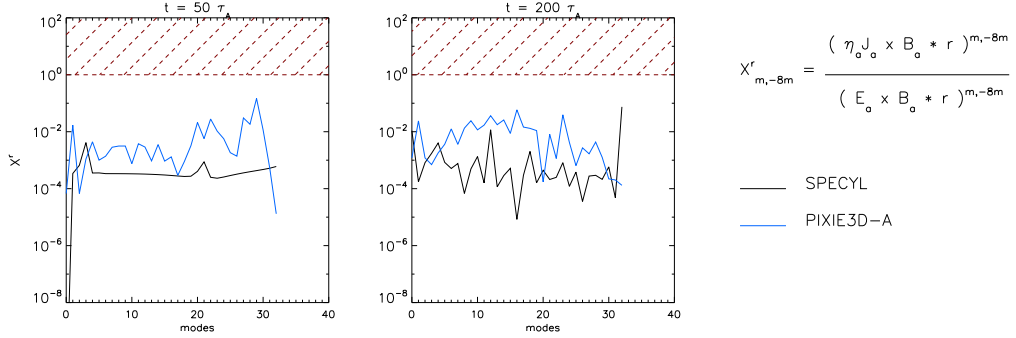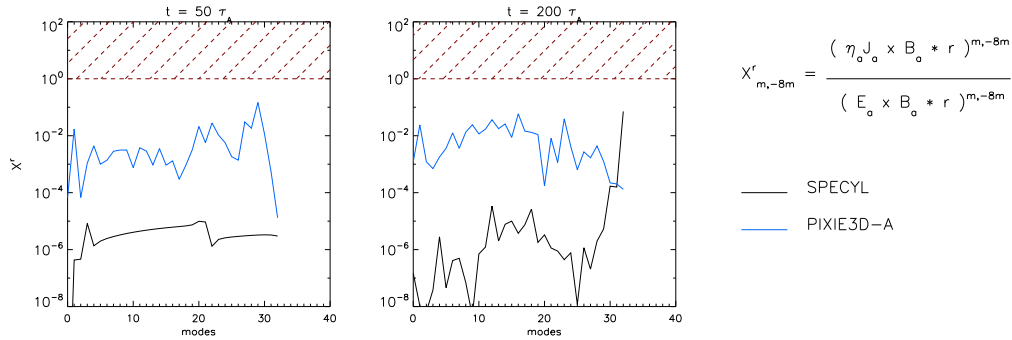
Figure 9.12: *Full magneto-fluid BCs, marginally resonant kink* $1, -8$. Self-consistency test on SpeCyl (black) and Pixie3D-A (blue), after the correction of a mistake in the implementation. The iterative method in the boundary conditions is now useless for this simple case study ($\mathcal{N}_B = \mathcal{N}_v = 1$).

already evaluated at corrector step.

After the correction of such a mistake, the role of the iterative method has much reduced in SpeCyl.2 simulations: Fig. 9.12 presents the same analysis as for the two previous figures, after the correction and for the same SpeCyl's simulation, with $\mathcal{N}_B = \mathcal{N}_v = 1$. The good performance of SpeCyl.2, after the correction of this mistake, is testified by Fig. 9.12: in fact, SpeCyl.2 exhibits the same performances already achieved before the correction of such mistake, now without the iterative method, in excellent agreement with Pixie3D, or actually even better.

We can thus conclude that

1) The $\mathbf{J} \times \mathbf{B} \cdot \hat{\mathbf{r}}$ diagnostics is a valid tool to highlight the presence of generic inconsistencies in the implementation of SpeCyl.2.

2) The final version of SpeCyl.2 is mostly capable of avoiding to use of the iterative formulation of its corrector step, involving better scalability to simulations with larger numbers of modes.

3) The iterative formulation of the corrector step has nonetheless a positive effect in the direction of enhanced self-consistency. This is still useful in presence of faster dynamics and in general of of extreme simulation parameters, as we will motivate in Chap. 10.

Table 9.5: Linear growth rates for the $(1, -8)$ marginally resonant mode.

BCs\code	SPECYL	PIXIE3D-A	PIXIE3D-B
$\boldsymbol{v}_{t,a} = 0$	$8.751 \cdot 10^{-2}$	$8.777 \cdot 10^{-2}$	$8.794 \cdot 10^{-2}$
$v_{\parallel,a} = 0$	$8.750 \cdot 10^{-2}$	$8.777 \cdot 10^{-2}$	$8.793 \cdot 10^{-2}$

9.7 General test-cases with both RW and full flow response: final results

In Section 9.6 we have presented several important tests that eventually led to the final implementation of SpeCyl.2, as it is presented in Chap. 8. This final version is the one which is used throughout the rest of this Thesis, from this Section to the whole of the next Chapter.

We consider here three different scenarios for our 2D helical-geometry verification study of the thin-shell resistive implementation in SpeCyl and Pixie3D: a marginally resonant $(1, -8)$ kink mode in the RFP (the same as considered in [Bonfiglio10] and in the rest of this chapter, up to this point), a non-resonant $(1, -6)$ mode still in the RFP, and an external kink mode $(1, -1)$ in tokamak configuration (the fundamental Kruskal-Shafranov limit, already discussed in Chap. 4).

9.7.1 The marginally resonant kink $(1, -8)$ in the RFP

Simulations considered here are the ones marked with a darker-green colour in Tab. 9.3: SpeCyl is compared to both versions of Pixie3D, and for the sake of full numerical verification all sets of fluid boundary conditions are enforced (despite the finitely conductive wall with $\tau_W = 10^2 \, \tau_A$ would prescribe no-slip BCs).

Figure 9.13 reports the time evolution of the normalised kinetic and magnetic energies of the first eleven modes, including the axisymmetric one, under $v_{\parallel,w} = 0$ BCs. The same plot enforcing no-slip BCs (not shown) yields no visible change compared to Fig. 9.13 in this specific case. SpeCyl (in black) and both versions of Pixie3D (blue and red) match quite well for both kinetic energies and magnetic energies.

Linear growth rates are reported in Table 9.5, and agree with each other within 0.2%. The nonlinear saturation agrees quite well in all panels. There is yet some slight difference in the non-axisymmetric part of kinetic energy plots, which will be further discussed below.

Figure 9.14 reports the radial profiles of plasma quantities after $300 \, \tau_A$
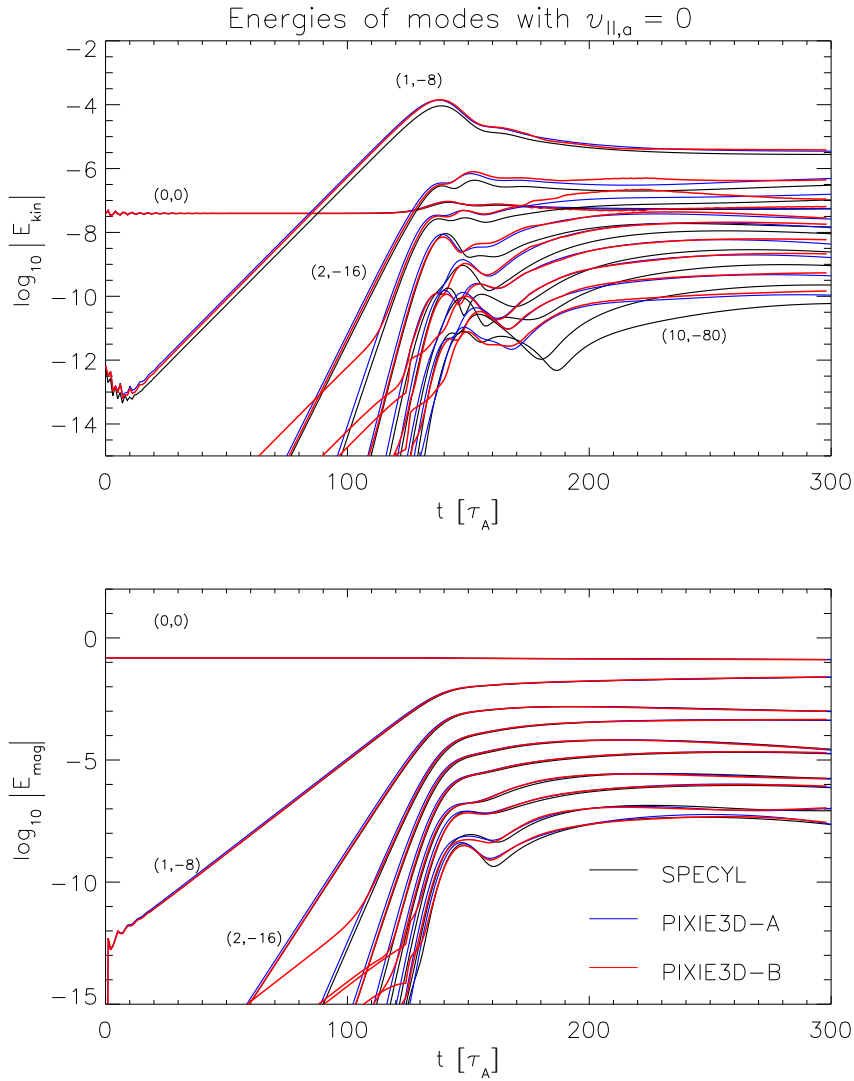
Figure 9.13: *Full magneto-fluid BCs, marginally resonant kink* $1, -8$, $\tau_W = 100\,\tau_A$. Time evolution of normalised kinetic and magnetic energies of modes, defined in D1, enforcing $v_{\parallel,a} = 0$ fluid boundary conditions for the nonresonant kink $(m = 1, n = -8)$ case study. SpeCyl (**black**) and the two implementations of Pixie3D (**blue** and **red**) match well during both linear growth and nonlinear saturation.
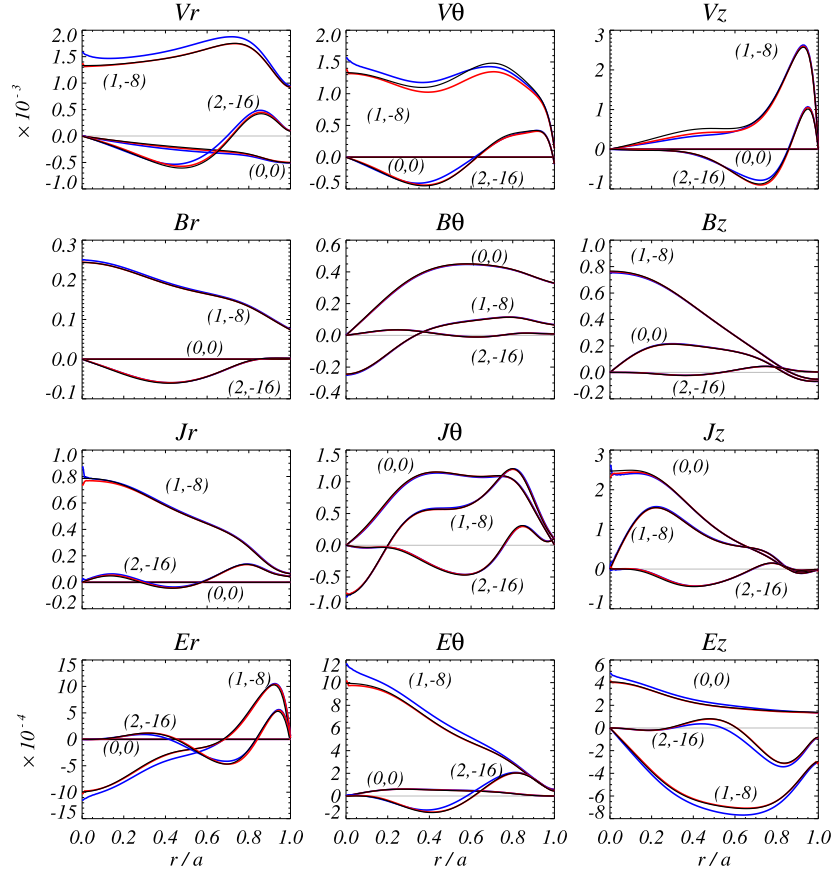
Figure 9.14: *Full magneto-fluid BCs, marginally resonant kink* $1, -8$, $\tau_W = 100\,\tau_A$. Radial plot of the main plasma quantities, after $300\,\tau_A$ from initial perturbation $(1, -8)$, with $\tau_w/\tau_A = 100$ and enforcing $v_{\parallel,a} = 0$. Fourier modes $m = 1, 2, 3$ are represented for SpeCyl (**black**), Pixie3D-A (**blue**), and Pixie3D-B (**red**). The usual SpeCyl units are adopted (see Fig. 9.3).
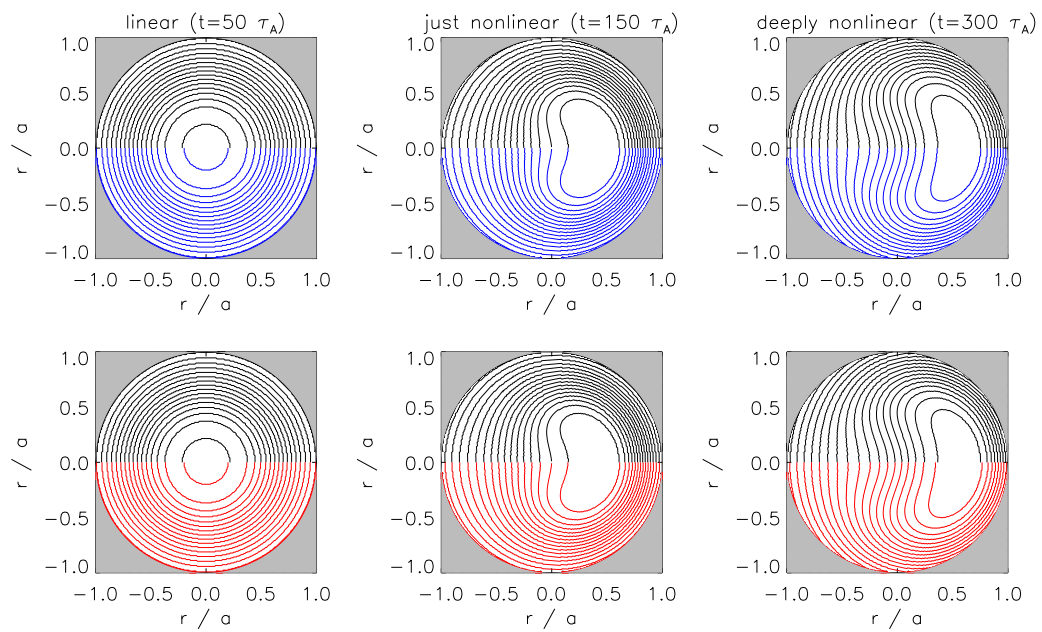
Figure 9.15: *Full magneto-fluid BCs, marginally resonant kink* $1, -8$, $\tau_W = 100\,\tau_A$. Evolution of the helical flux projection on the cylindrical cross section for Pixie3D-A (**blue**), Pixie3D-B (**red**), and SpeCyl (**black**). Faster growth and dominance of mode $m = 1$ with respect to Fig. 9.4 and field penetration on the RW time-scale are visible.

of evolution from initial perturbation, for SpeCyl (black), Pixie3D-A (blue)
and Pixie3D-B (red), enforcing $v_{\parallel,w} = 0$.

As already visible from Fig. 9.13, this final state has not reach complete
stationarity, yet: as we already noticed for the ideal wall limit case, this
is in agreement with the axisymmetric electric field components $\mathbf{E}_t^{0,0}$ radial
profiles, whose radial derivative is non-zero, motivating thus a finite $\partial_t \mathbf{B}_t$
through Faraday's law.

Once more, the similarity is remarkable, overall, with minor differences on
axis, or in the plasma core, away from the boundary. This is especially true
for the non-axisymmetric modes of the flow, where a small discrepancy be-
tween the profiles interests however a large portion of the radial domain. As
a matter of fact, this might well be at the origin of the discrepancy in the
kinetic energy of non-axisymmetric modes, as the extensive radial integration
over the velocity profiles could be cumulating an intensively small mismatch.
It must be also said that the same small discrepancy was already present in
[Bonfiglio10].

Finally, Fig. 9.15 compares the evolution of the helical flux from both SpeCyl
and Pixie3D, following the usual colormap convention. Agreement is excel-
lent, with both codes showing the emergence and dominance of mode $m = 1$.
Magnetic field penetration through the wall is apparent on timescales longer
than the RW time-constant $\tau_W = 100\,\tau_A$ (panels in the second and third
column).

9.7.2   The nonresonant kink $(1, -6)$ in the RFP

We consider the non-resonant $(1, -6)$ mode on the same RFP equilibrium
to study its stability with respect to the variation of the ideal wall proximity
to the edge of the plasma.

The simulations involved in this study are the ones associated to the apricot
colour shade in Tab. 9.3 and are performed once more with SpeCyl and both
implementations of Pixie3D.

Two different RW penetration time-scales have been examined: $\tau_W = 100\,\tau_A$ (a resistive thin shell with no-slip BCs), and $\tau_W = \tau_A$ (a vacuum-wall
with $v_{\parallel,a} = 0$). Figure 9.16 presents the growth-rate scan on the separation
of the ideal wall from the plasma for both RW configurations. For each sim-
ulation the growth rate is reported. When the ideal wall is attached to the
plasma, the kink mode $(1, -6)$ is linearly stable ($\gamma\,\tau_A \approx -5.37 \cdot 10^{-3}$). As
the ideal wall separates, the growth rate increases up to a marginal stabil-
ity threshold $(b/a)_{\mathrm{crit}}$ that depends on the value of τ_W. This is highlighted
in the side-panel (Fig. 9.16-bottom), with the detail of stability threshold
crossing. It is apparent that the larger τ_W, the slower the growth rate in-
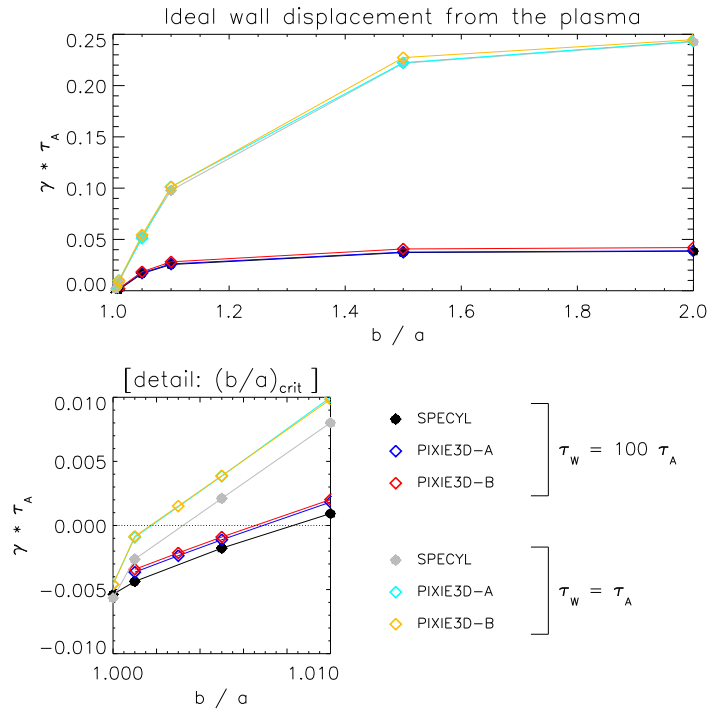
Figure 9.16: *Full magneto-fluid BCs, non-resonant kink* $1, -6$, $\tau_W = 100\,\tau_A$. Linear growth rate of the nonresonant mode $(1, -6)$ in RFP geometry, as a function of ideal wall proximity, in SpeCyl (black and grey dots) and Pixie3D-A (blue and cyan diamonds), and for two different values of τ_W. For the vacuum-wall limit case $(\tau_W = \tau_A)$, $v_{\parallel,a} = 0$ BCs are used. Below, we report the detail of the bottom-left corner, extended to negative growth rates to highlight marginal stability threshold. Units are normalised according to SpeCyl's conventions: velocities to $v_A = a/\tau_A$, magnetic fields to $B_0 = |\mathbf{B}(0)|_{t=0}$, currents and electric fields to $v_A\,B_0$ ($\eta = 1/S$).

creases. Both codes find $(b/a)_{\text{crit}} \approx 1.003$ for $\tau_W = \tau_A$, and $(b/a)^{\text{crit}} \approx 1.007$ for $\tau_W = 100\,\tau_A$. Overall the comparison shows excellent agreement between the two codes, particularly away from the stability threshold.

This study takes its inspiration from [Hender89] and from some preliminary studies performed bt Daniele Bonfiglio with SpeCyl.2.V00 in [Marrelli19, Bonfiglio19], to anticipate the effect on the energy of modes produced the displacement of the conductive structures of RFX-mod further from plasma edge, as foreseen for the design of RFX-mod2. Preliminarily, the instability threshold seems to be quite compatible with the initial predictions of SpeCyl.2.V00, but new simulations are planned to update the numerical prediction, in force of the excellent results of this verification study.

9.7.3 The Kruskal-Shafranov limit in the straight tokamak

The last case we consider in this Chapter is the stability of an external kink mode $(1,1)$ in the large aspect ratio tokamak (Kruskal-Shafranov limit, as in Chap. 4). This is a very academic case study, generally far from the experimental conditions, owing to its high disruptivity. It is however of interest due to its high current, producing more effective Ohmic heating: as we saw already in Chap. 4, a closely-fitting conductive shell is usually enough to make this configuration viable also experimentally [Hurst22].
This study is composed by those simulations that are associated with the lavender-pink colour in Tab. 9.3, performed with SpeCyl and Pixie3D-A only. The initial equilibrium is the one reported in Fig. 9.1.(f-l), and in the second line of Tab. 9.2, and is formally similar to the one typically used by Wesson in his theoretical works (which we introduced in Eq. 4.11).
Since we consider here a free-boundary instability, the vacuum-wall limit is adopted, with fast resistive-shell penetration time-scale $\tau_W \leq \tau_A$ and $v_{\parallel,a} = 0$. Unlike similar studies performed with other codes [Becerra16, Paccagnella07, Marx17, McAdams14, Strauss04], we keep uniform profiles of mass-density and viscosity.
Figure 9.17 demonstrates once more the good compatibility between SpeCyl and Pixie3D-B, also in the large aspect ratio ($R/a = 10$) tokamak geometry. We compare the linear growth rates γ found in simulations, for different input values of $\tau_W \leq \tau_A$: a strong inverse dependence between them is evident for $\tau_W > 0.01\,\tau_A$, followed by asymptotic saturation for faster penetration scales. A milder direct dependence of γ with the plasma resistivity and viscosity is also observed.

The increasing agreement of the two codes is evident as τ_W approaches τ_A, whereas some small discrepancy builds up for faster penetration time-scales. This is explained in terms of the different implementation of the same magnetic BCs in the two codes. In SpeCyl, the complex algebraic manipulation of Eqs. 8.16 in the corrector step eventually produces relations where τ_W is at the numerator. The fully implicit implementation for general (possibly not orthogonal) curvilinear coordinates in Pixie3D produces relations where τ_W is at the denominator.

This is generally not a limiting feature, since Pixie3D is especially designed to investigate the opposite regime of finite τ_W, which is more research-relevant and where the benchmark agreement with SpeCyl is optimal. Even in this very academic case of the stability of an ideal free-boundary MHD mode, reasonable agreement with SpeCyl is shown (within $5\,\%$ for $\tau_W = 0.01\,\tau_A$), at the price of a much finer time-step.

The spectral formulation in SpeCyl appears to be particularly advantageous for the specific purpose of linear MHD studies, allowing to compensate for the numerical cost of more accurate radial meshes and short time-steps with a reduction in the number of simulation modes.

A dotted-line in Fig. 9.17 marks the analytical expectation γ_{exp} for the growth rate of an external kink mode $(1,1)$, as computed through the energy principle. From our scaling results that this value is reliably approximated for faster penetration time-scales and lower plasma resistivity.

The increasing faithfulness to the ideal MHD theory for lower resistivity and viscosity is certainly a good sign, since it indicates that the asymptotic limit for $\eta, \nu \to 0$ does actually fall in the ideal MHD limit. Recall that this was not the case in presence of a pseudo-vacuum, in Chaps. 5-6, as well as in the simulations presented in Appendix B.

For the dependence of γ on τ_W, we speculate that the saturation is reached when the resistive penetration through the vacuum-wall is much faster than the characteristic growth rate of the instability, *i.e.*,

$$\tau_W \ll \frac{1}{\gamma_{\mathrm{exp}}} \sim \mathcal{O}(1)\,.$$

Similar studies on the dependence of γ on τ_W had already been performed with no visible results on past versions of SpeCyl: namely SpeCyl.2.V00 and the first explorative implementation of SpeCyl.2 (see Appendix B).

Fig. 9.18 presents a first successful nonlinear benchmark study of SpeCyl against the external kink mode $(1,1)$, performed with $\tau_W = 10^{-8}\,\tau_A$, $S = 10^7$, and $P = 1$ (referring to Tab. 9.3, these are the simulations associated with the colour gray). The theoretical growth rate is finally reproduced with ex-
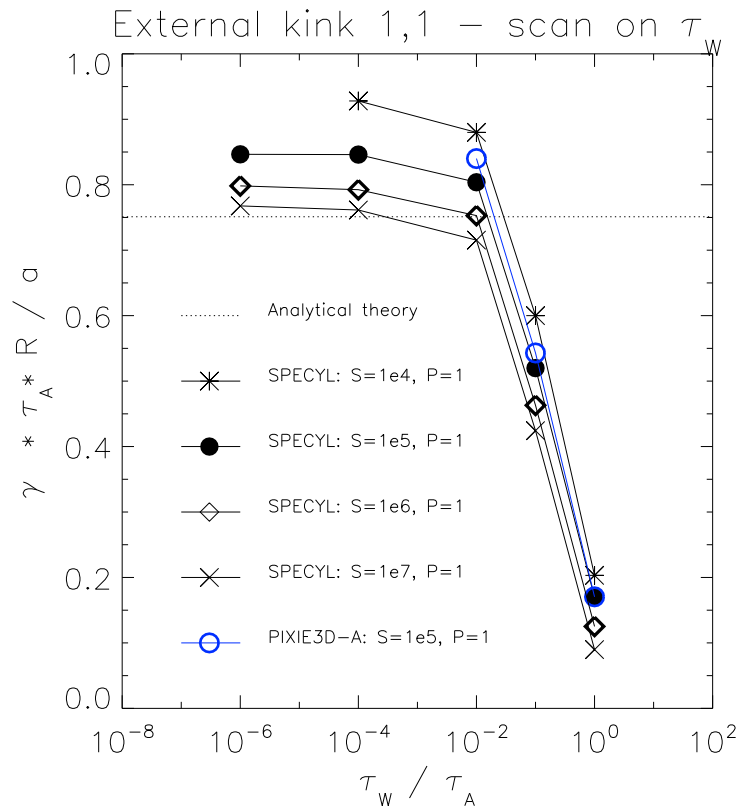
Figure 9.17: *Full magneto-fluid BCs, external kink* $1,1$ *in the tokamak.* Growth rate of the external kink $(1,1)$ in tokamak geometry, as a function of τ_W, for $q_a \approx 0.78$. Pixie3D-A (blue circles) and SpeCyl (black markers) agree well for the same numerical set-up ($S = 10^5$, $P = 1$). Linear theory expectation γ_{exp} is approached by SpeCyl for small η and ν, and provided that $\tau_W \ll 1/\gamma_{\mathrm{exp}}$.
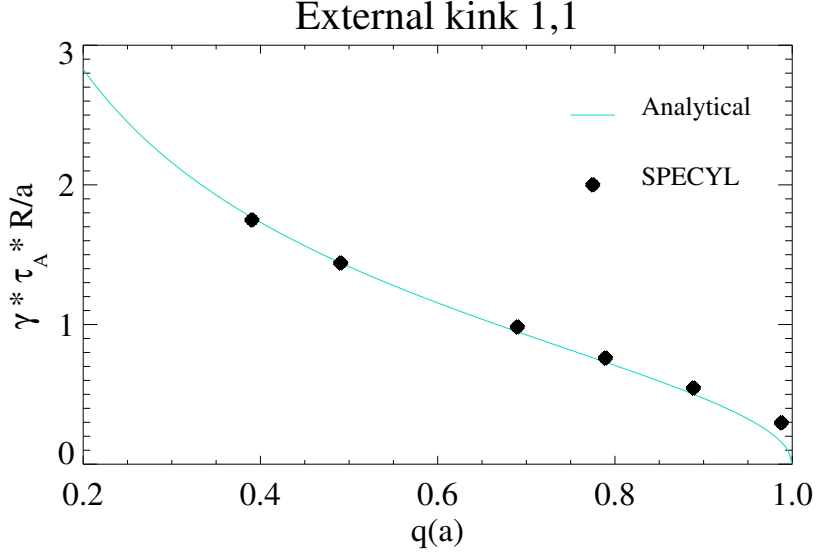
Figure 9.18: *Full magneto-fluid BCs, external kink* $1,1$ *in the tokamak.* Linear benchmark of SpeCyl's simulations against the ideal MHD external kink mode $(1,1)$. Slight disagreement around $q(a) \approx 1$ is due to resistive tearing modes, resonating at plasma edge. For this case: $R/a = 20$, $\tau_W/\tau_A = 10^{-8}$, $\eta(0) = \nu = 10^{-7}$.

cellent agreement by SpeCyl (small discrepancies at $q_a \approx 1$ are probably due to resistive modes resonating at plasma edge): this is strongly suggesting that similar results should be achieved also by Pixie3D, further decreasing the time-step width and refining the radial (and angular) mesh.

Finally, both in SpeCyl and in Pixie3D the radial profiles of $B_r^{1,1}$ and $v_r^{1,1}$ are extremely close to the theoretical expectations, as shown in Figure 9.19 for SpeCyl.

9.8 Conclusive summary

The cross-verification benchmark presented in this chapter has represented a challenging milestone in my PhD and an absolutely mandatory final step in the implementation of a new set of boundary conditions. We strongly reckon that a full and quantitative verification benchmark is a vital step in the development of any numeric tool that aims at making reliable predictions.
The key to the final success was the enforcement of a quantitative approach,
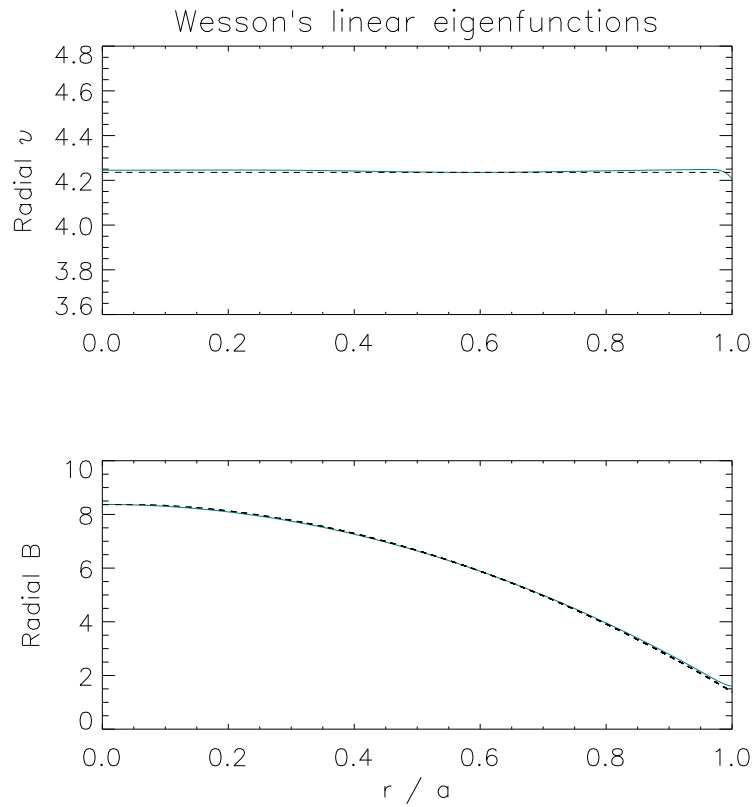
Figure 9.19: *Full magneto-fluid BCs, external kink* 1, 1 *in the tokamak.* SpeCyl's radial velocity and magnetic field for the dominant mode 1, 1 (teal, solid) against linear theory eigenfunctions (black, dashed), predicted for the Wesson's current model. The excellent agreement extends from axis to plasma boundary.

fostered by the definition of diagnostic tools formulated in such a way to highlight differences more than similarities: this is, *e.g.*, the case of the superposition of plots of the same quantity, produced by the two different codes (radial profiles, energies of modes, or helical flux), or the case of figures of merit such as the percent discrepancy between the linear growth rates.

We started with an introduction to the implementation of Pixie3D's two alternative sets of boundary conditions. This was instrumental to highlight another important aspect in this verification, which is the very different numerical schemes of the two codes. The most important of these has been for us the mostly non-spectral implementation in Pixie3D, which forced us to face several issues resulting from the complexity involved by convolutions.

After defining a common numerical set-up, in Sec. 9.2, we provided a schematic presentation of a method for the verification. Despite resenting of the peculiar direction that our specific case took, in Sec. 9.3 we aim at providing some useful and general tips for analogous works in the future. Among them, the most important lessons are possibly the aforementioned focus on quantitative diagnostics, the definition of some quick and quantitative test to measure the self-consistency in the implementation, and a general flavour of keeping things as simple as possible.
The diagnostics and figures of merit have been more thoroughly commented in Sec. 9.4.

Sections 9.5 and 9.6 contain a description by steps of the long verification work, starting from convenient limit cases, to districate the magnetic BCs from the fluid contribution and vice versa, to arrive to a comprehensive testing campaign of every single module in the two codes. We found particularly instructive the role that the $\mathbf{J} \times \mathbf{B} \cdot \hat{\mathbf{r}}$ diagnostics played in the final part of this process: its deployment led to the preliminary implementation of an iterative method that still retains a useful role in fostering time-stepping self-consistency, even after the correction of an impactful coding mistake.
Despite we mainly focused on the improvements and modifications required by SpeCyl, the same amount of work was needed for Pixie3D and performed by Luis Chacón, whose priceless collaboration has been a vital condition throughout this whole work.

Finally, Sec. 9.7 presented our final results, for two different case-studies in RFP geometry and one in the straight tokamak: a marginally resonant $(1, -8)$ kink, a non-resonant $(1, -6)$ kink, and an external kink mode $(1, 1)$ (Kruskal-Shafranov limit).

Concerning the first case, overall excellent agreement is found between SpeCyl and both formulations of Pixie3D, both enforcing no-slip and $v_{\parallel,a} = 0$ fluid boundary conditions. In fact, in this particular case, negligible difference is found between the predictions of the two fluid boundary formulations.

There are still some few discrepancies, mostly displaced towards the axis of the plasma, however suggesting that the boundary conditions treatment is finally in optimal agreement. Some tests of the physical predictions of the employed model have already been discussed and suggest promising self-consistency and faithfulness to physics. This is true for some properties of the electric field radial profiles (Fig. 9.14) and for the progressive penetration of the iso-flux surfaces in the resistive shell (Fig. 9.15).

In the second case, the stability of a nonresonant kink mode $(1, -6)$ has been investigated for diverse ideal wall proximities and for the two relevant cases of a resistive shell attached to the plasma and of a free-interface with vacuum. Also in this case the agreement of SpeCyl and Pixie3D-A is confirmed, both concerning the general study on the linear growth rates and regarding a more specific test on the instability threshold beyond some critical plasma-wall proximity.

The achieved agreement on this case specifically could be of interest in the contest of anticipating for RFX-mod2 the impact on MHD modes energies of a displacement of the conductive metal structures further away from the plasma [Marrelli19].

The third and last case confirms and extends the already proven agreement to the tokamak geometry, where however the challenging simulations parameters make the full verification benchmark too expensive for Pixie3D, whose implementation is more addressed towards the larger values of τ_W. Acceptable matching is nonetheless found in the common range of application, motivating the the expectation that SpeCyl results can be in line of principle achieved also by Pixie3D, through very expensive simulations.

The simulations of both codes find a strong dependence of the mode growth rate on the vacuum-wall penetration time and a milder dependence on the plasma resistivity and viscosity. In particular, for a penetration time much shorter than the inverse growth rate of the theoretical instability and for a very conductive and inviscid plasma, SpeCyl.2 finds excellent agreement with the analytical theory of ideal MHD instabilities, both concerning the growth rates and the eigenfunctions profiles. This is totally unprecedented in SpeCyl and is achieved without enforcing a pseudo-vacuum region at the plasma boundary.

In force of these final and strong results, we are very confident in assessing the mathematical correctness of both codes in the implementation of their

new magneto-fluid set of boundary conditions.

10

Final benchmark against linear theory

At the end of the previous Chapter we have already presented a first and successful benchmark against the linear theory of MHD instabilities. However, the external kink mode $(1, 1)$ is still a relatively safer case study, since nor the growth rates, neither the eigenfunctions are sensitive to the shape of the equilibrium profiles.

In this Chapter we extend our analysis to the more challenging kink mode $(2, 1)$, still in the straight tokamak geometry.

Sec. 10.1 presents the numerical set-up for the present study. The two usual current profiles by Shafranov and Wesson are reproduced, without enforcing a pseudo-vacuum region at plasma edge. The thin-shell is then meant to be a free-interface between the plasma and the outer vacuum, setting $\tau_W \ll \tau_A$ and enforcing $v_{\parallel,a} = 0$ BCs.

A useful rule of thumb is presented in Sec. 10.1.1, to choose the suitable radial mesh refinement for given simulation resistivity, viscosity, and the main characteristic time-scales. This rule is instrumental to understand the main numerical challenge faced throughout this Chapter, where very expensive radial meshes are put into use.

Sec. 10.2.1 presents the first numerical results, achieving a textbook agreement with the flat-current Shafranov's equilibrium, both concerning the growth rates and the profiles of both the flow and the magnetic field components.

Such a success is then extended (Sec. 10.2.2) to a scan in the proximity of the external ideal wall, finding again full compatibility with the theoretical expectations.

Sec. 10.2.3 presents a yet incomplete but important benchmark verification against the same instability for the Wesson's current model. Despite still unoptimised, the SpeCyl's simulations stand in very promising agreement

Table 10.1: General plasma and RW parameters used throughout the nonlinear benchmark study, unless specified, for the two initial equilibria of Shafranov's (flat-current) and Wesson's.

	R/a	η_0	ALET	BEET	GAET	ν	τ_W/τ_A	b/a	ρ
Shafranov	20	10^{-7}	1	2	0	10^{-7}	10^{-8}	100	1
Wesson	20	10^{-8}	0.01	2	-1	10^{-8}	10^{-8}	100	1

with the model expectations, both concerning the linear growth rates and the radial profiles.

Section 10.3 presents the usual conclusive summary for this Chapter.

10.1   Numerical set-up

This nonlinear benchmark study features the usual general set-up of SpeCyl's simulations, starting from the pressure-less paramagnetic pinch equilibrium already described (see Sec. 5.2.1), where the axisymmetric current density results from imposing a uniform and axisymmetric electric field and assigning a resistivity profile in the form of (Eq. 5.12):

$$\eta(r) = \eta_0 \left[1 - (\texttt{ALET} - 1) \, r^{\texttt{BEET}} \right]^{\texttt{GAET}} .$$

The viscosity is uniform and in the present study we will always assume that

$$\nu = \eta_0 \, .$$

Importantly, we also assume a uniform mass-density, identifying the entire simulation domain with the plasma region and effectively treating the resistive shell as a free interface with vacuum: $\tau_W \lll \tau_A$ and $v_{\parallel,a} = 0$.

Table 10.1 reports the main plasma and thin-shell parameters used throughout, unless otherwise specified, to reproduce the two usual reference equilibria already presented starting from Chap. 4: the flat-current model by Shafranov and the shaped current model used by Wesson in his theoretical works.

The Shafranov's flat-current initial equilibrium is reproduced by setting a flat resistivity profile over the full radial span of the simulation. The resulting profiles of axial equilibrium current and safety factor are represented in Fig. 10.1, along with the uniform mass-density profile. We highlight the optimal consistency with the analytical profiles, which is far better than the one obtained with pseudo-vacuum in Chap. 5.

Figure 10.1: Initial equilibrium for the nonlinear benchmark against Shafranov's flat-current profile, for the external kink mode $(2, 1)$.

The Wesson's profiles instead are obtained through a parabolic resistivity profile, as in the lower half of Fig. 10.2. Recall that the Wesson's profile (Eq. 4.11)

$$J_{0,z}^{\text{Wesson}} = j_0 \left[1 - \left(\frac{r}{a} \right)^2 \right]^{\nu'}, \qquad \nu' = 1$$

is supposed to be null at the plasma edge. This is infeasible in SpeCyl's simulations as it would require a singular resistivity $(\eta \sim 1/J_{0,z})$. Hence we slightly deform the plasma edge, so that it is small but still finite at the plasma edge. The resistivity-shaping parameters reported in the second line of Tab. 10.1 roughly correspond to the following current profile

$$J_{0,z}^{\text{SpeCyl}} = j_0 \left[1 - 0.99 \left(\frac{r}{a} \right)^2 \right]. \tag{10.1}$$

Despite being almost invisible by the eye, as reported in Figure 10.2, our profile is then a little flatter (more "radially stretched") than the Wesson's profile, and it presents a tiny pedestal at plasma edge $J_{z,a}^{0,0} \approx 0.01\, j_0$. This is also visible in the safety factor profile, whose edge value is generally little lower than the theoretical prescription.

We can more effectively model the SpeCyl's current profile by redefining a in Eq. 10.1, so as to make it formally identical to the general form of the Wesson's current Eq. 4.11:

$$J_{0,z}^{\text{SpeCyl}} = j_0 \left[1 - \left(\frac{r}{a_0} \right)^2 \right], \qquad \text{with} \quad a_0 = \frac{a}{\sqrt{0.99}}. \tag{10.2}$$
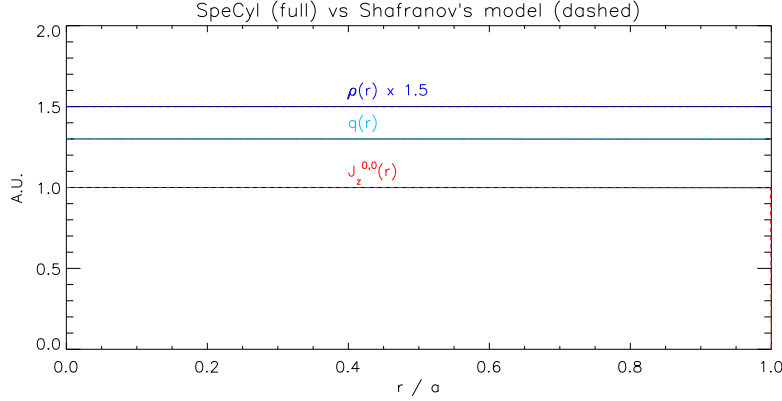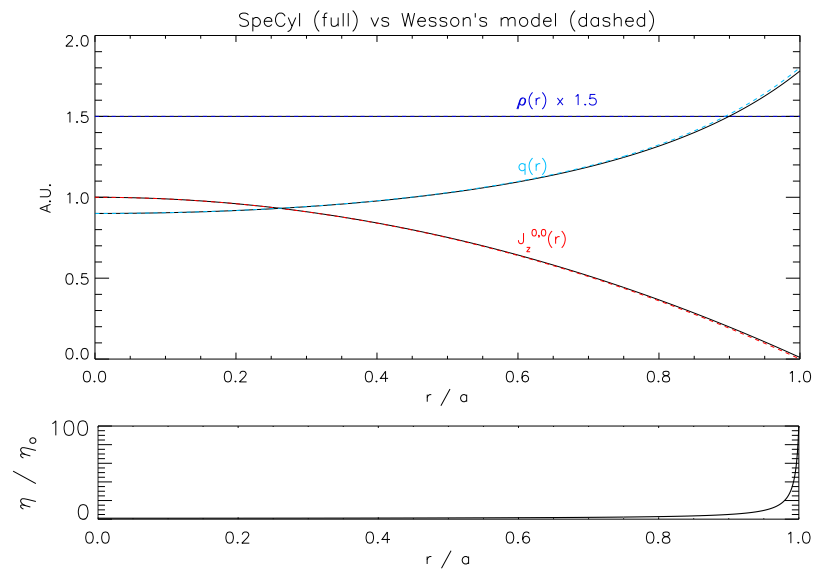
Figure 10.2: Initial equilibrium for the nonlinear benchmark against Wesson's current profile, for the external kink mode $(2, 1)$. Owing to numeric limitations, the current profile is slightly aberrant with respect to the model: it is vaguely flatter and presents a tiny edge pedestal, with some detrimental influence also on $q(r)$. Below: resistivity profile in SpeCyl.

10.1.1 The rationale for a very refined radial mesh

The simulations presented here are the final result of a parametric optimisation. It is usually observed that the choice of the numerical parameters may influence the physical outcome of a simulation, if, *e.g.*, simulation time-step Δt is too long (and becomes comparable with some relevant physical time-scale), or the radial mesh is too coarse to resolve entirely the phenomena one aims to describe.

Empirically, once the mesh gets refined enough, the numeric simulation performance decouples from that parameter, which is a necessary condition to achieve physically relevant interpretation of the code's predictions.

From very instructive discussions with Dr. Luis Chacón we learnt a rule of thumb to determine in advance what is a good guess for a physically acceptable mesh refinement, in our verification studies on boundary conditions.

The idea is that we need to let our BCs penetrate inside the plasma on a time-scale which needs to be faster or at least comparable to the faster characteristic time of the system.

Since the penetration of fluid-magnetic boundary conditions in the plasma is regulated by visco-resistive processes, the characteristic time of this phenomenon across at least one radial grid point is

$$\tau_\nu(\Delta r) \sim \frac{(\Delta r)^2}{\nu}\,, \qquad \tau_\eta(\Delta r) \sim \frac{(\Delta r)^2}{\eta}\,.$$

In the strong formulation the rule of thumb reads:

$$\tau_\nu(\Delta r),\,\tau_\eta(\Delta r) \le \Delta t \qquad \Longrightarrow \qquad \Delta r \le \min\left[\sqrt{\nu\,\Delta t},\,\sqrt{\eta\,\Delta t}\right], \quad (10.3)$$

where Δt is the simulation time-step. In practice, it is usually enough to rely on a weaker formulation of the same rule, where the characteristic time considered is the expected dynamic time of the instability we aim at reproducing in our simulation (which need to be longer that Δt, to be properly resolved):

$$\tau_\nu(\Delta r),\,\tau_\eta(\Delta r) \le \frac{1}{\gamma_{\exp}} \qquad \Longrightarrow \qquad \Delta r \le \min\left[\sqrt{\frac{\nu}{\gamma_{\exp}}},\,\sqrt{\frac{\eta}{\gamma_{\exp}}}\right], \quad (10.4)$$

where $\gamma_{\exp}$ is the expected growth rate of the instability we want to reproduce.

Eq. 10.4 has been successfully applied throughout this Chapter and seems to hold general validity.

Unfortunately, even the weak formulation of this principle, the ideal plasma

Table 10.2: Numerical set-up for the simulations presented in this Chapter: maximum expected growth rate, aspect-ratio, plasma viscosity and resistivity ($P = 1$), radial mesh size, time-step, number of modes with $m \geq 0$ (not included the complex conjugates with $m < 0$), number $\mathcal{N}_v$ of iterations of the fluid BCs in SpeCyl's corrector step, and number $\mathcal{N}_B$ of iterations of the full magneto-fluid set (see Sec. 8.2.3).

	$\tau_A \, \gamma_{\mathrm{exp}}^{\mathrm{max}}$	R/a	$\nu = \eta_0$	$1/\Delta r$	Δt	N_{modes}	$\mathcal{N}_v$	$\mathcal{N}_B$
Shafranov	$0.47 \cdot a/R$	20	10^{-7}	1000	10^{-5}	3	1	50
Wesson	$0.15 \cdot a/R$	20	10^{-8}	1000	10^{-5}	3	1	1

limit ($\eta \approx \nu \approx 0$) requires extremely refined radial meshes, also considering that the ideal kink modes tend to grow quite fast. Hence, numerical stability issues relating to very large radial meshes, pose a limit to the plasma viscosity and resistivity we are able to resolve reliably for fast-growing modes.

Such a requirement can be partially relaxed by working at large aspect ratio, since the kink modes dynamics is normalised on the toroidal Alfvén time

$$\tau_A^{\mathrm{toroidal}} = \tau_A \cdot \frac{R}{a} \, ,$$

which gets longer for a larger aspect-ratio. This comes however at the price of much longer simulations, to capture the slower evolution of the mode.

Table 10.2 presents the numerical set-up for the simulations we are going to discuss. The maximum expected growth rate for a given initial equilibrium (and for some particular q_a value) is obtained numerically, through our Euler's equation solver.

We can see that the radial meshes need to be very well refined, at the expense of the number of modes (which is not contributing much in the linear regime). The Shafranov's flat-current model, whose modes grow exceedingly fast, cannot be reliably reproduced with any numericaly affordable radial mesh for $\nu = \eta(0) < 10^{-7}$, while the slower kink mode in the Wesson's case can afford $\nu = \eta(0) = 10^{-8}$. In the last two columns we also report the employed number of iterations of the fluid and magneto-fluid boundary conditions in SpeCyl's corrector step. Also this number comes from a compromise between better performances and numeric stability. In the case of the Wesson model, the value of $\mathcal{N}_B$ is provisional, owing to stringent time constraints for my Thesis.

10.2 External kink

We present in this Section the results of the nonlinear benchmark of SpeCyl.2 against the linear MHD theory of the external kink mode $(2, 1)$ in the straighy tokamak limit.

Our study articulates on three subSections: in the first one the stability is investigated for the Shafranov's equilibrium and in no-wall conditions $(b/a \gg 1)$, the second subSection presents a scan on the stabilising effect of increasing the ideal wall proximity to the plasma edge, and the third subSection is dedicated to the stability analysis of the Wesson's current profile in the no-wall limit.

10.2.1 External kink mode $(2, 1)$ with Shafranov's equilibrium

This subSection deals with the stability analysis of the external kink mode $(2, 1)$ with a flat-current Shafranov's equilibrium. The simulations presented here correspond to the first line of Tab. 10.1-10.2 and are thus performed with a very large radial mesh and aspect ratio.

A preliminary scan was performed to assess the optimal set of parameters for the simulations, using as a representative case study the equilibrium characterised by $q_a = 1.5$. Apart from the considerations we already reported for the time-step, and the radial mesh, a very positive effect in the convergence of the growth rate to the theoretical value is found for the $\mathcal{N}_B$ SpeCyl parameter. In fact, Fig. 10.3 reports the relative error between the growth rate obtained from the simulations and the theoretical expectation:

$$\frac{|\Delta\gamma|}{\langle\gamma\rangle} = \frac{\left|\gamma_{\mathrm{SpeCyl}} - \gamma_{\mathrm{exp}}\right|}{\frac{1}{2}\left(\gamma_{\mathrm{SpeCyl}} + \gamma_{\mathrm{exp}}\right)} \ .$$

We can see that a significant improvement in the agreement is already achieved with a reduced number $\mathcal{N}_B$ of iterations of the boundary conditions enforcement within the corrector step. In fact, the aleady acceptable agreement within $\sim 6\,\%$ obtained with $\mathcal{N}_B$ can be improved to a compatibility within a $\sim 1\,\%$ tolerance, already at $\mathcal{N}_B = 20$.

In this case of almost linear dynamics, the lag coming from the convolutions nonlinearity is widely negligible (in fact, no effect is seen by increasing $\mathcal{N}_v$). However, in this case of relatively fast dynamics, the BCs self-consistency can be undermined by the evaluation of the magnetic field boundary with a prior-step evaluation of the edge flow: this must be why we observe such a beneficial effect of $\mathcal{N}_B$. The resulting stability analysis, performed with
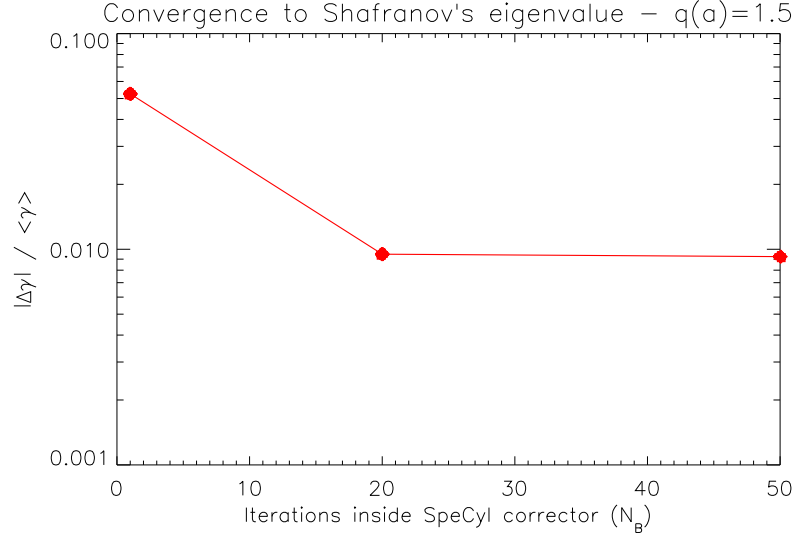
Figure 10.3: Impact on the convergence to the expected growth rate of the iterative method for the BCs in SpeCyl corrector. The discrepancy from linear theory improves from $\sim 6\,\%$ at $\mathcal{N}_B = 1$ (no iterations) to $\sim 1\,\%$ when $\mathcal{N}_B = 20$.

$\mathcal{N}_B = 50$, is reported in Figure 10.4. The overall agreement is remarkable: for all the unstable simulations, the linear growth rate maintains close to the expected growth rate, within a tolerance of $\approx 1\,\%$. Furthermore, the stability boundaries display excellent agreement with the analytical predictions. The modes within the stability region exhibit an almost purely oscillatory behaviour of the magnetic field, while the flow is particularly noisy and hard to fit. For these modes, any attempt of defining the growth rate in any of the usual ways (fitting the growth of either a plasma quantity at a given position or the kinetic or magnetic energy) gives poorly intellegible results, as it is evident from Fig. 10.5. The small oscillations in the energies of non-axisymmetric modes are due to some form of noise, but the overall trend is quite clearly not growing. This is in agreement with the theoretical expectation that predicts that the ideal mode growth rate must be either positive or null.

Not that in the present simulations we set an initial perturbation such that the dominant mode has a much larger kinetic energy also compared to the axisymmetric mode.

As for the unstable modes, Fig. 10.6 reports the radial profiles of the flow and magnetic field components of the dominant mode $(2, 1)$. The model
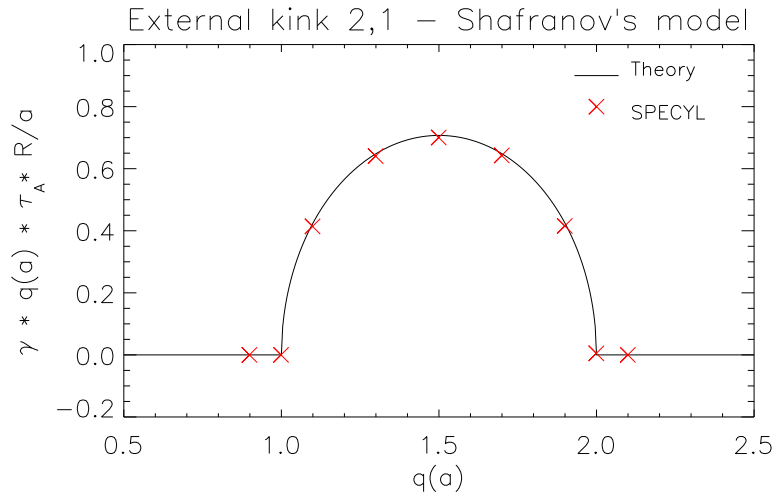
Figure 10.4: Stability analysis for the external kink mode $(2,1)$ with a Shafranov's flat-current initial equilibrium and far-displaced ideal wall. The normalised growth rates of SpeCyl's simulation (**red** crosses) lay on the top of the theoretical expectations (**black** curve) within a 1% tolerance.
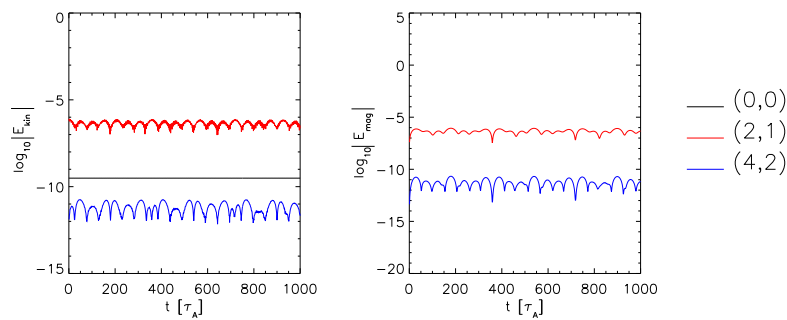
Figure 10.5: Kinetic and magnetic energy of the stable mode $(2,1)$ for $q_a = 0.9 < 1$. Apart from small oscillations due to some form of noise, the growth rate is compatibly null, in compliance with the ideal MHD theory.
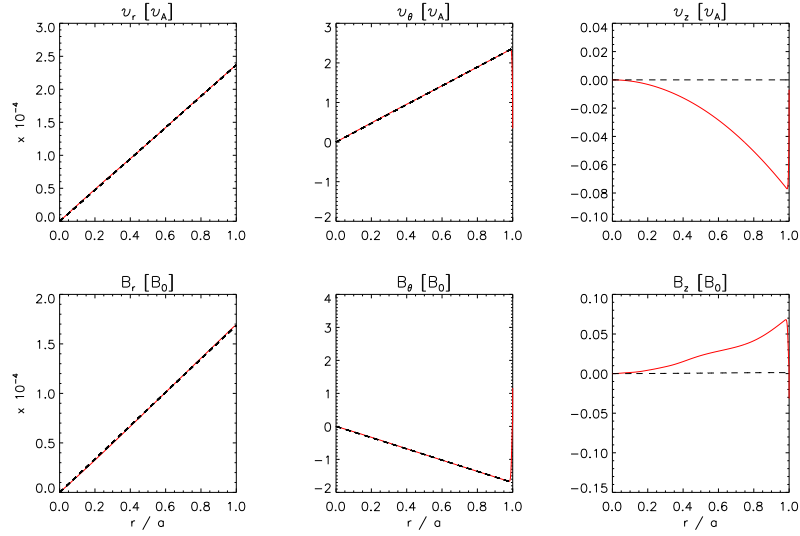
Figure 10.6:   Benchmark of mode $(2,1)$ radial profiles from SpeCyl (**red** solid curves) against the Shafranov's eigenfunctions (**black** dashed curves), for the external kink mode $(2,1)$.

predictions ($\boldsymbol{\xi}^{2,1}$ and $\mathbf{b}^{2,1}$ profiles) are reported as a black dashed line and are numerically computed through from Euler's and Newcomb's equation. Their value is normalised so that $\xi_r^{2,1}(r_0) \equiv \upsilon_r^{2,1}(r_0)$ and $b_r^{2,1}(r_0) \equiv B_r^{2,1}(r_0)$, with $r_0 = 0.6 \cdot a$ arbitrarily chosen, while the other components are scaled in such a way to enforce the incompressibility of the analytical eigenfunction $\boldsymbol{\xi}^{2,1}$ and the solenoidal property for $\mathbf{b}^{2,1}$.

Once more, the agreement between SpeCyl.2 vacuum-wall implementation and the theoretical expectations is almost perfect concerning the radial and azimuthal eigenfunctions.

The axial eigenfunctions, despite visually different from the model are nonetheless totally compatible with it. To understand this, recall that the straight tokamak limit descend from an asymptotic development of more general equations (Eq. 3.18 and 3.49), and it is only valid up to order $\varepsilon = a/R$. In the present case, $\varepsilon = 0.05$, and from the different scales on axes it is evident that

$$\frac{\upsilon_z}{\upsilon_r} \sim \frac{\upsilon_z}{\upsilon_\theta} \lesssim \mathcal{O}(\varepsilon)\,, \qquad \frac{b_z}{b_r} \sim \frac{b_z}{b_\theta} \lesssim \mathcal{O}(\varepsilon)\,.$$

10.2.2 Scan on ideal wall proximity

In this Section we extend the results of the previous stability analysis with the Shafranov's equilibrium to a scan on the ideal wall proximity. In doing this, we still interpret the thin shell as our plasma-vacuum free-boundary and by varying the outer ideal wall position (b/a), keeping $q_a = 1.1$.

The results are reported in Fig. 10.7, where each red cross corresponds to a simulation with $q_0 \approx q_a \approx 1.1$ and b/a ranging between 1.77 and 7.8. We see immediately that the remarkable agreement found for the no-wall limit case in the previous Section is indeed preserved also in presence of a conductive wall.

When the conductive wall is attached to the plasma edge, the modes are predicted to be stable. At a critical wall proximity $(b/a)_{\mathrm{crit}} \approx 1.77$ there is a stability threshold, beyond which the modes rapidly grow towards the asymptotic maximum growth rate for the given q_a value, which is the one reproduced in Fig 10.4.

A similar study, with a more rudimental formulation of SpeCyl.2 boundary conditions is reported in Appendix B, featuring also a qualitative benchmark against with the JOREK-STARWALL code in Fig. 5.3 of the PhD thesis of Rachel McAdams [McAdams14]. Both in the past exploratory study with the incomplete version of SpeCyl.2 and in the nonlinear benchmark study produced by McAdams a narrow psuedo-vacuum layer was modelled close to the plasma boundary, roughly occupying the region $0.9 \le r/a \le 1$.

The study performed with the preparatory formulation of SpeCyl.2 and pseudo-vacuum can be visualised in Fig. B.7. In that case a partially inconsistent formulation of the plasma edge flow was enforced (Sec. B.1), along with the present formulation of the magnetic boundary. The critical proximity could still be well resolved, but the no-wall limit would saturate on a much lower vale than the one predicted by theory, within a tolerance of $\sim 36\%$, as opposed to the present agreement within $\sim 1\%$.

The study performed with JOREK-STARWALL enforces interface boundary conditions that are thoroughly described in [Merkel15] and whose fluid constraints are summarised in Appendix B in Eqs. B.4-B.6. Also in this case, the interface is positioned inside a narrow pseudo-vacuum region, while the actual plasma coincides with the step-profile of the mass-density. In the results presented in Fig. 5.3 of [McAdams14] the critical stability threshold is very well reproduced, and the agreement with analytical expectation in the limit of $b \ll a$ is within a tolerance of $\sim 18\%$.

The fact that we have been able to obtain a much better agreement (to order 1% as mentioned above) testifies the substantial correctness and robustness of our final implementation for the RW boundary conditions.
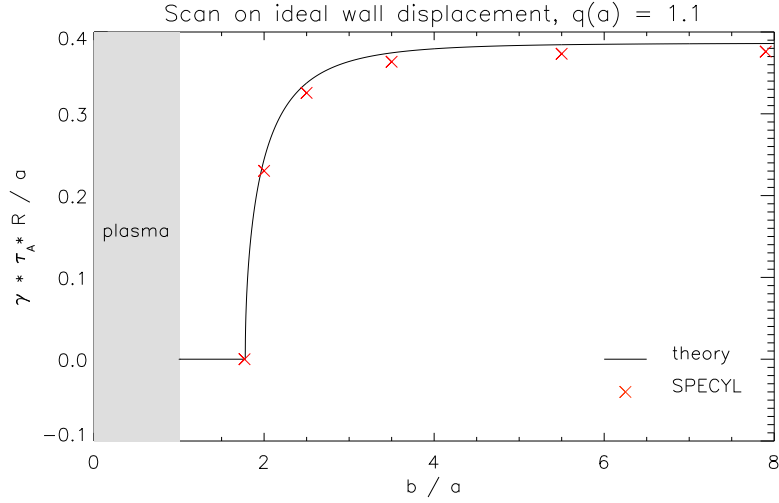
Figure 10.7: Scan of the growth rate variation for a given initial equilibrium (flat-current, $q_0 = q_a = 1.1$), as a function of ideal wall proximity to the plasma edge. SpeCyl (**red** crosses) against the theoretical expectations with the Shafranov's current model (**black** line), for the external kink mode $(2, 1)$.

10.2.3   External kink mode $(2, 1)$ with Wesson's equilibrium

Finally, this Section presents our results with the Wesson's equilibrium. This Section is to be considered as an advanced-preparatory study, and will be completed in the near future.

The set-up of the simulations we present is summarised at the second lines of Tabs. 10.1 and 10.2.

Figure 10.8 presents the stability analysis for the ideal kink mode $(2, 1)$ with a Wesson's initial equilibrium.

Each teal cross represents a simulation performed with SpeCyl.2, whereas the theoretical expectation for the Wesson's current model is reported as a black line. A second line in magenta reports the theoretically expected growth rate for the approximated current profile produced by SpeCyl, whose analytical formula is in Eq. 10.2 and whose plot is reported in black, in Fig. 10.2.

Concerning the Wesson's current expectation, a reasonable agreement is found, which is much improved when the actual current distribution obtained by SpeCyl is fed to the LENS code through the approximated formula in Eq. 10.2 (here represented by the curve in magenta). We see in particular that the left-hand-side stability boundary is perfectly reproduced.

SpeCyl's growth rates gradually detach from the model expectation as plasma

current is increased, yielding greater instability than what the model foresees. On a bright note, also the right-hand-side stability boundary seems reasonably compliant with the predictions of LENS, even if the plasma at $q_a \gtrsim 2$ is not expected to be totally stable, owing to the tearing mode instability (in fact, the point in $q_a \approx 2.1$ is linearly growing with $\gamma\tau_A \approx 7.88 \cdot 10^{-5}$). The activity of resistive modes near the edge of the plasma can in principle justify some aberration from the ideal MHD instability curve on its right side, but cannot account for all the discrepancy we see here, also considering the relatively high conductivity in SpeCyl's simulations for this case study.

Many could be the causes of this residual discrepancy. By looking at the $\mathbf{J}_a \times \mathbf{B}_a \cdot \hat{\mathbf{r}}$ diagnostics, it seems that we can rule out a strong influence of $\mathcal{N}_B$ on simulations performances: this is also confirmed by some preliminary empirical studies.

Better responsivity is observed concerning variations of plasma resistivity and viscosity, suggesting that the plasma ideality is possibly not yet reliably modelled with $S(0) = 10^8$ and $P = 1$. In fact, despite the large conductivity on axis, the edge resistivity is always two orders of magnitude larger for the Wesson's profile. This comes from the fact that the resistivity in SpeCyl is inversely proportional to the axi-symmetric equilibrium current. This way, despite having larger resistivity on axis, the Shafranov's flat-current model ends up having one order of magnitude lower resistivity at plasma edge.

Also consider that larger plasma resistivity has already been proven to raise SpeCyl.2's growth rate away from the theoretical expectations (see Fig. 9.17, regarding the external kink mode $(1, 1)$ with this same Wesson's current profile).

Unfortunately, further pushing on plasma resistivity and viscosity is not straightforward as it requires even larger radial meshes than the very refined ones already in use (and numerical stability is already a concern). The strategy we may adopt is to slow down the kink dynamics by taking a much larger aspect ratio (thus reducing γ_{exp}, as it is apparent from the label of the y-axis of Figure 10.8).

Concerning the analysis of the profiles of the flow ($\boldsymbol{v}^{2,1}$) and magnetic field ($\mathbf{B}^{2,1}$) in SpeCyl's simulations, Fig. 10.9 presents a qualitative comparison between their space components and the corresponding linear theory eigenfunctions $\boldsymbol{\xi}^{2,1}$ and $\mathbf{b}^{2,1}$, for the specific case of $q_0 = 0.8$ (and $q_a \approx 1.58$). Once more, the black curves represents the Wesson's current model, whereas the magenta profiles are computed feeding LENS with Eq. 10.2.

As already for the Shafranov's case, the analytical profiles are renormalised so that $\xi_r^{2,1}$ and $b_r^{2,1}$ match with the corresponding radial components of SpeCyl's counterparts, while $\boldsymbol{\xi}_t^{1,2}$ and $\mathbf{b}_t^{2,1}$ are normalised in such a way that
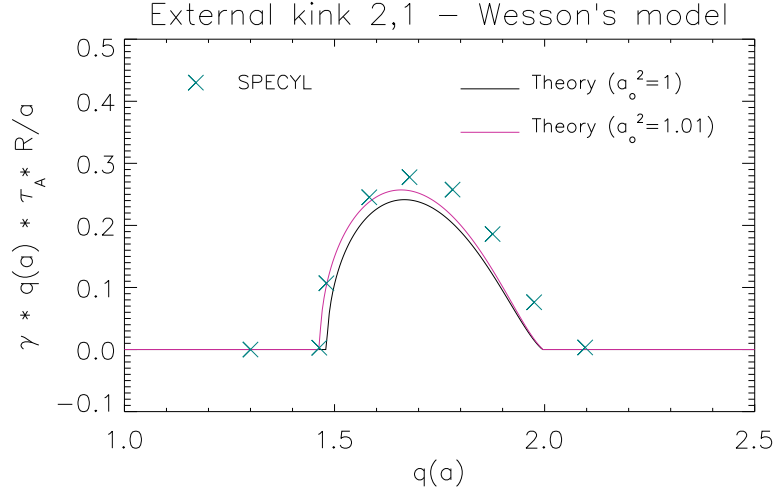
Figure 10.8: Benchmark of mode $(2, 1)$ radial profiles from SpeCyl (**teal** crosses) against the theoretical expectations with the Wesson's model (**black** curve) and for the approximated current profile deployed in SpeCyl and described in Eq. 10.2 (**magenta** curve) for the external kink mode $(2, 1)$.

$\nabla \cdot \boldsymbol{\xi}^{2,1} = \nabla \cdot \mathbf{b}^{2,1} = 0$.

As already observed from the growth rates, the agreement is close but not as much as in the Shafranov's case study. The radial velocity boundary seems now almost capable of reproducing also this shaped and non-trivial velocity profile. This marks a paramount step forward with respect to the initial achievements obtained with a resistive shell in SpeCyl.2.V00.

The same considerations hold for the azimuthal velocity, whose bursty profile is quite faithfully recreated almost up to the edge of the plasma. In the last few radial positions SpeCyl's azimuthal velocity drops to meet the boundary conditions. This is unavoidable and depends on the adopted closure for our system of equations in the vacuum-wall regime: $v_{\parallel,a} = 0$. In other words, since the magnetic field is mostly tangential throughout the linear phase (B_r is small with respect to $|\mathbf{B}_t|$), then $v_{\parallel,a} \approx v_{\theta,a}$ in the large aspect ratio limit. This feature was already present in the Shafranov's case study, even if less visible (see Fig. 10.6), and thus it is not concerning, considering the excellent agreement achieved with linear theory in that case.

Concerning the magnetic field, the radial component presents once more the better (almost perfect) agreement. The azimuthal and axial components are in optimal agreement with the profiles in magenta, meaning that SpeCyl has no problem in reproducing the theoretical profiles once the initial equilibrium is accurately reproduced. There is however a small detachment from either
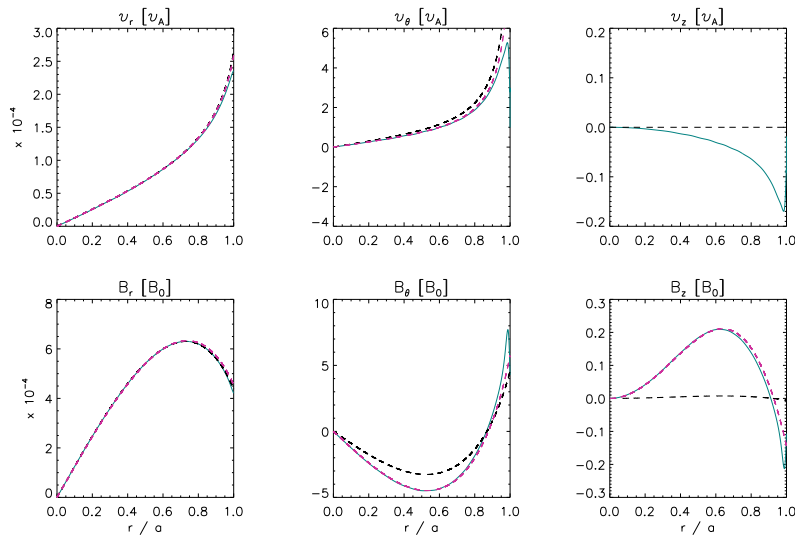
Figure 10.9: Benchmark of mode $(2, 1)$ radial profiles from SpeCyl (**teal** solid curves) against the Wesson's eigenfunctions (**black** dashed curves) and the eigenfunctions obtained for the approximated current profile obtained by SpeCyl (**magenta** dashed), for the external kink mode $(2, 1)$.

model in the outermost section of the radial coordinate, in correspondence with the higher resistivity and resistivity-gradient.

This could shed some light also on the mismatch in the growth rates at high current: since the Wesson's eigenfunction is more localised towards the edge when the resonance is just outside the plasma, the relatively stronger dissipation at plasma edge could be more detrimental to the performances of high-current simulations. To this regard, note that such a visible difference is not observed either for the flat-resistivity Shafranov model or for the radially-uniform-eigenfunction $m = 1$ external kink mode (studied at the end of the last Chapter, enforcing the same Wesson's model).

Finally the axial components of both fields are once more perfectly compatible with the analytical expectations within $\varepsilon = a/R = 0.05$.

10.3   Conclusive summary

This Chapter marks the successful end of a journey, from the initial attempts presented in Chap. 6 to produce a reliable agreement with the linear theory of the external kink modes, through the reformulation of the fluid boundary conditions and the thorough verification of mathematical correctness, with particular concern for self-consistency.

Already at the end of Chap. 9 a first successful nonlinear benchmark against the linear analytical theory was reported for the external kink mode $(1, 1)$, suggesting that it was about time for a final attempt to reproduce the ideal MHD results.

Indeed, after a detailed presentation of the numerical set-up and the definition of an useful rule of thumb in Sec. 10.1, Sec. 10.2.1 has presented a textbook agreement on the external kink mode $(2, 1)$ with a flat equilibrium current profile. Thanks to the final formulation of SpeCyl.2, owing also to the newly implemented iterative method in the corrector step, the linear growth rates of SpeCyl's simulations have been found in agreement with the expectations within a 1% tolerance. A specific analysis on stable and unstable cases finds for the first ones a compatibly null overall growth rate (in compliance to the theory), and for the latter an excellent compatibility of radial profiles, as well.

Sec. 10.2.2 has extended the agreement already discussed in Sec. 10.2.1 to various ideal wall proximities. The same compatibility (within $\sim 1\%$) has been confirmed in all simulations, also reproducing the expected stability threshold for $(b/a)^{\mathrm{crit}} = 1.77$. A qualitative benchmark has been issued with analogous results obtained enforcing a thin pseudo-vacuum region at plasma edge, either with an exploratory initial formulation of SpeCyl.2, or with the independent 3D nonlinear MHD code JOREK-STARWALL.

In Sec. 10.2.3 we presented a benchmark against the external kink mode $(2, 1)$, with the Wesson's current profile. In this, a slightly modified current model has been taken into account to meet the numerical limitations of SpeCyl in reproducing the model equilibrium. Yet, an acceptable agreement between the theoretical expectations and the - still unoptimised - SpeCyl's simulations has been proved. The insufficient ideality of SpeCyl's plasma is currently deemed responsible for the residual discrepancy, and a roadmap has been drawn in order to overcome this issue.

Although still unoptimised, the radial flow profile in SpeCyl's simulations is now visibly within reach of reproducing even the bursty radial eigenfunction of the linear theory for the Wesson's model. This represents an outstanding improvement from the initial failure, presented in Chap. 6, and characterised by the development of a resistive boundary domain at plasma edge.

This Chapter represents the first but successful kernel of a verification against analytical models of our new magneto-fluid set of boundary conditions. Such results provide solid foundations for an actual validation against experimental results.

Part VI

Final conclusions

Final conclusions

The work presented in this Thesis consists in the formulation, implementation and verification of new and more realistic boundary conditions for the MHD nonlinear code SpeCyl.

SpeCyl deals, presently, with a visco-resistive approximation of 3D nonlinear MHD in cylindrical coordinates. This approximation has been proved to be insightful in dealing with the helical self-organization processes observed in RFP devices, processes that are encountered in more geneal pinch configurations, and is expected to provide an essential tool to study 3D physics in the device RFX-mod2. RFX-mod2 is being upgraded thanks to PNRR funding for high priority infrastructures under "NEFERTARI project", operation is foreseen in 2024. Several 3D physics processes (cyclic magnetic relaxation, reconnection, internal barrier formation, magnetic chaos healing effect with structures formation, Alfvèn wave excitation, ...) can be described to a meaningful level within this modelling, without necessarily requiring the use of more complex and heavier 3D MHD codes like Pixie3D or JOREK, also available at RFX group, and that provided important means for comparison and benchmarking in several occasions.

The Chapters of this Thesis are articulated in four main parts, after the I) introduction: II) preliminary analytical and numerical study of the well-established theory of linear MHD instabilities; III) characterisation of the already existing preparatory boundary conditions against the linear MHD instabilities; IV) reformulation and implementation of a final set of boundary conditions; V) nonlinear verification.

At the end of each Chapter a detailed conclusive summary is reported. In addition, Part II and Part III also present specific conclusions. I present here only a brief overview of the main results.

Linear MHD theory studies (Part II)   Part II is devoted to an in-depth review of the well-established linear theory of MHD current-driven instabilities. The main focus is on two peculiar relaxation phenomena of magnetically confined pinch devices: namely the external kink mode and the tearing mode.

Two different approaches of linearisation of the MHD momentum balance equation are presented and derived almost from first principles: the New-comb's equation and the Euler's equation. Their complementary formulations are explored in the detail, in the context of the Energy Principle, highlighting the role of plasma inertia and flow, which will be central in the rest of my thesis.

I also developed the linear stability LENS code for the study of current-driven instabilities in cylindrical pinches: a verification study is presented, leveraging the advanced method of the manufactored solutions, and finding solid and general convergence. Not only is LENS instrumental to the thorough understanding of the mathematical notions of the linear theory, but it can be used to produce reliable and quantitative figures of merit for the benchmark verification of SpeCyl's boundary conditions.

Characterisation of the existing, preparatory boundary conditions (BCs) (Part III).   I thoroughly studied and reported the *status quo* in SpeCyl's implementation, including the existing BCs modules and the general work-flow. The one presented in my thesis is the most complete and accessible updated presentation of the SpeCyl code, and constitutes the initial kernel for a future comprehensive user guide.

At the beginning of my PhD, a first preparatory formulation of more realistic boundary conditions in SpeCyl had already been implemented, awaiting to be verified and completed. This was a general and flexible set-up, featuring a thin resistive shell in contact with the plasma edge, surrounded by a vacuum and an outer ideal wall: by tuning the thin shell resistivity, a full spectrum of experimental conditions could be in principle reproduced, from an ideal wall in contact with the plasma, to an infinitely resistive "free-interface" between plasma and vacuum. This first formulation was especially focused on the modelling of the magnetic boundary across the resistive shell, but was still assuming null edge radial flow (apart from the axisymmetric pinch velocity). Thanks to the linear stability code already developed, I issued a challenging and quantitative verification test against the stability of the external kinks in tokamak geometry, where the plasma flow plays a key role. This proved the preparatory formulation of SpeCyl's BCs to be incomplete and motivated a substantial reformulation of the fluid boundary conditions.

Formulation and implementation of new boudary conditions (Part IV).
To extend SpeCyl's BCs to a 3D velocity formulation, I implemented an original deconvolution technique. This is a valid and mandatory device that allows to solve semi-implicitly the model equations in SpeCyl, whose spectral formulation maps all products into highly nonlinear convolutions of MHD modes. The deconvolution module has been successfully tested in simplified conditions, enforcing an ideally conductive wall at the edge of the plasma.

Consequently, I present the new and comprehensive set of magneto-fluid boundary conditions. This is a very flexible set, which is capable of reproducing all the previous implementations of SpeCyl's BCs as limit cases and it combines the resistive-shell formulation for the magnetic boundary to two alternative formulations for the plasma edge flow, depending on whether the thin shell is intended as a physical wall or as a free-interface. I present the analytical re-derivation of the model prescriptions, so as to highlight all the hidden assumptions made in the derivation.

The latter is a fundamental passage to keep track of the self-consistency in numerical codes, which is easily undermined by the high complexity and the need for suitable assumptions to close their system of equations.

Nonlinear verification of our new boundary conditions (Part V). I conducted a rigorous and challenging nonlinear verification benchmark of our new boundary conditions against the independent implementation of analogous BCs in the nonlinear MHD code Pixie3D. This happened in collaboration with Dr. Luis Chacón from Los Alamos National Laboratory (USA) and featured my one-month visit at LANL, also thanks to their generous funding. The resistive shell modules of both codes were eventually found in optimal agreement on three different case studies of physical relevance: a marginally resonant kink mode $(1, -8)$ in the reversed field pinch (RFP), a non-resonant kink mode $(1, -6)$ still in RFP geometry, and a textbook Kruskal-Shafranov $(1, 1)$ external kink mode in tokamak geometry. For the second case study, the stability analysis was performed in dependence of diverse ideal wall proximities, and may have some preliminary relevance in anticipating the new layout of the experimental device RFX-mod2 (currently being upgraded). The third case of an $m = 1$ external kink mode in the tokamak found excellent agreement of both codes also with the linear MHD theoretical expectations.

In conclusion, I performed a further extended benchmark study against the external kink modes, highlighting now an almost textbook agreement with the theoretical expectations. Despite SpeCyl.2 is fully capable of enforcing various mass-density profiles, this latter verification benchmark was achieved with a uniform density profile, up to the edge of the plasma, and excellent

agreement with theory has been demonstrated using two different resistivity profiles, including uniform resistivity, up to the plasma edge.

Final prospectives

After the excellent agreement obtained in the extremely demanding test with the ideal kink modes already suggests robust reliability, the verification benchmark of the new thin-shell magneto-fluid boundary conditions against the analytical theory is going to be extended to other important current driven instabilities like, *e.g.*, the linear and the non-linearly saturated tearing modes.

In parallel, we will start to make use of the new set of magneto-fluid BCs for physics studies. Its natural call will be to explore the impact of a realistic fluid-magnetic boundary in the modelling of magnetic self-organisation in magnetically confined plasmas, with special regard to the case of the Quasi-Single Helical states in the RFP. The restart of the RFX-mod device, expected for the next year, will be good opportunity to test the predictive capability of the new code.

A further evolution of the geometry at boundary is also foreseen, featuring a second resistive shell in the vacuum region. Some preparatory studies on the magnetic field BCs have already been conducted by Daniele Bonfiglio, and need only to be matched with the complete fluid-magnetic BCs at the plasma interface. "SpeCyl.3", whose representation is reported in Fig. 10.10, will constitute a further important step towards an increasingly general and realistic representation of the plasma boundary. In particular, this will make possible to extend the benchmark and investigations to the resistive wall modes (RWM) that are stable external kink modes that become slowly unstable due to a conducting wall with finite resistivity. The final goal in the formulation of a realistic boundary conditions for SpeCyl would be the implementation of external coils and of a feedback MHD control system, in the form of a PID controller. This would allow a complete and self-consistent description of the plasma-boundary interaction in RFX-mod and RFX-mod2, performed for the first time with a 3D nonlinear MHD device as the SpeCyl code.

Figure 10.10: Foreseen representation for the next generation of SpeCyl's boundary conditions: SpeCyl.3 will keep unchanged the edge flow formulation of SpeCyl.2, reformulating the magnetic boundary to account for the presence of a second thin resistive shell, at tunable distance b in the vacuum region.
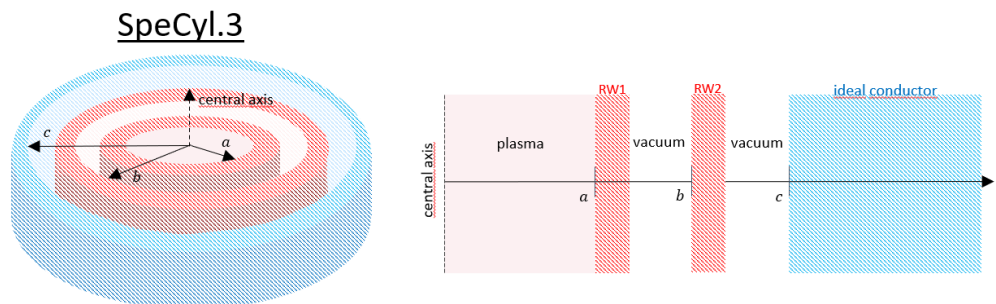
$\mathcal{A}$
Proofs of theorems of linear MHD theory

A.1 Proof for the corollaries of δW's self-adjointness

We report here the two fundamental corollaries of the self-adjointness of the operator δW, along with their proofs.

Property 1. Discrete modes are a basis
Whenever only a discrete set of $(\omega, \boldsymbol{\xi})$ couples is a solution to the eigenvalue problem in Eq. 3.38, this is a basis for all possible initial displacements.

Proof. This is the same as asking that the eigenvalue-eigenvector couples are an orthogonal set. The proof fits in one line, as for any $(\omega_1, \boldsymbol{\xi}_1) \neq (\omega_2, \boldsymbol{\xi}_2)$ we have

$$0 = \delta W(\boldsymbol{\xi}_1, \boldsymbol{\xi}_2^*) - \delta W(\boldsymbol{\xi}_2, \boldsymbol{\xi}_1^*) = \left((\omega_1)^2 - (\omega_2)^2\right) \int_V \frac{\rho_0}{2} \boldsymbol{\xi}_1 \cdot \boldsymbol{\xi}_2 \, \mathrm{d}\tau$$

whence $\langle \boldsymbol{\xi}_1 \mid \boldsymbol{\xi}_2 \rangle = 0$ with respect to the integral product, since $\omega_1 \neq \omega_2$ by hypothesis. $\square$

Property 2. Ideal modes either rotate or grow
All discrete eigenvalues ω^2 must be real.
This implies that ideal modes can either grow with purely imaginary rate $\omega \equiv -i\gamma$ or rotate with purely real frequency.

Proof. Also in this case, the proof is very simple, since for any eigenvector $\boldsymbol{\xi}$ of equation 3.38 must hold that

$$0 = \delta W(\boldsymbol{\xi}, \boldsymbol{\xi}^*) - \delta W(\boldsymbol{\xi}^*, \boldsymbol{\xi}) = \left(\omega^2 - (\omega^*)^2\right) \int_V \frac{\rho_0}{2} |\boldsymbol{\xi}|^2 \, \mathrm{d}\tau$$

whence $\omega^2 = (\omega^*)^2$, the asterisk indicating complex conjugation. $\square$

A.2   Proof for the variational form of MHD equations

In Sec. 3.5.3 we have claimed that we can equivalently re-write the MHD equations in a variational form, expressed by Eqs. 3.45-3.46, which we report below for completeness.

The same information contained in the MHD equations can be then expressed by the requirement that:

$$\omega^2(\boldsymbol{\xi} + \delta\boldsymbol{\xi}) - \omega^2(\boldsymbol{\xi}) = 0 \,, \qquad \text{for an arbitrary } \delta\boldsymbol{\xi} \to 0 \,,$$

with

$$\omega^2(\boldsymbol{\xi}) = \frac{\delta W(\boldsymbol{\xi}, \boldsymbol{\xi}^*)}{K(\boldsymbol{\xi}, \boldsymbol{\xi}^*)} \,; \qquad K(\boldsymbol{\xi}, \boldsymbol{\xi}^*) = \int_V \frac{\rho_0}{2} \, \boldsymbol{\xi} \cdot \boldsymbol{\xi}^* \, \mathrm{d}\tau \,.$$

To prove it, we just need to write the functional variation as:

$$\begin{aligned} \delta[\omega^2] &= \omega^2(\boldsymbol{\xi} + \delta\boldsymbol{\xi}) - \omega^2(\boldsymbol{\xi}) \\ &= \frac{\delta W(\boldsymbol{\xi} + \delta\boldsymbol{\xi}, \boldsymbol{\xi}^* + \delta\boldsymbol{\xi}^*)}{K(\boldsymbol{\xi} + \delta\boldsymbol{\xi}, \boldsymbol{\xi}^* + \delta\boldsymbol{\xi}^*)} - \frac{\delta W(\boldsymbol{\xi}, \boldsymbol{\xi}^*)}{K(\boldsymbol{\xi}, \boldsymbol{\xi}^*)} \end{aligned}$$

We consider $\delta\boldsymbol{\xi}$ to be a small perturbation to $\boldsymbol{\xi}$. What we want to do now is to derive the explicit form of the variation of the eigenvalue and then we will set it to zero to enforce functional stationary condition.

It is convenient to look at parts individually. The first one may be much simplified by using the fact that the potential energy variation is evidently linear in its second argument

$$\delta W(X, Y + Z) = \delta W(X, Y) + \delta W(X, Z)$$

along with self-adjointness, so that

$$\delta W(\boldsymbol{\xi} + \delta\boldsymbol{\xi}, \boldsymbol{\xi}^* + \delta\boldsymbol{\xi}^*) = \delta W(\boldsymbol{\xi}, \boldsymbol{\xi}^*) + \delta W(\boldsymbol{\xi}, \delta\boldsymbol{\xi}^*) + \delta W(\delta\boldsymbol{\xi}, \boldsymbol{\xi}^*) + \delta W(\delta\boldsymbol{\xi}, \delta\boldsymbol{\xi}^*) \,.$$

An analogous decomposition holds for K, so, if we drop second order terms in $\delta\xi/\xi$, we may write

$$\delta[\omega^2] = \frac{\delta W(\boldsymbol{\xi}, \boldsymbol{\xi}^*) + \delta W(\delta\boldsymbol{\xi}, \boldsymbol{\xi}^*) + \delta W(\boldsymbol{\xi}, \delta\boldsymbol{\xi}^*) + \delta W(\delta\boldsymbol{\xi}, \delta\boldsymbol{\xi}^*)}{K(\boldsymbol{\xi}, \boldsymbol{\xi}^*) + K(\delta\boldsymbol{\xi}, \boldsymbol{\xi}^*) + K(\boldsymbol{\xi}, \delta\boldsymbol{\xi}^*) + K(\delta\boldsymbol{\xi}, \delta\boldsymbol{\xi}^*)} - \frac{\delta W(\boldsymbol{\xi}, \boldsymbol{\xi}^*)}{K(\boldsymbol{\xi}, \boldsymbol{\xi}^*)}$$

$$\approx \frac{\delta W(\boldsymbol{\xi}, \boldsymbol{\xi}^*) + \delta W(\boldsymbol{\xi}, \delta\boldsymbol{\xi}^*) + \delta W(\delta\boldsymbol{\xi}, \boldsymbol{\xi}^*)}{K(\boldsymbol{\xi}, \boldsymbol{\xi}^*)} \left(1 - \frac{K(\delta\boldsymbol{\xi}, \boldsymbol{\xi}^*)}{K(\boldsymbol{\xi}, \boldsymbol{\xi}^*)} - \frac{K(\boldsymbol{\xi}, \delta\boldsymbol{\xi}^*)}{K(\boldsymbol{\xi}, \boldsymbol{\xi}^*)} \right) - \frac{\delta W(\boldsymbol{\xi}, \boldsymbol{\xi}^*)}{K(\boldsymbol{\xi}, \boldsymbol{\xi}^*)}$$

$$\approx \frac{1}{K(\boldsymbol{\xi}, \boldsymbol{\xi}^*)} \Big[\quad \delta W(\boldsymbol{\xi}, \delta\boldsymbol{\xi}^*) - \omega^2 K(\boldsymbol{\xi}, \delta\boldsymbol{\xi}^*) \quad + \quad \delta W(\delta\boldsymbol{\xi}, \boldsymbol{\xi}^*) - \omega^2 K(\delta\boldsymbol{\xi}, \boldsymbol{\xi}^*) \quad \Big]$$

Finally, enforcing the $\delta\omega^2 = 0$ condition and recovering the explicit form for kinetic and potential operators, we get

$$\int_V \left(\mathcal{F}(\boldsymbol{\xi}) + \omega^2 \rho_0 \boldsymbol{\xi} \right) \cdot \delta\boldsymbol{\xi}^* \, \mathrm{d}\tau + \int_V \left(\mathcal{F}(\boldsymbol{\xi}^*) + \omega^2 \rho_0 \boldsymbol{\xi}^* \right) \cdot \delta\boldsymbol{\xi} \, \mathrm{d}\tau = 0$$

and since $\delta\boldsymbol{\xi}$ is an arbitrary perturbation, this proves how our variational principle coincides with requiring

$$\mathcal{F}(\boldsymbol{\xi}) = -\omega^2 \rho_0 \boldsymbol{\xi} \,.$$

A.3   Vacuum contribution to $\boldsymbol{\delta W}$

We have seen in Sec. 3.5.4 that the minimisation of δW required by the energy principle can be split in the individual minimisation of three separate contributions, coming from the plasma, from the vacuum region outside it, and from the pressure balance on the plasma-surface:

$$\delta W = \delta W_p + \delta W_{\mathrm{v}} + \delta W_s$$

We deal here with the minimisation of the vacuum term, which is illustrated in Sec. 3.5.2 and is just the integral of the perturbed magnetic pressure. It is no surprise that we find back the same result already discussed as the vacuum limit of Newcomb's equations.

If we combine $\nabla \cdot \mathbf{b} = 0$ and $\nabla \times \mathbf{b} = 0$ and use the flux definition $\psi = -irb_r$, we find that

$$\delta W_{\mathrm{v}} = \frac{4\pi^2 R}{2\mu_0} \int_a^b \left[\frac{r}{H} \left(\frac{\mathrm{d}\psi}{\mathrm{d}r} \right)^2 + \frac{\psi^2}{r} \right] \mathrm{d}r \qquad (\text{A.1})$$

$$\equiv \int_a^b \mathcal{L}(\psi, \psi'; r) \, \mathrm{d}r \,,$$

whose minimisation yields the vacuum limit of Newcomb's equation, since

$$\frac{\partial \mathcal{L}}{\partial \psi} - \frac{\mathrm{d}}{\mathrm{d}r} \frac{\partial \mathcal{L}}{\partial \psi'} = \frac{\mathrm{d}}{\mathrm{d}r} \left(\frac{r}{H} \frac{\mathrm{d}\psi}{\mathrm{d}r} \right) - \frac{\psi}{r} = 0 \,. \qquad (\text{A.2})$$

Substituting Eq. A.2 into Eq. A.1, the vacuum contribution reduces to

$$\delta W_{\mathrm{v}}^{\min} = \frac{2\pi^2 R}{\mu_0} \int_a^b \frac{\mathrm{d}}{\mathrm{d}r} \left(\frac{r}{H} \cdot \frac{\mathrm{d}\psi}{\mathrm{d}r} \cdot \psi \right) \mathrm{d}r$$

$$= \frac{2\pi^2 R}{\mu_0} \left[\frac{r}{H} \cdot \frac{\mathrm{d}\psi}{\mathrm{d}r} \cdot \psi \right]_{r=a}^{r=b} \,,$$

which can be easily specialised to the required boundary conditions for the magnetic field in $r = b$. If the wall is assumed to be perfectly conductive ($\psi(b) = 0$), enforcing the matching condition at plasma edge[1] $\psi(a) = n\varepsilon_a B_{0,z}(1/q_a - n/m)\xi_a$ (subscript "a" indicating evaluation at radius $r = a$ and $\xi_a \equiv \xi_r(a)$), we can obtain our vacuum solution as

$$\psi(r) = B_{0,z}\xi_a\left(\frac{1}{q_a} - \frac{n}{m}\right)\frac{K'_m(n\varepsilon_b)I'_m(n\varepsilon) - I'_m(n\varepsilon_b)K'_m(n\varepsilon)}{K'_m(n\varepsilon_b)I'_m(n\varepsilon_a) - I'_m(n\varepsilon_b)K'_m(n\varepsilon_a)}\,n\varepsilon\,.$$

Thus, relying on Bessel's functions differential properties:

$$\frac{\mathrm{d}\psi}{\mathrm{d}r} = B_{0,z}\xi_a\left(\frac{1}{q_a} - \frac{n}{m}\right)\frac{K'_m(n\varepsilon_b)I_m(n\varepsilon) - I'_m(n\varepsilon_b)K_m(n\varepsilon)}{K'_m(n\varepsilon_b)I'_m(n\varepsilon_a) - I'_m(n\varepsilon_b)K'_m(n\varepsilon_a)}\,\frac{H}{r}$$

so that

$$\delta W_{\mathrm{v}}^{\min} = \frac{2\pi^2 R}{\mu_0}m^2 B_{0,z}^2\xi_a^2 n\varepsilon_a\lambda$$

$$\lambda = -\frac{K'_m(n\varepsilon_b)I_m(n\varepsilon_a) - I'_m(n\varepsilon_b)K_m(n\varepsilon_a)}{K'_m(n\varepsilon_b)I'_m(n\varepsilon_a) - I'_m(n\varepsilon_b)K'_m(n\varepsilon_a)}\,,$$

which is our final result (Eqs. 3.51-3.52).

A.4 Derivation of the dispersion relation for the resistive tearing mode

In the resistive domain enclosing the resonance, plasma dynamics is described by the resistive Ohm's law. By enforcing Faraday's and Ampère's laws this reads

$$-\frac{\partial \mathbf{B}}{\partial t} + \nabla \times (\boldsymbol{v} \times \mathbf{B}) = \frac{\eta}{\mu_0}\nabla \times \nabla \times \mathbf{B}$$

Making use of $\nabla \cdot \mathbf{B} = 0$, its radial projection, to linear order in the perturbation reads:

$$-\frac{\partial b_r}{\partial t} + \mathbf{B}_0 \cdot \nabla v_r = -\frac{\eta}{\mu_0}\nabla^2 b_r$$

and, via Eq. 3.11-3.13,

$$\gamma\psi - B_{0,\theta}\left(m - nq\right)v_r = \frac{\eta}{\mu_0}\nabla^2\psi\,. \tag{A.3}$$

---

[1]This is the case when no surface currents are present or they just live on a thin layer: see pp. 356-358 of [Freidberg14]

In the thin layer, $\nabla^2 \approx \frac{1}{r}\partial_r r \partial_r \approx \partial_r^2$ and we can approximate

$$q(r - r_s) = \frac{m}{n} + q_s' \cdot (r - r_s) + \ldots \qquad \rightarrow \qquad m - nq = -m\frac{q_s'}{q_s} \cdot (r - r_s)$$

since $q_s = m/n$ by definition. Hence

$$\frac{1}{\psi_s}\frac{\mathrm{d}^2\psi}{\mathrm{d}r^2} = \frac{\mu_0\gamma}{\eta}\left(1 + \frac{B_{0,\theta}}{\gamma}m\frac{q_s'}{q_s} \cdot (r - r_s)\frac{v_r}{\psi_s}\right) \tag{A.4}$$

Finally

$$\Delta_{in}' = \frac{1}{\psi_s}\int_{-\lambda/2}^{\lambda/2}\frac{\mathrm{d}^2\psi}{\mathrm{d}s^2}\,ds = \frac{\mu_0\gamma}{\eta}\int_{-\lambda/2}^{\lambda/2}\left(1 + \frac{B_{0,\theta}}{\gamma}m\frac{q_s'}{q_s}\frac{v_r}{\psi_s}s\right)\,ds$$

We need now to discuss v_r/ψ_s within the layer and to do this we will need once more the curl of momentum balance equation. However this time we need to include the inertial term containing velocity, under the simplifying assumption of incompressible flow inside the layer. In fact, along with the straight tokamak assumption, it implies ordering separation in

$$0 = r\nabla \cdot \boldsymbol{v} = \frac{\mathrm{d}}{\mathrm{d}r}(rv_r) + imv_\theta - i\varepsilon v_z$$

such that

$$v_\theta = \frac{i}{m}\frac{\mathrm{d}}{\mathrm{d}r}(rv_r)\,, \qquad v_z = 0\,.$$

As before, we may assume that the thin layer geometry brings an ordering also in derivaties: $\frac{\mathrm{d}}{\mathrm{d}r} \gg \frac{\mathrm{d}}{\mathrm{d}\theta}, \frac{\mathrm{d}}{\mathrm{d}z}$. Thus, assuming also uniform mass density,

$$\nabla \times \left(\rho_s\frac{\partial\boldsymbol{v}}{\partial t}\right) \approx \left(\rho_s\nabla \times \frac{\partial\boldsymbol{v}}{\partial t}\right)_\theta \approx \frac{\gamma\rho_s}{m}ir_s\frac{\mathrm{d}^2 v_r}{\mathrm{d}r^2}$$

Equating this term with the large aspect ratio limit of the torque (Eq. 3.33) and enforcing our usual thin layer ordering of derivatives we get to

$$\frac{i\gamma\rho_s}{m}r_s\frac{\mathrm{d}^2 v_r}{\mathrm{d}r^2} = -\frac{B_{0,\theta}(m - nq)}{r_s}\frac{\mathrm{d}^2\psi}{\mathrm{d}r^2} + m\frac{\mathrm{d}J_{0,z}}{\mathrm{d}r}\psi_s \tag{A.5}$$

Eliminating $\mathrm{d}^2\psi/\mathrm{d}r^2$ with Eq. A.4 we get to a inhomogeneous differential equation for v_r/ψ_s. Renormalizing all terms, this can be written as:

$$\frac{\mathrm{d}^2 y}{\mathrm{d}x^2} = -x\left(1 - xy\right)$$

being

$$h = \left[\left(\frac{\rho \eta \gamma r^2 q^2}{B_{0,\theta} m^2 q'^2} \right)^{1/4} \right]_{r=r_s} \ll \lambda \tag{A.6}$$

the typical space-variation scale inside the layer, $x = s/h$ and

$$y = \frac{\rho_s \gamma r_s^2 q_s}{m B_{0,\theta}(r_s) q'_s h^3} \frac{v_r}{\psi_s}$$

In these units, we can finally compute the integral of Eq. A.4.

$$\Delta'_{in} = \frac{\mu_0 \gamma h}{\eta_s} \int_{-\lambda/2h \to -\infty}^{\lambda/2h \to \infty} (1 - xy)\, dx$$

This is done numerically, giving

$$\Delta'_{in} = 2.12 \frac{\mu_0 \gamma\, h}{\eta_s} \tag{A.7}$$

which is the same as Eq. 4.16.

A.5 Elements for the derivation of Bondeson-Sobel's dispersion relation

In this Appendix we extend the derivation performed in Appendix A.4 to include viscous effects in the resonant layer and ultimately derive an alternative dispersion relation corresponding to the case when the dynamics in the layer is dominated by viscosity rather than resistivity.

Let us consider again the momentum balance equation in a generic visco-resistive plasma

$$\rho \frac{D\boldsymbol{v}}{Dt} = \mathbf{J} \times \mathbf{B} - \nabla p + \nabla \cdot (\nu \nabla \boldsymbol{v}) \ .$$

Nonetheless, in our derivation of Δ'_{in} inside the resistive layer we only considered the first addend at first member. This produced a vorticity balance equation (curl of momentum balance equation) in the shape of Eq. A.5. However, a more general (linear) form for such an equation is:

$$\frac{i\rho_s}{m} r_s \left(\gamma \frac{d^2}{dr^2} + \nu \frac{d^4}{dr^4} \right) v_r = -\frac{B_{0,\theta}(m - nq)}{r_s} \frac{d^2\psi}{dr^2} + m \frac{dJ_{0,z}}{dr} \psi_s\,, \tag{A.8}$$

having treated

$$\nabla \times [\rho_s \nabla \cdot (\nu \nabla \boldsymbol{v})] \approx \rho_s \nu \nabla^2 (\nabla \times \boldsymbol{v})_\theta \approx \frac{\rho_s \nu}{m} i r_s \frac{\mathrm{d}^4 v_{\mathbf{r}}}{\mathrm{d}r^4}$$

in the usual thin-layer assumptions.

In Sec. 4.2.1 we solved Eq. A.8 for the case in which the inertial term proportional to γ is dominant, yielding the dispersion relation in Eq. 4.17. There is yet another analytical solution for the case of dominant viscosity: if we keep only the term proportional to ν at the first member of eq. A.8 and couple it with Farady-Ohm's law Eq. A.3 we finally get to

$$\gamma = 0.4754 \left[\left(\frac{\eta}{\mu_0} \right)^{5/6} \nu^{-1/6} \left(\frac{m B_{0,\theta} \, q'}{\sqrt{\mu_0 \rho} \, rq} \right)^{1/3} \right]_{r_s} \Delta', \qquad (A.9)$$

which is the same as Eq. 4.22.

$\mathcal{B}$ Exploratory simulations with 3D edge flow and resistive thin shell, enforcing a narrow pseudo-vacuum region

In this appendix we present an exploratory nonlinear benchmark study against the ideal external kink, performed with a provisional set of boundary conditions, midway between SpeCyl.2.Vr00 and SpeCyl.2: the magnetic boundary is already well shaped, as in SpeCyl.2, but the fluid boundary, albeit already including non-axisymmetric modes, still lacks of self-consistency. A physically informed radial $\boldsymbol{v}_{r,a}$, already in the form of Eq. 8.23, is coupled with mathematically fixed tangential components $\boldsymbol{v}_{t,a}$, either with a Dirichlet condition or with a von Neumann condition. This is briefly described in Sec. B.1.

The first tentative studies with this configuration in the vacuum-wall limit resulted in the same delusive achievements, already presented in Chap. 6 for SpeCyl.2.V00: the formation of a "resistive transition layer" at boundary, in which the plasma flow radial profiles significantly depart from the analytical predictions of models, with its regrettable implications on the modes stability analysis.

We report here a rich nonlinear benchmark study performed against the ideal external kink modes $m = 1$ and $m = 2$, enforcing a pseudo-vacuum region at plasma edge, much alike what we did in Chap. 5 with SpeCyl.1. The difference is however that we can now afford a much thinner pseudo-vacuum region. In fact, setting the resistive shell time constant to a low value and displacing the ideal wall at a large radius, the magnetic field effectively sees a no-wall case. Concerning the flow, instead, a narrow pseudo-vacuum region is sufficient to damp the velocity boundary enough for it to become less relevant.

The results of this study are published on [Spinicci22], and feature - among the rest - a qualitative benchmark study against some results previously obtained with the JOREK-STARWALL code [McAdams14].

B.1 The provisional set of BCs, used for this study

As we anticipated, the magnetic formulation used for this benchmark study is the same as for SpeCyl.2, and was thus already described in Chap. 8.

Concerning the radial flow velocity, we almost retain unchanged Eq. 8.23:

$$\underline{v_{r,a}} = \frac{1}{\left(\underline{B^2}\right)^0} \left[\underline{\underline{E_{W,\theta}}} \cdot \underline{B_z} - \underline{\underline{E_{W,z}}} \cdot \underline{B_\theta} - \underline{\underline{\langle B^2 \rangle}} \cdot \underline{v_{r,a}^{\text{old}}} \right], \tag{B.1}$$

with

$$\underline{B^2} = \underline{B_r} \cdot \underline{B_r} + \underline{B_\theta} \cdot \underline{B_\theta} + \underline{B_z} \cdot \underline{B_z}.$$

The only difference from Eq. 8.23 is that here the whole $\underline{B^2}$ is used, rather than just $\underline{B_t^2} = \underline{B^2} - \underline{B_r^2}$. This difference implies a small physical inconsistency in the model used here, which we eventually found and corrected, owing to the intricate analytical re-derivation of our model equations, as presented in Chap. 8.

The architecture of the main loop is left unchanged from the other versions of SpeCyl's boundary conditions. After the corrector step has completed (including the backwards step of the Thomas algorithm), the final value of the magnetic field components is used to update $\underline{B^2}$, and both components of $\mathbf{E}_W$, to compute $\underline{v_{r,a}}$. This value is then assigned as the initial condition for the inwards integration of Thomas algorithm for the velocity at the subsequent time-step.

For the tangential components of the flow velocity, we adopt here either no-slip (Dirichlet) boundary conditions:

$$\boldsymbol{v}_{t,a} = 0, \tag{B.2}$$

or no-stress (von Neumann) boundary conditions:

$$\frac{\mathrm{d}\boldsymbol{v}_{t,a}}{\mathrm{d}r} = 0. \tag{B.3}$$

Also in this case, these physically unrelated constrains were eventually overcome in SpeCyl.2, owing to the analytical re-derivation of the model equations.

B.2 Linear benchmark against the external kink

This section presents the results of a nonlinear benchmark against the ideal MHD external kink of the new set of BCs, SpeCyl.2.

Despite the initial intent of modelling a self-consistent plasma-vacuum interface, the first explorative studies in this direction still found very similar outcomes to those described in Chap. 6: a resistive boundary region would form in the proximity of the plasma edge, where the velocity profile would depart significantly from the model predictions, also defying the "frozen-in law" of the magnetic flux.

Hence, in this intermediate study we enforce a pseudo-vacuum region, much alike what we did in Chap. 5, setting a step-like profile for the plasma density and shaping the resistivity profile in such a way that it is constant and relatively very high near plasma edge. In doing so, we assume that our plasma edge is not anymore the thin resistive shell, but rather the radial position of the step in mass-density profile.

The main difference from what was done previously is that we can now set the resistive wall time to a very small value ($\tau_W \lesssim \tau_A$) so that it becomes effectively transparent to the magnetic fields. This allows to take a thinner pseudo-vacuum region (just enough to exclude the resistive boundary region from the plasma domain). The vacuum region outside our plasma is then represented by the pseudo-vacuum from the plasma radius ($r = a$) to the thin shell ($r = r_{\text{wall}}$), and by the actual vacuum, treated analytically, up to the position of the outer ideal wall (in $r = b$).

This approach based on a pseud-vacuum region is inspired by what is done in most nonlinear MHD codes, such as DEBS [Paccagnella07], NIMROD [Becerra16], XTOR-2F [Marx17], and M3D [Strauss04]. In particular, the chance of modelling the plasma-vacuum free interface with an instantly-penetrated mathematical surface, inside a narrow pseudo-vacuum region, is present in several works done with the JOREK code, coupled to the STAR-WALL module [McAdams14, Merkel15, Artola18].

B.2.1 Numerical set-up

The geometry of the system is represented in Fig. B.1: we have a plasma of almost uniform density from the axis to $r = a$, where the mass density should ideally exhibit a sharp step. From the plasma edge to the resistive wall, in $r = r_{\text{wall}}$, we have a pseudo-vacuum region, and then an actual vacuum up until the ideal wall radius, $r = b$. The mass density profile is
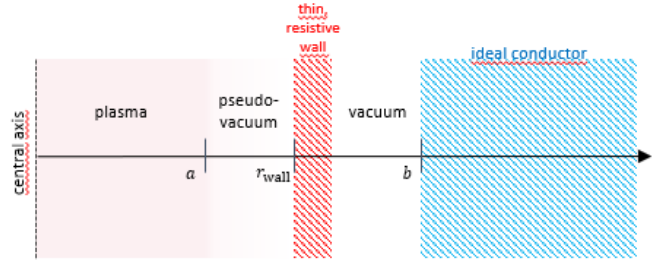
Figure B.1: Geometry of the system.

rendered in the same way already seen in Chap. 5 (Eq. 5.11):

$$\rho(r) = \left[1 - \alpha_\rho\right] \cdot \left\{\frac{1}{2} - \frac{1}{\pi}\arctan\left[\beta_\rho \cdot (r - a)\right]\right\} + \alpha_\rho \,,$$

with $\rho(0) = 1$, $\alpha_\rho = 0.1$ and $\beta_\rho = 100$.
For the rest, the aspect ratio is $R/a = 20$, compatible with the straight toka-mak limit, and the resistive time of the wall is $\tau_W = \tau_A$ (we also tried smaller values, down to $\tau_W/\tau_A = 10^{-3}$, finding irrelevant changes). Unless otherwise specified, the ideal wall is far-displaced, in $b = 10$.
Concerning the tangential velocity, both no-stress and no-slip BCs were at-tempted with similar results. In the following, since we assume our resistive wall to behave as a free interface, the less binding von Neumann BCs are enforced.

We focused on two initial equilibria that aim at the Shafranov's flat-current model and the Wesson's model. The Shafranov current distribution is achieved in the same way already discussed in Chap. 5, through Eq. 5.12:

$$\eta(r) = \texttt{ETAO} \cdot \left[1 + (\texttt{ALET} - 1)\, r^{\texttt{BEET}}\right]^{\texttt{GAET}} \,.$$

with $\texttt{ALET} = a^{-80} + 1$, $\texttt{BEET} = 80$, and $\texttt{GAET} = 1.025$, corresponding to a sharpness parameter $\lambda = 40$, as in Chap. 5. The plasma radius for this case study is fixed in $a = 0.9 \times r_{\text{wall}}$. Figure B.2 represents the corresponding initial equilibrium, for the case of $q(0) = 1.2$.

For the Wesson's profile, the choice of plasma radius must be a bit more careful, since in SpeCyl we shape the equilibrium current density as a result of an input resistivity profile. This means that the outermost portion of
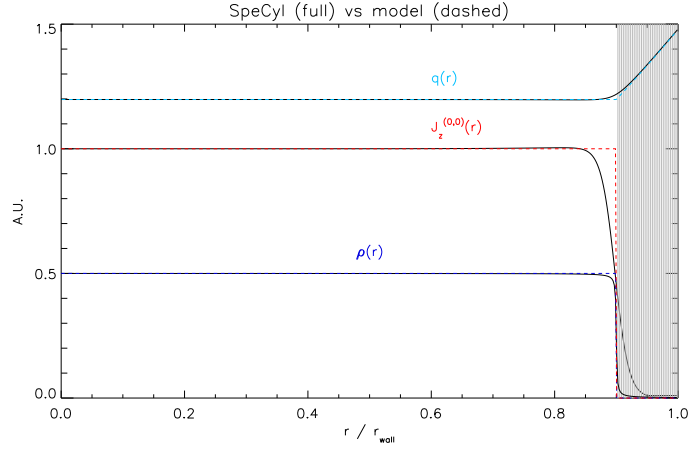
Figure B.2: Initial equilibrium for the nonlinear benchmark against the ideal external kink $(2, 1)$ with a flat current distribution.

the Wesson's current profile already needs a relatively high resistivity ($\sim 10 \times \eta(0)$). We aim at a current profile in the form of

$$J_{0,z}(r) = j_0 \left[1 - \left(\frac{r}{0.9 \, r_{\text{wall}}} \right)^2 \right].$$

The corresponding resistivity profile, still enforcing Eq. 5.12, has `ALET` $= -0.234568$, `BEET` $= 2$, and `GAET` $= -1$. In practice, to avoid having a singular resistivity in $0.9 \times r_{\text{wall}}$, we impose that as soon as $\eta(r) = 100 \times \eta(0)$, its profile must stick to this value.

To cut out the higher resistivity region, an analogous mass-density profile is chosen with respect to the flat-current case, but with $a = 0.8 \times r_{\text{wall}}$. Figure B.3 presents the resulting initial equilibrium for this case-study. Indeed, to avoid complications related to this challenging reconstruction of the Wesson's initial equilibrium, we tested it only against the current shape insensitive external kink $m = 1$.

For both current profiles, a scan on both resistivity and viscosity was performed, to determine the optimal value for the benchmark. Since we aim at the ideal MHD theoretical predictions, one could expect that a very conductive and inviscid simulation plasma should fulfil the task. This is indeed the case for viscosity: in the simulations presented hereafter, we set $Re = 10^{10}$. Concerning resistivity, however, we observe a negative trend, as in Fig. B.4. This is in general agreement with Figure 6.9 in [McAdams14] and we hypothesise is related to the presence of the pseudo-vacuum region:
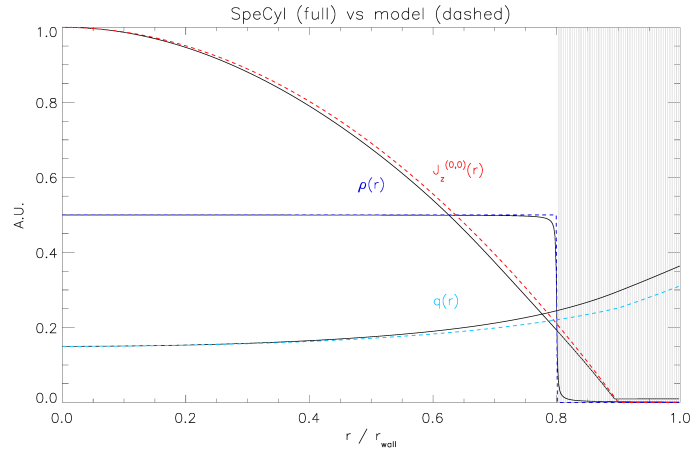
Figure B.3: Initial equilibrium for the nonlinear benchmark against the ideal external kink $(1, 1)$ with a Wesson's current distribution.

following analogous considerations to what already observed for Fig. 5.7, we suspect that the pseudo-vacuum region becoming too conductive, in presence of small but finite mass-density, may spoil the beneficial effects of a higher conductivity in the plasma region.

Hence, in the the following analysis we will set $\eta(0) = 10^{-5}$, corresponding to $S = 10^5$ and $P = 10^5$.

B.2.2   Results for the external kink $m = 1$

For the current-profile insensitive case of the external kink $1, 1$ (see Chap. 4), both current profiles were tested.

Figure B.5 reports the outcomes of the nonlinear benchmark against the Shafranov's profile. From panel (a) we can see that the stability boundary is very well reproduced by SpeCyl.1. The growth rates appear to be very accurate on the right-hand side of the unstable domain (when the resonance is very close to the edge of the plasma): this matching becomes a little less evident as we move the resonance away from the plasma surface. This can be probably explained by recalling from Fig. 4.3.(a) that this case study has diverging growth rate for $q_a \approx 0$: this fights with the limitations of our numeric approach, since we would need an increasingly refined radial mesh and a vanishingly small time-step to resolve the extremely fast growth of these modes.

Panel B.5.(b) presents the profiles of the velocity and magnetic field radial eigenfunctions, whose agreement whit the theoretical expectations is excellent, within the plasma region and (only $B_r^{1,-1}$) also in the pseudo-vacuum
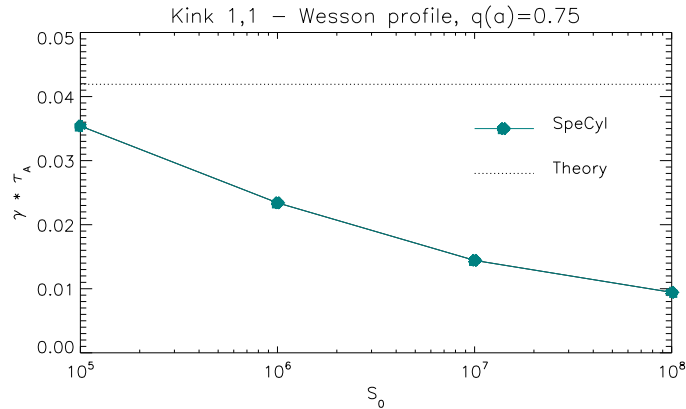
Figure B.4: Scan on the Lundquist number on axis (S_0) for an external kink $1, 1$ with Wesson's profile. Higher plasma resistivity produces growth rates more faithful to the linear theory, as in [McAdams14]. This is probably related to the presence of a pseudo-vacuum region with finite ρ.

region (shaded in the plot).

Similar considerations apply to Fig. B.6, where we illustrate the nonlinear benchmark against the external kink $1, 1$, but using a Wesson's current profile. Also this time, the growth rates are quite more accurate on the right-hand side of the unstable domain, despite being overall a bit less agreeing with the theoretical expectations with respect to the Shafranov's case. This can be however be easily explained by means of the much more problematic modelling of the initial equilibrium, yielding a higher conductivity in the vacuum region (recall from Fig. B.3 that a small tail of the current density flows inside the "cold plasma halo" constituting our pseudo-vacuum region). The apparent large discrepancy in the growth rate beyond $q_a = 1$ is motivated by the excitation of some internal mode (possibly a tearing or a resistive kink), allowed by the finite shear of Wesson's model: as a matter of fact, the shear-less flat-current model represented in Fig. B.5.(a) cannot intercept any internal resonance and thus presents no internal modes.
Panel B.6.(b) shows again excellent agreement between the theoretical eigenfunctions and the radial profiles of velocity and magnetic field fluctuations.

(a) Growth rates.

(b) Radial profiles of $v_r^{1,-1}$ and $B_r^{1,-1}$.
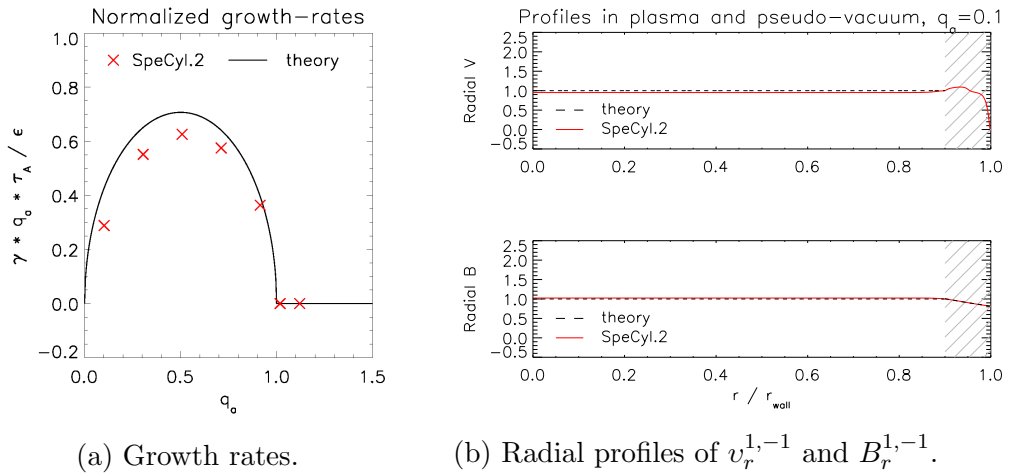
Figure B.5: Nonlinear benchmark of SpeCyl.2 against the external kink $1, 1$ for the Shafranov's flat-current model.

(a) Growth rates.

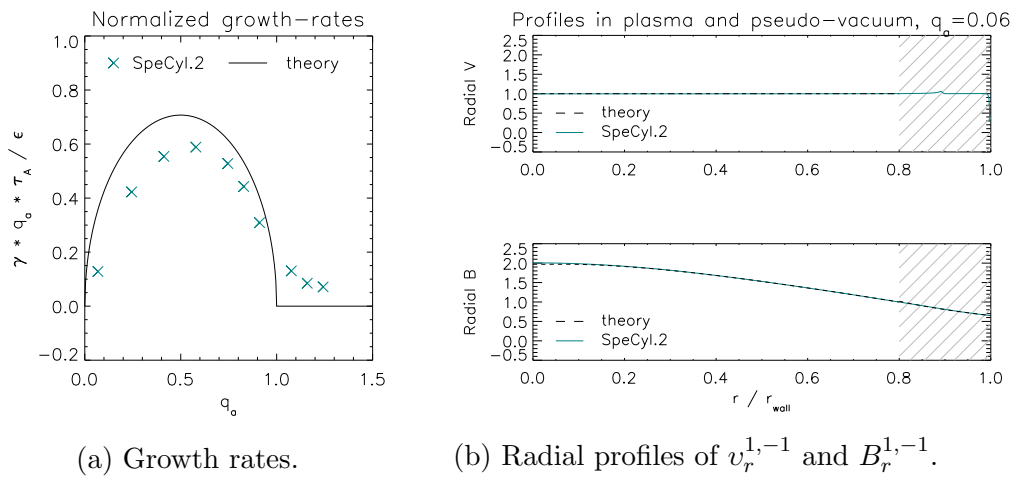(b) Radial profiles of $v_r^{1,-1}$ and $B_r^{1,-1}$.

Figure B.6: Nonlinear benchmark of SpeCyl.2 against the external kink $1, 1$ for the Wesson's model ($\nu = 1$).

B.2.3 Results for the external kink $m = 2$ (and qualitative comparison with JOREK results)

The external kink mode 2, 1 was only studied with a flat-current profile, as reported in Fig. B.7. The stability analysis in the first panel is very accurate concerning the stability boundaries. Unlike what was observed in Chap. 5 and in Fig. B.5, this time the stable modes are not simply oscillating with averagely null growth rate, but rather present a negative "damping" rate, which is not predicted by the ideal MHD theory[1]. The origin of this effect, which is more manifest in the right-side stable region, is not understood.

Panel B.7.(b) shows once more a remarkable agreement in the magnetic and velocity eigenfunctions within the plasma region. The magnetic field in the vacuum region (shaded) is still quite close to the theoretical trend and only resents of the smoothness of the step in the resistivity profile, causing the derivative-change across the interface to blur over a wider region than a single radial pixel.

Finally, panel B.7.(c) shows the outcome of a study on the outer ideal wall proximity (defined as b/a) for a fixed initial equilibrium ($q_0 \approx q_a = 1.1$). In this figure, the plasma radius is normalised to 1, so that the resistive shell is in the position $r_{\text{wall}}/a = 1.1$. SpeCyl's simulations are all obtained by enforcing $\tau_W = \tau_A$ and by varying the ideal wall position from $b/a = 1.2$ to $b/a = 7.8$

On the bright side, the instability threshold $(b/a)^{\text{crit}} \approx 1.77$ (here obtained numerically, through the solver for the Euler's equation) is faithfully reproduced by SpeCyl.2. Also, the general trend in the unstable domain is very similar between the theory and our simulations, up to a variable scaling factor (asymptotically: $\gamma_{\text{theory}} \approx 1.44 \times \gamma_{\text{SpeCyl}}$ for $b \gg a$).

The analogous of Fig. B.7.(c) is Figure 5.3 of the PhD thesis of Rachel McAdams [McAdams14], obtained for an equivalent set-up with the JOREK-STARWALL code, enforcing a pseudo-vacuum region in $0.9 < r < 1$, for the same flat-current profile and for $q_a = 1.1$. The boundary conditions at interface ($r = 1$, within the pseudo-vacuum region) are thoroughly discussed on [Merkel15]:

$$\mathbf{B} \cdot \hat{\mathbf{n}} = \mathbf{B}_0 \cdot \nabla \left(\boldsymbol{\xi} \cdot \hat{\mathbf{n}} \right) \qquad \text{linearised frozen-in law,} \tag{B.4}$$

$$\hat{\mathbf{n}} \cdot \nabla \boldsymbol{\xi} = 0 \qquad \text{von Neumann in the normal direction,} \tag{B.5}$$

$$\boldsymbol{\xi} \times \hat{\mathbf{n}} = 0 \qquad \text{Dirichlet in the tangent direction.} \tag{B.6}$$

Outside the interface, the STARWALL code computes the vacuum response,

---

[1] Recall that ideal modes can either have positive growth rates or null.

featuring a multiply-connected thin resistive shell (of very high resistivity, in the present case study) and an outer ideal wall.

Albeit a precise quantitative benchmark is precluded by the lack of some information (such as the detailed profiles of the initial equilibrium quantities), our results are qualitatively similar to the ones found by McAdams. In particular, also on [McAdams14] the simulation growth rates underestimate the theoretical one by a variable and similar factor (asymptotically: $\gamma_{\text{theory}} \approx 1.2 \times \gamma_{\text{McAdams}}$ for $b \gg a$), which is reasonably compatible with SpeCyl's achievement, and the critical proximity $(b/a)^{\text{crit}}$ is very well reproduced. The main differences are that the growth rate is actually null in the stability region and that, even if reasonably compatible with SpeCyl, the agreement of JOREK results with the model predictions is slightly better. The better agreement found by JOREK can be possibly explained in terms of the different choice in the boundary conditions: the fluid part (Eqs. B.5-B.6) should have a minor role since the flow velocity is already quite damped at the interface radius (see Fig. B.7.(b) for SpeCyl), whereas the condition on the normal magnetic field ($\hat{\mathbf{n}} = \hat{\mathbf{r}}$ in SpeCyl) could indeed make some difference. In fact, while SpeCyl has a general thin-shell condition, JOREK enforces a linearised ideal MHD relation, that is possibly more adequate to reproduce an ideal kink in the straight tokamak.

B.3   Final summary

This Appendix has presented our first structured formulation of a full-spectrum magneto-fluid set of boundary conditions: SpeCyl.2. It combines the thin-shell modelling for the magnetic boundary described in Chap. 6 and the full-spectrum edge velocity generalisation presented in Chap. 7, with the further addition of possibly finite full-spectrum tangential velocity components. We have presented an overview of this explorative set in Sec. B.1: despite some important aspects of the fluid part of our boundary will need being substantially reformulated (see Chap. 8), the magnetic part and the overall structure are already in their final version.

Section B.2 presented a rich nonlinear benchmark against the ideal external kink modes $(1,1)$ and $(2,1)$. As already for the previous formulations of SpeCyl (SpeCyl.1 and SpeCyl.2.V00), the instability of modes cannot be achieved without enforcing a pseudo-vacuum region. However, when compared to SpeCyl.1, for the same ideal wall proximity, the width of the pseudo-vacuum region is now much reduced, with a consequent significant reduction of computational time. As a matter of fact, for an ideal wall displacement

(a) Growth rates.

(b) Radial profiles of $v_r^{1,-1}$ and $B_r^{1,-1}$.

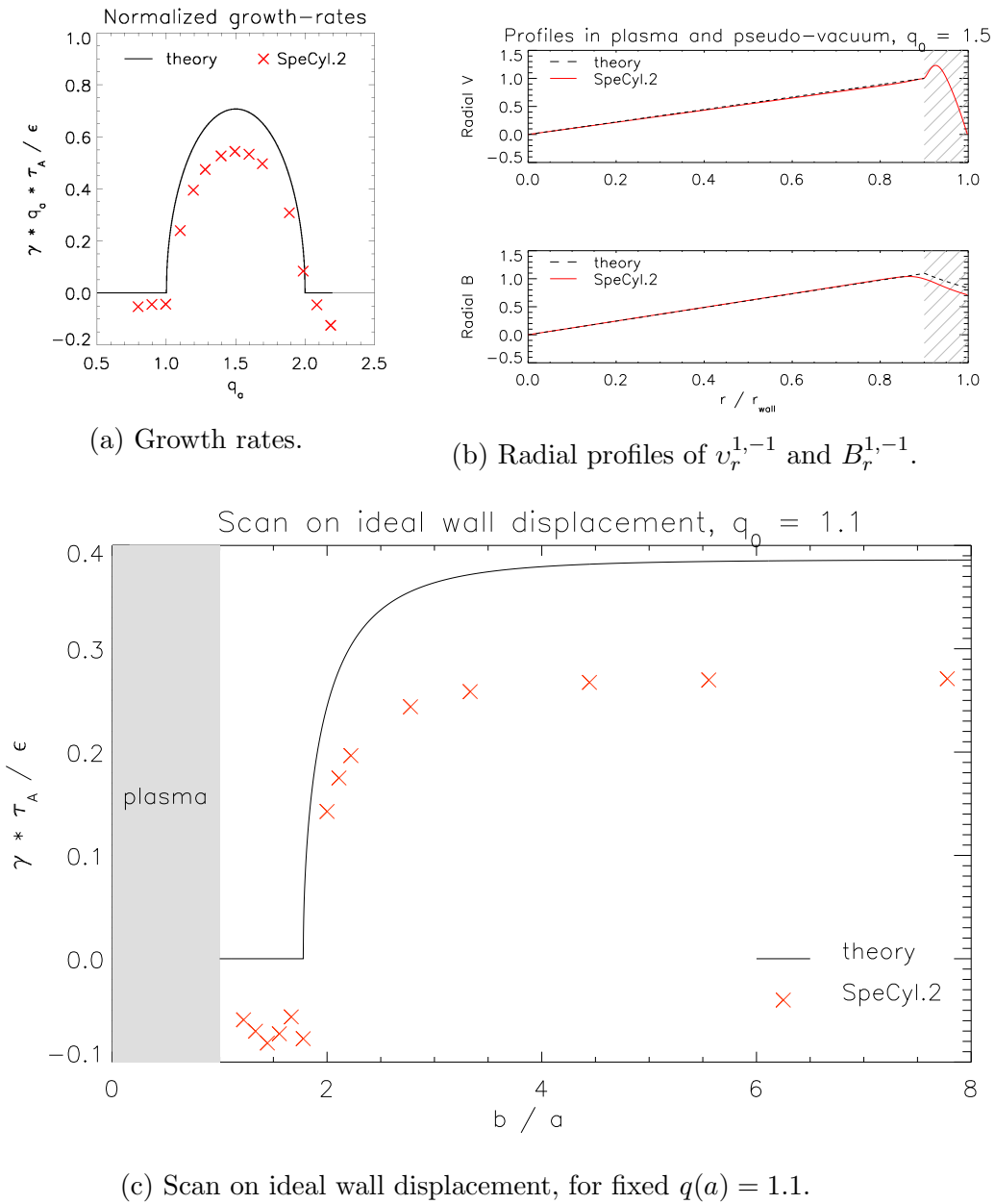(c) Scan on ideal wall displacement, for fixed $q(a) = 1.1$.

Figure B.7: Nonlinear benchmark of SpeCyl.2 against the external kink $2,1$ for the Shafranov's flat-current model.

$b/a = 3$ (no-wall limit) and with the general set-up for the nonlinear bench-mark against kink modes $2, 1$ with $R/a = 20$, the computational time has been reduced from around 1.5 days to approximately 3 hours.

The results presented in Sec. B.2 show very promising achievements for the mode $(1, 1)$, especially for the flat-current model, both concerning profiles and growth rates. A relatively good agreement is also obtained for modes $(2, 1)$, in fair agreement with some works performed with JOREK-STARWALL in a similar set-up. In particular, the surprising negative trend in the benchmark agreement rate with varying Lundquist number is observed in both codes and we think it can be possibly related to the presence of a pseudo-vacuum region that need to keep as resistive as possible. Also, a study of the stabilising effect of the outer ideal wall has found interesting similarities between the two codes, albeit not perfectly compatible initial set-ups and the enforcement of two different sets of boundary conditions.

Albeit qualitatively good, the presented numerical results remain unsatisfactory for more than one aspect. First of all, the need for a pseudo vacuum region seems to reduce the relevance of the complex reformulation of our fluid boundary conditions. It can be objected that the real physical case of an experiment does never present a sharp density edge and that a cold and resistive plasma halo is always present around the hot core: SpeCyl.2 could capture more effectively the dynamics of this halo, its impinging on wall with finite velocity or extracting particles inflows. The question remains whether this contribution is such to motivate the great deal of work spent on it.

Also, even by enforcing the pseudo-vacuum regime at plasma boundary, the numerical benchmark results are not completely satisfying and would need further optimisation. There are indeed examples in literature of a better non-linear benchmark agreement than the one presented here [Becerra16, Marx17, Merkel15].

Bibliography

[Alimonti17] Alimonti, G., Brambilla, R., Pileci, R., Romano, R., Rosa, F., and Spinicci, L.: "Edible energy: balancing inputs and waste in food supply chain and biofuels from algae", Eur. Phys. J. Plus, **132**, 14 (2017)

[Artola18] Artola Such, F. J.: "Free boundary simulations of MHD plasma instabilities in tokamaks", PhD thesis at the Univ. of Aix-Marseille, chap. 2-3: `https://tel.archives-ouvertes.fr/tel-02012234` (2018)

[Baruzzo11] Baruzzo, M., Bolzonella, T., Cavazzana, R., In, Y., Marchiori, Marrelli, L., G., Martin, P., Martinez, E., Okabayashi, M., Paccagnella, R., Piovesan, P., Piron, L., Soppelsa, A., Terranova, D., and Zanca, P.: "Feedback control of the $m = 2, n = 1$ mode in RFX-mod tokamak plasmas with $q_{\text{cyl}}(a) \approx 2$", 38th EPS Conference, P2.091 (2011)

[Baruzzo12] Baruzzo, M., Bolzonella, T., Liu, Y. Q., Manduchi, G., Marchiori, G., Soppelsa, A., Takechi, M., and Villone, F.: "RWM control studies on RFX-mod with a limited set of active coils", Nucl. Fusion, **52**, 103001 (2012)

[Becerra16] Becerra, A.L.: "Resistive wall and error field studies using the extended MHD code NIMROD", MSc thesis at the University of Wisconsin - Madison, chap. 3: `https://cptc.wisc.edu/wp-content/uploads/sites/327/2017/09/UW − CPTC_17 − 2.pdf` (2016)

[Bertin82] Bertin, G.: "Effects of local current gradients on magnetic reconnection", Phys. Rev. A, **25**, 1786-1789 (1982)

[Betti16] Betti, R., Hurricane, O. A.: "Inertial-confinement fusion with lasers", Nature Phys., **12**, 435–448 (2016)

[Bettini17] Bettini, P., Finotti, C., Grando, L., Marchiori, G., Specogna, R: "Modeling of the magnetic field errors of RFX-mod upgrade", Fus. Eng. and Design, **123**, 518-521 (2017)

[Bolzonella01] Bozonella, T., Martin, P., Martini, S., Marrelli, L., Pasqualotto, R., and Terranova, D.: "Quasistationary Magnetic Fluctuation Control in the Reversed Field Pinch: A Proof of Principle Experiment", PRL, **87**, 19, 195001 (2001)

[Bondeson84] Bondeson, A., Sobel, J.R.: "Energy balance of the collisional tearing mode", Phys. of Fluids, 27 (8), 2028-34 (1984)

[Bonfiglio05] Bonfiglio, D., Cappello, S., Escande, D. F.: "ominant Electrostatic Nature of the Reversed Field Pinch Dynamo", PRL, **94**, 145001 (2005)

[Bonfiglio07] Bonfiglio, D., Cappello, S., Piovan, R., Spizzo, G., Terranova, D.: "Preliminary results of 3D non–linear MHD simulations for ultra-low q plasmas and OPCD RFP discharges", 12th IEA/RFP Workshop, Kyoto (28 March 2007)

[Bonfiglio10] Bonfiglio, D., Chacòn, L., Cappello, S.: "Nonlinear three-dimensional verification of the SPECYL and PIXIE3D magnetohydrodynamics codes for fusion plasmas", Phys. of Pl., **17**, 082501 (2010)

[Bonfiglio13] Bonfiglio, D., Veranda, M., Cappello, S., Escande, D. F., and Chacón, L.: "Experimental-like helical self-organization in reversed-field pinch modeling", PRL, **111**, 085002 (2013)

[Bonfiglio19] Bonfiglio, D., Cappello, S., Escande, D. F., Di Giannatale, G., Kryzhanovskyy, A., Veranda, M., Marrelli, L., and Zanca, P.: "Effect of a realistic boundary on the helical self-organization of the RFP", 46th EPS Conference, Milan, P1.1049 (2019)

[Bustreo19] Bustreo, C., Giuliani, U., Maggio, D., and Zollino, G.: "How fusion power can contribute to a fully decarbonized European power mix after 2050", Fus. Eng. and Design, **146**, B, 2189-1293 (2019)

[Calabrese13] Calabrese, E.: "Modelli teorici per stati elicoidali nella con gurazione Reversed-Field Pinch", MSc Thesis at the University of Padova (2013)

[Cappello92] Cappello, S., Paccagnella, R.: "Nonlinear plasma evolution and sustainment in the reversed field pinch", Phys. of Fluids B, **4**, 3, 611-618 (1992)

[Cappello96] Cappello, S., Biskamp, D.: "Reconnection processes and scaling laws in reversed field pinch magnetohydrodynamics", NF **36**, 571 (1996)

[Cappello00] Cappello, S., Escande, D. F.: "Bifurcation in Viscoresistive MHD: The Hartmann Number and the Reversed Field Pinch", PRL, **85**(18), 3838-41 (2000)

[Cappello03] Cappello, S.: "MHD nonlinear behaviour and dynamo in RFP with external drive of poloidal electric field (PPCD)", 9th IEA/RFP Workshop Tsukuba (5-7 March 2003)

[Cappello04] Cappello, S.: "Bifurcation in the MHD behaviour of a self-organizing system: the reversed field pinch (RFP)", Plasma Phys. Control. Fusion, **46**, B313 (2004)

[Cappello06] Cappello, S., Bonfiglio, D., Escande, D. F.: "Magnetohydrodynamic dynamo in reversed field pinch plasmas: electrostatic drift nature of the dynamo velocity field", Phys. of Plasm., **13**, 056102 (2006)

[Cappello08] Cappello, S., et al.: "The Reversed Field Pinch toward magnetic order: a genuine self-organization", American Institute of Physics 978-0-7354-0600 (2008)

[Chacón04] Chacón, L., "A non-staggered, conservative, $\nabla \cdot b = 0$ finite-volume scheme for 3d implicit extended magnetohydrodynamics in curvilinear geometries", Computer Physics Communications **163**, 143–171 (2004)

[Chacón06] Chacón, L., and Knoll, D. A.: "A fully implicit 3D extended magnetohydrodynamics algorithm", 33rd EPS conference proceedings, **30I**, 1.164, (19-23 June 2006)

[Chacón08] Chacón, L.: "An optimal, parallel, fully implicit Newton–Krylov solver for three-dimensional viscoresistive magnetohydrodynamics", Phys. of Pl., **15**, 056103 (2008)

[Chapman10] Chapman, I. T., et al.: "Saturated ideal modes in advanced tokamak regimes in MAST", Nucl. Fus., **50**, 045007 (2010)

[Chapman14] Chapman, I. T., Brunetti, D., et al.: "Three-dimensional distortions of the tokamak plasma boundary: boundary displacements in the presence of saturated MHD instabilities", Nucl. Fusion, **54**, 54 (2014)

[Cianciosa17] Cianciosa, M., Wingen, A., Hirshman, S. P., Seal, S. K., Unterberg, E. A., Wilcox, R. S., Piovesan, P., Lao, L., and Turco, F.: "Helical core reconstruction of a DIII-D hybrid scenario tokamak discharge", Nucl. Fusion, **57**, 076015 (2017)

[Delgado13] Delgado-Aparicio, L., et al.: "Formation and Stability of Impurity "Snakes" in Tokamak Plasmas", PRL, **110**, 065006 (2013)

[Delzanno08] Delzanno, G.L., et al.: "Electrostatic mode associated with the pinch velocity in reversed field pinch simulations", Phys. of Pl., **15**, 122102 (2008)

[DiGiannatale19] Di Giannatale, G.: "Magnetic confinement properties of 3D equilibria for fusion plasmas: non linear MHD modelling and experimental comparisons", PhD Thesis at the University of Padova (2019)

[Ebrahimi03] Ebrahimi, F., Prager, S. C., Sarff, J. S., and Wright, J. C.: "The three-dimensional magnetohydrodynamics of ac helicity injection in the reversed field pinch", Phys. of Plasm., **10**, 999-1014

[Escande13] Escande, D.: "What is a reversed field pinch?", ffhal-00909102f (2013)

[Fellin95] Fellin, L., Kusstatscher, P., Rostangni, G.: "Overall plant design, layout and commissioning", Fusion Eng. and Design, **25**, 315-333 (1995)

[Ferraro16] Ferraro, N. M., Jardin, S. C., Lao, L. L., Shephard, M. S., and Zhang, F.: "Multi-region approach to free-boundary three-dimensional tokamak equilibria and resistive wall instabilities", Phys. of Plasm., **23**, 056114 (2016)

[Fil15] Fil, A.: "Modélisation des disruptions déclenchées par injection massive de gaz dans les plasmas de tokamaks", PhD thesis at IRFM, CEA, Cadarache (2015)

[Finn92] Finn, J. M., Nebel, R., and Bathke, C.: "Single and multiple helicity Ohmic states in reversed-field pinches", Phys. of Fluids B: Plas. Phys., **4**, 5, 1262-1279 (1992)

[Finn95] Finn, J. M.: "Resistive wall stabilization of kink and tearing modes", Phys. of Pl., 2, 198 (1995)

[Fitzpatrick99] Fitzpatrick, R.: "Formation and locking of the "slinky mode" in reversed-field pinches", Phys. of Plasm., **6**(4), 1168 (1999)

[Fitzpatrick13] Fitzpatrick, R.: "Computational physics", tutorial from Austin Univ.: `https://archive.org/details/flooved3259` (2013)

[Fitzpartick22] Fitzpatrick, R.: "Plasma Physics, an introduction", CRC Press (2022)

[Freidberg14] Freidberg, J.P.: "Ideal MHD", chap. 8 and 11, Cambridge Univ. Press (2014)

[FRS73] Furth, H.P., Rutherford, P.H., and Seldberg, H.: "Tearing mode in the cylindrical tokamak", The Phys. of Fluids, 16, 1, 1054 (1973)

[Gill92] Gill, R. D., Edwards, A. W., Pasini, D., Weller, A.: "Snake-like density perturbations in JET", Nucl. Fus., **32**, 723 (1992)

[Gimblett86] Gimblett, C.G.: "On free boundary instabilities induced by a resistive wall", Nucl. Fus., **26**, 5, 617 (1986)

[Gormezano04] Gormezano, C., Becoulet, A., Buratti, P., Carraro, L., Crisanti, F., Esposito, B., Giruzzi, G., Guirlet, G., Hoang, G. T., Joffrin, E., Litaudon, X., Luce, T., Pericoli-Rodolfini, V., Sauter, O., Sips, A. C. C., Tuccillo, A., and the JET EFDA Contributors: "Hybrid advanced scenarios: perspectives for ITER and new experiments with dominant RF heating", Plasma Phys. Control. Fusion, **46**, B435 (2004)

[Gottlieb03] Gottlieb, S., et al.: "Strong stability preserving properties of Runge-Kutta time discretization for linear constant coefficient operators", Journal of Scient. Comput., 18, 1 (2003)

[Greenwald10] Greenwald, M.: "Verification and validation for magnetic fusion", Phys. of Plasmas, **17**, 058101 (2010)

[Gregoratto98] Gregoratto, D., et al.: "Behaviour of electron density profiles and particle transport analysis in the RFX reversed field pinch", NF **38**, 1199 (1998)

[Griffiths22] Griffiths, T., Pearson, R., Bluck, M., and Takeda, S.: "The commercialisation of fusion for the energy market: a review of socio-economic studies", Prog. Energy, **4**, 042008 (2022)

[Hagens20] Hagens, N. J.: "Economics for the future – Beyond the superorganism", Ecol. Econ., **169**, 106520 (2020)

[Han09] Han, W. E., Wards, D. J.: "Revised assessments of the economics of fusion power", Fusion Eng. and Design, **84**, 895-898 (2009)

[Haines13] Haines, M. G., Gimblett, C. G., and Hastie, R. J.: "Intrinsic rotation due to mhd activity in a tokamak with a resistive wall", Plasma Physics and Controlled Fusion **55**, 055002 (2013)

[Hender89] Hender, T. C., Gimblett, C. G., Robinson, D. C.: "Effects of a resistive wall on magnetohydrodynamic instabilities", Nucl. Fus., **29**, 1279 (1989)

[Hirshman83] Hirshman, S. P., and Whitson, J. C.: "Steepest-descent moment method for three-dimensional magnetohydrodynamic equilibria", Phys. of Fluids, **26**, 3553-3568 (1983)

[Hirshman85] Hirshman, S. P., and Meier, H. K.: "Optimized Fourier representations for three-dimensional magnetic surfaces", Phys. of Fluids, **28**, 1387-1391 (1985)

[Hu22] Hu, Y., He, K., Wang, J, Xu, X.: "Neutral beam current drive in a tokamak", eprint arXiv:2211.10900 (2022)

[Hurst22] Hurst, N. C., Chapman, B. E., Almagri, A. F., Cornille, B. S., Kubala, S. Z., McCollam, K. J., Sarff, J. S., Sovinec, C. R., Anderson, J. K., Den Hartog, D. J., Forest, C. B., Pandya, M. D., and Solsrud, W. S.: "Self-organized magnetic equilibria in tokamak plasmas with very low edge safety factor", Phys. of Plasmas, **29**, 080704 (2022),

[IEA98] "The Link Between Energy and Human Activity", IEA, Paris, License: CC BY 4.0 (1998)

[Jackson99] Jackson, J. D.: "Classical Electrodynamics", 3rd edition, p. 195-196, Wiley (1999)

[JET22] "Annual Report and Accounts: 2021-22", UK Atomic Energy Authority, Abingdon (2022)

[Koliner16] Koliner, J. J., Cianciosa, M. R., Boguski, J., Anderson, J. K., Hanson, J. D., Chapman, B. E., Brower, D. L., Den Hartog, D. J., Ding, W. X., Duff, J. R., Goetz, J. A., McGarry, M., Morton, L. A., Parke, E.: "Three dimensional equilibrium solutions for a current-carrying reversed-field pinch plasma with a close-fitting conducting shell", Phys. of Plasm., **23**(3), 032508 (2016)

[Kruger04] Kruger, S. E., Sovinec, C. R., Schack, D. D., Held, E. D.: "Free-boundary simulations of diii-d plasmas with the nimrod code", Comput. Phys. Commun., **164**, 1-3, 34-39 (2004)

[Lee23] Lee, H., et al.: "Synthesis report of the IPCC sixth assessment report", IPCC AR6 SYR (2023)

[Liu08] Liu, Y., et al.: "An analytical demonstration of coupling schemes between magnetohydrodynamics codes and eddy current codes", Phys. Pl., **15**, 072516 (2008)

[Lorenzini09] Lorenzini, R., Martinez, E., Piovesan, P., et al.: "Self-organized helical equilibria as a new paradigm for ohmically heated fusion plasmas", Nature, Phys., **5**, 570-574 (2009)

[Marchiori09] Marchiori, G., Luchetta, A., Manduchi, G., Marrelli, L., Soppelsa, A., Villone, F., Zanca, P.: "Advanced MHD mode active control at RFX-mod", Fus. Eng. and Design, **84**, 1249–1252 (2009)

[Marchiori12] Marchiori, G., Baruzzo, M., Bolzonella, T., Liu, Y. Q., Soppelsa, A., and Villone, F.: "Dynamic simulator of RWM control for fusion devices: modelling and experimental validation on RFX-mod", Nucl. Fusion, **52**, 023020 (2012)

[Marrelli19] Marrelli, L., et al.: "Upgrades of the RFX-mod Reversed Field Pinch and expected scenario improvements", Nucl. Fus., **59**, 076027 (2019)

[Marrelli21] Marrelli, L., et al.: "The reversed field pinch", Nucl. Fusion, **61**, 023001 (2021)

[Marx17] Marx, A., Lütjens, H.: "Free-boundary simulations with the XTOR-2F code", Plasma Phys. Control. Fusion, **59**, 064009 (2017)

[McAdams14] Mc Adams, R.: "Non-linear Magnetohydrodynamic Instabilities In Advanced Tokamak Plasmas", PhD thesis at the University of York, chap. 5: `https://etheses.whiterose.ac.uk/7723/` (2014)

[Merkel15] Merkel, P., and Strumberger, E.: "Linear MHD stability studies with the STARWALL code", arXiv:1508.04911 (2015)

[Merlin89] Merlin, D., Biskamp, D.: "Numerical studies of MHD tubulence in the reversed field pinch", IPP 6/276 (1989)

[Militello04] Militello, F., Huysmans, G., Ottaviani, M., and Porcelli, F.: "Effects of local features of the equilibrium current density profile on linear tearing modes", Phys. of Plasm., **11**(1), 125 (2004)

[Nalesso80] Nalesso, G. F., Costa, S.: "The influence of a thick resistive wall on the stability of a pinch", Nucl. Fus., **20**, 4 (1980)

[NIF22] National ignition facility yearly report of activities (2022): $\mathtt{https://annual.llnl.gov/fy-2022/national-ignition-facility-2022}$

[Ono22] Ono, M., Bertelli, N., Shevchenko, V., Idei, H., and Hanada, K.: "Efficient electron cyclotron current drive regime for plasma current start-up in fusion reactors", Phys. Rev. E, **106**, L023201 (2022)

[Paccagnella07] Paccagnella, R., Terranova, D., Zanca P.: "Modelling and interpretation of MHD active control experiments in RFX-mod", Nucl. Fus., **47**, 990-996 (2007)

[Peeters00] Peeters, A. G.: "The bootstrap current and its consequences", Pl. Phys. and Contr. Fus., **42**, B231 (2000)

[Peruzzo18] Peruzzo, S., et al.: "Detailed design of the RFX-mod2 machine load assembly", Fus. Eng. and Design", **136**, 1605-1613 (2018)

[Petrie07] Petrie, G. J. D.: "Potential Magnetic Field around a Helical Flux-rope Current Structure in the Solar Corona", The Astroph. Journal, **661**, 551-557 (2007)

[Petty16] Petty, C. C., et al.: "High-beta, steady-state hybrid scenario on DIII-D", Nucl. Fusion, **56**, 016016 (2016)

[Piovesan11] Piovesan, P., Bonfiglio, D., Bonomo, F., Cappello, S., Carraro, L., Cavazzana, R., Gobbin, M., Marrelli, L., et al.: "Influence of external 3D magnetic fields on helical equilibrium and plasma flow in RFX-mod", Plas. Phys. and Contr. Fus., **53**, 084005 (2011)

[Piovesan13] Piovesan, P., Bonfiglio, D., Auriemma, F., Bonomo, F., Carraro, L., Cavazzana, et al.: "RFX-mod: A multi-configuration fusion facility for three-dimensional physics studies", Phys. of Plasmas, **20**, 056112 (2013)

[Piovesan17] Piovesan, P., Bonfiglio, D., et al.: "Role of a continuous MHD dynamo in the formation of 3D equilibria in fusion plasmas", Nucl. Fus., **57**, 076014 (2017)

[Porcelli87] Porcelli, F.: "Viscous resistive magnetic reconnection", Phys. of Fl., **30**, 1734 (1987)

[Proll14] Proll, H. E. P.: "Trapped-particle instabilities in quasi-isodynamic stellarators", PhD thesis at IPP Greifswald, Germany (2014)

[Puiatti03] Puiatti, M. E., Cappello, S., Lorenzini, R., et al.: "Analysis and modelling of the magnetic and plasma profiles during PPCD experiments in RFX", Nucl. Fus., **43**, 1057-1065 (2003)

[Ramasamy22] Ramasamy, R., et al.: "Modeling of saturated external MHD instabilities in tokamaks: A comparison of 3D free boundary equilibria and nonlinear stability calculations", Phys. of Plasmas, **29**, 072303 (2022)

[Rezaee21] Rezaee, A., Bozorg-Haddad, O., Singh, V. P.: "Economical, Political, and Social Issues in Water Resources", chap. 11, Elsevier (2021)

[Salari02] Salari, K., Knupp, P.: "Code verification by the method of manufactured solutions", Journal of Fluids Eng., 124(1), 4-10 (2002)

[Sarff94] Sarff, J. S., Hokin, S. A., Li, H., Prager, S. C., Sovinec, C. R.: "Fluctuation and transport reduction in a reversed field pinch by inductive poloidal current drive", PRL, **72**, 3670 (1994)

[Sarff15] Sarff, J. S., et al.: "Overview of results from the MST reversed field pinch experiment", Nucl. Fusion, **55**, 104006 (2015)

[Shafranov70] Shafranov, V. D.: "Hydromagnetic stability of a current-carrying pinch in a strong longitudinal magnetic field", Sov. Tech. Phys. Tech., 15, 2, 175 (1970)

[Schnack86] Schack, D. D., Barnes, D. C., et al.: "Semi-implicit magnetohydrodynamics calculations", Jour. of Comp. Phys. **70**, 330-354 (1987)

[Smil94] Smil, V.: "Energy in the World History", Westview Press, Boulder (1994)

[Spinicci21] Spinicci, L., Bonfiglio, D., Cappello, S., and Veranda, M.: "Numerical benchmark and improvement of SpeCyl's boundary conditions", 19th EFTC conference, #55 (14/10/2021)

[Spinicci22] Spinicci, L., Bonfiglio, D., Cappello, S., Veranda, M., and Chacón, L.: "Formulation and numerical benchmark of improved magneto fluid-dynamics boundary conditions for 3D nonlinear MHD code SPECYL", 48th EPS conference proceedings, #79, P5b.102 (1st July 2022)

[Strauss04] Strauss, H. R., Pletzer, A., Park, W., Jardin, S., Breslau, J., and Sugyama, L.: "MHD simulations with resistive wall and magnetic separatrix", Computer Phys. Communications, **164**, 40-45 (2004)

[Süli14] Süli, E.: "Numerical solution of ordinary differential equations", tutorial from the Math. Inst. (Oxford), chap. 1: `http://people.maths.ox.ac.uk/suli/nsodes.pdf` (2014)

[Tang02] Tang, W. M.: "Advanced computations in plasma physics", Phys. of Plasmas, **9**, 1856 (2002)

[Terranova07] Terranova, D., Alfier, A., Bonomo, F., Franz, P., Innocente, P., and Pasqualotto, R.: "Enhanced Confinement and Quasi-Single-Helicity Regimes Induced by Poloidal Current Drive", PRL **99**, 095001 (2007)

[Terranova13] Terranova, D., Marrelli, L., Hanson, J. D., Hirshman, S. P., Cianciosa, M., and Franz, P.: "Helical equilibrium reconstruction with V3FIT in the RFX-mod Reversed Field Pinch", Nucl. Fusion, **53**, 113014 (2013)

[Veranda13] Veranda, M., Bonfiglio, D., Cappello, S.: "Stimulated Quasi Helical dynamics in pinch configurations", 40th EPS Conference, P4.121 (2013)

[Veranda17] Veranda, M., Bonfiglio, D., Cappello, S., Escande, D. F., Auriemma, F., Borgogno, D., Chacón, L., Fassina, A., Franz, P., Gobbin, M., Grasso, D., Puiatti, M. E.: "Magnetohydrodynamics modelling successfully predicts new helical states in reversed-field pinch fusion plasmas", Nucl. Fus., **57**, 11, 116029 (2017)

[Veranda20] Veranda, M., Bonfiglio, D., Cappello, S., Di Giannatale, G., Escande, D. F.: "Helically self-organized pinches: dynamical regimes and magnetic chaos healing", Nucl. Fus., **60**, 016007 (2020)

[Viterbo99] Viterbo, M.: "Analisi della formazione di una perturbazione magnetica localizzata in un plasma RFP (Interazioni elettrodinamiche con un fluido conduttore)", PhD Thesis at the University of Padova (1999)

[Weller87] Weller, A., Cheetham, A. D., Edwards, A. W., Gill, R. D., Gondhalekar, A., Granetz, R. S., Snipes, J., and Wesson, J. A.: "Persistent Density Perturbations at Rational-q Surfaces Following Pellet Injection in the Joint European Torus", PRL, **59**, 20 (1987)

[Wesson78] Wesson, J. A.: "Hydromagnetic stability of tokamaks", Nucl. Fus., 18, 1 , 87 (1978)

[Wesson04] Wesson, J. A.: "Tokamaks", 3rd ed., chap. 6, Oxford Univ. Press (2004)

[White06] White, R. B.: "The theory of toroidally confined plasmas", 2nd ed., chap. 4, World Scientific (2006)

[Wilson] Wilson, H.: "Modelling the neoclassical tearing mode", Tutorial for Ipam, download from: $https://www.ipam.ucla.edu/abstract/?tid = 5334$ (download date: 26 March 2023)

[Zanca12] Zanca, P., Marrelli, L., Paccagnella, R., Soppelsa, A., Baruzzo, M., Bolzonella, T., Marchiori, G., Martin, P., and Piovesan, P.: "Feedback control model of the $m = 2$, $n = 1$ resistive wall mode in a circular plasma", Plasma Phys. Control. Fusion, **54**, 094004 (2012)

[Zhang14] Zhang, X. J., et al.: "Lower hybrid current drive and ion cyclotron range of frequencies heating experiments in H-mode plasmas in Experimental Advanced Superconducting Tokomak", Phys. of Plas., **21**, 061501 (2014)

[Zohm96] Zohm, H.: "Edge localized modes (ELMs)", Plasma Phys. Control. Fusion, **38**, 105 (1996)

[Zuin17] Zuin, M., et al.: "Overview of the RFX-mod fusion science activity", Nucl. Fusion, **57**, 102012 (2017)